INVESTIGATIONS ON NOVEL PROCESSING METHODS FOR CERAMIC FOAMS

A Thesis submitted

in partial fulfilment for the Degree of

Doctor of Philosophy

by

SUJITH VIJAYAN

Department of Chemistry

INDIAN INSTITUTE OF SPACE SCIENCE AND TECHNOLOGY

Thiruvananthapuram- 695547

November, 2017

CERTIFICATE

This is to certify that the thesis entitled **Investigations on Novel Processing Methods of Ceramic Foams**, submitted by Sujith Vijayan, to the Indian Institute of Space Science and Technology, Thiruvananthapuram, in partial fulfillment for the award of the degree of **Doctor of Philosophy**, is a *bona fide* record of research work carried out by him under my supervision. The contents of this thesis, in full or in parts, have not been submitted to any other Institution or University for the award of any degree or diploma.

Dr. K. Prabhakaran
Supervisor
Associate Professor
Department of Chemistry

Thiruvananthapuram
November, 2017

Counter signature of HOD with seal

DECLARATION

I declare that this thesis entitled **Investigations on Novel Processing Methods for Ceramic Foams** submitted in partial fulfillment of the degree of **Doctor of Philosophy** is a record of original work carried out by me under the supervision of Dr. K. Prabhakaran, and has not formed the basis for the award of any other degree or diploma, in this or any other Institution or University. In keeping with the ethical practice in reporting scientific information, due acknowledgements have been made wherever the findings of others have been cited.

Sujith Vijayan

SC12D009

Thiruvananthapuram - 695 547

16/11/2017

ACKNOWLEDGEMENTS

I would like to thank all people who have helped and encouraged me during my study at Indian Institute of Space Science and Technology.

First and foremost, I would like to express my heartfelt gratitude towards my supervisor Dr. K. Prabhakaran for giving me the opportunity to work under his supervision and also for his academic guidance, continuous support and encouragement throughout this research work. I have been extremely lucky to have a supervisor who cared so much about my work, and who responded to my questions and queries so promptly by providing with is precious time.

I use this opportunity to thank Dr. V.K. Dadhwal, Director, IIST and Dr. K.S. Das Gupta, former Director, IIST for providing me with all the necessary facilities. It is my pleasure to extent my deep gratitude to Prof. Kuruvilla Joseph, Dean (Student Activities) and Prof. Nirmala Rachel James, Head Department of Chemistry for their continuous support and encouragement during my stay. The financial assistance from IIST is gratefully appreciated.

I extend my heartfelt thanks to doctoral committee members, Dr. H.K. Verma, Dr. U.S. Hareesh, Dr. Siby Varghese, Dr. P. Chakravarthy and Dr. Jobin Cyriac. I am very grateful to their guidance, constructive criticism and enthusiastic support during my research. I am indebted to all the faculty members of Department of Chemistry for their whole hearted support.

I am deeply indebted to members of VSSC, NIIST, SCTIMST, SAIF IIT Madras and CESS for the characterization of my samples throughout

my research. I am greatly indebted to Dr. Sreeja Remani, ICMPD VSSC for her help with my experimental work and also for sharing her lab resources with me. I offer my sincere appreciation especially to Dr. R. Narasimman, and Mr. Praveen Wilson who have shared lot of knowledge during experimental and also for their fruitful discussions during my thesis work. I am thankful to my friends Dr. Vinu RV, Dr. Raneesh Konnola, Dr. Mohammed Mukthar Ali, Mr. Rakesh R, Mr. Najeeb PK, Mr. Abhishek Chakraborty, Mr. Swagat Ranjan Das and Mr. Sabu Maria for their sincere help and support. I am also thankful to my fellow research scholars Mr. Manjunath Ganiga, Dr. Deepthi Sivadas, Ms. Reshma C, Mrs. Aswathy, Ms. Meegle Mathew and Ms. Devirenuka K of Department of Chemistry for their sincere help and whole hearted support. I would like to sincerely thank Mr. Sreekumaran Nair for his effort to correct my thesis. I also take this opportunity to thank Mr. Dileep Kumar, Mr. Loveson, Mrs. Rehna, Mrs. Jayashree R and Mrs. Jayashree L for their friendship and kind assistance. I would like to thank staffs of Library IIST for their assistance in setting and printing of this thesis.

Last but not least, I would like to thank my parents and my sister for their constant love and support during the time of this thesis. They always cheered me up and kept me motivated. I would like to extend my sincere gratitude to each and every one who has rendered their help directly or indirectly during this research.

Abstract

Ceramic foams are macroporous ceramics with porosity greater than 60 vol.%. They have high specific strength, low density, low thermal conductivity, controlled permeability, high surface area, corrosion resistance, high temperature stability, good bio-affinity, chemical inertness and low dielectric constant. Ceramic foams find excellent applications as high temperature thermal insulation, filter media for molten metals, lightweight structural parts, catalyst support, bio-implants, scaffold for tissue engineering and pre-form for polymer-ceramic and metal-ceramic composites. Ceramic foams are prepared via powder pressing and colloidal processing techniques. The powder pressing method mostly limited to ceramic foams of lower porosity while the colloidal processing produces foams of higher porosity. The current processing methods for the preparation of ceramic foams use synthetic organic polymers or monomers, surfactant molecules and solvents as the processing additives. Replacement of these processing additives with non-toxic naturally renewable molecules is of great economic and environmental importance. Controlling the porosity, pore size and pore morphology is of utmost importance as it can change the properties of the ceramic foams. The main objective of this thesis is to study novel methods for the preparation of ceramic foams with a wide range of porosity and cell size. Another objective is to use bio-renewable resources as processing additives for the preparation of ceramic foams.

The naphthalene-in-aqueous alumina slurry emulsions (AAS) with naphthalene to alumina slurry volume ratios in the range of 1 to 1.86 prepared from slurries of 10, 20 and 30 vol.% alumina concentration are studied to prepare ceramic foams. The emulsions show a viscosity (at 9.3 s^{-1} shear rate) and yield stress in the ranges of 0.175 to 1.025 Pa.s and 0.7 to 5.3 Pa, respectively. The emulsions cast in the glass moulds form stable gels on cooling to room temperature (~30 ^{o}C) due to the solidification of naphthalene and physical cross-linking of the carrageenan present in the alumina slurry. Alumina foams obtained by drying, oil removal and sintering of the gelled emulsion bodies show porosity in the range of 65 to 90 vol.%. The average compressive strength and Young's modulus values obtained are in the

ranges of 0.60 to 28.75 MPa and 36 to 1230 MPa, respectively, for the alumina foams with porosity in the range of 65 to 90 vol.%.

The freeze gelcasting of hydrogenated vegetable oil-in-aqueous alumina slurry (HVO-in-AAS) emulsions is studied to prepare ceramic foams. Medium to high internal phase emulsions (HVO to AAS volume ratio from 1.34 to 2.69) are prepared by dispersing HVO containing sodium dodecyl sulphate emulsifying agent in 10, 20 and 30 vol.% AAS containing carrageenan at 85 ^{o}C. The HVO-in-AAS emulsions show an increase in viscosity (0.225 to 2.07 Pa.s at shear rate of 9.3 s^{-1}) and yield stress (0.3 to 10.3 Pa) with an increase in HVO to AAS volume ratio and alumina concentration in the AAS. The emulsions cast in moulds undergo gelation on cooling to room temperature due to the solidification of HVO and physical cross-linking of carrageenan. Compressive strength (20 to 150 kPa) and Young's modulus (120 to 1550 kPa) of the gelled emulsion bodies increase with an increase in HVO to AAS volume ratio and AAS concentrations. The alumina foams obtained by drying, oil extraction and sintering of gelled emulsion bodies show interconnected cellular structure with near spherical cell morphology. Alumina foams with porosity in the range of 70.7 to 92.5 vol.% could be prepared by the freeze casting of HVO-in-AAS emulsions. The cell size and cell interconnectivity of the foams depend on the alumina slurry concentration and HVO to AAS volume ratio. The compressive strength (39.6 to 2.74 MPa) and Young' modulus (2350 MPa to 64.5 MPa) of alumina foams depends on HVO to AAS volume ratio and alumina slurry concentration.

Thermo-foaming of alumina powder dispersions in molten sucrose is used for the preparation of alumina foams. The hydrophilic interactions between the alumina particle surface and sucrose hydroxyl groups promote the alumina powder dispersion in the molten sucrose. The bubbles produced in the alumina powder dispersions due to the water vapour generated by the –OH to –OH condensation are stabilized by the alumina particles adsorbed on the gas-liquid interface and the increase in viscosity. The foaming and setting time of alumina powder dispersions decreases with an increase in foaming temperature and an increase in alumina powder to sucrose weight ratio ($\mathbf{W_{A/S}}$). The foam volume increases considerably with an increase in foaming temperature, reaches a maximum at a critical foaming

temperature and then decreases due to foam collapse. The sintering shrinkage decreases largely with an increases in $\mathbf{W_{A/S}}$ and marginally with an increase in foaming temperature. The porosity (83.4 to 94.6 vol.%) and cell size (0.55 to 1.6 mm) of the alumina foams depend on the foaming temperature (120 to 170 ^{o}C) and $\mathbf{W_{A/S}}$ (0.8 to 1.6). The compressive strength and Young's modulus of the alumina foams decrease with an increase in foaming temperature at all studied $\mathbf{W_{A/S}}$. A sintering strategy involving an initial pyrolysis step is optimized to prevent cracking of large foam bodies. The carbon produced by pyrolysis of sucrose polymer binds the alumina particles during the initial stages of shrinkage. The compressive strength (1.3 to 2 MPa) of the carbon bonded alumina foam bodies are high enough to make them amenable for machining operations such as milling and drilling. Magnesium nitrate (**MN)** is used as a blowing and setting agent for the alumina powder dispersions in molten sucrose for the preparation of alumina foams. The **MN** decreases the melting point of sucrose from 180 to 160 ^{o}C which makes the preparation of the powder dispersions easy. The H^{+} ions produced by the hydrolysis of **MN** catalyzes the –OH to –OH condensation reaction leading to faster foaming and setting of alumina powder dispersions in molten sucrose. A clear transition from partially interconnected cellular to completely interconnected reticulate-like foam structure occurs when the **MN** concentration increases from 4 to 8 wt%.

Thermo-foaming of alumina-silica co-dispersions in molten sucrose is studied for the preparation of mullite foams. The foaming & setting time decrease and foam rise increases with an increase in ceramic powder to sucrose weight ratio, foaming temperature and **MN** concentration. The phase pure mullite foam is formed by the reaction sintering of thermo-foamed bodies at 1600 ^{o}C. The reaction sintering of the thermo-foamed bodies without **MN** showed porous cell walls and struts due to improper densification. The MgO produced from **MN** aids the densification of mullite by forming a liquid phase as evidenced from the non-porous struts and cell walls at higher **MN** concentrations. The interconnectivity of the cells increases with an increase in **MN** concentration and reaches the level of reticulate-like foams at **MN** concentration of 12 wt% and above. The maximum porosity of 94.92 and 96.28 vol.% achieved without and with **MN**, respectively, is the highest reported for mullite foams. The maximum compressive strength of 1.34 MPa achieved at 93.6

vol.% porosity is more than four times that of mullite foams of similar porosity prepared by other processing routes.

Thermo-foaming of silicon powder dispersion in molten sucrose is studied for the preparation of SiC foams. The carbon produced by the pyrolysis of sucrose polymer is utilized for the formation of SiC by reaction sintering. Stable foams are obtained at foaming temperatures of 130 and 140 ^{o}C whereas partial foam collapse is observed at 150 ^{o}C. The composition of a sucrose-silicon powder mixture for producing SiC foam without considerable unreacted carbon is optimized. The sucrose in the sucrose-silicon powder mixture leave 24 wt% carbon during pyrolysis. The sintering additives such as alumina and yttria promoted the carbon-silicon reaction. Carbon enriched SiC nanowires of diameter in the range of 35 to 55 nm are observed on the cell wall surfaces as well as in the fractured strut region. The growth of nanowires is by both vapour-liquid-solid and vapour-solid mechanisms. Accelerated foaming & setting and increase in foam volume of silicon powder dispersions in molten sucrose is achieved in presence of **MN** blowing and setting agent. The compositions of sucrose–silicon powder mixture in the presence of 2 to 6 wt% **MN** are optimized to achieve stoichiometric carbon-silicon composite foams for reaction sintering as the **MN** decreases the carbon yield of sucrose. The SiC foam density (0.168 to 0.080 g/cm^3) and cell size (1.12 to 0.55 mm) decrease with an increase in **MN** concentration. The SiC foam prepared at 4 wt% **MN** shows the highest compressive strength (0.324 MPa) and specific compressive strength (3.43 MPa g^{-1}cm^3).

TABLE OF CONTENTS

List of Tables

LIST OF FIGURES

Abbreviations

AM	Acrylamide
AlN	Aluminum Nitride
Al_2O_3	Aluminium Oxide or Alumina
AAS	Aqueous Alumina Slurry
BSA	Bovine Serum Albumin
TBA	t-butyl alcohol
CTAB	Cetyltrimethylammonium Bromide
CS	Compressive Strength
DLVO	Derjaguin-Landau-Verwey-Overbee
DHF	2,5-dimethoxy-2,5-dihydrofuran
DSC	Differential Scanning Calorimetry
DTG	Derivative Thermogravimetric
EPS	Epispastic Polystyrene
EM	Expandable Microspheres
HAPES	High Alkane Phase Emulsions
HIPE	High Internal Phase Emulsion
HA	Hydroxyapatite
HEMA	2-hydroxyethyl methacrylate
HVO	Hydrogenated Vegetable Oil
IPC	Interpenetrating Composite
IUPAC	International Union of Pure and Applied Chemistry
PZN	Lead Zirconium Niobate

PZT	Lead Zirconium Titanate
MN	Magnesium Nitrate
MBAM	N,N'-methylene Bisacrylamide
PVA	Polyvinyl Alcohol
PDC	Polymer Derived Ceramics
$PEG_{1000}DMA$	Poly(ethylene glycol 1000) Dimethacrylate
PMMA	Polymethylmethacrylate
Tween 20	Poly(oxyethylene)sorbitan Monolaurate
PMS	Polymethylsilsesquioxane
RPM	Rotation Per Minute
SEM	Scanning Electron Microscopy
SiC	Silicon Carbide
Si_3N_4	Silicon Nitride
SiOC	Silicon Oxycarbide
SDS	Sodium Dodecyl Sulphate
Span 60	Sorbitan Monostearate
TEOS	Tetraethylorthosilicate
TTAB	Tetradecyltrimethylammonium bromide
TGA	Thermogravimetric Analyzer
TiC	Titanium Carbide
TiO_2	Titanium Dioxide or Titania
VLS	Vapour Liquid Solid
VOC	Volatile Organic Compound
VS	Vapour Solid

XRD	X-Ray Diffractometer
YM	Young's Modulus
Y_2O_3	Yttrium oxide or Yttria
YSZ	Yttria Stabilized Zirconia
ZrO_2	Zirconium Dioxide or Zirconia
ZTA	Zirconia Toughened Alumina

Notations

α	Alpha
$W_{A/S}$	Alumina powder to sucrose weight ratio
θ	Angle of diffraction
k	Boltzmann constant
$W_{P/S}$	Ceramic powder to sucrose weight ratio
z_i	Charge of ions
σ_0	Compressive strength of dense solid
σ	Compressive strength of foam
n_i	Concentration of ions
ε	Dielectric constant of a liquid
$1/\kappa$	Debye length
ρ_0	Density of dense solid
ρ	Density of foam
θ	Equilibrium contact angle
h	Minimum separation between particle surfaces
ε_0	Permittivity of vacuum
V_A	Potential energy due to attraction
V_{elect}	Potential energy due to electrostatic repulsion
V_R	Potential energy due to repulsion

γ	Shear rate
τ_S	Shear stress
Ψ_0	Surface potential
T	Temperature
V_T	Total potential energy
vol.%	Volume percentage
wt%	Weight percentage
τ_Y	Yield stress
E	Young's modulus of foam
E_0	Young's modulus of dense solid

Chapter 1

Introduction

Advanced structural ceramic components are increasingly used in automotive, defense and aerospace industries owing to their low density, high-temperature stability, excellent mechanical strength at high temperature, corrosion resistance, and creep resistance (Rahaman & Rahaman, 2006; P. M. Rice et al., 1997; Richerson, 2005). These components are processed with extreme care to avoid the formation of any residual pores as the pores limit their mechanical performance. On the other hand, pores are intentionally created in ceramic materials to introduce many functional properties. The pores created in ceramic materials decrease their thermal conductivity, bulk density and dielectric constant and increase their permeability, surface area and acoustic absorption property. The ceramic materials with the intentionally created porosity within its structure are called porous ceramics. By definition, a ceramic is considered porous if it contains a minimum of 20 vol.% porosity (Liu & Chen, 2014). Porous ceramics can be classified according to their porosity content and pore size. Depending on the porosity content, porous ceramics are divided into four categories (Guzman, 2003)

a) Ceramics with low porosity (porosity below 30 vol.%)
b) Ceramics with medium porosity (porosity 30-60 vol.%)
c) Ceramics with high porosity (porosity 60-75 vol.%)
d) Ceramics with super high porosity (porosity above 75 vol.%)

The International Union for Pure and Applied Chemistry (IUPAC) has defined porous materials as microporous, mesoporous and macroporous according to their

pore sizes. This definition is also applicable to porous ceramics. The porous ceramics with a pore size less than 2 nm are called microporous ceramic. The porous ceramics with pore sizes in the range of 2 to 50 nm are called mesoporous ceramic. Macroporous ceramics are the one with a pore size greater than 50 nm. The microporous and mesoporous ceramics are limited to filtration applications such as micro-filtration, nano-filtration, ultra-filtration and reverse osmosis (Ohji & Fukushima, 2012; Studart, Gonzenbach, Tervoort, & Gauckler, 2006) where the pore size requirements fall within 1 to 50 nm range. On the other hand, macroporous ceramics find applications in diverse fields such as lightweight structural parts, high-temperature thermal insulation, catalyst support, bio-implants, acoustic absorption, molten metal filtration and pre-form for ceramic-polymer & ceramic-metal composites (Ohji & Fukushima, 2012; Studart et al., 2006). Among the macroporous ceramics, those falling in the high porosity and super high porosity range are more important in the application point of view. The macroporous ceramics with porosity in the high and super high porosity range are called ceramic foams. A ceramic foam is a continuous ceramic matrix consisting of a three-dimensional array of pores (called cells) interconnected to each other via struts (P. Liu & Chen, 2014; Scheffler & Colombo, 2005). Ceramic foams are also known as cellular ceramics. They are characterized by their low density, brittle mechanical behavior, cell size, cell morphology and cell interconnectivity. Ceramic foams can be divided into three categories based on their cell morphology and cell interconnectivity. They are open cellular, closed cellular and reticulated ceramics. In the case of open cellular ceramics, the neighboring cells are interconnected through one or more cell windows which facilitate the transport of materials

between them. In the case of closed cellular ceramic foams, the cells are isolated from each other preventing the transport of matter. Reticulated ceramics can be considered as an extension of open cellular ceramics, where the entire foam is an interconnected network of pore struts. Typically, reticulated ceramics have a very high porosity (< 95 vol. %) and low mechanical strength. In addition to these three types, there are foams with a combination of open and closed pores. Fig 1 shows the microstructure of the different types of ceramic foams.

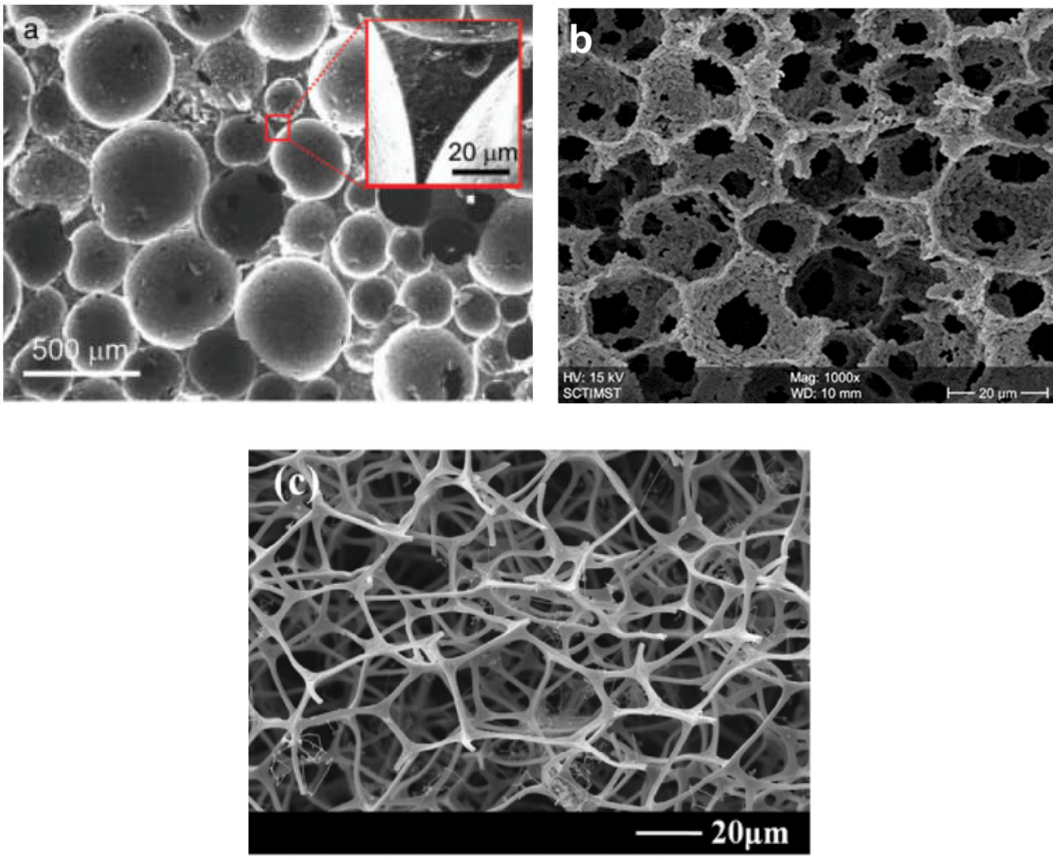

Fig 1.1 SEM images of (a) closed cell (Studart et al., 2006), (b) open cell and (c) reticulated ceramic (Wang et al., 2017) foams.

Due to their low density, high specific strength, low thermal conductivity, high permeability & surface area, low dielectric constant, high-temperature stability

and good bio-compatibility the ceramic foams find applications in various high technology areas. A brief description about the applications of ceramic foams is given below

1.1 Applications of Ceramic foams

1.1.1 High-temperature thermal insulation

The need for thermal insulation is not only very critical for technological development, but many industrial processes would not be possible without adequate thermal insulation (Hammel et al., 2014). The use of thermal insulation helps to reduce power consumption during processing of materials at high temperatures and also protects the surrounding spaces from the heat produced by the processing environment. The properties of ceramic foams such as low density, low thermal conductivity, chemical inertness, high-temperature stability and thermal shock resistance make them an ideal candidate for thermal insulation applications (Scheffler & Colombo, 2005). The use of ceramic foams with closed pore morphology is preferred since it prevents the convective component of heat transfer (Hammel et al., 2014). Alumina, zirconia, SiC and mullite foams are used as insulating materials due to their high-temperature stability.

1.1.2 Acoustic absorbing materials

The mechanism of sound absorption by ceramic foams is as follows: When sound waves enter a porous ceramic body, the air in the pores vibrates and creates friction with the strut (Gibson & Ashby, 1997). Due to the viscous effect, the sound waves convert into thermal energy and will be absorbed. The requirements of a ceramic foam used for acoustic absorption application are small pore sizes (20–150 μm),

high porosity (above 60 vol.%), and high mechanical strength (Liu & Chen, 2014). Their good fire and weather resistance are added advantages for them to be used as sound absorbing materials in the high-rise buildings, subways, tunnels, TV emission center and cinema centers.

1.1.3 Molten metal filtration

In most molten-metal processing, undesirable nonmetallic inclusions are introduced into the melt during the acts of melting, transporting, and alloying the metal before casting into moulds (Scheffler & Colombo, 2005). Once the metal is cast, these inclusions can result in defects that render the product unusable. Reticulated ceramic foams are used for the filtration of molten metal before casting (Blome, 1981; Pryor & Gray, 1976). To act as filters for molten metal, ceramic foams should have appropriate pore size and pore interconnectivity, sufficient strength, high-temperature stability, good thermal shock resistance and good erosion resistance (Liu & Chen, 2014). The selection of the ceramic foam as a filter material depends on the molten metals which have to be filtered. For filtration of ferrous metals and alloys with high chemical activity and high casting temperatures, alumina and silicon carbides with great chemical stability are usually selected. The multi-compositional ceramics are also used to form a filtration system. For example, ceramic foam filters made from a composition containing alumina, SiC, cordierite and zirconia are used for the filtration of molten Al, Cu, Zn, and bronze (Liu & Chen, 2014).

1.1.4 Catalyst support

Ceramic foams are extensively employed as a support for metal catalyst particles used in multiphase catalysis. Alumina, titania, zirconia, silica, and silicon carbide foams are used for this purpose (Scheffler & Colombo, 2005). Supports play a major role in the promotion of the reaction. The tortuous channels in ceramic foams can generate turbulence and then ensure good mixing of the reactants. Compared to the reactor with filled stacking particles, the reactor with a ceramic foam core can reduce the drop in pressure (Richardson et al., 2000). A large surface area is needed to achieve good contact between the catalysts and the flowing reactants. The ceramic foams have relatively high surface area and the surface area can be further increased by coating them with other microporous materials such as zeolites or aerogels (Landau et al., 2006). Some of the specific examples in which ceramic foams are used as catalyst support includes oxidation of ammonia, decomposition of organics by photo catalysis, and destruction of volatile organic compounds (VOCs) by incineration (Giroux et al., 2005; Landau et al., 2006; Ribeiro et al., 2011).

1.1.5 Bio-implants

Bio-scaffolds are utilized for bone tissue engineering applications in order to facilitate the repair of bone that has been flawed due to illness, injuries or deterioration (Roohani-Esfahani et al., 2013; Seol et al., 2013). The scaffold structure must be three-dimensional and facilitate cell interaction by providing an avenue to transport nutrients and oxygen and to allow tissues and capillaries to develop (Hutmacher, 2000; Seol et al., 2013). Additionally, the materials used to

fabricate the scaffold must be biocompatible, bioactive, or biodegradable (Seol et al., 2013). Hydroxyapatite and tricalcium phosphate have similar chemical composition as that of the natural bones. Development of porous bone replacement materials from hydroxyapatite is addressed to mimic the micro- and macroporous architecture of the mineral phase of living bone. Macro- and microporous bioactive ceramics show high true surface area which facilitates appropriate contact osteogenesis (Hammel et al., 2014). This prevents interference of connective tissue formation which will obstruct the long-term stability of the implant. For bone repair strategies, macroporous hydroxyapatite ceramics with a highly interconnected pores are required to provide in-growth access of surrounding host tissues, facilitating further deposition of newly formed tissue in the spherical cavities (Netti, 2014). Hydroxyapatite (HA) foam when used as implants become filled with mature new bone tissue and osteoid without any immune or inflammatory reactions after the period of implantation (Mathieu et al., 2006). This is attributed to the high biocompatibility of HA and the suitability of foam network in providing good osteointegration. Porous hydroxyapatite ceramics with gradient porosity (Tampieri et al., 2001) and bimodal pore structure (Krajewski et al., 2000; Yokozeki et al., 1998) are also studied for bone graft applications. In addition, porous hydroxyapatite ceramics are used as drug releasing agents (Komlev et al., 2003; Krajewski et al., 2000; Palazzo et al., 2005; Sopyan et al., 2005)

1.1.6 Pre-form for composites

Due to their poor fracture toughness, ceramics are unusable for some of the industrial applications. But due to low density compared to metals and better thermal properties compared to polymers, the use of ceramics is ideally more

preferred. Toughening the ceramics by incorporating a secondary phase (mostly metals) to reinforce the matrix to form ceramic matrix composites is researched widely. Recently, the development of interpenetrating composites (IPCs) where both matrix and reinforcement phase are continuous throughout the composite is of great interest (Clarke, 1992; Travitzky, 2012). IPCs of ceramics with both metals and polymers as reinforcement phase have been developed (Kalita et al., 2003; Mattern et al., 2004). One of the methods for fabrication of ceramic-metal and ceramic-polymer composites is by infiltration of ceramic foams with the respective metal or polymer. (Konopka et al., 2003; Mattern et al., 2004). Polymer infiltrated porous ceramics are studied for dental (He & Swain, 2011) & bioresorbable applications (Mathieu et al., 2006) and as piezoelectric transducers (Bowen, 1994).

1.2 Processing of Ceramic Foams

The ceramic foams are prepared from respective ceramic fine powders or pre-ceramic polymers. The conversion of ceramic powder to ceramic foams is achieved through either dry powder pressing or colloidal processing. In the dry pressing method, a mixture of ceramic powder and pore forming agent is consolidated by pressing. Removal of the pore template by burnout followed by sintering, results in formation of ceramic foam. The powder pressing method mostly limited to ceramic foams of lower porosity. On the other hand, the colloidal processing route uses a well dispersed suspension of the ceramic powder in an aqueous or non-aqueous medium for the fabrication of macroporous ceramics. Various processing methods are used to transform the colloidal suspension to macroporous ceramic bodies (Ohji & Fukushima, 2012; Studart et al., 2006). The colloidal processing produces macroporous ceramics of higher porosity compared to the powder pressing using

pore templates. Moreover, the macroporous ceramics produced from colloidal suspensions have dense cell walls and struts that result in better mechanical strength. The first and very important step in any colloidal processing method is the preparation of a well dispersed powder suspensions in a solvent medium. The following section briefly describes the fundamentals of powder dispersions.

1.3 Powder Dispersion

The ceramic powder dispersions in a solvent medium are prepared by mechanically mixing the ceramic powder, solvent and an optimum amount of a dispersing agent. Acids, alkali, polymers, simple long chain molecules with hydrophilic head groups and poly electrolytes are used as dispersant (Bergström, 2001). Among them, the acid, alkali and poly electrolytes are effective in aqueous medium. On the other hand, the polymeric stabilizers and long chain molecules with hydrophilic head groups are effective in non-aqueous medium. The powder dispersion in a solvent medium is achieved by producing repulsive interactions between the particles to overcome the natural interparticle van der Waals attractive forces responsible for particle agglomeration.

There are three mechanisms of powder dispersions depending on the nature of the repulsive interaction between the particles. They are (i) Electrostatic, (ii) Steric and (iii) Electrosteric mechanisms (Bergström, 2001; Lewis, 2004). The electrostatic and electrosteric mechanisms operate in aqueous medium and steric mechanism operates in non-aqueous medium. In the electrostatic mechanism, pH adjustment using either acid or alkali is used to disperse ceramic powders in aqueous medium. The particle surface acquires positive or negative charge

depending on the pH. The quantity of surface charge depends not only on the pH but also on the surface characteristic of the powder, nature of electrolyte in the solution and ionic strength. Generally, the pH of the medium is adjusted away from the isoelectric point of the particle surface to achieve maximum surface charge. At pH away from the isoelectric point the particle surface achieves positive or negative charge by ionization of the surface functional groups. In the case of oxide ceramic materials, pH adjustment away from the isoelectric point results in protonation or de-protonation of surface hydroxyl groups resulting either positive or negative surface charge (Bellmann, 2004). The counter ions from the solution are attracted to the interface form a diffused ion cloud adjacent to the particle surface and thus create an electrical double layer. A schematic of electrostatic stabilization is shown in **Fig. 1.2**. The thickness of this double layer is determined by the concentration and valance of the ions in the solution. When the concentration of the ions in the solution is high, it results in a thin double layer. The thickness of the double layer can be defined in the terms of Debye length ($1/\kappa$) which is given by equation (1) (Bergström, 2001),

$$\frac{1}{\kappa} = \left(\frac{\mathcal{E}\,\mathcal{E}_0\,k\,T}{e^2 \sum_i n_i z_i^2}\right) \text{---------- (1)}$$

where, e is the electronic charge, k is the Boltzmann constant, T is the temperature, n_i is the concentration of ions with charge z_i, ε is the dielectric constant of the liquid and ε_0 is the permittivity of vacuum. The potential energy due to the repulsion of spherical particles (V_{elect}) due to the double layer can be given by equation (2) (Lewis, 2004),

$$V_{elect} = 2\pi\varepsilon_r\varepsilon_0 a\Psi_0^2 e^{-\kappa h} \text{---------- (2)}$$

where, Ψ_0 is the surface potential, h is the minimum separation between the particle surfaces.

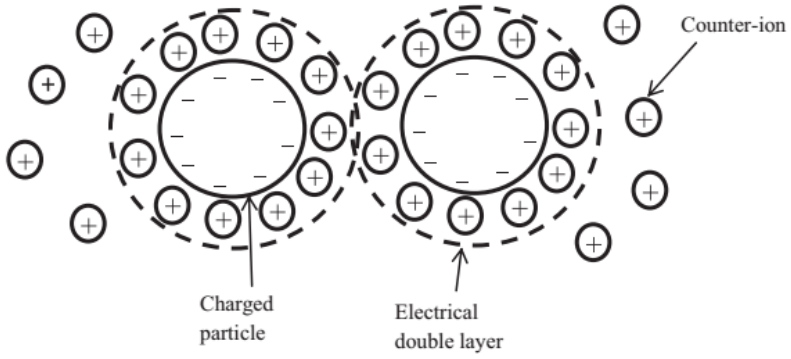

Fig 1.2 Schematic of electrostatic stabilization (Chin et al., 2015)

In the case of non-aqueous medium, controlling the pH does not yield stable dispersions. In such cases, suitable polymeric dispersants are added to prepare stable colloidal suspensions. The polymeric molecules adsorb on the surface of the particles and form monolayer coverage. Upon the close approach of two particles covered with adsorbed polymer layers, the interpenetration of the polymer layers give rise to a repulsive force known as steric hindrance resulting in steric stabilization. To be effective, the adsorbed polymer layers must be of sufficient thickness and density in order to overcome the van der Waals attraction between particles (Bergström, 2001). Long chain amphiphilic molecules such as fish oil, phosphate esters, oleic acid, linoleic acid, and cardanol etc. (Bellmann, 2004; Bergström, 2001), used as dispersant in non-aqueous medium do not have sufficient chain length to offer complete steric stabilization. Therefore, they are called semi-steric stabilizers. The steric stabilization can be further explained in terms of

osmotic effect. When two spherical particles with the adsorbed polymer layer come together, it creates an area of low solvent concentration. Due to the osmotic pressure, the solvent molecules force into this area and separate the particles. **Fig 1.3** shows the schematic of steric stabilization.

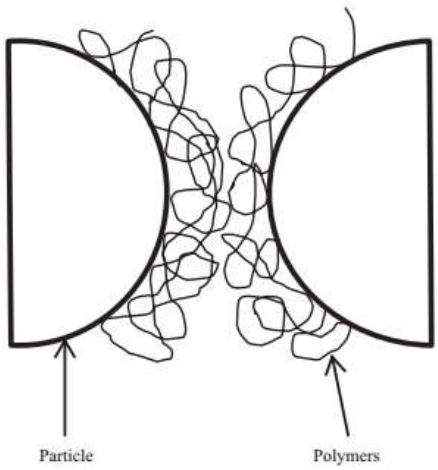

Fig 1.3 Schematic of steric stabilization (Chin et al., 2015)

The poly electrolytes such as ammonium poly(acrylate) works as a dispersing agent in aqueous medium. The adsorbed poly electrolytes on the particle surface create negative surface charge due to the ionization of $–COONH_4$ and offer steric stabilization due to the osmotic effect as explained above. That is, poly electrolytes effectively stabilize the particle in aqueous medium through a combination of electrostatic and steric mechanism called electrosteric mechanism. The schematic of electrosteric stabilization is given in **fig 1.4**.

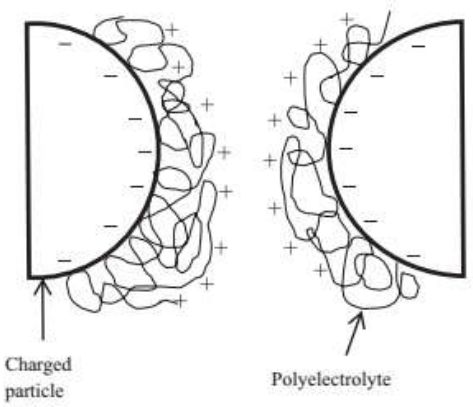

Fig 1.4 Schematic of electrosteric stabilization (Chin et al., 2015)

Ceramic powder dispersion in a solvent medium involves the manipulation and control of the interparticle forces such as van der Waals, electrostatic and polymer-induced steric forces in powder suspensions (Bergström, 2001). The inherent van der Waals forces between the particles tend the particles to agglomerate in a medium. The electrostatic or steric repulsive forces created on the particle surface overtake the van der Waals attractive interactions and thereby prevents the particle agglomeration. There are many theories which explain the stability of colloidal suspensions of which the Derjaguin-Landau-Verwey-Overbee (DLVO) theory (Derjaguin & Landau, 1941; Verwey & Overbeek, 1948) is most prevalent. It states that dispersion is stable if a potential energy barrier, larger than the average kinetic energy of the particles exists. In simple terms it states that the total potential (V_T) between the particles is the sum of the attractive (V_A) and repulsive (V_R) potentials [equation (3)].

$$V_T = V_A + V_R \quad \text{----------} \quad \textbf{(3)}$$

where the attractive potential is due to the van der Waals forces arises as a result of interaction between oscillating and rotating dipoles within the media. The

repulsive potential is due to the electrostatic, steric or electrosteric interactions. **Fig.1.5** shows the potential energy curve of particles in a powder dispersion according to DLVO theory. The total interparticle potential increases with decrease of interparticle distance and reaches a maximum and then decreases to a primary minimum. The height of the potential maximum depends on zeta potential and electrolyte concentration. For achieving a stable powder dispersion, the potential maximum in the total potential energy curve should be greater than 25kT. At the primary minimum, attractive forces overpower the repulsive forces due to which particles coagulate and become difficult to be dispersed. A shallow secondary minimum also appears at higher interparticle distance at which the particles form a weakly attractive network. The particles in the secondary minimum can be easily redispersed by mechanical agitation.

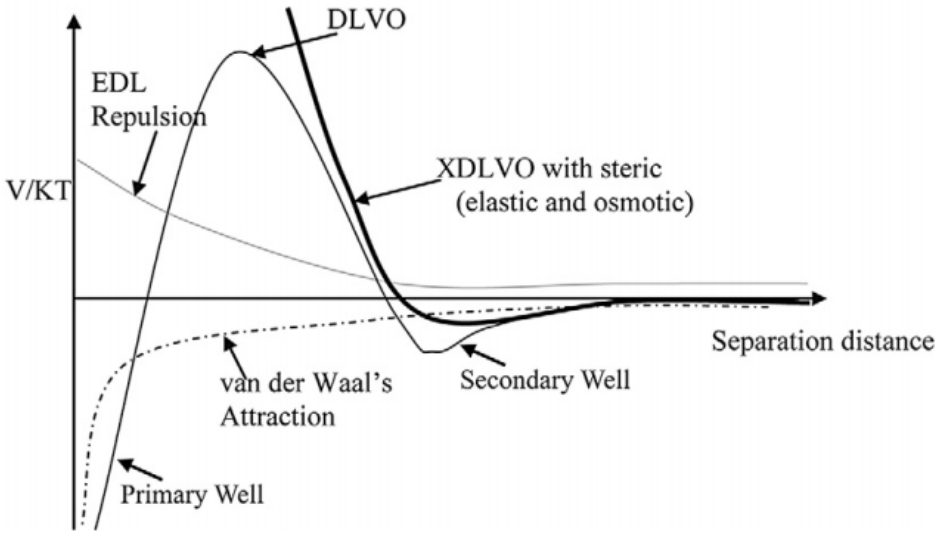

Fig 1.5 Total Potential as a function of separation distance (Hotze et al., 2010)

1.4 Processing methods of ceramic foams

A brief description of various methods for the preparation of ceramic foams is given below

1.4.1 Sacrificial template method

The sacrificial template method involves the use of fugitives which act as the pore forming agents. These fugitives are first homogeneously dispersed within the ceramic slurry. The slurry containing the fugitive particles is then consolidated by casting and setting in a mold. The fugitives are removed either by evaporation, pyrolysis or leaching out using strong acids or bases. The green body obtained is then sintered to get the porous ceramic. The porosity can be controlled by adjusting the amount of the sacrificial phase. The size and shape of the fugitives affect the pore size and pore morphology of the ceramic foams. The pore forming agents are generally classified into synthetic organic matters, natural organic matters and metallic & inorganic matters (Ohji & Fukushima, 2012; Studart et al., 2006). Synthetic and natural organics are often extracted through pyrolysis by applying long thermal treatments at temperatures between 200 and 600^{o}C. The long periods required for complete pyrolysis of the organic component and the extensive amount of gaseous by-products generated during this process are the main disadvantages of using organic materials as sacrificial phase. Most of these drawbacks can be partially overcome by using a solid phase that can be easily sublimated. Even though the extraction of pore template by sublimation is time consuming, it uses lower temperatures for removal without generating undesired toxic gases. Also

sublimation avoids excessive stresses during pore template removal. A schematic representation of fugitive template method is shown in **Fig. 1.6.**

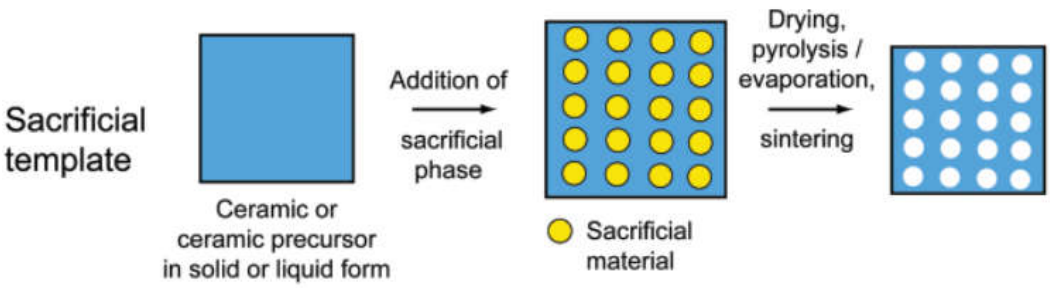

Fig. 1.6 Schematic of the sacrificial template method (Studart et al., 2006)

Polymethylmethacrylate (PMMA) beads and microbeads have been frequently employed as sacrificial fugitives. Cruz et al used a colloidal processing technique with PMMA sacrificial templates, to fabricate macro-porous yttria-stabilized zirconia ceramics. Descamps et al (Descamps et al., 2008; Descamps et al., 2008) produced macroporous β-tricalcium phosphate (TCP) ceramics by using PMMA balls. Andersson and Bergstrom (Andersson & Bergström, 2008) used isobutene gas filled expandable microspheres as a sacrificial template to produce macroporous alumina ceramics by gel-casting. As low amounts as 1–2 wt% of the micro-spheres are required to create a final porosity above 80 vol.%.

Li et al (Li et al., 2010) fabricated porous silicon nitride with fibrous β-grain structure, using naphthalene powder as the pore-forming agent and gas-pressure sintering at high temperatures above 1700 ^{o}C. Chen et al (Chen et al., 2007) developed porous silicon nitride by using phosphoric acid as the pore-forming agent and pressure less sintering between 1000-1200 ^{o}C. Yang et al (Yang et al., 2005) prepared silicon nitride ceramics with rod-shaped pores using sintering additives by

slip casting with fugitive organic whiskers. Prabhakaran et al (Prabhakaran et al., 2007) used wheat particles as both pore forming agent and gelling agent for the preparation of macroporous alumina ceramics with pore size ranging from 20- 800 μm. Ding et al (Ding et al., 2007) used graphite as the pore-former to fabricate mullite-bonded porous silicon carbide ceramics in air from SiC and α-Al_2O_3 through *in situ* reaction bonding technique.

Zhang et al (Zhang et al., 2004) produced porous alumina ceramics with unidirectionally aligned continuous pores via the slurry coating of mercerised cotton threads. They adjusted the pore size by using cotton threads of different diameters, and the porosity could be controlled by changing the solids concentration of the slurry. Synthetic fibers such as carbon (Isobe et al., 2006), nylon-66 (Isobe et al., 2007) and rayon (Okada et al., 2009, 2010) have also been used as fugitives for the preparation of porous alumina and mullite ceramics with unidirectionally aligned pore by extrusion. The pore sizes and porosities could be controlled by varying the fiber diameter and fiber content.

1.4.2 Replication technique

The replication technique is frequently used to prepare reticulated ceramic foams. The replication technique involves the use of a template, which is porous in nature. The template used needs to have adequate flexibility, shape recovery ability and homogeneous open cell structure. Various synthetic and natural cellular structures are used as templates. Polymer foams, natural resources of porous structures such as woods, corals, sea sponge, etc. have been used as replica templates. The schematic of the replication process is shown in **Fig. 1.7**

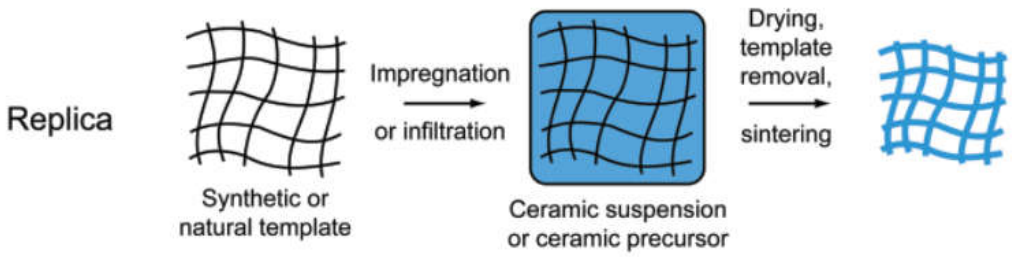

Fig. 1.7 Schematic of the replication technique (Studart et al., 2006)

Polymeric foams such as polyurethane are the most commonly used synthetic templates. The polyurethane foams are impregnated with the ceramic slurry by soaking in it. The excess slurry is then drained by centrifugation or roller compression. The slurry impregnated templates are dried and then pyrolyzed to decompose the organic sponges. After the pyrolysis, the ceramic layers are sintered at higher temperatures for densification. A disadvantage of the polymer foam replica technique is the fact that the struts of the reticulated structure are often cracked during pyrolysis of the polymeric template, markedly degrading the final mechanical strength of the porous ceramic. Many attempts have been made to avoid this shortcoming. Some of them includes, improving the wetting of the suspension on the sponge with the help of additives, performing a second impregnation step to fill the cracks in the ceramic struts, and introducing fibers or reactive compounds to enhance the material's integrity. Zhu et al (Zhu et al., 2001) recoated repeatedly with thinner slurry of the same composition to improve the strength of reticulated ceramics. Vogt et al (Vogt et al., 2010) attempted the vacuum infiltration of ceramic slurry to fill up the struts in the pre-sintered foam. In this, the hollow struts caused by burnout of the polyurethane template could be completely filled up, which resulted in a considerable increase in compressive strength. Jun et al (Jun et al., 2007; Jun et al., 2006) produced hydroxyapatite scaffolds coated with bioactive

glass–ceramics using the polymer foam replication method, to enhance their mechanical properties and bioactivities. Luyten et al (Luyten et al., 2005) used a reaction bonded, modified replica technique to produce ceramic foam with strong struts.

Naturally occurring cellular structures like corals are interesting due to their special pore morphology and intricate microstructures, which are difficult to produce artificially. White et al (White et al., 1972) used a method named ‘‘replamineform’’ to replicate the structure of corals and other marine invertebrate skeletons. In this technique, the coral is first impregnated with wax under vacuum to obtain a negative form of the cellular structure. After hardening the wax, the calcium carbonate of the coralline skeleton is leached out using a strong acidic solution. The macroporous ceramic is obtained by impregnating the negative wax model with a ceramic suspension and subsequently removing the organic material by pyrolysis. Roy and Linnehan (Roy & Linnehan, 1974) used a hydrothermal exchange reaction to prepare porous ceramics reaction using coral as replica template and ammonium hydrogen phosphate. They could prepare porous hydroxyapatite and whitlockite ceramics by using high temperature and pressures. Hu et al (Hu et al., 2001) modified the hydrothermal exchange method using Australian coral to prepare porous hydroxyapatite ceramics with pore size in the range of 200-300 μm.

Wood, specifically carbonized wood, is another natural template for the preparation of macroporous ceramics. The presence of oriented vessels in the structure of wood enables the preparation of macroporous ceramics with highly anisotropic aligned pores which cannot be achieved with the other replica

techniques. The most common approach is to first prepare a carbon cellular pre-form by heat treating the wood structure under inert atmosphere at temperatures within 600–1800ºC. The carbon pre-form is subsequently infiltrated with gaseous or liquid ceramic precursors at high temperatures to obtain the macroporous ceramic. Alternatively, the carbon pre-form is infiltrated at room temperature with liquid sols and afterwards oxidized to render the cellular ceramic. The pore size distribution of wood-derived porous ceramics is determined by the microstructure of the original wood template.

Greil et al (Greil et al. 1998a, 1998b; Sieber et al., 2000; Vogli et al., 2002; Zollfrank, et al., 2004) have prepared biomorphic cellular SiC and SiOC ceramics using carbonized wood templates. For the preparation of SiC ceramics, they (Greil et al., 1998a, 1998b; Sieber et al., 2000; Vogli et al., 2002) have infiltrated the wood template using Si metal, both liquid and vapour phase. In the case of the SiOC ceramics (Zollfrank et al., 2004), Si-H functionalized polymethylhydrosiloxane polymer is impregnated into maleic acid anhydride-modified wood template. The microstructures of the cellular SiC ceramics prepared by liquid phase and vapour phase infiltration of silicon in carbonized pine wood is shown in **fig. 1.8**.

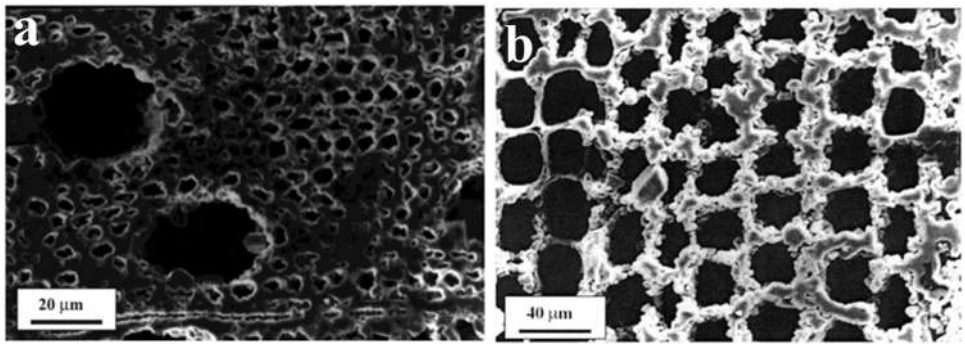

Fig.1.8 Microstructure of cellular SiC ceramics prepared by (a) liquid phase and (b) vapour phase Si metal infiltration (Sieber et al., 2000)

Sun et al studied the preparation of porous TiC (Sun et al., 2002) and TiC/C (Sun et al., 2004) ceramics by infiltrating tetrabutyl titanate into carbon preform obtained by the pyrolysis of wood. The TiO_2 produced by the decomposition of tetrabutyl titanate reacted with carbon from the wood at 1400 ^oC to give porous TiC ceramics. Ota et al (Ota et al., 2000) prepared porous TiO_2 ceramics with wood-like structure by sol gel route using natural wood templates. They impregnated the wood template using titanium tetraisopropoxide via vacuum infiltration, hydrolyzed the iso-propoxide and finally sintered to get the porous TiO_2 ceramics. The same methodology was adopted by Mizutani et al (Mizutani et al., 2005) to prepare porous titania, zirconia and alumina ceramics which are analogous to silicified wood.. Cao et al (Cao et al., 2004) used a similar approach by impregnating pine wood using low viscous alumina-, titania- and zirconia-sols. They could prepare biomorphous Al_2O_3, TiO_2 and ZrO_2 ceramics with microcellular structure which mirrored the microstructure of the pine wood.

1.4.3 Freeze casting

In the freeze casting process, the ceramic powder suspension cast in a mould is set by freezing the dispersion medium which is subsequently removed by sublimation. The space created by the removal of the dispersion medium remains as the pores within the ceramics after sintering. In the early days, freeze casting was mainly used as a near-net-shape forming technique (Jones, 1999; Sofie & Dogan, 2004). Freeze casting of ceramic powder suspensions is now widely studied for the preparation of porous ceramics with a range of porosity and pore structure. The freeze casting produces porous ceramics with both homogenous cellular and unidirectional lamellar microstructures. The cellular microstructure structure can be obtained by suppressing the directional solidification of the solvent. This is done by controlling freezing condition and freezing rate throughout the sample. On the other hand, the lamellar microstructure is obtained by allowing directional cooling of the dispersion medium by introducing a temperature gradient. In both cases, the porous ceramics prepared by freeze casting have open pore microstructure. **Fig. 1.9** is the schematic showing the development of pores in freeze casting technique. There are four major steps in the freeze casting process: preparation of the slurry, controlled solidification of the slurry, sublimation of the solvent and finally sintering of the green body. The dispersion medium is the most important factor in the freeze casting process as it affects both the process as well as the final product. Water, camphene, naphthalene, t-butyl alcohol, etc., are the commonly used dispersion medium.

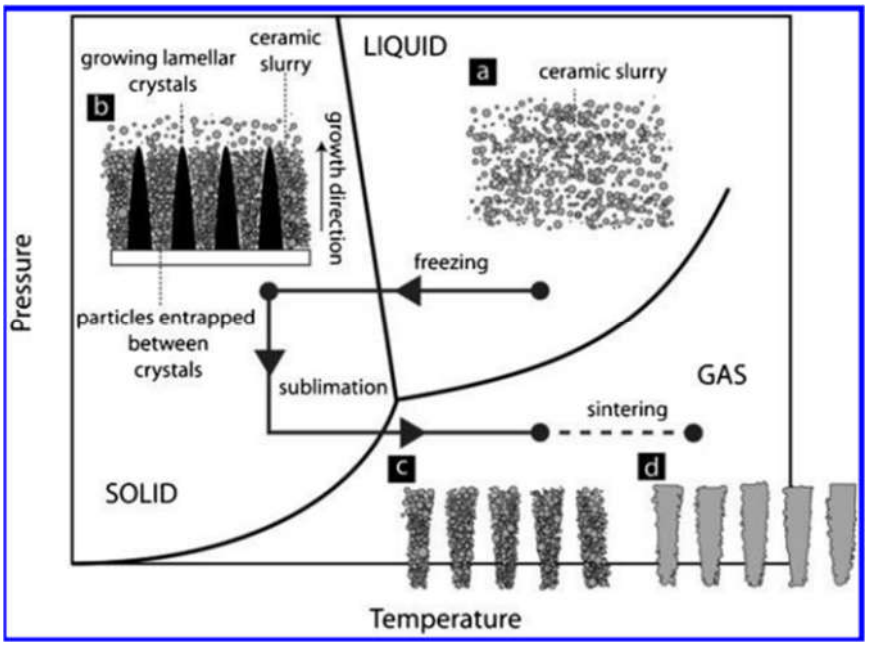

Fig.1.9 Schematic of freeze casting technique (Deville, 2008)

Water is the most commonly used freeze casting dispersion medium due to its environmentally friendly and abundant nature. The directional solidification behaviors of aqueous systems during freeze casting has been studied by Deville et al (Deville, 2008; Deville et al., 2006, 2007). They investigated the relationships between the freezing conditions and the final porous structures, for moderate to highly concentrated suspensions. The morphology of the porous structures, i.e. the content, dimensions, shape and orientation of pores, could be adjusted by varying the initial slurry compositions and the freezing conditions. Waschkies et al (Waschkies et al., 2009) used a novel double side cooling method to control the lamellar spacing during freeze casting. Fu et al (Fu et al., 2008a, 2008b) prepared porous hydroxyapatite ceramics by freeze casting. They studied the manipulation of the microstructure of the ceramics by controlling the substrate temperature and solvents used. They used water-glycerol and water-dioxane mixtures and substrate

temperatures in the range of -20 to -196 ^{o}C. By reducing the substrate temperature they could prepare ceramics with finer lamellar structure. Ji et al (Ji et al., 2010) prepared porous mullite composites by freeze casting aqueous coal fly ash/alumina slurries. They could prepare mullite ceramics with porosities in the range of 55-67 vol.% with a maximum compressive strength of 41 MPa. Zhang et al (Zhang et al., 2012) prepared novel graded porous Si_3N_4 ceramics by an aqueous freeze casting method. A characteristic of this process is the formation of a dense surface layer with a 2.5 μm thickness. They could prepare porous Si_3N_4 ceramics with a maximum porosity of 76.8 vol.% with flexural strength of 14.3 MPa and a dielectric constant of 1.78.

Many studies have been carried out using additives such as polyvinyl alcohol (PVA), glycerol and gelatin to adjust the pore morphology and microstructure of porous ceramics prepared by freeze casting. Zuo et al (Zuo et al., 2010a, 2010b) used PVA to modify the pore morphology and structure of hydroxyapatite ceramics. By altering the cooling rate along with addition of PVA, they could prepare porous hydroxyapatite with smooth cell walls at lower cooling rate and with small dendritic formation on cell walls at higher cooling rate. They (Zuo et al., 2011) also tried to influence the microstructure of freeze cast porous hydroxyapatite ceramics by using PMMA beads. **Fig. 1.10** shows the microstructure of cell wall of the hydroxyapatite ceramics prepared using PVA as pore structure modifier. Zhang et al (Zhang et al., 2009) used gelatin as additive for the preparation of porous hydroxyapatite ceramics. On the addition of gelatin the microstructure of the ceramics showed a large variation, the pore morphology changed from two-dimensional flat to a three dimensional reticulated one. The use

of glycerol as an additive in aqueous freeze casting process to improve the mechanical strength of porous alumina ceramics is studied by Zhang et al (Zhang et al., 2010). The porous alumina ceramics prepared by this process show an axial and radial compressive strength of 96.4 and 29.7 MPa, respectively, at 64 vol.% porosity.

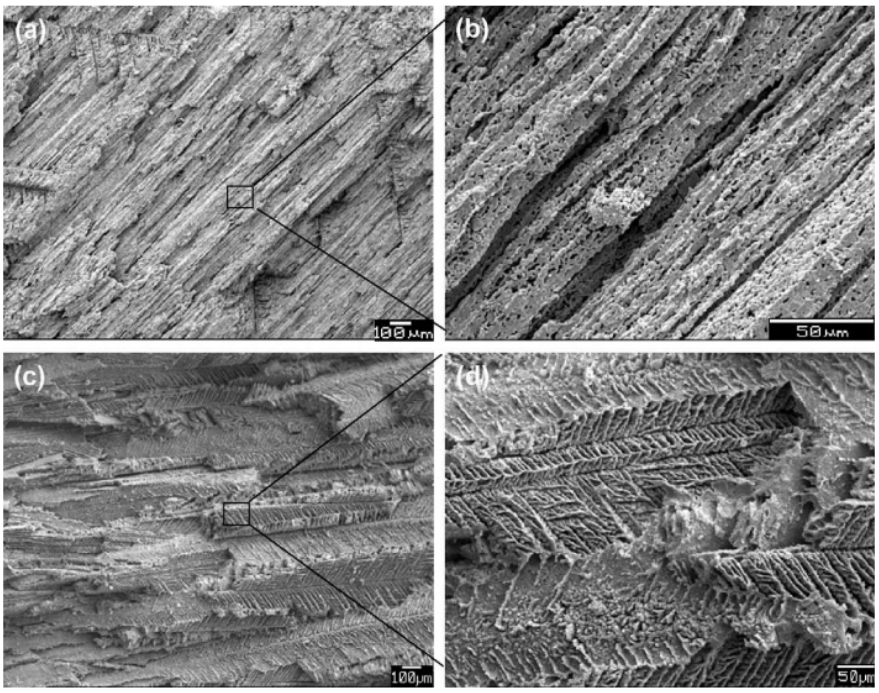

Fig 1.10 High and low magnification images of hydroxyapatite ceramics formed at (a) & (b) low and (c) & (d) high cooling rates (Zuo et al., 2010b)

The use of camphene as solvent allows the avoidance of extremely cold temperature for the freeze casting process. Araki and Halloran (Araki & Halloran, 2004a, 2004b, 2005) studied the use of camphene as a solvent for the preparation of porous alumina ceramics by freeze casting. In this, slurries of alumina powder in the molten camphene are prepared at 55 ^{o}C. The slurries quickly solidify when they are poured into polyurethane moulds and cooled at room temperature. The

advantage of using camphene is easy removal of the solvent by sublimation. Hong et al (Hong et al., 2009; Hong et al., 2010) prepared ultra-high-porosity zirconia ceramics with interconnected pores by freezing zirconia/camphene slurries with solid loading ranging from 10 to 20 vol.%. Yoon et al prepared highly porous hydroxyapatite (Yoon, Koh et al., 2007; Yoon, Park et al., 2008) and alumina (Yoon, Koh et al., 2008) ceramics by freeze casting camphene based ceramic slurries. They could prepare porous hydroxyapatite scaffolds with dense shells (Yoon, Park, et al., 2008) and large pore channels (> 100 μm) (Yoon, Koh, et al., 2007) for bone tissue engineering applications. Moon et al (Moon et al., 2011) prepared highly aligned porous alumina ceramics by extruding frozen alumina/camphene bodies. Further they tried to increase the pore size of the alumina ceramics by heat treating the extruded alumina/camphene body at a temperature near its solidification point (Moon et al., 2012). They could increase the pore size from 51±8 to 125±27 μm by increasing heat treatment time from 1 to 24 h. The heat treatment resulted in the increase in mechanical strength while retaining the highly aligned pore structure. The camphene based freeze casting process has been applied for the preparation of porous yttria stabilized zirconia (YSZ) (L. Hu et al., 2010), β-SiAlON (Hou et al., 2012), Si_3N_4 (Xia et al., 2012) and piezoelectric lead zirconate titanate–lead zinc niobate (PZT-PZN) (Lee et al., 2007) ceramics.

The use of t-butyl alcohol (TBA) as a vehicle for the freeze casting process has also been studied. Chen et al (Chen et al., 2007) prepared alumina ceramics with 65 vol.% porosity by freeze gelcasting TBA/acrylamide/alumina slurries. Yang et al studied the preparation of porous mullite (Yang et al., 2010), hydroxyapatite (Yang et al., 2010) and alumina/zirconia composite (Choi et al.,

2012) ceramics by freeze casting using TBA. Tang et al (Tang et al., 2016) prepared alumina ceramics with unidirectionally aligned gradient pore structure by freeze casting using TBA-water system.

1.4.4 Emulsion templating

An alternative method for the preparation of macroporous ceramics is by using oil droplets as pore template. In this, the oil droplets are dispersed within the aqueous ceramic powder suspension or sol using an emulsifying agent. Subsequently, the oil droplets are removed after gelation and drying of the emulsion. The oil removed emulsion bodies are sintered to produce the ceramic foams. The high internal phase emulsion based method is successfully studied for the preparation of various macroporous polymer materials (Imhof & Pine, 1997; Menner et al., 2006). The emulsion templating method is also reported for the preparation of macroporous ceramics with ordered pores through sol-gel route (Alves-Rosa et al., 2013; Imhof & Pine, 1997; Imhof & Pine, 1998; Manoharan et al., 2001). In this, non-aqueous emulsion (oil-in-formamide) fractionated into a narrow droplet size was mixed with sols prepared by the hydrolysis and condensation of the metal alkoxides in formamide medium. Further condensation of the pre-polymer sol resulted in the deposition of ceramic layer over the emulsion droplet and gelation of the sol. The void spaces created by the removal of the emulsion droplet from the gel remain as macropores. However, the gels undergo large shrinkage during drying and sintering. The preparation starting from ceramic powders is more economically viable than the sol-gel route. Recently, a method based on a high alkane phase emulsions (HAPES) using decane as the oil phase (Barg et al., 2009, 2008; Ewais et al., 2011) has been studied for the preparation of macroporous ceramics. In this,

the emulsions cast in an open mould could be removed from the mould only after partial or complete drying. A solution to this problem is to use an oil phase which becomes solid on cooling. Vitorino et al (Vitorino et al., 2013) reported the preparation of alumina foams by emulsion templating method using liquid paraffin as the oil phase. **Fig. 1.11** shows the SEM photomicrograph of ceramic foam prepared by high alkane phase emulsion method.

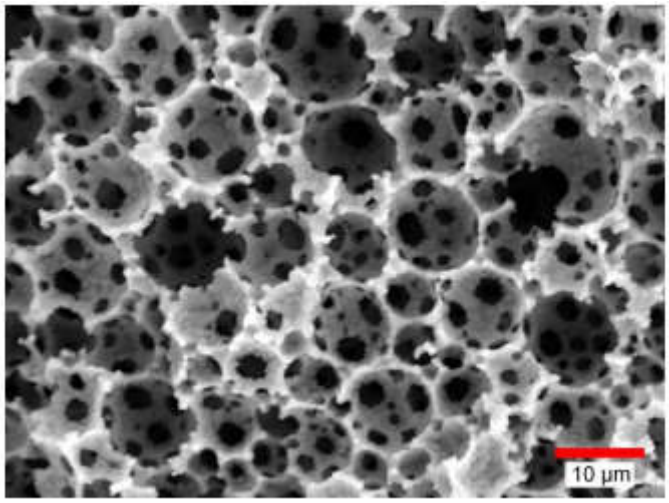

Fig.1.11 SEM photomicrograph of ceramic foam prepared by high alkane phase emulsion method.

1.4.5 Direct foaming

In direct foaming techniques, ceramic powder suspension which is foamed by incorporating air or a gas is stabilized, dried and then sintered to obtain ceramic foams. This technique allows low-cost and easy production of highly porous ceramic foams. Porous ceramics with unidirectional channels have been also developed recently by using continuous bubble formation in ceramic slurry (Zhang et al. 2006a). However, due to the thermodynamic instability, the gas bubbles are likely to coalesce in order to reduce the total Gibbs free energy of the system,

resulting in large pores in the final porous bodies. It is, therefore, critically required to stabilize the air or gas bubbles in ceramic powder suspension. The stability of the bubbles is important as they influence the final cell size distribution, wall thickness and microstructure of the solid foams. One of the most frequently used approaches for the bubble stabilization is to use surfactants which reduce the energy of the gas–liquid interfaces. A surfactant is a substance that, when present at low concentration in a system, has the property of adsorbing onto the surfaces or interfaces of the system and of altering to a marked degree the surface or interfacial free energies of those surfaces (Rosen & Kunjappu, 2012). The driving force behind surfactant adsorption is the lowering of the free energy of the phase boundary. A brief description of surfactants used for the foaming of ceramic powder suspensions is given below.

The structure of a surfactant can be referred to as 'amphiphilic', a non-polar hydrophobic portion, called a tail attached to a polar or ionic portion (hydrophilic) termed head. The hydrophobic part is mostly a hydrocarbon, either branched or straight, consisting of 8-18 carbon atoms. In many cases fluorinated hydrocarbons form the hydrophobic part. The surfactants are classified into four categories based on their head group. They are cationic, anionic, non-ionic and amphoteric or zwitterionic (Rosen & Kunjappu, 2012; Tadros, 2006). The structures of representative cationic, anionic, non-ionic and zwitterionic surfactants are shown in **Fig. 1.12**.

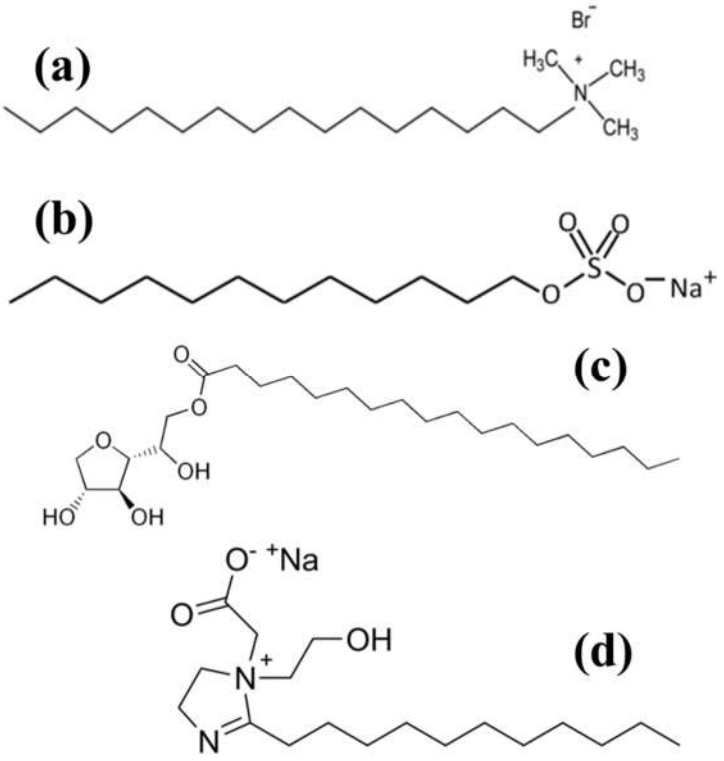

Fig 1.12 Structure of (a) Cetyltrimethylammonium bromide (cationic), (b) Sodium dodecyl sulphate (anionic), (c) sorbitan monostearate (Span 60) (non-ionic) and (d) Sodium lauroamphoacetate (zwitterionic) surfactants.

The nature of surfactant used for foaming affects the microstructure and properties of the ceramic foams. Fuji et al (Fuji et al., 2006) studied the effect of surfactants on the microstructure, thermal conductivity and sound absorption property of porous ceramics. They studied a number of anionic and nonionic surfactants for this purpose and selected two anionic (ammonium lauryl sulphate and fatty alcohol ethoxy sodium) and one nonionic [poly(oxyethylene)sorbitan monolaurate (Tween 20)] surfactants. The anionic surfactants show good foaming capability and the foams prepared using them show interconnected and open pore structure with relatively high porosity. The foams prepared using the non-ionic surfactant (Tween 20) has high density and less interconnected pores. Wang et al

(Wang et al., 2012) studied the microstructure control in ceramic foams using a mixture of cationic and anionic surfactants. They used cetyl trimethylammonium bromide (CTAB) a cationic surfactant and sodium dodecyl sulfate (SDS) an anionic surfactant for this study. They prepared silica foams through three different systems: CTAB alone, SDS alone and CTAB-SDS mixed system. They concluded that the foams prepared using mixed CTAB-SDS system had long term stability as well as good foaming ability compared with the stand alone ones.

Protein molecules are also used as foaming agent for ceramic powder suspensions for the preparation of ceramic foams. The protein molecules not only stabilize the bubbles in slurry medium but also set the foamed suspensions by coagulation on heating. He et al (He et al., 2009) used a direct protein foaming method to prepare porous alumina ceramics with 3D interconnected pores. They used egg white protein and whey protein isolate for this method. The foams prepared using egg white protein had porosity of 87 vol.% with compressive strength value of 7.87 MPa while those prepared using whey protein isolate had compressive strength value of 6.36 MPa at 86.5 vol.% porosity. The foams prepared using egg white protein also showed a narrower pore size distribution. Yin et al (Yin et al., 2013b) prepared Si_3N_4 foams by direct foaming method using egg white protein and fish collagen as the foaming agents. Si_3N_4 foams with open porosity of 84.8–86.9 vol.%, average pore size of 216–266 μm and compressive strength of 8.7–13.7 MPa have been prepared by this method. The study showed that the addition of fish collagen gave regular shape to the cells and reduced the number of smaller cells.

The surfactant provides only interim stabilization to the bubbles in foamed ceramic powder suspension. That is the bubbles stabilized by surfactant molecules are not thermodynamically stable. The following transformations in the bubble structure occur after the generation of the surfactant stabilized foams (Wilson, 1989).

1. Smaller bubbles dissolve, while bigger ones may grow in size, by diffusion of gas through the continuous phase called Ostwald ripening.
2. Bubbles rapidly cream, thereby causing segregation into a foam layer on top of a bulk liquid.
3. Bubbles deform one another, leading to a polyhedral foam.
4. Liquid drains from the foam to the bulk.
5. Lamellae between foam bubbles rupture, leading to their coalescence.

The foamed suspensions stabilized by surfactants undergo foam collapse during drying due to any of the above process. In order to prevent the bubble enlargement and foam collapse, the foamed ceramic powder suspensions are set in to solid/gel immediately after foaming. The *in situ* polymerization of organic monomer and cross-linker added in the ceramic powder suspension is the commonly used method for the setting of foamed ceramic powder suspensions and the method is called gelcasting. A brief description of gelcasting is given in the following section.

1.4.6 Gelcasting

In gelcasting, the ceramic powder suspension cast in a mold is set in to strong gel by immobilizing the particles by *in situ* polymerization of inorganic monomer and

cross-linking agent present in the system. The method was originally developed by Omatete et al (Omatete et al., 1991) at Oak Ridge national laboratory for the fabrication of dense near-net-shape ceramics. During gelcasting, the macromolecular gel network results from the in situ polymerization of the organic monomers added in the ceramic suspension hold the ceramic particles together. The strong particle gel develops sufficient strength to support its own weight, thus avoiding deformation during handling. The process has aqueous and non-aqueous versions depending on the nature of solvent medium used. The major developments in the gelcasting technology happened with the aqueous version due to the high cost and environmental hazards of the non-aqueous solvents. Originally, the aqueous gelcasting system was developed with the use of acrylamide as the main gelling substance (Omatete et al., 1997). Alternative gelling systems have been investigated in order to substitute acrylamide because of its neurotoxic character. Janney et al (Janney et al., 2005) demonstrated that a range of monomers, such as ammonium acrylate, N-hydroxymethyl acrylamide, methacrylic acid, methacrylamide and methylene bisacrylamide can be applied to set ceramic suspensions. Later the gelcasting process has been modified for the preparation of porous ceramics. In this, the ceramic powder suspension containing organic monomer, cross-linking agent, initiator, catalyst and a surfactant is foamed by incorporating gas bubbles. The foamed suspension cast in a mould is set by *in situ* polymerization of the organic monomer and cross-linking agent. The wet foams removed from the mould after gelation are subsequently dried, binder removed and sintered to produce ceramic foams.

Binner and Sepulveda (P Sepulveda & Binner, 1999) studied the aqueous gelcasting system for the fabricating of alumina foams. They prepared alumina foams with maximum porosity of 93 vol. % using a water soluble acrylate monomer as the gelling agent. **Fig 1.13** shows the SEM photomicrograph of the alumina foam prepared by this method. Laurent et al (Rul, Laurent, Peigney, & Rousset, 2003) prepared $Mg_{0.9}Co_{0.1}Al_2O_4$ solid solution foam by gelcasting method using 2-hydroxyethyl methacrylate (HEMA) as monomer and 40% aqueous solution of poly(ethylene glycol 1000) dimethacrylate ($PEG_{1000}DMA$) as cross-linking agent. The prepared foams have a porosity of 98%. Zhou et al (X. Guo, Zhou, Ma, et al., 2012; X. Guo, Zhou, Wang, et al., 2012) prepared pore-gradient Al_2O_3 foams by gelcasting using the epispastic polystyrene (EPS) sphere template using acrylamide (AM) as the monomer and N,N'-methylene bisacrylamide (MBAM) as the cross linker.

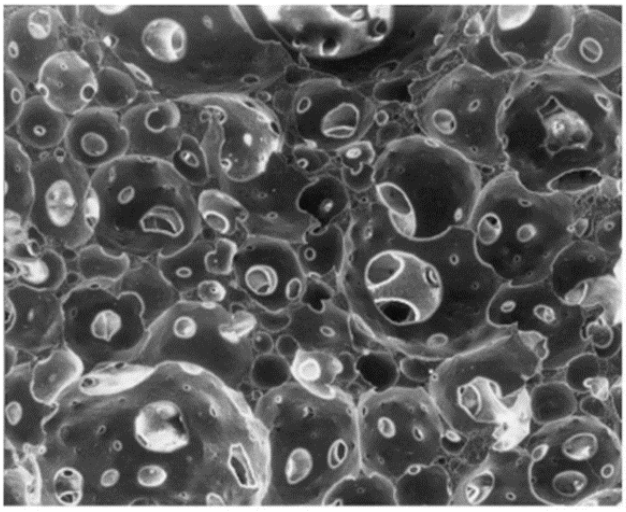

Fig. 1.13 SEM photomicrograph of gelcast alumina foam with 91 vol.% porosity (Sepulveda & Binner, 1999)

Sepulveda et al (Sepulveda et al., 2000) prepared bio medical grade open-cell HA foams with relative porosities ranging from 72 to 90 vol.% by gelcasting using water soluble acrylic monomers. The compressive strength of the HA foams varied within the range of 1.6 to 5.8 MPa. Zhang et al (Zhang et al., 2006b) reported a continuous gelcasting process for fabrication of ceramic foams. The key characteristic of this method is the mixing of slurry and N_2 bubbles, formed from a separated canister containing a surfactant prior to foaming of slurry, in a spiral mixer. Compared to conventional methods using N_2 gas to generate bubbles, porous ceramic produced using the new method displayed lower density, higher open and total porosities, and broad pore size distribution. They used methacrylamide and methylene bisacrylamide as monomer and crosslinking agent, respectively. The ceramic raw materials used are industrial and mining wastes such as powdered glass bottles and low-grade silica & alumina, respectively. The porous ceramics obtained have total and open porosities of 73 and 68.3 vol.%, respectively. The schematic of the experimental setup used for the new method is shown in **fig 1.14**.

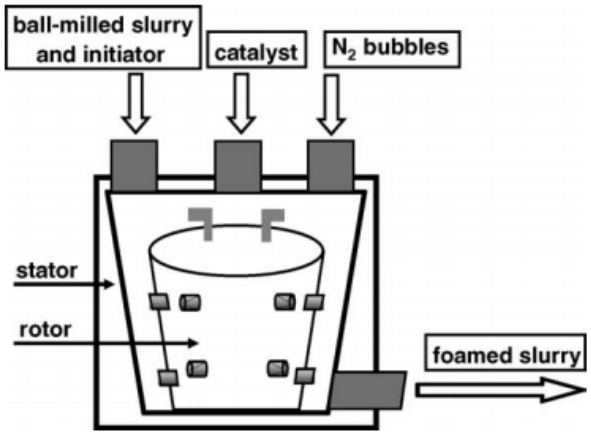

Fig 1.14 Schematic of the experimental setup for continuous gelcasting (Zhang et al., 2006b)

Gelcasting techniques utilizing environmentally friendly biopolymers as gel-formers in manufacturing of ceramic foams are intensively studied. Different biopolymers such as gelatin, proteins like ovalbumin and bovine serum albumin, agar, starch, and wheat particles have recently been applied as non-toxic gelling agent for the fabrication of ceramic foams. In this, foaming of the suspension containing dissolved gelatin or agar is carried out at higher temperature (80-90 ^{o}C). The foamed suspension cast in a mould is set by physical gelation of gelatin or agar by cooling. In the case of protein based system, the gelation of the foamed powder suspension is by the coagulation of the protein on heating and the process is called protein forming. On the other hand, the starch based systems undergo gelation by the absorption of water for the swelling of the starch and the process is called starch consolidation casting.

Lyckfeldt and Ferreira (Lyckfeldt & Ferreira, 1998) used starch as both pore former and consolidating agent for the preparation of porous alumina ceramics with porosities in the range of 23 to 73 %. Lorenzo et al (Lorenzo et al., 2002) prepared porous hydroxyapatite bodies of porosity in the range of 45 to 70 vol.% using starch consolidation method. Mao et al (Mao et al., 2008) prepared silica foams using foaming and starch consolidation. The foams prepared have porosities in the range of 70 to 82 vol.% and compressive strength in the range of 4 to 17 MPa. **Fig 1.15** shows the SEM photomicrographs of the silica foam prepared using starch consolidation casting.

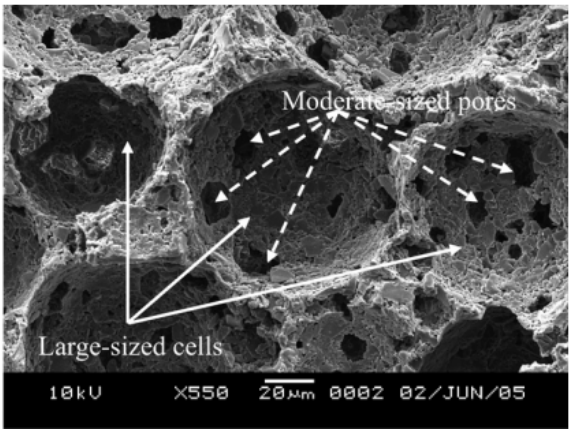

Fig 1.15 SEM photomicrographs of the silica foams (Mao et al., 2008)

Mouazer et al (Mouazer et al., 2004) prepared SiC foams by gelcasting using agar as the gelling agent. The SiC foams prepared have porosities in the range of 74 to 88 vol.% with flexural strength in the range of 2.5 to 10.8 MPa. Tulliani et al (Tulliani et al., 2013) prepared ceramic foams by using a combined gelcasting-fugitive phase process. Alumina & alumina-zirconia powders are used as the raw materials, agar is used as the gelling agent and polyethylene spheres are used as the pore formers. Alumina foams and alumina-zirconia foams with maximum porosities of 83 and 73 vol.%, respectively, have been prepared. Potoczek et al (Potoczek et al., 2009) prepared highly porous hydroxyapatite scaffold with porosity as high as 90 vol.% via gel-casting using agarose as the gelling agent. The obtained porous hydroxyapatite scaffold had macropores of ~500 μm, interconnecting windows of ~100 μm and a small amount of microcells of 0.2–0.9 μm. Potoczek prepared hydroxyapatite (Potoczek, 2008b) and alumina foams (Potoczek, 2008a) by gelcasting using agarose. By varying the ceramic powder loading and agarose content hydroxyapatite and alumina foams with porosities in the ranges of 73 to 92 vol.% and 85.7 to 89.9 vol.%, respectively, have been

prepared. Ortega et al (Ortega et al., 2003) studied the use of gelatin and polyvinyl alcohol as gelling agent for the gelcasting of ceramic foams.

Lemos and Ferreira (Lemos & Ferreira, 2004) prepared porous hydroxyapatite bio ceramics by a new direct consolidation method using fresh egg white. The egg whites acted as both the foaming agent and the gelling agent. The albumin protein present in the egg whites foamed the ceramic suspensions on agitation and the foamed suspensions are gelled on heating due to the denaturing of the protein. Hydroxyapatite ceramics with porosity as high as 75 vol.% have been prepared by this method. Dhara and Bhargava (Dhara & Bhargava, 2003) prepared ceramic foams via foaming and direct casting using ovalbumin based aqueous ceramic slurries. The foamed suspensions were set using nitric acid and sucrose. The addition of acid resulted in excessive shrinkage and cracking of foams at low slurry concentration. The addition of sucrose suppressed shrinkage leading to defect free foams. Alumina foams with porosity as high as 96 vol.% have been prepared using the ovalbumin-sucrose combination. Garrn et al (Garrn et al., 2004) used bovine serum albumin (BSA) as binder and deflocculating agent to prepare alumina foams. They prepared alumina foams with maximum porosity of 92.3 vol.% by this method.

1.4.8 Particle stabilized foams

The use of surfactants and biomolecules like lipids and proteins to reduce the interfacial energy by adsorbing at the liquid-gas interface provide only kinetic stability and not thermodynamic stability to the bubbles formed in a slurry medium. Colloidal particles have been used for the stabilization of oil droplets in emulsions.

Such emulsions are known as pickering emulsions after S.U. Pickering (Pickering, 1907), who noted that particles which were wetted more by water than by oil acted as emulsifiers for oil-in-water emulsions by residing at the interface. As observed in the case of Pickering emulsions, colloidal particles could be used to stabilize the gas-liquid interface in foams (Binks, 2002). Du et al (Du et al., 2003) reported the outstanding stability of particle stabilized bubbles compared to surfactant stabilized ones. They generated air bubbles beneath a planar air-water interface, stabilized by partially hydrophobic quasi-spherical silica particles of 20 nm diameter in pure water. Binks and Horozov (Binks & Horozov, 2005) reported the case of aqueous foams stabilized solely by silica nanoparticles. They used silica nanoparticles of different hydrophobicities to stabilize foams in pure water and in presence of salt. The wetting behavior of the particle surface is extremely crucial. It determines the attachment of the particle at the gas-liquid interface which requires the optimum balance between, solid-liquid, solid-gas and gas-liquid interfaces. Adsorption at fluid interfaces occurs when particles are not completely wetted by any of the fluids, thus exhibiting a finite equilibrium contact angle at the triple phase boundary (Binks, 2002). The equilibrium contact angle (θ) is determined by a balance between the interfacial tensions involved. Controlling the contact angle of particles at the interface is of major importance since it determines the type and stability of the initial particle-stabilized foams and emulsions. The contact angle of colloidal particles at fluid interfaces depends on the surface chemistry, roughness, purity and size of the particle, as well as on the composition of the fluid phases (van Oss & Giese, 2003).The contact angle determines the type of mixtures to be formed (Binks, 2002). Oil-in-water emulsions and foams are obtained for contact angles

lower than 90°, whereas water-in-oil emulsions and mists (aerosols) are produced for contact angles varying from 90 to 180° (Aveyard, Binks, & Clint, 2003). **Fig 1.16** shows the spherical particle at different contact angles at water-air or oil interfaces.

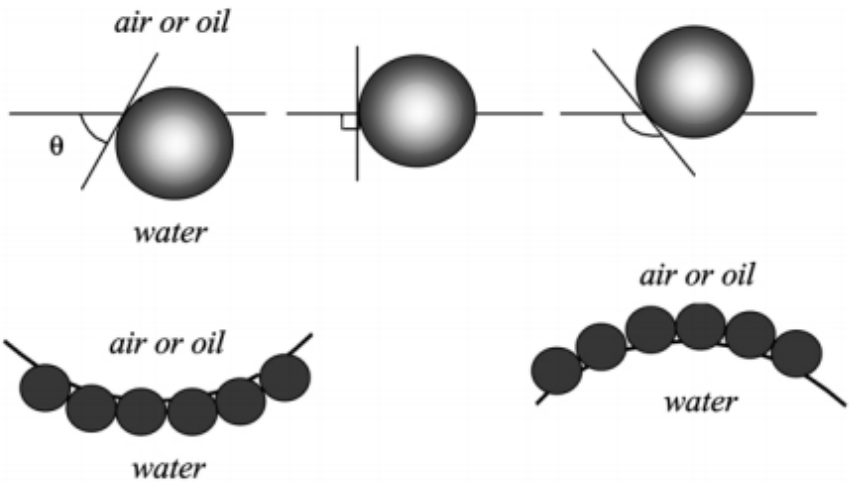

Fig 1.16 Spherical particle at different contact angles at water-air or oil interfaces (Binks, 2002)

Gonzenbach et al (Gonzenbach et al., 2006) reported a simple and versatile approach to prepare ultrastable particle-stabilized foams that percolate throughout the entire liquid phase and exhibit no drainage or creaming effects. The novelty of their method is that it enables the surface modification of high concentration of colloidal particles in the liquid phase, thus allowing the stabilization of a large gas–liquid interfacial area against disproportionation, coalescence, drainage, and creaming. They modified Al_2O_3, SiO_2, ZrO_2 and $Ca_3(PO_4)_2$ particles by lyophobization of their surfaces using short amphiphiles (<8 carbon atoms). **Fig.**

1.17 shows the approaches to attach colloidal particles at gas–liquid interfaces by tuning their surface-wetting properties (Gonzenbach et al., 2006).

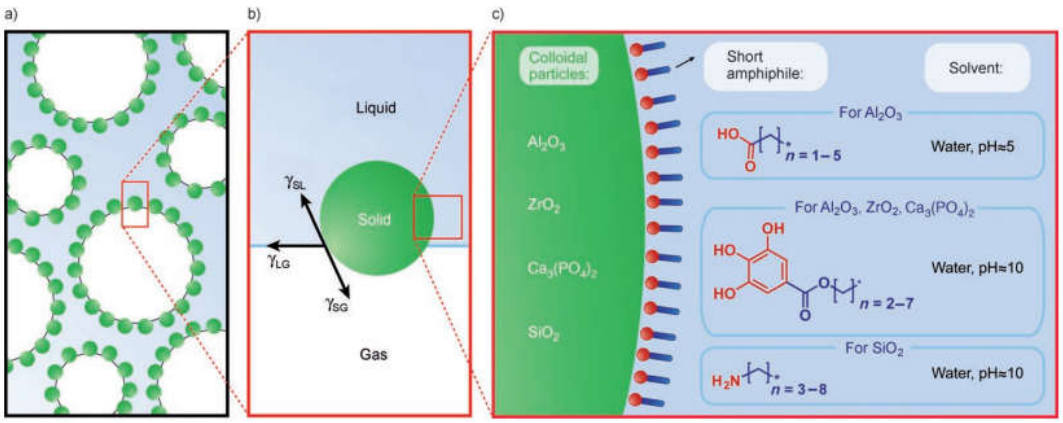

Fig. 1.17 Schematic showing (a) stabilization of gas bubbles with colloidal particles, (b) adsorption of partially lyophobic particles at gas-liquid interface and (c) surface modification of colloidal particles which are originally hydrophilic in nature. (Gonzenbach et al., 2006)

Studart et al (Studart et al., 2007) reported the processing routes for the preparation of macroporous ceramics from particle stabilized foams and emulsions. Gonzenbach et al (Gonzenbach et al., 2007; Gonzenbach et al., 2007) reported the preparation of macroporous alumina ceramics from particle stabilized wet foams. They (Gonzenbach et al., 2007) used butyric acid and propyl gallate as short chain amphiphiles to modify the surface of alumina particles to prepare macroporous alumina foams with a maximum of 86.5 vol.% porosity. The foams prepared have an average cell size of 35 μm, and a remarkable compressive strength of 16.3 MPa at 86.5 vol.% porosity. In another study, they (Gonzenbach et al., 2007) used short-chain carboxylic acids such as propionic, butyric, valeric, and enanthic acids to modify the alumina particle surface to form particle stabilized wet foams. The

macroporous alumina foams prepared by this method showed average cell sizes ranging from 10 to 300 μm and porosities between 45 and 95 vol.%. A high compressive strength of up to 16 MPa is seen in alumina foams with porosity of 88 vol.%.

Chuanuwatanakul et al (Chuanuwatanakul et al., 2011) produced porous cellular alumina ceramic green bodies by combining the particle stabilized foam method with gelcasting. The foamed suspensions are stabilized by particles rendered weakly hydrophobic with short chain sulfonate surfactants. Poly vinyl alcohol (PVA) and 2,5-dimethoxy-2,5-dihydrofuran (DHF) were used as the gelling reagents. Juillerat et al (Juillerat et al., 2011; Juillerat et al., 2010) presented a novel method to produce self-setting inorganic foams with unique hierarchical pore structures. They added calcium aluminate cement to alumina suspensions modified with propyl gallate and foamed the suspensions by mechanical frothing. Lithium carbonate is added as setting accelerator for the cement. Use of the calcium aluminate cement bypassed drying and sintering process and zero-shrinkage, crack-free samples are produced. The foams prepared have a maximum porosity of 76 vol.% and an average macropore size of 200 μm.. In another method, they (Juillerat et al., 2012) prepared porous calcium aluminate cement by foam stabilization via in-situ hydrophobization. The self-hardening calcium aluminate foams obtained in this study show average macropore sizes between 89 and 1652 μm and porosities up to 92.1 vol.%.

Yu et al (Yu et al., 2012) prepared Si_3N_4 foam ceramics with nest-like cell structure from particle-stabilized aqueous foams. They modified the surface of the

Si_3N_4 particles using octylphenol ethoxylate and propyl gallate. The Si_3N_4 particle-stabilized foams had high stability, with little shrinkage observed during drying. The nest-like pores are joined by elongated rod-shaped β-Si_3N_4 grains as seen in f**ig 1.18.** Ahmad et al (Ahmad et al., 2013) studied the preparation of particle stabilized ultra-low density zirconia toughened alumina (ZTA) foams. Valeric acid is used to modify the surface of alumina and zirconia particles. Ultra-low density ZTA foams having single strut wall thickness, cell size ranging from 80 μm to 200 μm, and porosity above 90 vol.% have been successfully fabricated via the particle-stabilized direct foaming method. Liu et al (Liu et al., 2013) prepared porous PZT ceramics from particle stabilized foams via gelcasting. They prepared PZT ceramics with porosities ranging from 27.8 to 72.4 vol.% by gelcasting of particle stabilized foams. They (Liu et al., 2013) also studied the effect of foam composition on the microstructure and piezoelectric properties of macroporous PZT ceramics from ultra-stable particle-stabilized foams. In both the studies they have used valeric acid as the surface modifier.

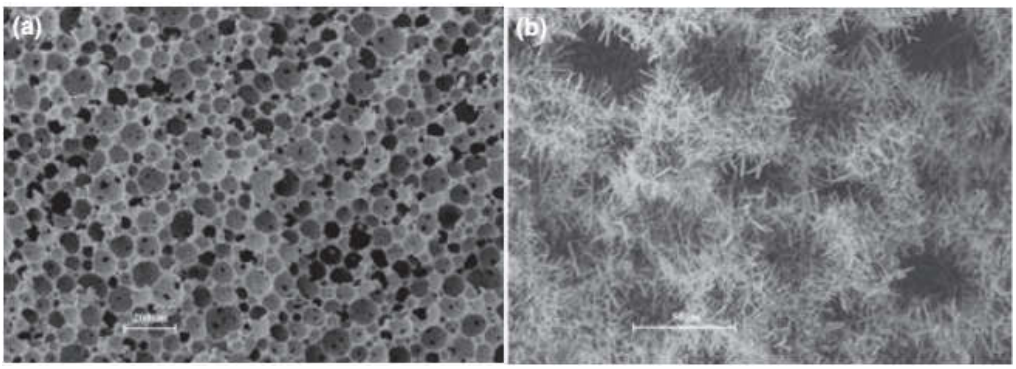

Fig 1.18 SEM images of Si_3N_4 foams showing nest-like cell structure (Yu et al., 2012)

1.5 Ceramic foams from pre-ceramic polymers

A pre-ceramic polymer is a polymer which on pyrolysis yields a ceramic. Poly(organocarbosilanes), poly(organosiloxanes), poly(organosilazanes) and poly(organosilylcarbodiimides) are the most commonly used pre-ceramic polymers (Colombo et al., 2010). The ceramic materials obtained by the pyrolysis of pre-ceramic polymers are called polymer derived ceramics (PDC). They include silicon carbide (SiC), silicon oxycarbide (SiOC), silicon nitride (Si_3N_4), SiO_2, SiNC, etc. **Fig. 1.19** shows the general structure of pre-ceramic polymers used for the preparation different types PDCs.

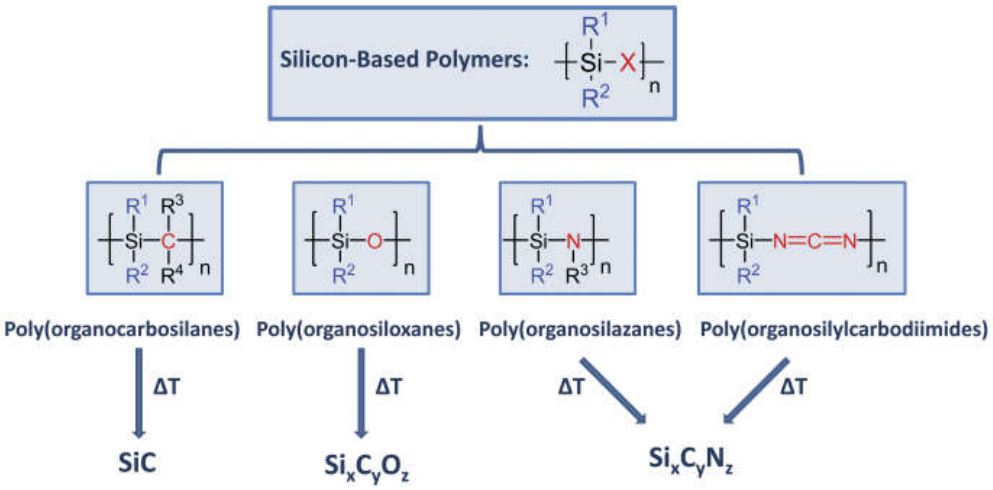

Fig 1.19 Structure of pre-ceramic polymers and the PDC obtained by their pyrolysis (Colombo et al., 2010)

The direct foaming, polymer foam replication and sacrificial templating methods are used for the preparation of ceramic foams from pre-ceramic polymers (Colombo et al., 2010; Eom et al., 2013). The direct foaming of pre-ceramic polymer melt and pre-ceramic polymer solution using blowing agents are studied. In melt foaming, the gases generated by thermally induced crosslinking of the pre-

ceramic polymer generate bubbles, which are stabilized by setting due to the crosslinking reactions. The green foam thus obtained is then pyrolyzed in inert conditions to get the ceramic. In some cases, the foaming is due to blowing agents mixed with the precursor prior to the melt foaming stage. In the second case, the pre-ceramic precursor solution is foamed at room temperatures using blowing agents and set by the cross-linking of the polymer precursor. The green foam is dried and then pyrolyzed or sintered to get the final product. The polymer foam replication method involves the use of a polyurethane foam template. The precursor solution is impregnated into the polyurethane foam till maximum coverage is ensured. The excess solution is then drained by roller pressing. The green foam obtained by drying and template removal by pyrolysis at 600 ^{o}C is sintered in inert atmosphere to get the ceramic foam. In the final method, sacrificial templates such as polymer beads, expanded microspheres, microbeads, etc. are first dispersed within the pre-ceramic polymer precursor and then set by thermally induced crosslinking reactions at temperature in the range of 180-250 ^{o}C. The green body is then pyrolyzed to remove the template and sintered in inert atmosphere to get the ceramic foam.

Colombo et al have extensively studied the preparation of SiOC foams. They (Colombo et al. 1998; Colombo & Modesti, 1999, 2004) have prepared amorphous SiOC foams by direct foaming of a solution containing polyurethane precursors and pre-ceramic polymer. In this, foaming is due to the evaporation of dichloromethane solvent, carbon dioxide produced by the hydrolysis of excess diisocyanate used and water vapour generated by the cross-linking of the pre-ceramic polymer. The SiOC foams prepared by this route have an average pore

diameter ranging from 200 to 400 μm and an open porosity of 80 to 92 vol%. They (Colombo & Hellmann, 2002) have also used foaming of pre-ceramic polymer solutions using an external blowing agent and studied a variety of pre-ceramic polymers which are poly-silsesquioxanes containing cross-linkable Si–OH and Si-bonded alkoxy groups. Colombo and Bernardo (Colombo & Bernardo, 2003) prepared macrocellular and microcellular SiOC foams from methyl polysilsesquioxane polymer. The macrocellular foams are prepared by the direct foaming of polyurethane precursor and pre-ceramic polymer solutions. The microcellular foams are prepared by mixing PMMA microbeads with pre-ceramic polymer powder followed by heating at 150 ^{o}C for cross linking of the polymer and shaping by uniaxial pressing. The compacts are sintered in inert atmosphere after PMMA removal by heating at 300 ^{o}C in air atmosphere to form microcellular SiOC ceramics. **Fig 1.20** shows the SEM images of the macro and micro cellular SiOC foams.

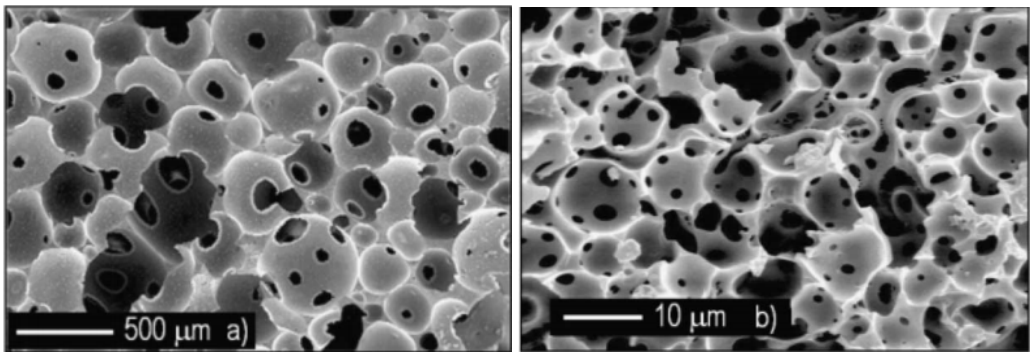

Fig 1.20 SEM images of (a) macrocellular and (b) microcellular SiOC foams (Colombo & Bernardo, 2003)

Zeschky et al (Zeschky et al., 2003; Zeschky et al., 2005) prepared ceramic foams by melt foaming of a methyl phenyl poly(silsesquioxane) polymer with

formula $[(C_6H_5)_{0.62}(CH_3)_{0.31}(R)_{0.07}SiO_{1.5}]_n$ where (n=20) containing additional cross-linking active groups R=[-OH] and [-OC2H5]. The polymer was mixed with quartz (Zeschky et al., 2003) and Si/SiC (Zeschky et al., 2005) powders to prepare SiOC foams. In this, they could prepare SiOC foams with gradient porosity having porosity in the range of 40 to 90 vol.%.. Takahashi et al (Takahashi et al., 2001; Takahashi & Colombo, 2003; Takahashi et al., 2001) have reported the preparation of SiOC foams using methylsilicone pre-ceramic polymer. They used both the melt foaming of the polymer (Takahashi & Colombo, 2003) and physical blowing of polyurethane precursor/pre-ceramic polymer solutions (Takahashi et al., 2001; Takahashi et al., 2001). The melt foaming method yielded SiOC foams with a bulk density in the range of 0.22 to 0.53 g/cm^3 with a maximum compressive strength and flexural strength of 4.5 and 5.5 MPa, respectively. Rocha et al (Rocha et al., 2008) synthesized SiOC foams with a maximum porosity of 84 vol.% by electron beam irradiation of methylsilicone resin. Kim et al (Kim et al., 2002; Kim et al., 2003; Kim et al., 2003; Kim & Park, 2003) prepared microcellular ceramic from polycarbosilane and polysiloxane using CO_2 as blowing agent. The pre-ceramic powders are first uniaxially pressed to form compacts, kept in a pressure chamber where they are saturated using gaseous, liquid or supercritical CO_2. The bubbles are nucleated in the system by creating a thermodynamic instability by rapidly lowering the pressure or increasing the temperature. The foamed pre-ceramic polymers are heated up to 200 ^oC in air for crosslinking and then pyrolyzed in inert atmosphere to get the microcellular ceramics. A pictorial representation of the process is shown in **fig 1.21**.

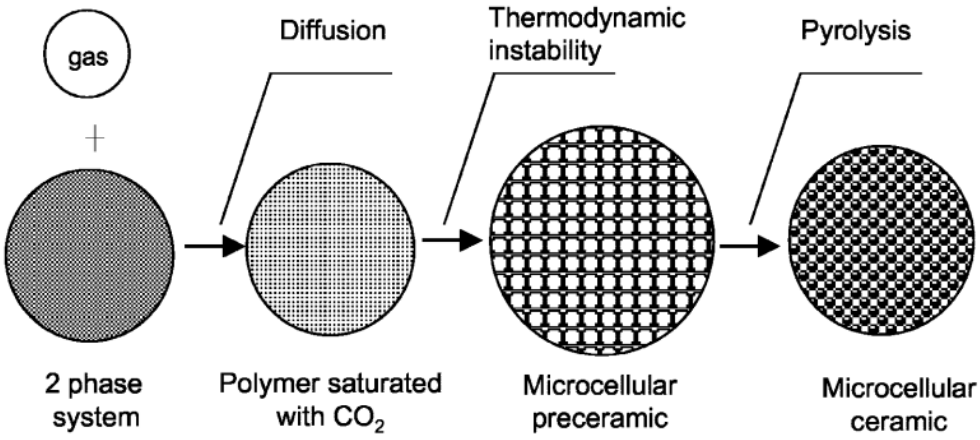

Fig 1.21 Foaming of pre-ceramic polymers using CO_2 (Kim, Kim, et al., 2003)

Kim et al (Kim et al., 2011; Kim et al., 2005) prepared microcellular silicon carbide ceramics by sacrificial template method using polysiloxane as the pre-ceramic polymer. They used both poly(methyl-methacrylate-co-ethylene glycol dimethacrylate) microbeads (Kim et al., 2005) and hollow spheres consisting of thermoplastic shell (copolymer of vinylidene chloride, acrylonitrile, and methyl-methacrylate) encapsulating a hydrocarbon gas (Kim et al., 2011) as the pore templates. In the former method (Kim et al., 2005), they used Al_2O_3 and Y_2O_3 as sintering additives and phenolic resin as carbon source. The compacts obtained by pressing the mixture of pre-ceramic polymer, phenolic resin, pore templates and additives are cross-linked by heating up to 180^oC in air. The cross linked compacts are pyrolyzed in N_2 atmosphere at 1200 ^oC to get porous SiOC containing free carbon, which are further sintered at 1650 ^oC to get the microcellular SiC ceramics. In the latter method (Kim et al., 2011), carbon black is used as carbon source with AlN and Y_2O_3 as sintering additives. The pre-ceramic polymer, carbon black, pore templates and additive mixtures are steam chest moulded at an absolute steam pressure of 0.47 MPa. The bodies are cross-linked by heating in air at 200 ^oC,

pyrolyzed at 1200 ^{o}C and sintered at 1650 ^{o}C to get the microcellular SiC ceramics. In the first case (Kim et al., 2005), open cell, microcellular silicon carbide ceramics with porosities ranging from 60 to 95 vol.% could be prepared while in the second case (Kim et al., 2011), yielded a maximum porosity of 62 vol.%. Shibuya et al (Shibuya et al., 2007) prepared microcellular silicon oxycarbide foams from methylsilicone resin and PMMA beads. The SiOC foams prepared by this method had a minimum bulk density of 0.4 g/cm^3. Biasetto et al (Biasetto et al., 2008) prepared SiOC microcellular ceramic foams possessing soft-ferromagnetic properties from polysiloxane pre-ceramic polymer, PMMA microbeads and iron silicide micro-powders. Jang et al (Jang et al., 2006) prepared highly porous open cell, microcellular SiC foams using polysiloxane and expandable microspheres as sacrificial template. They could prepare SiC foams with a porosity in the range of 77 to 94 vol.%. Song et al (Song, Kwon, Kim, & Kim, 2010) reported the preparation of microcellular SiC ceramics with a duplex pore structure from a polysiloxane, carbon black, SiC, Al_2O_3, and Y_2O_3 using two types of pore former, expandable microspheres (EM) and PMMA microspheres. Jin and Kim (Jin & Kim, 2010) reported the preparation of highly porous SiC ceramics (a maximum of 88 vol.% porosity) using polycarbosilane as a precursor for SiC, polymer microbeads [poly(methyl methacrylate-co-ethylene glycol dimethacrylate)] as a pore template, and a polysiloxane as a binder.

Yoon et al (Yoon et al., 2007; Yoon et al., 2007) prepared highly aligned porous SiC ceramics from a pre-ceramic polymer by freeze casting technique. They (Yoon et al., 2007) prepared porous SiC ceramics by freezing either a camphene solution of polycarbosilane (Yoon et al., 2007) or SiC powder dispersion in a

camphene solution of polycarbosilane (Yoon et al.. 2007). The SEM image of the porous SiC ceramics is shown in **fig 1.22**. In the second case, (Yoon et al., 2007), polycarbosilane is used as a binder for SiC powder. They have observed nanowire growth on the cell wall surface of the SiC foam and the polycarbosilane acts as the precursor for the SiC nanowires. The SEM images of porous SiC with nanowires grown on the surface is shown in **fig 1.23**.

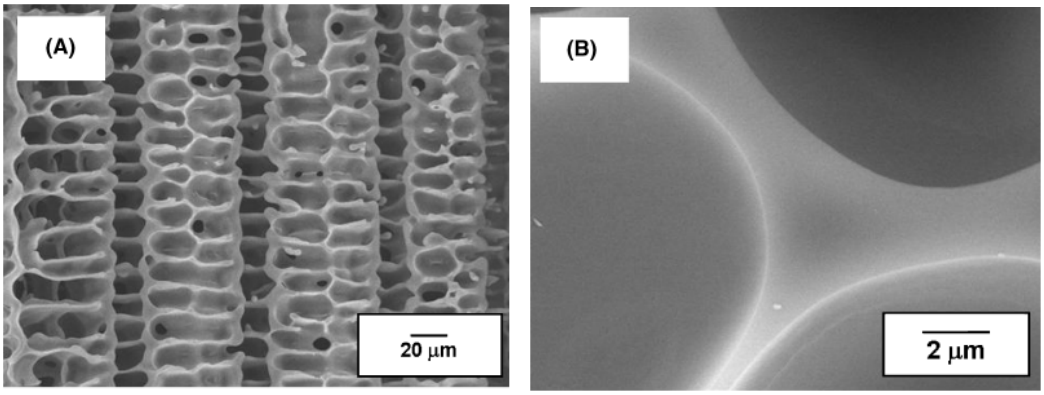

Fig 1.22 SEM image of SiC foams prepared by freeze casting of polycarbosilane solution in camphene showing (a) highly aligned pores and (b) the cell wall (Yoon, Lee, et al., 2007)

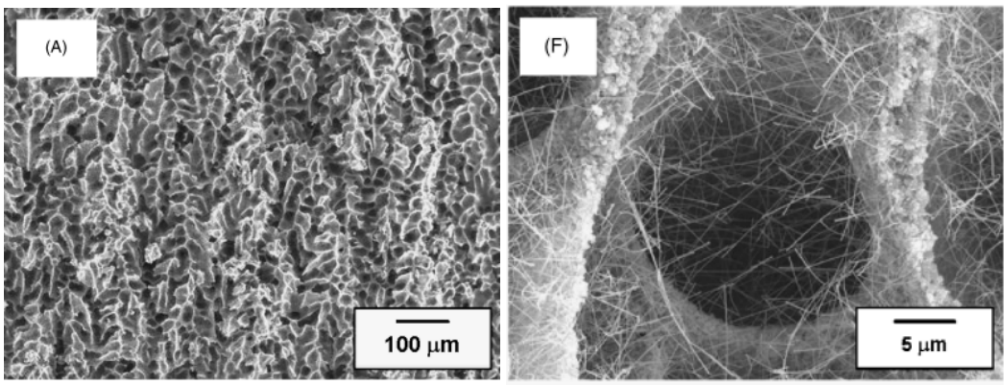

Fig 1.23 SEM images of SiC foam prepared by freeze casting of SiC powder dispersion in camphene solution of polycarbosilane showing (a) highly aligned pores and (f) nanowire growth on the cell wall surface (Yoon, Park, et al., 2007)

Emulsion based techniques are also used for the preparations ceramic foams from pre-ceramic polymers. Bakumov et al (Bakumov et al., 2009) fabricated porous Si/C/(O) bodies from pre-ceramic polymer via an emulsion templating route. They emulsified polysiloxane and polycarbosilane precursor solution and water by intensive stirring and ultra-sonication in presence of surfactants. Ungureanu et al (Ungureanu et al., 2011) prepared tough silicon carbide macro/mesocellular crack-free monolithic foams via a high internal phase emulsion route (HIPE). The high internal phase emulsion is prepared using aqueous tetraethylorthosilicate (TEOS) solution, Tetradecyltrimethylammonium bromide (TTAB) as emulsifying agent and dodecane as the oil phase. The silica foam monolith obtained from the high internal phase emulsion is impregnated with polycarbosilane solution followed by cross-linking, pyrolysis and silica removal by leaching with HF solution to form SiC foam. Vakifahmetoglu et al (Vakifahmetoglu et al., 2011) prepared SiOC foams via emulsion templating route. Polymethylsilsesquioxane (PMS) dissolved in toluene is emulsified with an aqueous solution of Tween 80 using zirconium acetylacetonate as a cross-linking agent. The emulsified monolith is pyrolyzed in N_2 atmosphere at 1200 ^oC to get the SiOC foam.

1.6 Scope and Objectives

Among the reported processing methods for the preparation of cellular ceramic foams, the emulsion templating and direct foaming are the most promising ones as they produce foams with high porosity. In emulsion templating method, a good control of cell size is achieved by controlling the size of the oil droplets. The droplet

size can be varied by varying the mixing speed, surfactant concentration and the amount of the oil phase. Most of the reported emulsion templating methods use a liquid oil phase. This necessitates partial drying of the cast emulsion before mould removal. This in turn decreases the production rate. A solution to this problem is to use an oil phase which is solid at room temperature. On the other hand, the current direct foaming methods for the preparation of ceramic foams use synthetic organic polymers or monomers, surfactant molecules and solvents as the processing additives. Replacement of these processing additives with non-toxic naturally renewable molecules is of great economic and environmental importance. Sucrose is a naturally renewable molecule of agricultural origin. The use of sucrose in place of synthetic additives reduces our dependency on petroleum-based materials.

The main objective of this thesis is to study novel methods for the preparation of ceramic foams. In the first part of the thesis (Chapter 2 and 3), the preparation of alumina foams by an emulsion templating method using two novel oil phases which are solid at room temperature is studied. In the second part (Chapter 4, 5 and 6), thermo-foaming of powder dispersions in molten sucrose is studied for the preparation of alumina, mullite and SiC ceramic foams.

The specific objectives of this research work are summarized below:

- To study the preparation of ceramic foams by freeze gelcasting of oil-in-aqueous alumina slurry emulsions.
- To study oil phase which is a solid at room temperature for the preparation of ceramic foams by emulsion templating method
- To study the preparation of ceramic foams (alumina and mullite) by thermo-foaming of powder dispersions in molten sucrose.

- To study the preparation of large ceramic foam bodies by optimizing the sintering conditions.
- To study the preparation of SiC foams by thermo-foaming of silicon powder dispersions in molten sucrose
- To utilize carbon derived from the sucrose polymer for SiC formation
- To study the effect of magnesium nitrate blowing agent on the thermo-foaming process and properties of the ceramic foams.

1.7 Organization of the thesis

This thesis describes the research on the processing of ceramic foams via two novel methods, emulsion templating of alumina powder suspensions using an oil phase which is solid at room temperature and thermo-foaming of ceramic powder dispersions in molten sucrose. The thesis is presented in seven chapters. The research problem and objectives of the investigations are well defined at the end of **Chapter 1.** This chapter also provides a state-of-the-art literature survey on the processing of ceramic foams along with their potential applications.

Chapter 2 deals with the preparation of alumina foams by freeze gelcasting of naphthalene-in-aqueous alumina slurry emulsions. The effect of naphthalene to alumina slurry volume ratio and alumina powder concentration in the aqueous slurry on the porosity, cell size, cell morphology, compressive strength and Young's modulus of the alumina foams have been discussed. The rheological characteristics of the emulsions and compressive strength & drying behaviour in ambient conditions of the gelled emulsion bodies are also described.

The preparation of alumina foams by freeze gelcasting of hydrogenated vegetable oil-in-aqueous alumina slurry (HVO-in-AAS) emulsions is described in **Chapter 3**. The removal of HVO from the dried gel bodies via soxhlet extraction and also by immersion in petroleum ether is described. The effect of HVO to AAS volume ratio and alumina powder concentration in aqueous slurry on porosity, cell size, cell morphology, compressive strength and Young's modulus of the alumina foams is discussed.

The preparation of alumina foams by the thermo-foaming of powder dispersions in molten sucrose is presented in **Chapter 4.** The dispersion of alumina powder in molten sucrose, and mechanism of foaming & foam setting are discussed. The effect of alumina powder concentration & foaming temperature on the foaming time, foam setting time and foam rise of the powder dispersions in molten sucrose is described. The effect of foaming temperature and alumina powder concentration on the cell size, porosity and mechanical properties of the alumina foams is discussed. The effect of an additional pyrolysis step for the preparation of large alumina foam bodies is revealed. The effect of magnesium nitrate blowing agent on the thermo-foaming process is also discussed.

Chapter 5 deals with the preparation of mullite foams by thermo-foaming of alumina-silica co-dispersions in molten sucrose. The reaction sintering of alumina and silica at elevated temperatures to form mullite is described. The effect of foaming temperature, powder concentration and magnesium nitrate blowing agent on the thermo-foaming process and mullite foam properties is discussed.

The preparation of silicon carbide foams by thermo-foaming of silicon powder dispersions in molten sucrose is described in **Chapter 6.** The use of carbon derived from sucrose polymer for the preparation of SiC by reaction with silicon is also described. The effect of foaming temperature on the foaming characteristics and foam properties is discussed. The effect of magnesium nitrate on the thermo-foaming process and properties of the SiC foams is also presented.

The results of the current work are summarized in **Chapter 7**. A mention of the scope for future research on this subject is also made.

Chapter 2

Processing of Alumina Foams by Freeze Gelcasting of Naphthalene-in-Aqueous Alumina Slurry Emulsions

2.1 Introduction

Macroporous ceramics with very high porosity and highly interconnected pore structure are used for a variety of applications. By controlling the porosity and pore size of the macroporous ceramics, we can tune its properties and applications. The use of emulsions as templates for the preparation of macroporous ceramics has been reported by Pine et al (A Imhof & Pine, 1997; Arnout Imhof & Pine, 1998; Manoharan et al., 2001). Oil droplets are ideal pore templates for the preparation of macroporous ceramics as they can be uniformly distributed in the aqueous ceramic powder suspensions by mechanical mixing in the presence of a suitable surfactant to form emulsions. The pore size could be manipulated by controlling the droplet size, which can be obtained by adjusting the emulsifying agent concentration and mixing speed. In addition, loading of liquid template even higher than 74 vol.% of the emulsion could be possible. Such emulsions are known as high internal phase emulsions (Lissant, 1970). Recently, Barg et al (Barg et al., 2009, 2008; Ewais et al., 2011) have reported the preparation of macroporous ceramics from powder suspensions through a high alkane phase emulsion based process using decane as the oil phase. In this, the emulsion cast in a mould need to be partially dried before the mould removal which limits the production rate. This could be easily remedied by using an oil phase which is a solid at room temperature. An emulsion templating method based on liquid paraffin as pore template and collagen as consolidating

agent has been reported by Vitorino et al (Vitorino et al., 2013). In the present Chapter, we report an emulsion templating method for the preparation alumina foams from aqueous powder suspension using naphthalene as the oil phase. Herein, the emulsion is prepared by dispersing the molten naphthalene in an alumina powder suspension using an emulsifying agent. The gelation of the emulsion cast in a mould is achieved by the solidification of the naphthalene and physical cross-linking of the carrageenan gelling agent present in the aqueous alumina slurry. The subsequent drying of gelled bodies, naphthalene removal by sublimation and sintering produces the alumina foams. **Fig 2.1** shows the schematic of the process.

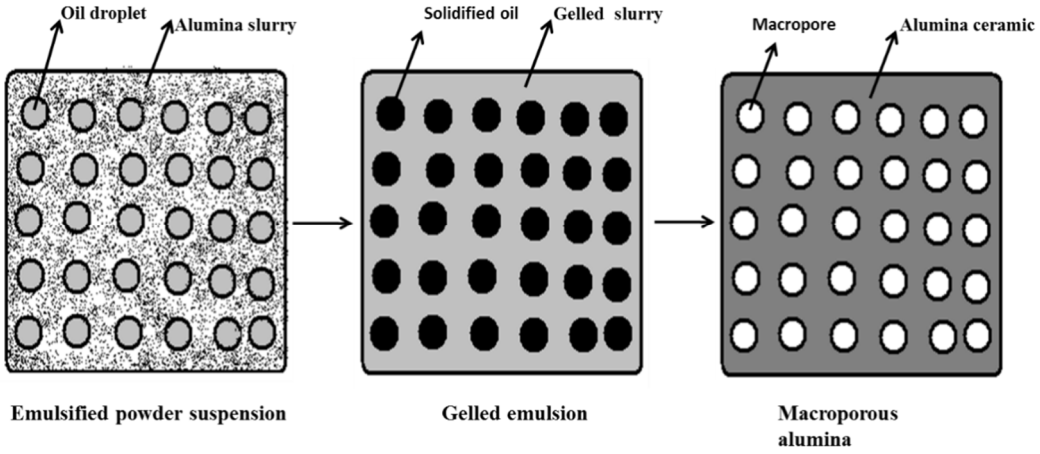

Fig 2.1 Schematic of the emulsion templating process

2.2 Experimental

2.2.1 Materials

α-Alumina powder of average particle size 0.34 μm and specific surface area 10.4 m^2/g was procured from ACC Alcoa, Kolkata, India. The alumina powder contains particles of irregular shape. The particle size distribution and SEM photomicrograph of the alumina powder is shown in **Fig. 2.2.** Analytical reagent

grade naphthalene and sodium dodecyl sulphate (emulsifying agent) were procured from Merck India Ltd., Mumbai. A 35 wt% aqueous ammonium poly(acrylate) solution (Darvan 821A**)** used as dispersant was received from Vanderbilt Company Inc., USA. The carrageenan used as gelling agent was procured from Aldrich Chemical, USA. Distilled water was used for the preparation of alumina powder suspensions.

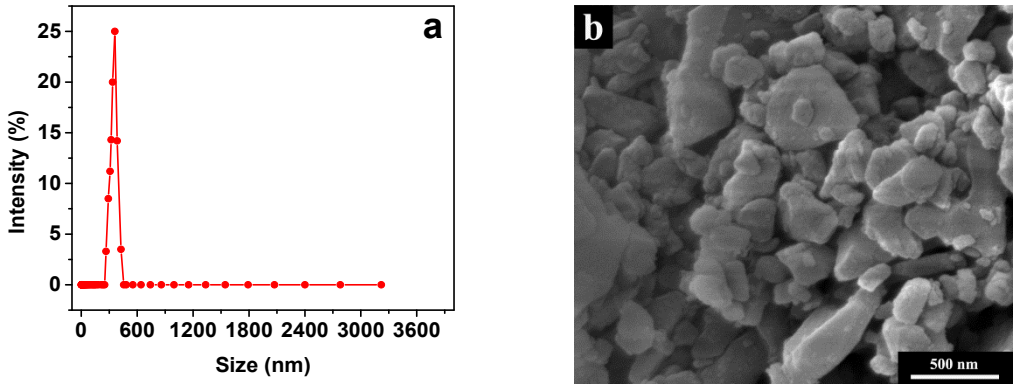

Fig 2.2 (a) particle size distribution and (b) SEM photomicrograph of the alumina powder

2.2.2 Preparation of alumina foam

The flow chart of the emulsion gelcasting process is shown in **Fig. 2.3**. Slurries of 10, 20 and 30 vol.% alumina loadings were prepared by dispersing the alumina powder in water using the ammonium poly(acrylate) dispersant. The slurries were ball milled in polyethylene bottles using zirconia grinding media on a roller ball mill for 12 hours. The slurries were transferred to 500 ml round bottom flasks. The suspensions were heated in a water bath at 90 ^{o}C with mechanical stirring using a Teflon paddle after adding carrageenan. The amount of carrageenan used was 1.5 wt% of the water present in the aqueous alumina slurry. Naphthalene

and sodium dodecyl sulphate (emulsifying agent) taken in a beaker was melted in a water bath at 90 ^{o}C. The amount of emulsifying agent used was 0.3 wt% of the naphthalene. The molten naphthalene containing the emulsifying agent was added to the alumina slurry containing the gelling agent and the stirring was further continued for another one hour to form stable naphthalene-in-aqueous alumina slurry emulsions. The emulsions were prepared at naphthalene to alumina slurry volume ratios in the range of 1.0 to 1.86. The mixing speed used throughout the study was 350 rpm. The emulsions thus obtained were cast in cylindrical glass moulds and allowed to cool naturally to room temperature for gelation. The cooling process can be shortened by keeping the cast emulsion bodies in a refrigerator at 5 ^{o}C for 30 minutes. The gelled bodies removed from the mould were dried in air atmosphere at room temperature. The dried bodies were kept in an air oven at 70 ^{o}C for the removal of the naphthalene. The naphthalene removed bodies were sintered at 1550 ^{o}C in an electrically heated furnace for two hours. The heating rate used was 2 ^{o}C/minute up to 600^{o} C and then at 5 ^{o}C/minute. The sintered bodies were unloaded after natural cooling of the furnace to room temperature.

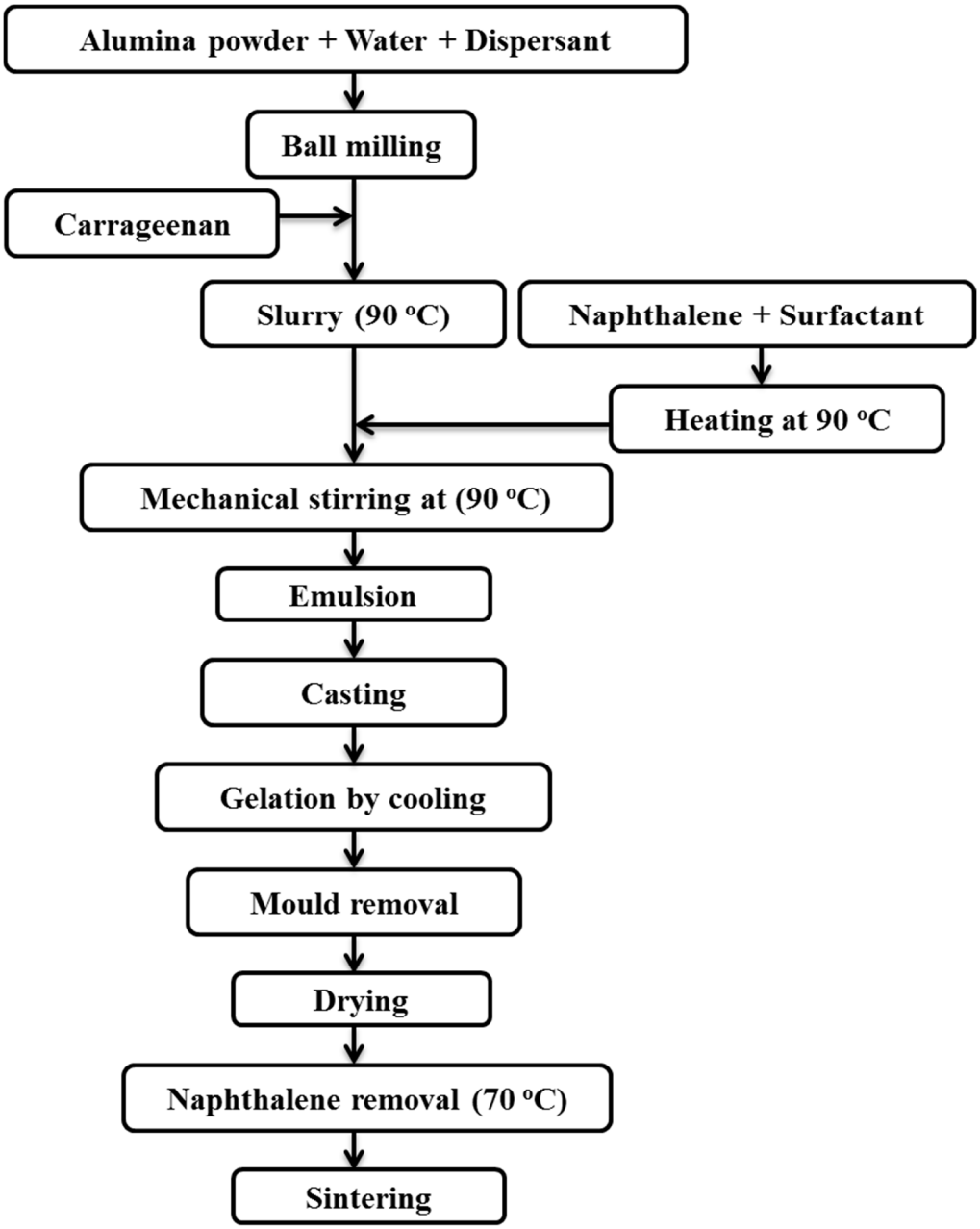

Fig 2.3 Flowchart for the preparation macroporous alumina by freeze gelcasting of naphthalene-in-aqueous alumina slurry emulsions

2.2.3 Naphthalene removal kinetics

Dried emulsion bodies after complete removal of water were kept at 70 ºC in air oven. The weight of the bodies were taken at a regular interval of 4 hours till a constant weight was achieved.

2.2.4 Characterization

2.2.4.1 Viscosity Measurements

Viscosity measurements of the alumina suspensions were carried out in a RVT model Brookfield viscometer [Brookfield Engineering Inc., USA] using a small sample adapter of coaxial geometry and cylindrical spindles (SC-21 and SC-29). The viscosity of the emulsions was measured at 85 ^{o}C using the same spindles with the help of a thermosel accessory along with the viscometer. The yield stress of the emulsions was calculated using Casson model (Equation 4)

$$\sqrt{\tau_S} = m\sqrt{\gamma} + \sqrt{\tau_y} \qquad (4)$$

where, τ_S is shear stress, γ is shear rate τ_Y is yield stress and m is the slope

2.2.4.2 Porosity measurement

The bulk density of the alumina foams was calculated from the weight and dimensions. From the bulk density, the relative density was calculated by equation (5),

$$\rho = \frac{bulk\ density}{theorectical\ density} \qquad (5)$$

The porosity of the foams are calculated from their relative densities by the equation (6),

$$\text{Porosity} = [(1 - \rho) \times 100]\% \qquad (6)$$

2.2.4.3 Microstructure analysis

The microstructure of the sintered ceramics was observed on fractured surfaces using a scanning electron microscope (SEM, Hitachi S-2400, Hitachi High Technologies Corporation, Japan). The samples were sputter coated with gold before the analysis.

2.2.4.4 Cell size measurement

The average pore size of the ceramics was measured from the respective microstructures with the help of ImageJ software.

2.2.4.5 Compressive Strength Measurements

Stress-strain measurements of the gelled emulsion bodies and sintered alumina ceramics were carried out using a universal testing machine (Instron 4469, Instron USA). The loading rate used was 5 mm/minute and 1 mm/minute, respectively, for gelled emulsion bodies and sintered alumina ceramics. Cylindrical samples of 22 mm diameter and 45 mm length were used for the stress-strain measurement of the gelled emulsion bodies. On the other hand, sintered ceramic samples used were having 17 mm diameter and 35 mm length. The compressive strength and Young's modulus were obtained from the stress-strain graph.

2.3 Results and Discussion

2.3.1 Dispersion of alumina powder

The dispersion of alumina powder by ammonium poly(acrylate) was first reported by Cesarno and Aksay (Cesarno & Aksay, 1988). Chang et al (Chang, Lange, & Pearson, 1994) established that the powder dispersion by the ammonium

poly(acrylate) dispersant is due to the electrosteric mechanism. That is, the adsorbed poly(acrylate) layer produces a steric contribution and the surface charges created by the ionization of the carboxylate groups present in the adsorbed poly(acrylate) molecules produce an electrostatic contribution. **Fig. 2.4** shows the effect of dispersant concentration on the viscosity of 50 vol.% alumina powder suspensions in water. The viscosity minimum is achieved at a dispersant concentration of 0.33 wt%. At this concentration, the ammonium poly(acrylate) form a monolayer coverage on the particle surface.

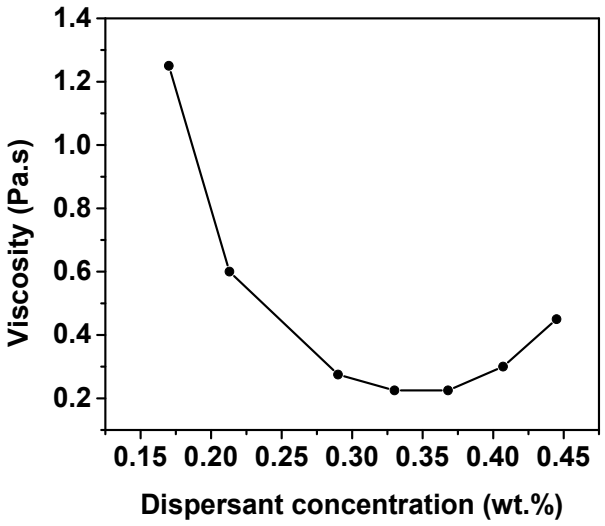

Fig 2.4 Effect of dispersant concentration on the viscosity of 50 vol.% alumina powder suspensions in water.

Guo et al (Guo et al., 1997) studied the effect of temperature on the adsorption of ammonium poly(acrylate) on alumina powder surfaces and reported an increase in the extent of adsorption with the increase of temperature. That is, higher concentration of the dispersant is required to form a dispersant surface coverage and to establish the adsorption equilibrium at higher temperatures. This is

further evidenced from the **Fig. 2.5** showing the effect of temperature and dispersant concentration on the viscosity at various shear rates of 50 vol.% aqueous alumina powder suspensions. The aqueous alumina powder suspension at 80 ^{o}C using 0.35 wt% dispersant shows much higher viscosity and shear thinning behavior than that prepared at the room temperature. On the other hand, the suspension prepared using 0.8 wt% dispersant has viscosity more or less same at 80 ^{o}C and room temperature. To prevent the agglomeration of alumina particle during emulsification due to insufficient dispersant surface coverage at the temperature of emulsification (90 ^{o}C), a higher dispersant concentration of 1 wt% is used.

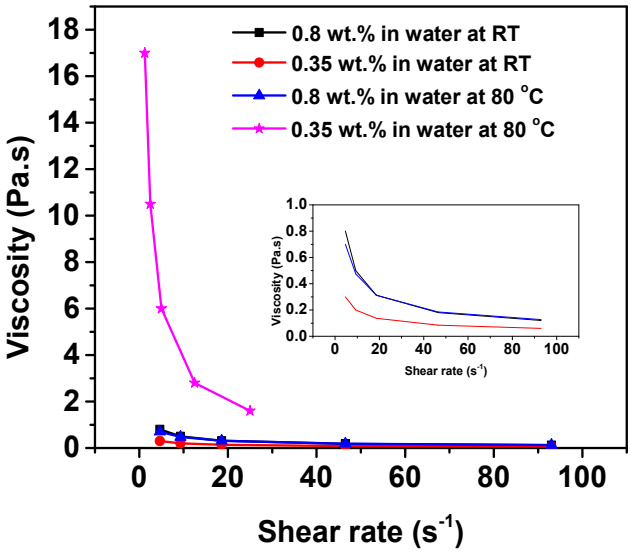

Fig 2.5 Effect of temperature and dispersant concentration on the viscosity at various shear rates of 50 vol.% alumina powder suspensions in water

2.3.2 Dispersion of naphthalene in aqueous alumina slurry

The carrageenan dissolves in the aqueous medium when the alumina slurry containing carrageenan is heated at 90 ^{o}C. The molten naphthalene containing the

emulsifying agent disperses uniformly in the aqueous alumina slurry containing the carrageenan gelling agent to form a naphthalene-in–aqueous alumina slurry emulsion when the two are mechanically mixed at 90^{o}C. The naphthalene-in-aqueous alumina slurry emulsions with a naphthalene to alumina slurry volume ratio up to 1.86 could be prepared. The density of molten naphthalene at 90^{o}C, 0.972 g/cm^{3}, was used for all the volume ratio calculations. At naphthalene to alumina slurry volume ratio higher than 1.86, partial separation of naphthalene as a top layer is observed as soon as stirring is stopped. The naphthalene to water ratio in the emulsion at the highest naphthalene loading is 2.66. This is close to the minimum oil phase to water ratio (2.85) required for the formation of a high internal phase emulsion (Lissant, 1970). Therefore, the naphthalene-in-aqueous alumina slurry emulsions at naphthalene to alumina slurry volume ratios in the range of 1 to 1.86 (naphthalene to water ratios in the range of 1.42 to 2.66**)** are medium internal phase emulsions (Lissant, 1970). **Fig. 2.6** shows the effect of composition on the viscosity of emulsions measured at a shear rate of 9.3s^{-1} and at 85 ^{o}C. In the case of aqueous slurry of a specified alumina concentration, the viscosity of the emulsions increases with an increase in naphthalene to alumina slurry volume ratio. On the other hand, at fixed naphthalene to aqueous alumina slurry volume ratio, the viscosity of the emulsions increases with an increase in alumina slurry concentration. The emulsions with naphthalene to alumina slurry volume ratios in the range of 1 to 1.86 prepared from aqueous alumina slurries of concentrations in the range of 10 to 30 vol.% showed a viscosity in the range of 0.175 to 1.025 Pa.s at a constant shear rate of 9.3 s^{-1}.

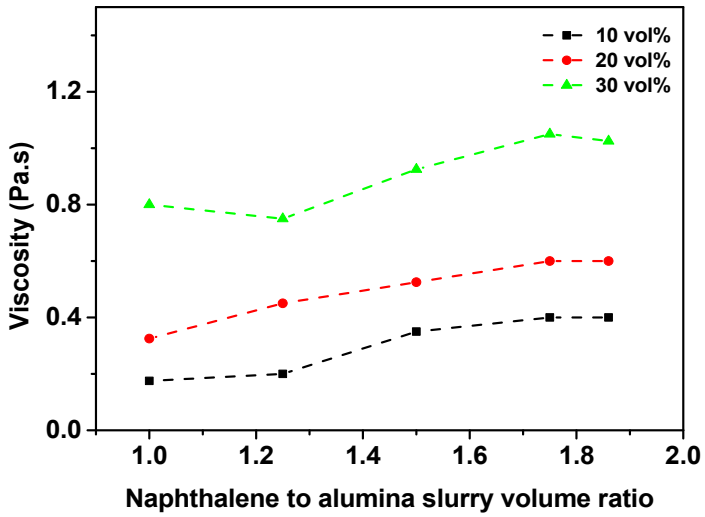

Fig 2.6 Effect of naphthalene to alumina slurry volume ratio and alumina slurry concentrations on the viscosity of naphthalene-in aqueous alumina slurry emulsions (shear rate- 9.3 s^{-1}).

The flow behavior of powder suspensions and emulsions depends on the interparticle and inter droplet Van der Waals interactions (Ewais et al., 2011; Parfitt, 1973). In the case of naphthalene-in-aqueous alumina slurry emulsions, there are three types of possible Van der Waals interactions. They are between the alumina particles in the aqueous phase, between the naphthalene droplets and between alumina particles in the aqueous phase and naphthalene droplets. It is well known that these interparticle interactions increase with an increase in particle concentration and decrease in particle size. The naphthalene-in-aqueous alumina slurry emulsions in general showed shear thinning flow behavior. The shear thinning behavior of the emulsions increases with an increase in alumina concentration in the slurry and an increase in naphthalene to aqueous alumina slurry volume ratio. **Fig. 2.7** shows viscosity versus shear rate plots of emulsions with naphthalene to alumina slurry volume ratios of 1 and 1.86 prepared from aqueous

slurries of 10, 20 and 30 vol.% alumina concentrations. The increase in viscosity and shear thinning behavior of the emulsions with an increase in naphthalene to alumina slurry volume ratio and alumina slurry concentration is due to this increase in the interparticle interactions.

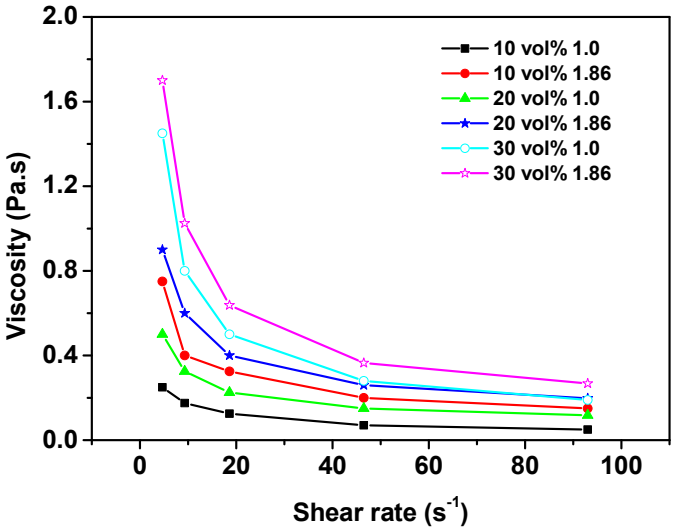

Fig 2.7 Viscosity versus shear rate plot of the emulsions prepared at naphthalene to alumina slurry volume ratios of 1.0 and 1.86 at different alumina slurry concentrations.

The emulsions obey Casson model (Chang et al., 1994). That is, a plot of square root of shear stress versus square root of the shear rate gave a straight line graph. The yield stress obtained by extrapolating the straight lines to the Y-axis plotted as a function of naphthalene to alumina slurry volume ratio and alumina concentration in the aqueous slurry is shown in **Fig. 2.8**. As in the case of viscosity, the yield stress of the emulsions also increased with an increase in naphthalene to alumina slurry volume ratio and alumina concentration in the aqueous slurry. The yield stress observed was in the range of 0.7 to 5.3 Pa for the emulsions with naphthalene to alumina slurry volume ratios in the range of 1 to 1.86 prepared from aqueous

slurries of alumina concentration in the range of 10 to 30 vol.%. Viscosity and yield stress of the emulsions are sufficiently low to flow into any mould during casting.

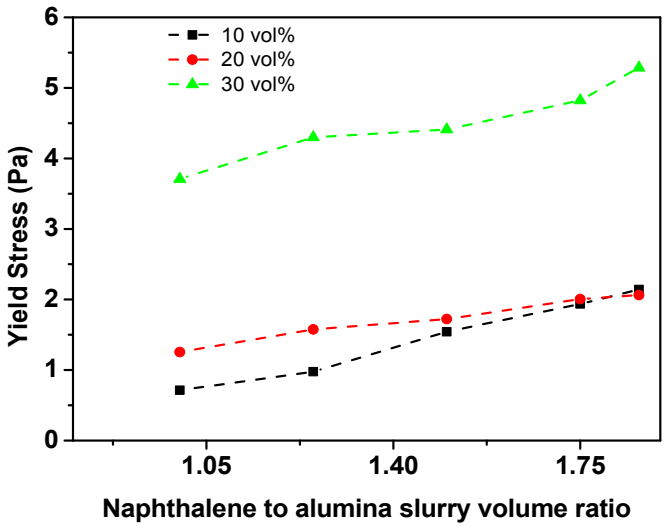

Fig 2.8 Yield stress of emulsions prepared at various naphthalene to alumina slurry volume ratios prepared from aqueous slurries at different alumina concentrations.

2.3.3 Gelation

The emulsions prepared from slurries of alumina concentrations in the range of 10 to 30 vol.%, gel on cooling to room temperature in a mould. The gelation is due to the solidification of the naphthalene droplets and physical cross-linking of the carrageenan during cooling of the emulsions. The gelation time of the emulsion could be obtained from the cooling curve as the cooling curves show an under cooling, recalescence and a thermal arrest region (Askeland & Phulé, 2003). The cooling curve of the emulsions prepared at various naphthalene to aqueous alumina slurry volume ratios are shown in **Fig. 2.9**.

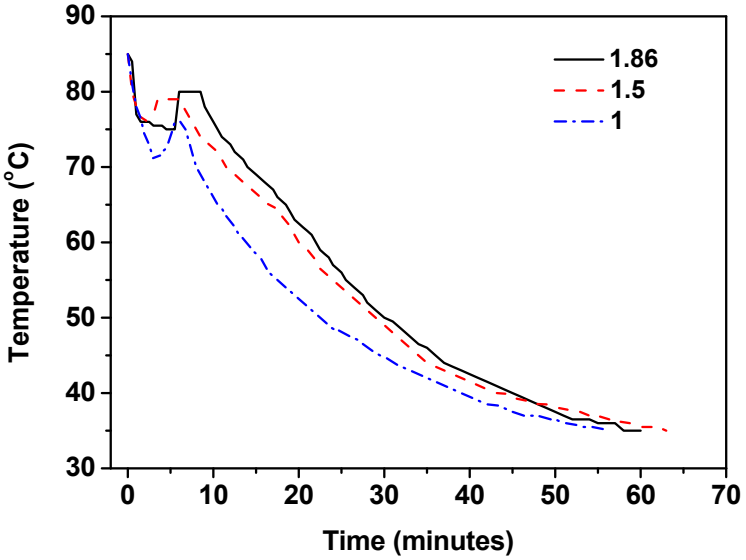

Fig 2.9 Cooling curve of the naphthalene-in-aqueous alumina slurry emulsions at various naphthalene to alumina slurry volume ratios.

During the recalescence the emulsions did not come back to the melting point of naphthalene as the latent heat released is utilized to heat naphthalene as well as the aqueous alumina slurry. This explains why the emulsions with lower naphthalene to aqueous alumina slurry volume ratio reach to lower temperatures after the recalescence as observed in the cooling curves. The solidification of naphthalene is completed at the end of the thermal arrest region. That is, the solidification of naphthalene in the emulsions took nearly 10 minutes. As a result of this, the emulsion turned to a gel as soon as the temperature falls below the melting point of naphthalene. However, the gels produced are too weak to remove immediately from the mould. On the other hand, the gels achieve sufficient strength on cooling to room temperature due to the physical cross-linking of carrageenan present in the aqueous alumina slurry at a temperature below 60 ^{o}C. Therefore, the gelled emulsion bodies are removed from the mould after cooling to room

temperature. The emulsion cast in the glass moulds took nearly 1 hour to reach room temperature by natural cooling. However, faster cooling by keeping in a refrigerator could be used to shorten the time for mould removal. **Fig. 2.10** shows the photograph of a gelled emulsion body immediately after the mould removal.

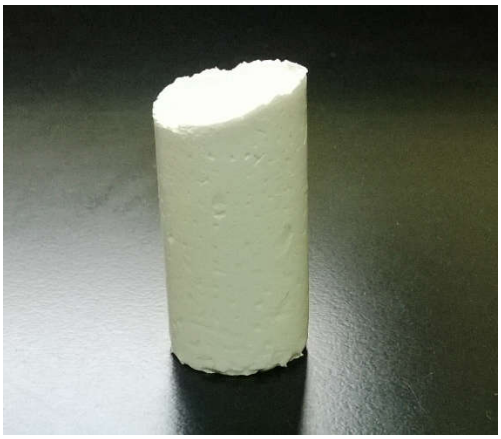

Fig 2.10 Photograph of a gelled emulsion body immediately after mould removal.

2.3.4 Gel strength

. Unlike the high alkane phase emulsion based method (Barg et al., 2009), the freeze gelcasting of naphthalene-in-aqueous alumina slurry emulsion enables the mould removal immediately after gelation. This resulted in a higher production rate. For the successful mould removal, the gelled emulsion bodies should have sufficient strength and Young's modulus. **Fig. 2.11** shows the representative stress-strain graphs of the gelled emulsion bodies. The stress-strain graphs show an initial linear region followed by a yield point and a stress maximum. After reaching the maximum, either the stress declines with increase of strain or does not change significantly depending on the composition of the gelled emulsion. The slope of the linear region is taken as the Young's modulus and the stress maximum is taken as the compressive strength. The gelled emulsion bodies prepared from

aqueous slurry of 10 vol.% alumina concentration fail after reaching the stress maximum due to the development of cracks irrespective of naphthalene to alumina slurry volume ratio. On the other hand, the gelled emulsion bodies prepared from 30 vol.% alumina slurry undergo sagging at the bottom after reaching the stress maximum at all naphthalene to alumina slurry volume ratios. The gelled emulsion bodies prepared from 20 vol.% alumina slurry at naphthalene to alumina slurry volume ratios higher than 1.5 fails by development of crack and the same prepared at lower naphthalene to alumina slurry volume ratios fail by sagging at the bottom.

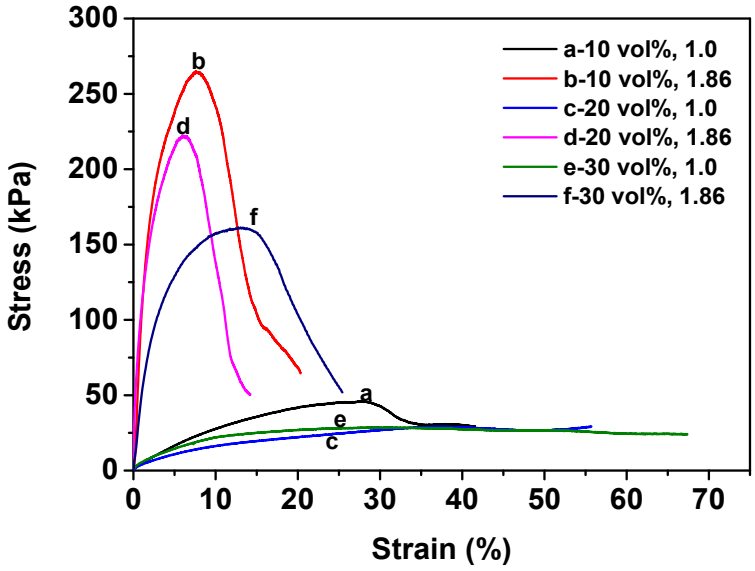

Fig 2.11 Representative stress-strain graphs of gelled emulsions showing the effect of naphthalene to alumina slurry volume ratio and alumina slurry concentration

Fig. 2.12 shows the compressive strength and Young's modulus of gelled emulsion bodies obtained at various naphthalene to alumina slurry volume ratios prepared from aqueous slurries of different alumina concentrations. At 30 vol.% alumina slurry concentration, the compressive strength of the gelled emulsion

bodies increases linearly with an increase in the naphthalene to aqueous alumina slurry volume ratio. However, at 10 and 20 vol.% alumina slurry concentrations, the gel strength increases slowly with naphthalene to alumina slurry volume ratio up to 1.5 and then rapidly. On the other hand, the Young's modulus increases slowly with naphthalene to aqueous alumina slurry volume ratio up to 1.5 and then rapidly at all alumina slurry concentrations. At particular naphthalene to alumina slurry volume ratio, the compressive strength and Young's modulus of gelled emulsion bodies decrease with an increase in concentration of alumina slurry. The average compressive strength and Young's modulus of gelled emulsion bodies obtained are in the ranges of 26.7 to 241 kPa and 0.25 to 10.57 MPa, respectively. The obtained compressive strength and Young's modulus values are sufficient to resist deformation of the gelled emulsion bodies during mould removal and further handling.

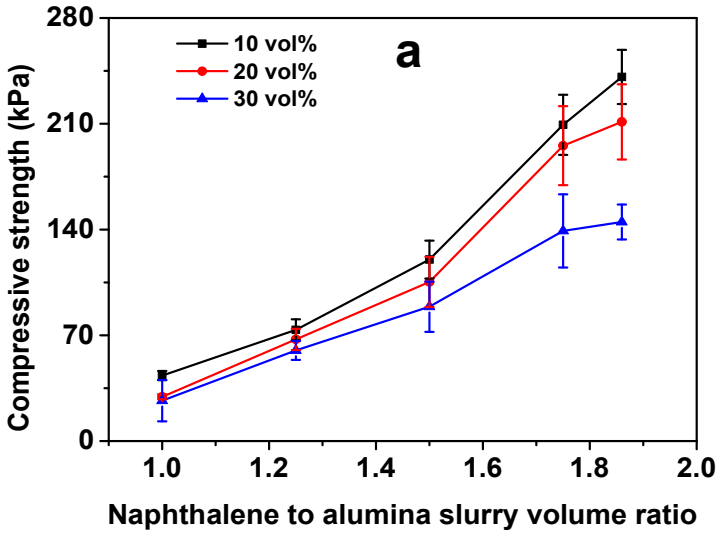

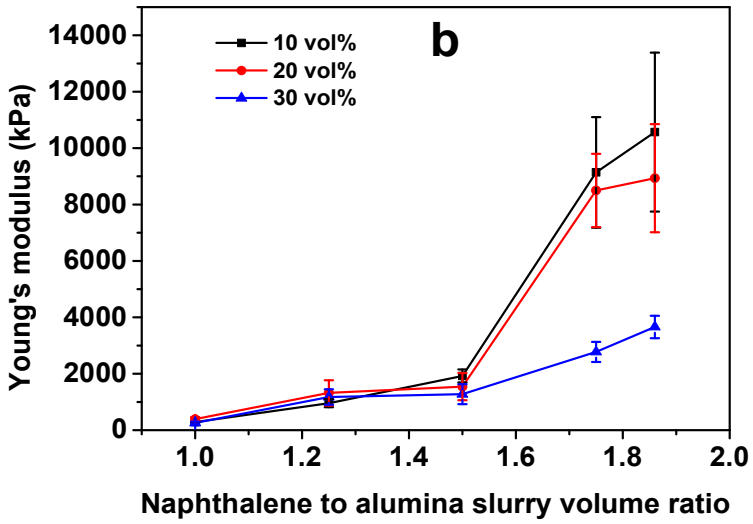

Fig 2.12 Effect of composition on (a) compressive strength and (b) Young's modulus of the gelled emulsion bodies.

The gelled emulsion body is a composite of solidified naphthalene droplets dispersed in a continuous matrix of gelled alumina slurry. The strength and modulus of a composite depend on the corresponding values of the matrix and reinforcement and the extent of stress transfer from the matrix to the reinforcement (Amirbayat & Hearle, 1969). The stress transfer depends on the nature of the matrix-reinforcement interface. The gel obtained by cooling 1.5 wt% aqueous solution of carrageenan in a refrigerator at 5 ^{o}C showed a compressive strength of 19 kPa and Young's modulus of 95 kPa. On the other hand, gelled bodies prepared from 10, 20 and 30 vol.% alumina slurries with the same concentration of carrageenan (without naphthalene) showed compressive strength values of 14, 12.7 and 10.8 kPa, respectively. The corresponding Young's modulus values obtained are 90, 84 and 72 kPa, respectively. The decrease in strength and Young's modulus with an increase in alumina concentration indicates that the alumina particles disrupt the secondary interactions between carrageenan molecules, which

are responsible for the gel formation. The compressive strength and Young's modulus of solid naphthalene measured using cylindrical bodies of length 45 mm and diameter 22 mm are 1.63 MPa and 84.3 MPa**,** respectively. The compressive strength and Young's modulus calculated using simple rule of mixtures for the gelled emulsion bodies from the corresponding values of gelled alumina slurries and solid naphthalene are in the ranges of 0.82 to 10.68 MPa and 41.99 to 54.87 MPa**,** respectively. These values are much higher than the experimentally measured compressive strength and Young's modulus. This large difference is due to the poor stress transfer from the gelled alumina slurry to solid naphthalene as a result of weak gelled alumina slurry-naphthalene interface.

2.3.5 Drying of the gelled bodies

The drying of gels is a critical step in gel assisted methods such as sol-gel processing and gelcasting (Scherer, 1990). Generally, humidity controlled conditions are used for the drying of gels to prevent the formation of cracks due to capillary pressure. However, in the present case, the gelled emulsion bodies are dried in open air atmosphere at room temperature (~ 30 ^{o}C) without any humidity control. The cylindrical gelled emulsion bodies of 22 mm diameter and 50 mm length took nearly 140 hours for the drying irrespective of the naphthalene to alumina slurry volume ratio. In all the cases, more than 55 % of the water present is removed in the first 24 hours. Thereafter, the drying rate was slow and took nearly 116 hours to remove the rest of the water. In all these measurements, the naphthalene loss due to sublimation at room temperature is ignored. The typical drying behavior of a gelled emulsion body is shown in **Fig. 2.13**.

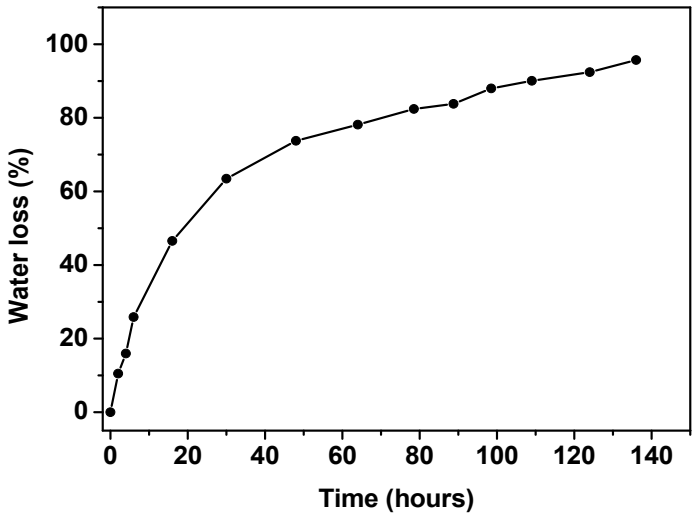

Fig 2.13 Typical drying behavior of a gelled emulsion body

The drying shrinkage of the gelled emulsion bodies decreased with an increase in the naphthalene to alumina slurry volume ratio. The gelled emulsion bodies prepared at the naphthalene to alumina slurry volume ratios in the range of 1 to 1.86 showed a diametrical shrinkage in the range of 8.78 to 7.85 %. Even though the drying was performed in an open air atmosphere without any humidity control, no crack or deformation was observed. In the gelled emulsion bodies, solid naphthalene particles are present in the closely packed cells of gelled alumina slurry. It appears that the difference in the shrinkage of naphthalene and alumina slurry during gelation creates an extremely narrow gap in the naphthalene-gelled alumina slurry interface. This narrow gap between the gelled alumina slurry and naphthalene is saturated with vapour due to the evaporation of water from the gelled alumina slurry. That is, a high humidity condition is prevailing in the gap at the naphthalene-gelled alumina slurry interface, which is responsible for the drying without any crack in the normal air atmosphere. The water vapour produced at the naphthalene-gelled alumina slurry interface is transported to the surface of the

gelled emulsion body through the gap at the naphthalene-gelled alumina slurry interface and interconnections between the gelled alumina slurry cells.

2.3.6 Removal of naphthalene

The naphthalene present in the dried alumina body could be completely removed by heating at 70 ^{o}C in an air oven as naphthalene undergoes sublimation. More than 95% of the naphthalene present in the dried bodies is removed in 48 hours. The typical naphthalene removal kinetics of a dried emulsion body is shown in **Fig. 2.14**. The dried emulsion bodies did not show any measurable shrinkage during naphthalene removal by sublimation at 70 ^{o}C. In addition, no crack or blister is created on the bodies during naphthalene removal.

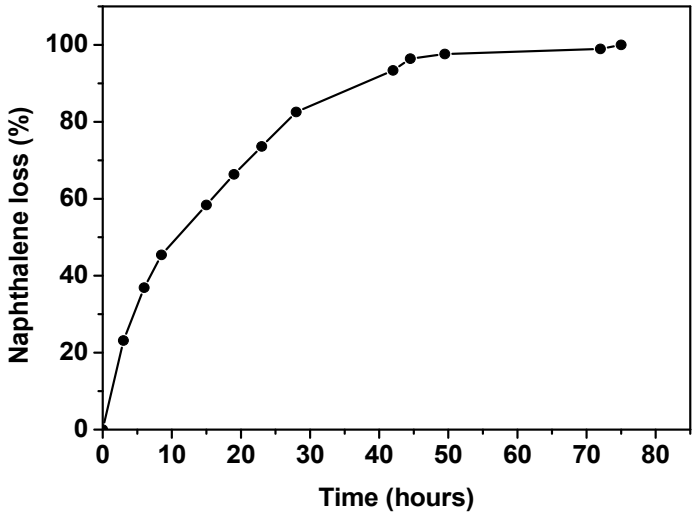

Fig 2.14 Typical naphthalene removal kinetics of a dried emulsion body

2.3.7 Sintering and porosity

The naphthalene removed green bodies on sintering at 1550 ^{o}C shows a diametrical shrinkage in the range of 7.8 to 10.2 %. No visible crack or deformation is developed during the sintering. **Fig. 2.15** shows the porosity of the alumina ceramics foams plotted as a function of naphthalene to alumina slurry

volume ratio and alumina concentration in the aqueous slurry. Porosity of the alumina ceramics obtained from the emulsions prepared from aqueous slurry of a specific alumina concentration increased with an increase in naphthalene to alumina slurry volume ratio. On the other hand, at particular naphthalene to aqueous alumina slurry volume ratio, the porosity of the alumina foams increases with a decrease in alumina concentration in the aqueous slurry. Alumina foams obtained from emulsions of naphthalene to alumina slurry volume ratios in the range of 1 to 1.86 prepared from alumina slurries of concentration in the range of 30 to 10 vol.%, shows porosity in the range of 65 to 90%. The maximum porosity achieved, at a naphthalene to alumina slurry volume ratio of 1.86, increases from 78 to 90 vol.% when the alumina slurry concentration decreases from 30 to 10 vol.%.

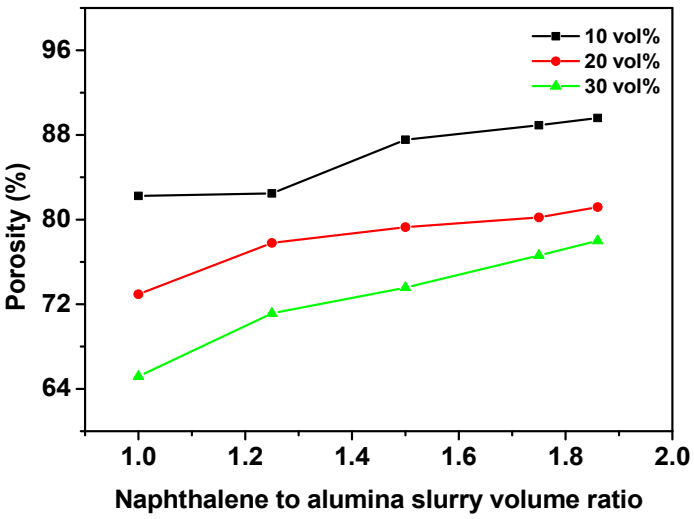

Fig 2.15 Effect of naphthalene to alumina slurry volume ratio and alumina slurry concentration on porosity of the alumina foams.

2.3.8 Effect of surfactant concentration on microstructure and cell size

Fig. 2.16 shows the microstructure of the alumina ceramics prepared from the emulsions at various emulsifying agent concentrations and at constant naphthalene to alumina slurry volume ratio of 1.25. The macropores (cells) in the ceramics prepared at the emulsifying agent concentrations in the range of 0.1 to 0.3 wt% of naphthalene have near spherical shape. Distortion from spherical morphology starts at an emulsifying agent concentration of 0.4 wt%. Beyond 0.5 wt% the microstructure showed completely distorted macropores. The distortion of spherical shape is due to the deformation of naphthalene droplets under shear due to the low interfacial energies at the higher emulsifying agent concentrations. The average cell size decreases from 35.1 to 9.3 μm when the emulsifying agent concentration increases from 0.1 to 0.4 wt%. The measurement of cell size from the SEM images is difficult at the emulsifying agent concentrations above 0.4 wt% due to their irregular shape. The decrease in cell size with an increase in emulsifying agent concentration is also due to the decrease in interfacial energy. The effect of emulsifying agent concentration on the cell size of the alumina ceramics is shown in **Fig. 2.17**. There is no observed change in porosity with the emulsifying agent concentration.

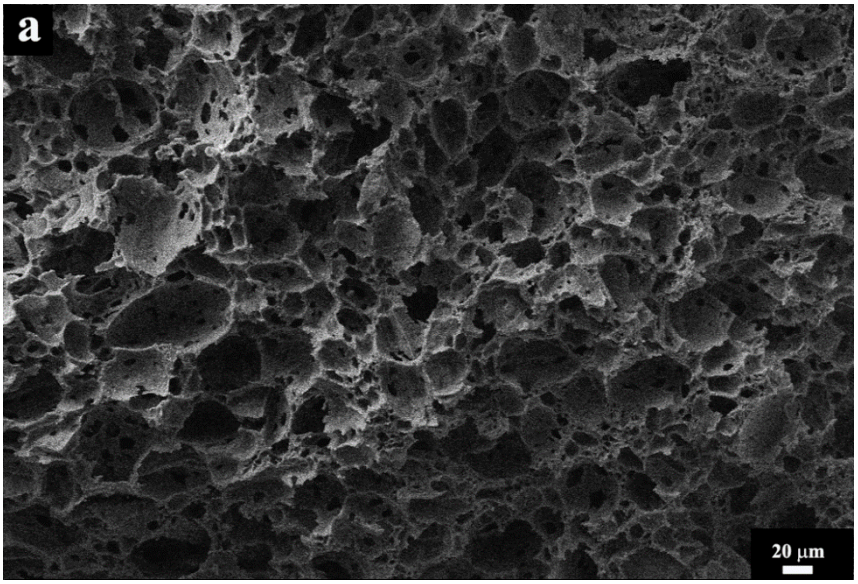
a
20 μm

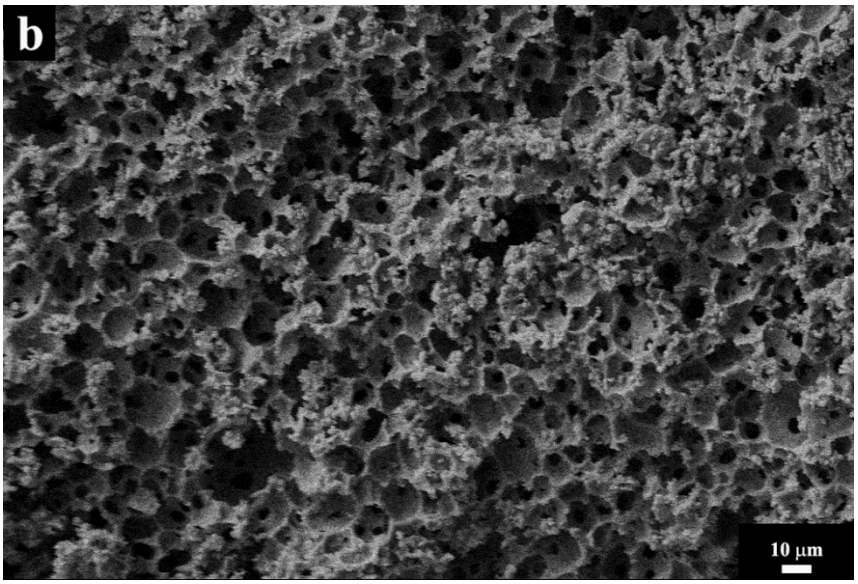
b
10 μm

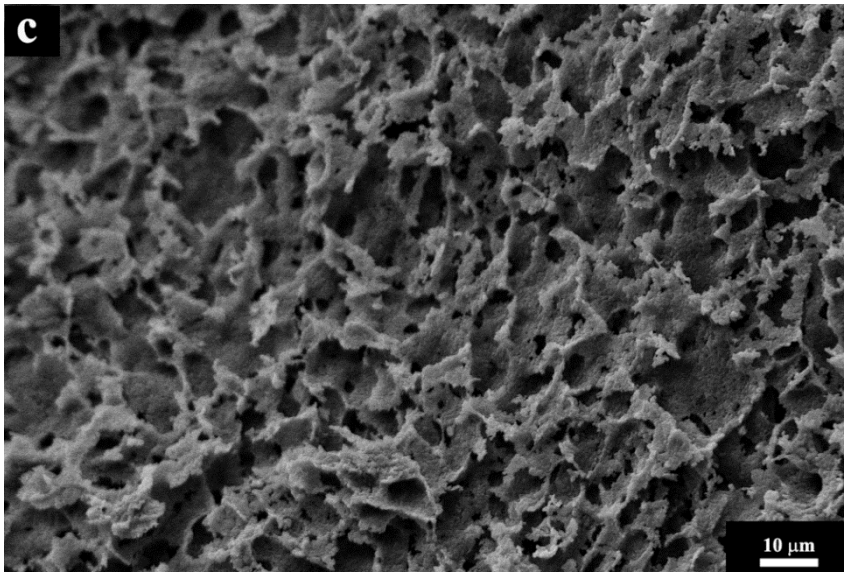

Fig 2.16 SEM photomicrograph of alumina foams prepared at a naphthalene to alumina slurry volume ratio of 1.24 and at emulsifying agent concentrations of (a) 0.1 wt%, (b) 0.3 wt% and (c) 0.6 wt%

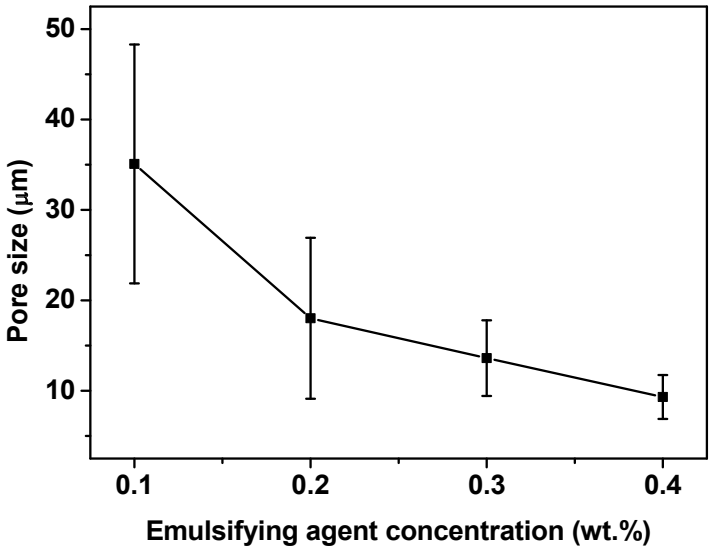

Fig 2.17 Cell size as a function of emulsifying agent concentration

2.3.9 Effect of emulsion composition on microstructure and cell size

Fig. 2.18 shows the microstructure of the alumina foams obtained from naphthalene-in-aqueous alumina slurry emulsions of naphthalene to alumina slurry volume ratios 1.0 and 1.86 prepared from slurries of 10, 20 and 30 vol.% alumina loading. Majority of the macropores (cells) show distorted spherical shape. The cells show large distortion from the spherical morphology irrespective of the naphthalene to aqueous alumina slurry volume ratio due to low interfacial energy. The interconnectivity of the cells increased with a decrease in alumina concentration in the slurry and an increase in naphthalene to alumina slurry volume ratio. The thickness of struts and cell walls showed a decreasing trend with a decrease in alumina slurry concentration and an increase in naphthalene to alumina slurry volume ratio. A representative high magnification image showing the grain structure in the cell wall and strut of the alumina foams is given in **Fig.2.19**. Fine grained dense strut and cell wall structure is evidenced in the micrograph. The average grain size calculated from the high magnification image is 1.43 μm.

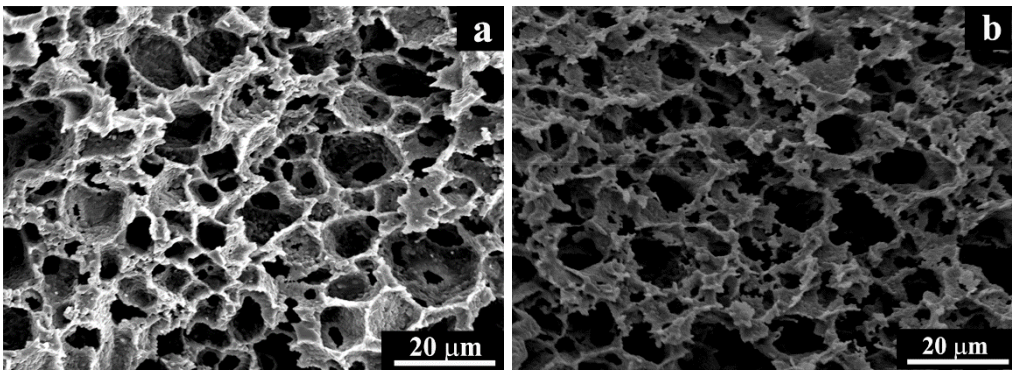

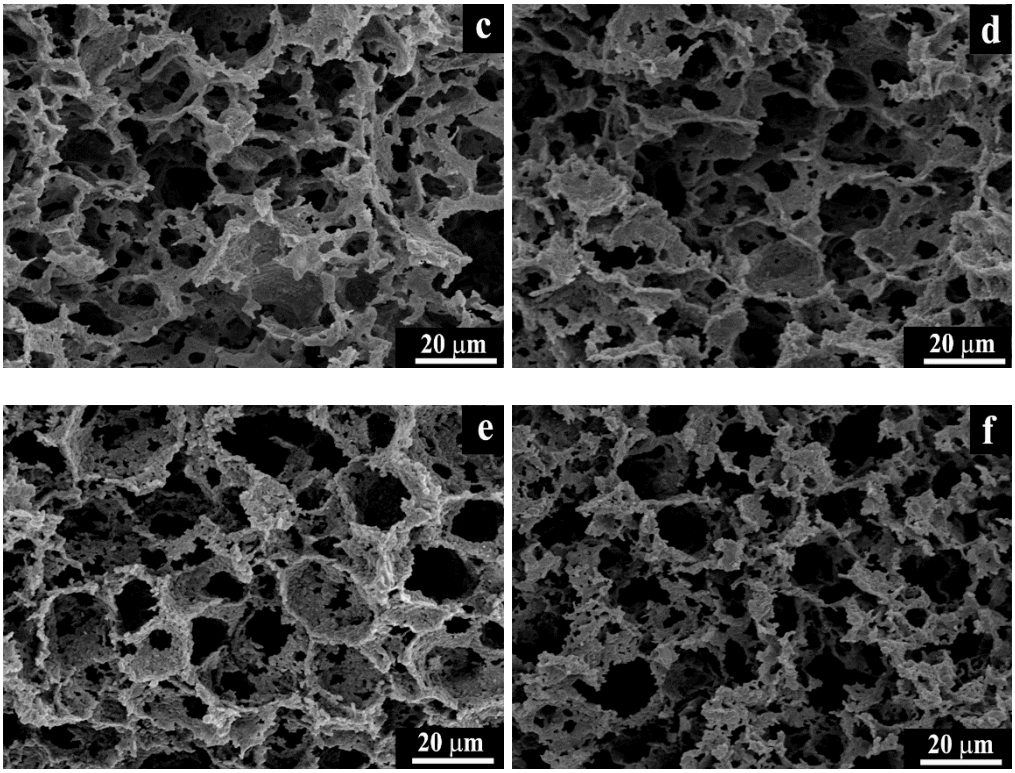

Fig 2.18 Photographs (SEM) of alumina foams obtained from slurries prepared at different alumina loading. (a) 1.0; 30 vol.%, (b) 1.86; 30 vol.%, (c) 1.0; 20 vol.%,(d) 1.86; 20 vol.%, (e) 1.0; 10 vol.%, and (f) 1.86; 10 vol.%.

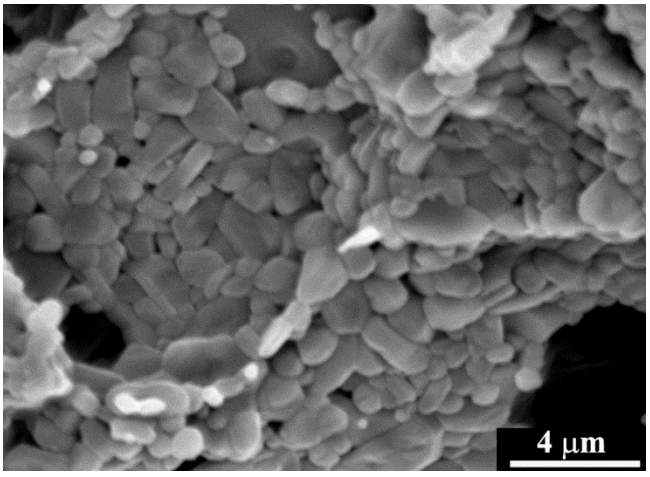

Fig 2.19 High magnification SEM image of the alumina foam.

The average cell size measured from the SEM micrographs using ImageJ software plotted as a function of alumina concentration in the slurry and

naphthalene to alumina slurry volume ratio is shown in **Fig. 2.20**. In the case of alumina ceramics obtained from the emulsions prepared at 30 vol.% alumina slurry, the average cell size decreases linearly from 10.9 to 4.9 μm when the naphthalene to alumina slurry volume ratio increases from 1 to 1.86. On the other hand, at the alumina slurry concentrations of 20 and 10 vol.%, the average cell size first decreases with an increase in naphthalene to alumina slurry volume ratio, reaches a minimum and then increases. The naphthalene to alumina slurry volume ratio at which the cell size minimum obtained is 1.75 and 1.5 for alumina slurry concentrations 20 and 10 vol.%, respectively. This is attributed to the decrease in the effectiveness of stirring due to the large volume of emulsions at higher naphthalene to alumina slurry volume ratios prepared from slurries of lower alumina concentration (same weight of alumina powder is used for all emulsion preparation). The average cell size obtained at 20 and 10 vol.% alumina slurry are in the ranges of 14.8 to 8.3 and 13.1 to 8.1 μm, respectively.

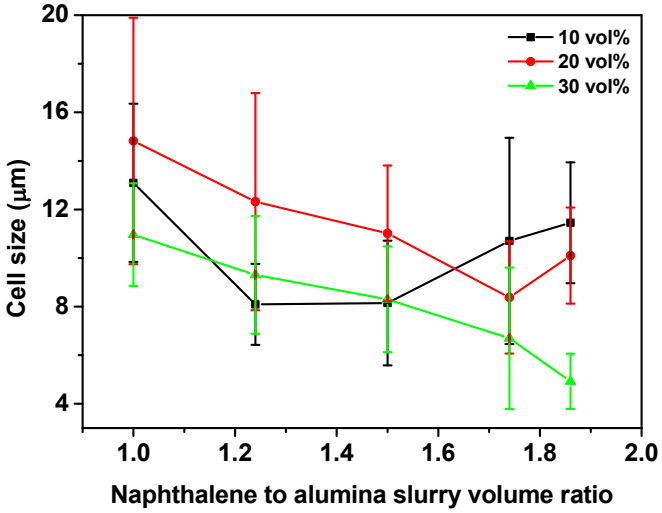

Fig 2.20 Effect of naphthalene to aqueous alumina slurry volume ratio and alumina slurry concentration on the average cell size of the alumina foams.

2.3.10 Compressive strength of the alumina foams

The compressive strength and Young's modulus of macroporous brittle solids depend on porosity, pore size, pore interconnectivity and nature of struts & cell walls (Chen et al., 2014; Gonzenbach et al., 2007; Liu, 1997; Rice, 1993). The compressive-stress stain behavior of the macroporous ceramics prepared at various naphthalene to aqueous alumina slurry volume ratios are shown in **Fig. 2.21**. The stress initially increases linearly with the elastic response and reaches a maximum for all of the fabricated samples. After reaching the maximum, the stress drop was rapid in the case of the macroporous ceramics prepared at naphthalene to aqueous alumina slurry volume ratio 1.5 and below, as in a brittle solid material. On the other hand, at naphthalene to aqueous alumina slurry ratios above 1.5 the stress-strain graph shows a plateau region after the maximum stress as in the case of a brittle elastic foam material.

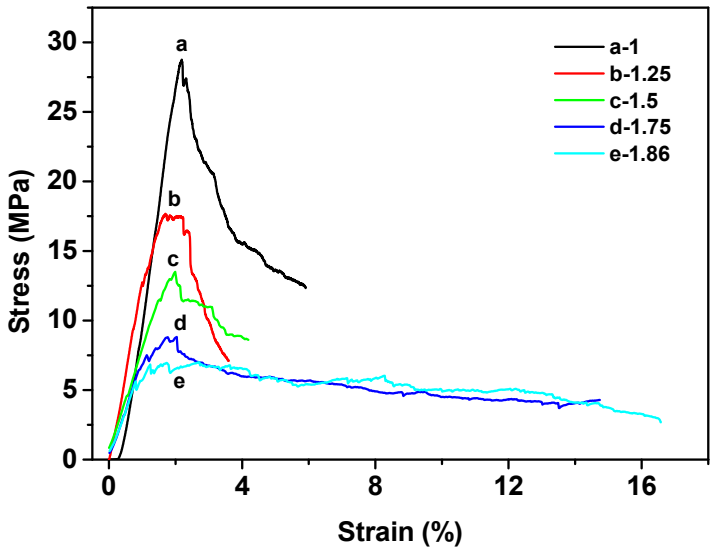

Fig 2.21 Stress-strain behavior of the alumina foams prepared at various naphthalene to aqueous alumina slurry volume ratios.

The effect of alumina slurry concentration and naphthalene to alumina slurry volume ratio on the compressive strength and Young's modulus of the alumina foams is shown in **Fig. 2.22**. At a particular alumina slurry concentration, the compressive strength and Young's modulus decreases with an increase in naphthalene to alumina slurry volume ratio. On the other hand, at a particular naphthalene to alumina slurry volume ratio the compressive strength and Young's modulus decreases with a decrease in alumina slurry concentration. This is due to the increase in porosity in the alumina ceramic. The average compressive strength and Young's modulus values obtained are in the ranges of 0.60 to 28.75 MPa and 36 to 1230 MPa, respectively, for the alumina ceramics of porosity in the range of 65 to 90 vol.%.

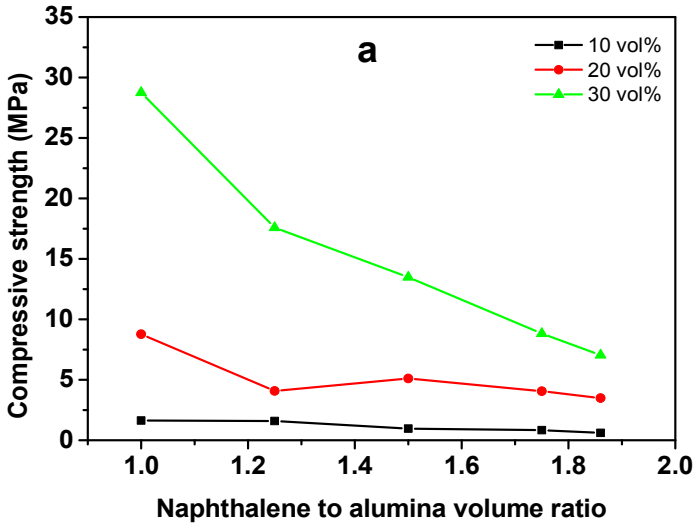

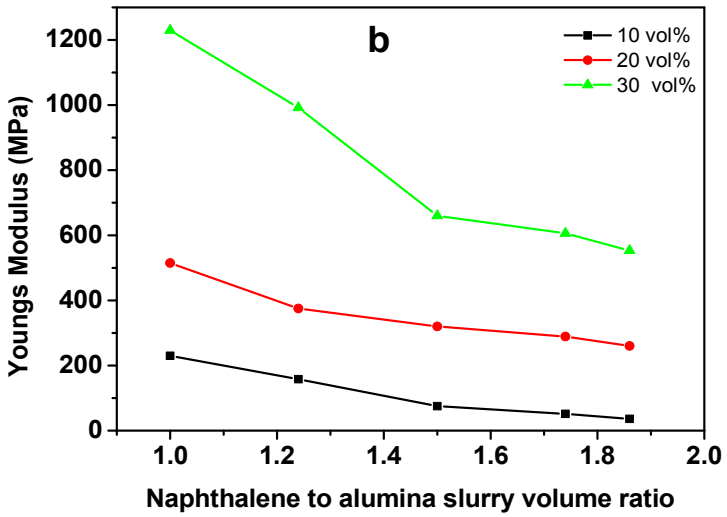

Fig 2.22 Effect of naphthalene to alumina slurry volume ratio and alumina slurry concentration on the (a) compressive strength and (b) Young's modulus of the alumina foams.

The Young's modulus of brittle open cellular solids is best modelled using the following equation (7) proposed by Gibson and Ashby (Gibson & Ashby, 1997).

$$\frac{E}{E_0} = C\left(\frac{\rho}{\rho_0}\right)^n \text{---------- (7)}$$

Where, E_0 and E are the Young's modulii of the fully dense solid and open cellular solid, respectively. ρ and ρ_0 are the densities of open cellular and fully dense solid, respectively. The C and n are constants depending on the pore geometry and microstructure. Verma et al (Verma et al. , 2013) used similar equations to model the compressive strength of open cellular ceramics. **Fig. 2.23** shows the plots of $\ln(\sigma/\sigma_0)$ versus $\ln(\rho/\rho_0)$ and $\ln(E/E_0)$ versus $\ln(\rho/\rho_0)$ of the alumina foams. The model plots are generated by considering the strength (σ_0) and Young's modulus (E_0) of fully dense alumina as 3 GPa and 416 GPa, respectively (Munro, 1997). The

values of model constants C and n as well as the correlation coefficient R^2 are given in **Table 2.1**. The model fitting with the compressive strength and Young's modulus data showed fairly high correlation co-efficient at all studied alumina slurry concentrations. The values of C and n for the relation between E/E_0 and ρ/ρ_0 are expected to be ~ 1 and ~ 2, respectively, for brittle open cellular foams with a cubic array of cells. On the other hand, the corresponding values expected for the relation between σ/σ_0 and ρ/ρ_0 are ~ 0.65 and ~1.5, respectively (Gibson & Ashby, 1997; Magdeski, 2010; Verma et al., 2013). The values of C and n obtained in the present case differ from those values proposed by Gibson and Ashby. This difference is attributed to the deviation from the spherical shape of the cells and presence of micropores in the struts and cell walls.

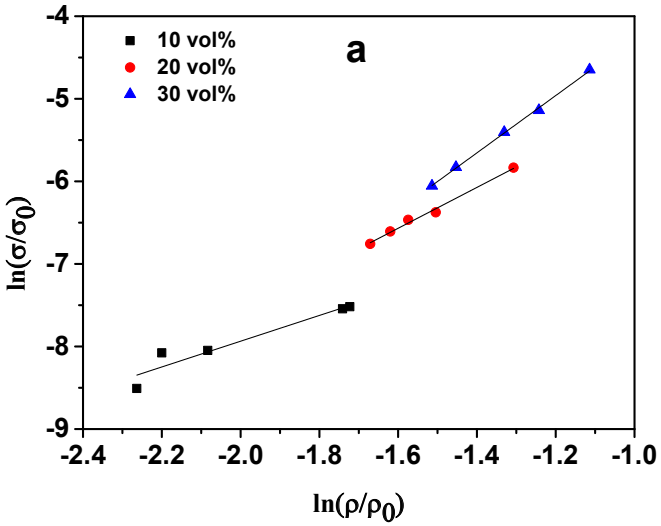

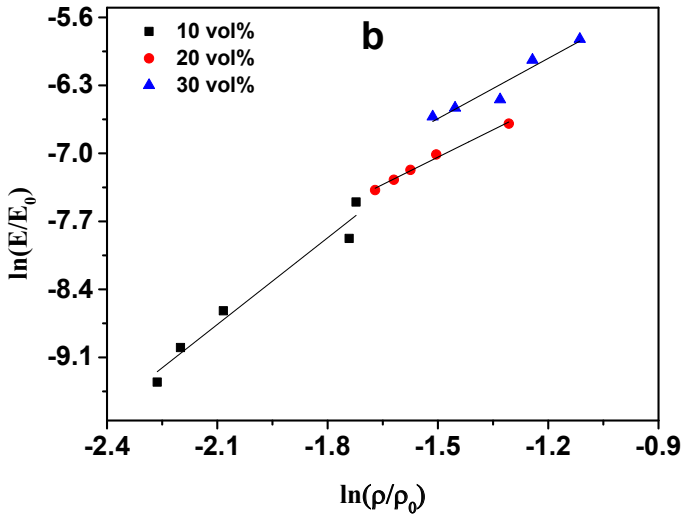

Fig. 2.23 Log-log plots of (a) σ/σ_0 against ρ/ρ_0 and (b) E/E_0 against ρ/ρ_0

Table 2.1. Values of model constants C, n and correlation coefficient R^2

Alumina Slurry concentration	Compressive strength			Young's modulus		
	n	C	R^2	n	C	R^2
10 vol.%	1.5602	0.0081	0.89189	2.9748	0.08092	0.9576
20 vol.%	2.4752	0.0841	0.98996	1.8761	0.01463	0.9902
30 vol.%	3.470	0.45088	0.99851	2.06771	0.02899	0.9107

2.3.11 Preparation of large alumina foam bodies

The naphthalene in aqueous alumina slurry emulsion based process is amenable to the preparation of relatively large foam bodies. Rectangular gelled bodies of 10 cm x 10 cm x 2 cm size were fabricated by casting the emulsions in steel mould. **Fig 2.24** shows the photograph of emulsion cast in a mould and gelled emulsion body. The gelled emulsion bodies could be dried, naphthalene removed and sintered without creating any crack. **Fig 2.25** shows the photograph of the large alumina

foam bodies prepared from the gelled naphthalene-in-aqueous alumina emulsions by emulsion templating method.

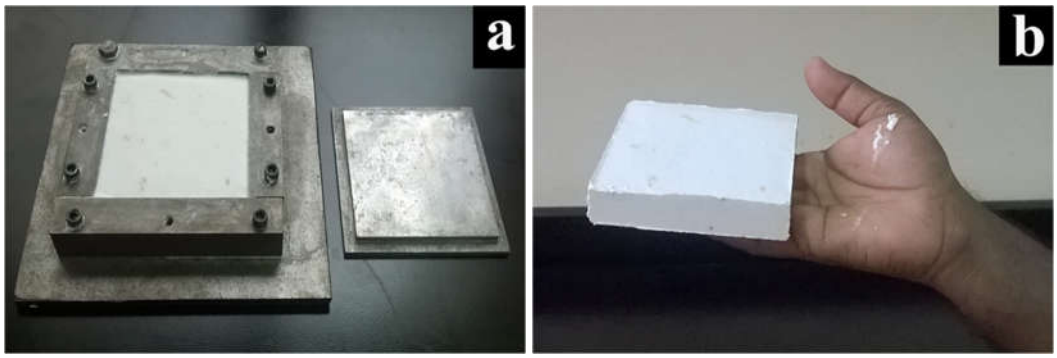

Fig 2.24 Photograph of (a) emulsion cast in a mould and (b) gelled emulsion body.

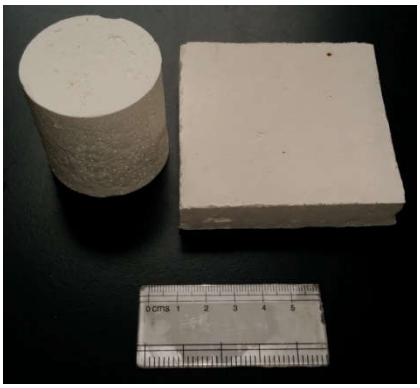

Fig 2.25 Photographs of sintered alumina foam bodies fabricated by casting naphthalene-in aqueous alumina slurry emulsion

2.4 Conclusions

Freeze-gelcasting of naphthalene-in-aqueous alumina slurry emulsions prepared from slurries of 10, 20 and 30 vol.% alumina concentration is studied to prepare alumina foams of high porosity. The viscosity, shear thinning character and yield stress of the naphthalene-in-aqueous alumina slurry emulsions increase with an increase in naphthalene to alumina slurry volume ratio and alumina slurry

concentration. The compressive strength and Young's modulus of the gelled emulsion bodies increase with an increase in naphthalene to alumina slurry volume ratio and decrease in alumina slurry concentration. The alumina foams have interconnected cellular structure with near spherical cell morphology up to 0.3 wt% sodium dodecyl sulphate and show large distortion from spherical morphology at higher sodium dodecyl sulphate concentrations. The average cell size (14.8 to 4.9 μm) depends on the alumina slurry concentration and naphthalene to alumina slurry volume ratios. Maximum porosity of the macroporous ceramics obtained at a naphthalene to alumina slurry volume ratio of 1.86 increases from 78 to 90 vol.% when the alumina concentration in the slurry decreases from 30 to 10 vol.%. The compressive strength and Young's modulus of the alumina foams obey the model proposed by Gibson and Ashby.

Chapter 3

Processing of Alumina Foams by Freeze Gelcasting of Hydrogenated Vegetable Oil-in-Aqueous Alumina Slurry Emulsions

3.1 Introduction

The emulsion templating is an ideal method for the preparation of macroporous ceramics with controlled porosity and an ordered pore structure. The size and dispersion of oil droplets within the ceramic suspension can be controlled by the mixing speed and surfactant concentration. High alkane phase emulsions based on decane (Barg et al., 2009), decalin (Alves-Rosa et al., 2013) and paraffin (Vitorino et al., 2013) in aqueous powder suspensions have been studied for the preparation of macroporous ceramics. In the previous chapter, we have reported the use of naphthalene as oil phase in emulsion templating method to facilitate setting of the emulsions cast in a mould. Though the naphthalene-in- aqueous alumina slurry emulsions produce alumina ceramics of a wide range of porosity, the toxicity of naphthalene limits its use in large scale applications. Hydrogenated vegetable oil (HVO) is an edible oil which is a solid at room temperature. The HVO is produced from vegetable oils which are naturally renewable. The representative structure of HVO is given in **fig. 3.1**. Preparation and characterization of alumina foams by emulsion templating method using HVO as the oil phase is reported in this chapter. This method is very simple, low cost and eco-friendly.

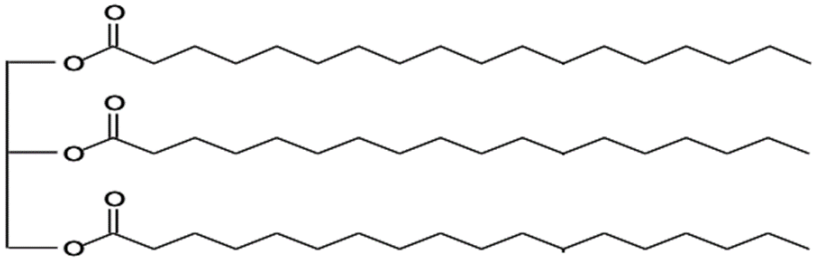

Fig 3.1 Representative structure of HVO

3.2 Experimental

3.2.1 Materials

α-Alumina powder (A16SG grade) of average particle size 0.34 μm and specific surface area 10.4 m^2/g was procured from ACC Alcoa, Kolkata, India. The food grade HVO (Dalda, Bunge India Pvt. Ltd., India) procured from a local market has a melting range of 40 to 41 ^oC. Analytical reagent grade sodium dodecyl sulphate (Merck India Ltd., Mumbai) and carrageenan (Sigma Aldrich, USA) were used as emulsifying agent and gelling agent, respectively. A 35 wt% aqueous ammonium poly(acrylate) solution (Darvan 821A, Vanderbilt company Inc., Norwalk, CA**)** was used as a dispersant. Distilled water was used for the preparation of the alumina powder suspensions. Analytical reagent grade toluene and petroleum ether used were procured from Merck India Ltd. Mumbai.

3.2.2 Preparation of alumina foams

Aqueous alumina slurries (AAS) of 10, 20 and 30 vol.% alumina loadings were prepared by dispersing the alumina powder in water using the ammonium poly(acrylate) dispersant. The amount of dispersant used was 1 wt% of the alumina powder. The slurries were ball milled in polyethylene bottles using zirconia

grinding media of 10 mm diameter on a roller ball mill for 12 hours. The alumina powder to the zirconia ball weight ratio used was 1:4. The procedure for the preparation of macroporous ceramics by freeze gelcasting of HVO-in-AAS emulsions is shown as a flowchart in **Fig. 3.2.** The AAS were transferred to 500 ml round bottom flasks. The carrageenan (1.5 wt.% of water in the slurry) was added to the slurry. The slurries were heated in a water bath at 90 ^{o}C with stirring using a mechanical stirrer with a Teflon paddle for 30 minutes to dissolve the carrageenan. The HVO and sodium dodecyl sulphate (0.4 wt% of the HVO) emulsifying agent taken in a beaker were heated at 85 ^{o}C in a water bath to melt the HVO and to dissolve the emulsifying agent. Emulsions of various HVO to AAS volume ratios were prepared by mixing aqueous alumina slurries containing carrageenan with HVO containing the emulsifying agent in a round bottom flask at 85 ^{o}C for 1 hour. Aqueous alumina slurries used were of 10, 20 and 30 vol.% concentrations. The mixing was done by mechanical stirring at a constant speed of 350 RPM. The emulsions were cast in cylindrical glass moulds of 22 mm diameter and 50 mm length and then cooled by keeping in a refrigerator at 5 ^{o}C for 30 minutes. The gelled emulsion bodies removed from the moulds were dried at room temperature (~ 30 ^{o}C) in an open air atmosphere. The HVO present in the dried emulsion bodies was removed either by soxhlet extraction using toluene or by immersing in petroleum ether in a closed vessel at room temperature. The HVO removed bodies were dried to remove the solvent and then sintered in an electrically heated furnace at 1550 ^{o}C for 2 hours. The heating rate used was 2 ^{o}C/minute up to 600^{o}C and then at 5 ^{o}C/minute.

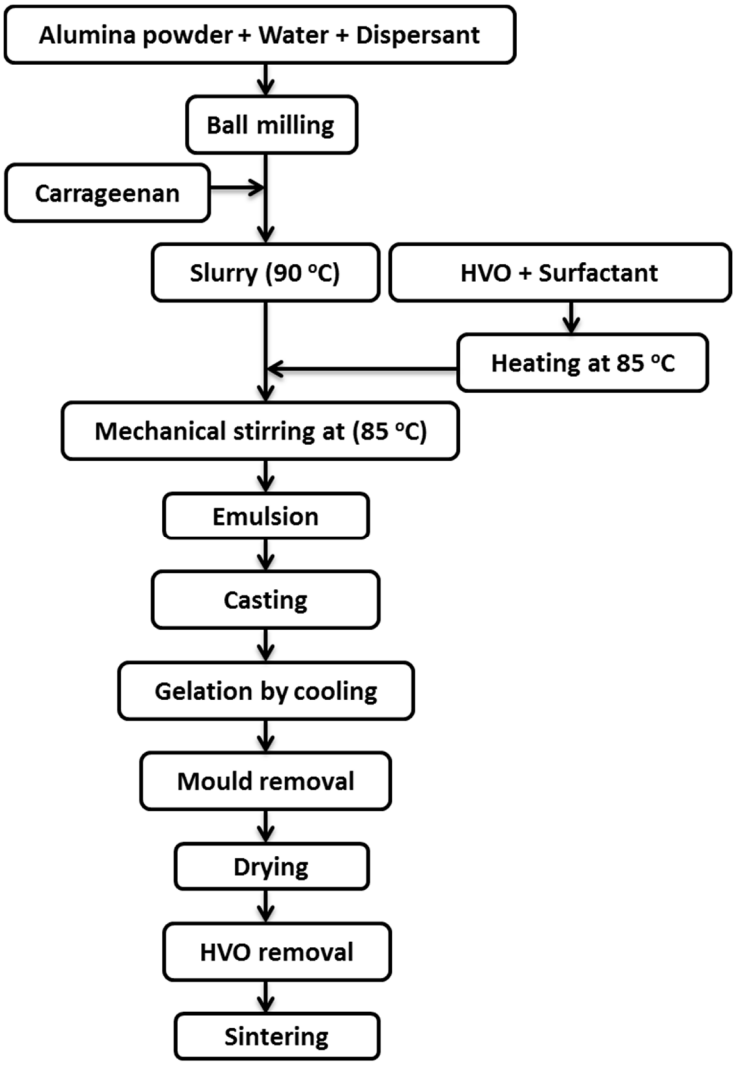

Fig 3.2 Flowchart of the emulsion gelcasting process

3.2.3 Characterization

3.2.3.1 Viscosity measurements

The viscosity of the emulsions was measured at 85 °C using a RVT model Brookfield viscometer (Brookfield Engineering Inc., Middleboro, MA) with a small sample adapter and a cylindrical spindle (SC 21). A thermosel accessory along with the viscometer was used for heating the emulsions during the viscosity measurements.

3.2.3.2 Shrinkage measurements

Shrinkage of the bodies during drying and sintering was calculated from the initial and final dimensions

3.2.3.2 Porosity measurement

The porosity of the foams was calculated based on the density obtained from their weights and dimensions.

3.2.3.3 Microstructure analysis

The microstructure of the sintered ceramics was observed on fractured surfaces using a scanning electron microscope (SEM, Hitachi S-2400, Hitachi High Technologies Corporation, Japan). The samples were sputter coated with gold before the analysis.

3.2.3.4 Cell size measurement

The average cell size of the foams was measured from the respective SEM images with the help of ImageJ software. The values reported were the average of cell sizes measured from minimum three images of one sample.

3.2.3.5 Compressive strength measurements

The stress-strain measurement of the gelled emulsion bodies was carried out using a universal testing machine (Instron 5500, Instron USA) at a loading rate of 5 mm/minute. Emulsion bodies removed from the mould were immediately used for the stress-strain measurements. The diameter and length of the cylindrical gelled emulsion bodies used for the stress-strain measurement were 22 and 45 mm, respectively. The compressive strength and Young's modulus were obtained from

the stress-strain graph. The compressive strength of the alumina foams was measured on cylindrical bodies of 18 mm diameter and 36 mm length using the same universal testing machine. The loading rate used was 1 mm/minute.

3.3 Results and Discussion

3.3.1 Dispersion of HVO in aqueous alumina slurry

The carrageenan dissolves in water present in the alumina slurry when heated at 90^{o}C for 30 minutes. The HVO containing the surfactant slowly disperse in the aqueous alumina slurry when the two are mixed by mechanical stirring to form HVO-in-AAS emulsion. The stable emulsions with HVO to AAS volume ratio in the range of 1.34 to 2.69 could be prepared. This corresponds to an HVO concentration in the range of 65.8 to 79.4 vol.% when calculated by excluding the volume of the alumina powder, carrageenan and sodium dodecyl sulphate. The density of HVO is taken as 0.897 g/cm^3 for all the volume ratio calculations. It is well known that the oil-in-water emulsions with 30 to 74 vol.% of oil phase are medium internal phase emulsions and those with higher than 74 vol.% oil phases are high internal phase emulsions (Lissant, 1970). Herein, the emulsions at the HVO to AAS volume ratios in the range of 1.34 to 1.88 are medium internal phase emulsions as they contain 65.8 to 72.9 vol.% HVO. On the other hand, the emulsions at the HVO to AAS volume ratios in the range of 2.15 to 2.69 are high internal phase emulsions as they contain 75.5 to 79.4 vol.% HVO. Nearly 30 minutes are required for the complete dispersion of the oil in the aqueous slurry up to an HVO to AAS volume ratio of 2.41. Higher mixing time of nearly 2 hours is required for the complete dispersion of HVO in AAS at HVO to AAS volume ratio

of 2.69. In all the cases, an additional stirring for 30 minutes was provided after the complete dispersion of the HVO in the AAS.

3.3.2 Rheological properties of HVO-in-AAS emulsions

The emulsions with low viscosity and yield stress are desirable for casting in a mould for the preparation of macroporous ceramic bodies. The viscosity of the emulsions at various HVO to AAS volume ratios prepared from 10, 20 and 30 vol.% alumina slurries measured at a shear rate of 9.3 s^{-1} is shown in **Fig. 3.3**. The viscosity of the emulsions at a particular HVO to AAS volume ratio increases with an increase in alumina slurry concentration. On the other hand, the emulsions prepared from slurry of a specified alumina concentration show a gradual increase in viscosity with an increase in HVO to AAS volume ratio up to 2.42. Further increase in HVO to AAS volume ratio to 2.69 rapidly increases the emulsion viscosity. The viscosity of the emulsions, prepared from aqueous slurries of alumina concentration in the range of 10 to 30 vol.% with HVO to AAS volume ratios in the range of 1.34 to 2.69, is in the range of 0.225 to 2.07 Pa.s.

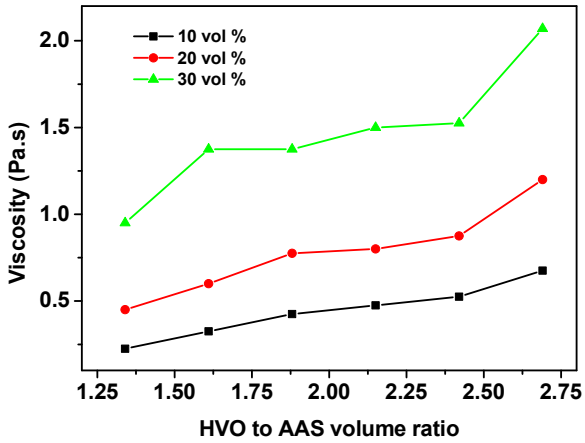

Fig 3.3 Effect of composition on the viscosity of the emulsions measured at a shear rate of 9.3 s^{-1}

There are three types of particle-particle Van der Waals interactions possible in HVO-in–AAS emulsions. They are (1) interaction between the alumina particles in the aqueous medium, (2) interaction between the oil droplets and (3) interaction between the alumina particles in the aqueous medium and the oil droplets (Barnes, 1994; Pal, 1996; Parfitt, 1973). The extent of these interactions increases with an increase in particle concentration and a decrease in particle size. The increase in viscosity with an increase in alumina concentration and HVO to AAS volume ratio is due to an increase in the particle-particle interactions. It appears that these interactions reach the maximum when the HVO to AAS volume ratio approaches to the maximum possible value. Further, these particle-particle interactions influence the flow behavior and yield stress of the emulsions. The emulsions in general show shear thinning flow behavior. At a particular HVO to AAS volume ratio the shear thinning character increases with an increase in alumina slurry concentration. On the other hand, the shear thinning character of the emulsions prepared from slurry of a specified alumina concentration increases with an increase in HVO to AAS volume ratio. **Fig. 3.4** shows the viscosity versus shear rate plot of the emulsions at the lowest and highest HVO to AAS volume ratios prepared from 10, 20 and 30 vol.% aqueous alumina slurries.

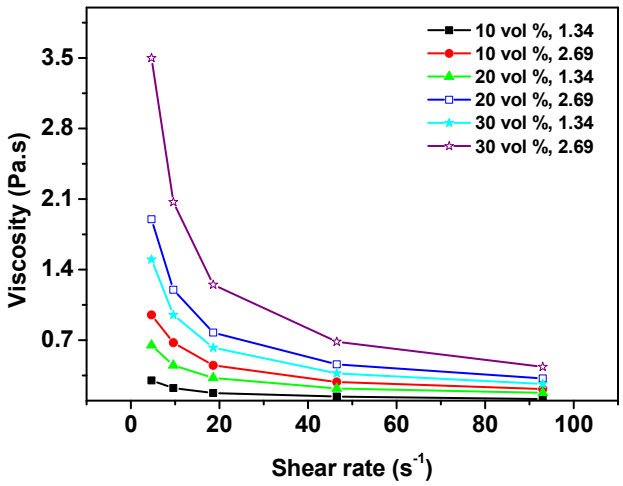

Fig 3.4 Viscosity versus shear rate plot of the emulsions

The emulsions obey Casson model (Chang et al., 1994). The yield stress of the emulsions calculated from the Casson model plotted as a function of alumina slurry concentration and HVO to AAS volume ratio is shown in **Fig. 3.5**. The yield stress of emulsions also increases with an increase in HVO to AAS volume ratio and alumina slurry concentration. The yield stresses of the emulsions observed are in the range of 0.3 to 10.3 Pa. The viscosity and yield stress of the emulsions are low enough to cast them in a mould for the preparation of gelled emulsion bodies.

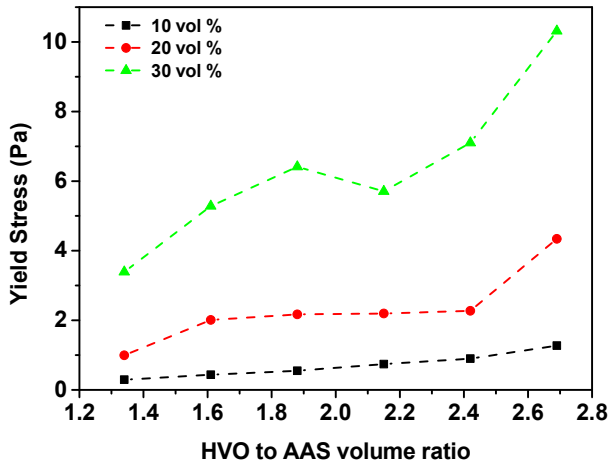

Fig 3.5 Effect of composition on yield stress of the emulsions.

3.3.3 Gelation and gel strength

The HVO-in-AAS emulsion cast in a mould undergoes gelation due to the physical cross-linking of the carrageenan and solidification of the HVO. The emulsion cast in a cylindrical glass mould of 25 mm diameter and 50 mm height took nearly 2 hours to achieve sufficient strength to remove from the mould without any deformation when naturally cooled to room temperature. On the other hand, the emulsions achieve very good handling strength in 30 minutes when cooled in a refrigerator at 5 ^{o}C. **Fig. 3.6** shows the photograph of a gelled emulsion body immediately after the mould removal.

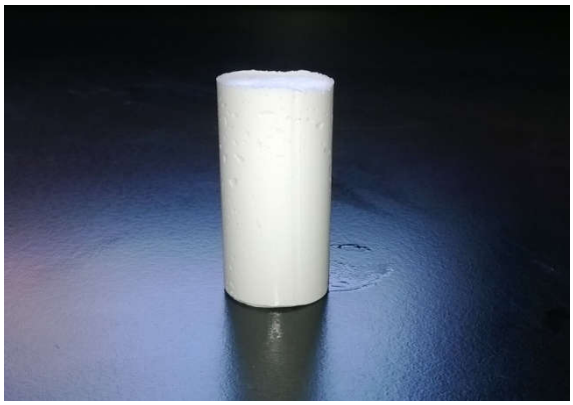

Fig 3.6 Photograph of a gelled emulsion body immediately after the mould removal

Mould removal immediately after gelation is a necessity to increase the production rate. For the successful removal from the mould, the gelled emulsion bodies should have sufficient strength to withstand the stresses during the mould removal (Prabhakaran et al., 2009). Representative graphs showing the stress-strain behavior of gelled emulsion bodies is shown in **Fig. 3.7**. The graphs show an initial linear portion followed by a yield point and a stress maximum. The maximum stress in the stress-strain graph is taken as the compressive strength and the slope of the

initial linear portion is taken as the Young's modulus. **Fig. 3.8** shows the effect of HVO to AAS volume ratio and alumina slurry concentration on the compressive strength and Young's modulus of the gelled emulsion bodies. The compressive strength of the gelled emulsion bodies prepared from slurry of a specified alumina concentration increases with an increase in the HVO to AAS volume ratio. On the other hand, at a particular HVO to AAS volume ratio, compressive strength of the gelled emulsion bodies increases with an increase in alumina slurry concentrations. The Young's modulus of the gelled emulsion bodies also shows the similar trend. The compressive strength (20 to 150 kPa) and Young's modulus (120 to 1550 kPa) are adequate for the mould removal and further handling without any deformation of the gelled emulsion bodies.

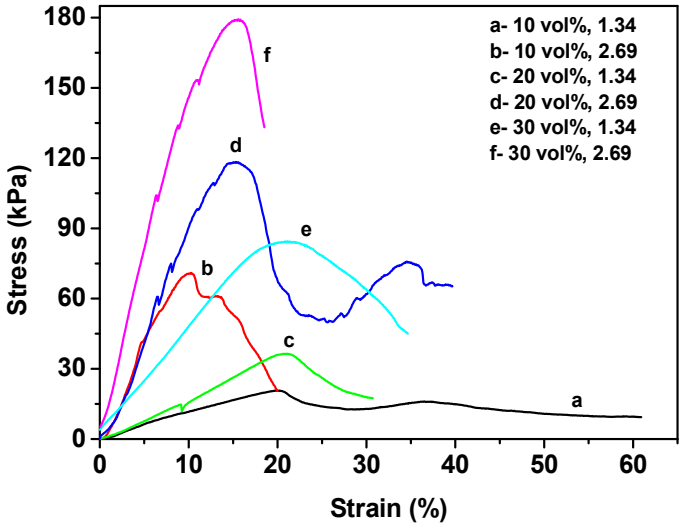

Fig 3.7 Representative graphs showing the stress-strain behavior of the gelled emulsion bodies

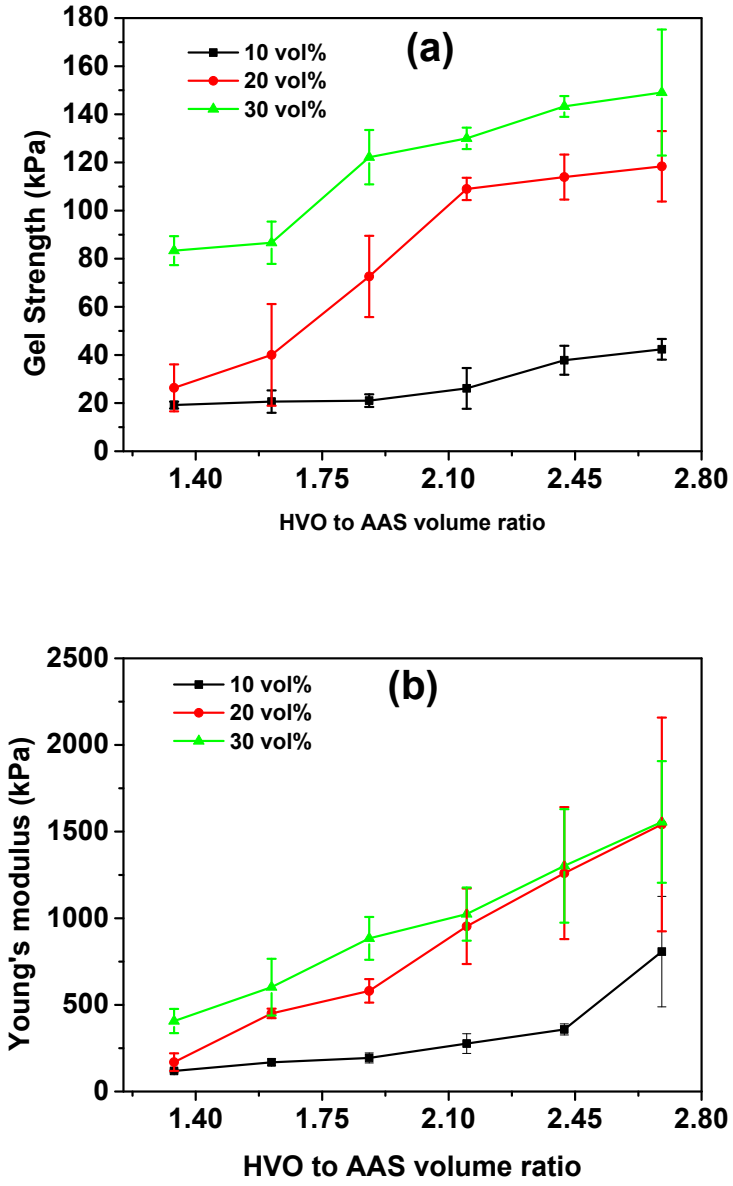

Fig.3.8 Effect of emulsion composition on (a) the compressive strength and (b) Young's modulus of the gelled emulsion bodies

The gelled emulsions can be considered as composites of solid HVO particles uniformly dispersed in a continuous matrix of gelled alumina slurry. The strength of a composite depends on the stress transfer from the continuous matrix phase to the dispersed reinforcement. The matrix to reinforcement stress transfer depends on the matrix-reinforcement interface (Hull & Clyne, 1996). The gels obtained by

cooling the aqueous alumina slurries containing the carrageenan (without HVO) show relatively low compressive strength and Young's modulus. The compressive strength values obtained are 14, 12.7 and 10.8 kPa for slurries of alumina concentrations 10, 20 and 30 vol.%, respectively. The corresponding Young's modulus values are 90, 84 and 72 kPa. On the other hand, the cylindrical bodies prepared by cooling the HVO in a glass mould show a relatively high compressive strength and Young's modulus of 292 kPa and 10340 kPa, respectively. The decrease in strength of gelled alumina slurry with an increase in alumina concentration indicates that the alumina particles interrupt the secondary interactions between the carrageenan molecules which are responsible for the gel formation. The compressive strength and Young's modulus of gelled emulsions calculated using the rule of mixtures from the corresponding values of gelled alumina slurries and solidified HVO is given in **Table 3.1**. The calculated compressive strength (175 to 215 kPa) and Young's modulus (5959 to 7556 kPa) of gelled emulsions bodies are very much higher than that of the experimentally measured compressive strength (20 to 150 kPa) and Young's modulus (120 to 1550 kPa). That is, in the mechanical behavior of the gelled emulsion bodies the characteristics of the gelled alumina slurry dominates rather than that of the solidified HVO particles. This is due to the poor stress transfer from the gelled alumina slurry matrix to the solid HVO particles because of the weak gelled alumina slurry-solid HVO particle interface. The increase in compressive strength of gelled emulsions with an increase in alumina slurry concentrations is contrary to the observed trend in the compressive strength of the gelled alumina slurries. This indicates that stress transfer from the gelled alumina slurry matrix to the solid HVO

particles increases with an increase in alumina slurry concentration. The increase in stress transfer can be due to the increase in roughness of the gelled slurry surface with an increase in alumina concentration which makes the gelled alumina slurry-solid HVO particle interface stronger by mechanical interlocking (Hull & Clyne, 1996).

Table 3.1 Compressive strength and Young's modulus of gelled emulsion bodies calculated by using rule of mixtures.

Alumina slurry Concentration (vol. %)	HVO to AAS volume ratio	Compressive Strength kPa	Young's Modulus kPa
10	1.34	173.21	5960.17
	1.61	185.50	6413.22
	1.88	195.48	6781.2
	2.14	203.46	7075.37
	2.42	210.71	7342.9
	2.69	216.66	7562.25
20	1.34	172.65	5957.61
	1.61	185	6410.93
	1.88	195.02	6779.11
	2.14	203.04	7073.46
	2.42	210.33	7341.14
	2.69	216.30	7560.62
30	1.34	171.84	5952.48
	1.61	184.27	6406.33
	1.88	194.37	6774.95
	2.14	202.44	7069.64
	2.42	209.77	7337.63
	2.69	215.79	7557.37

3.3.4 Drying of the gelled emulsions

The drying of gels is a critical step in gel assisted methods such as sol-gel processing and gelcasting (Scherer, 1990). Humidity controlled conditions are generally used for the drying of gels to prevent the formation of cracks due to capillary pressure. However, in the present case, the gelled emulsion bodies are dried in open air atmosphere at room temperature (~ 30 ^{o}C) without any humidity control. No crack or deformation is observed during the drying. **Fig. 3.9** is a typical drying curve of a gelled emulsion body. The drying rate is relatively faster in the initial period as more than 80% of water present in the gelled emulsion body is removed in 24 hours. Further the drying rate slows down and takes nearly 65 hours to remove the remaining water present in the gelled body. The drying shrinkage of the gelled emulsion bodies decreases with an increase in HVO to AAS volume ratio. The diametrical drying shrinkage observed is in the range of 11.9 to 6.6 %. **Fig 3.10** shows the photograph of a gelled emulsion body immediately after the mould removal and after drying showing their relative sizes.

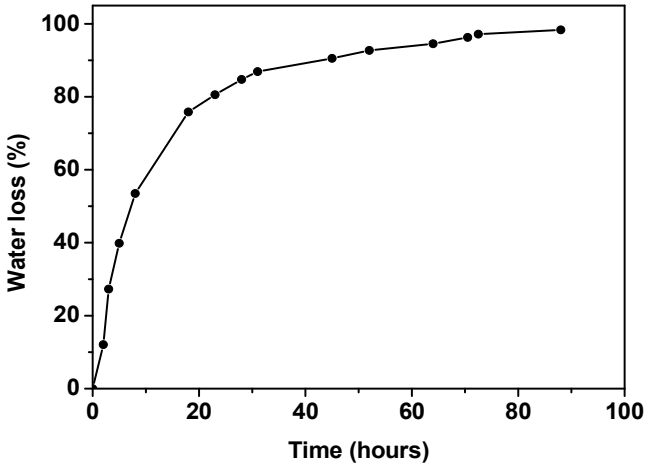

Fig 3.9 Typical drying kinetics of a gelled emulsion body

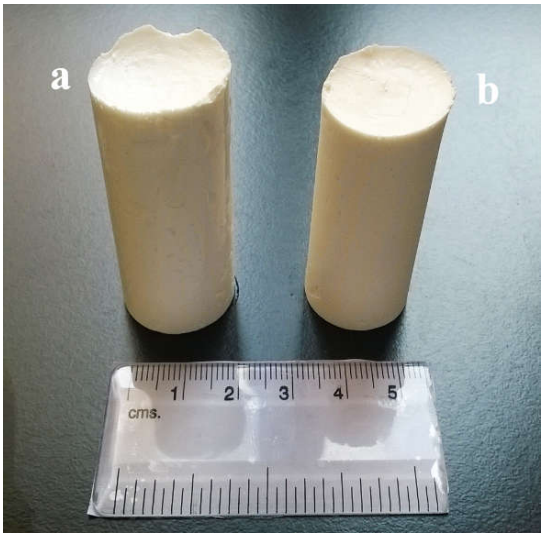

Fig 3.10 Photograph of a gelled emulsion body (a) immediately after mould removal and (b) after drying.

The gelled emulsion can be viewed as solid oil particles encapsulated in closely packed cells of AAS gel. The HVO droplets undergo slight shrinkage during the solidification resulted in the formation of extremely small gap at the HVO- AAS interface. It appears that the gap in the HVO-AAS gel interface is saturated with the water evaporated from the AAS gel. That is, the AAS gel surface is exposed to an environment similar to the high humidity condition created in a humidity chamber. The water vapour produced in the interface is transported to the surface of the body by diffusion through the gap and interconnections between the cells. This is the reason for crack free drying of the gelled emulsions bodies in normal air atmosphere.

3.3.5 HVO removal

The HVO is soluble in toluene. The solidified HVO droplets present in the dried emulsion bodies slowly dissolve in toluene when extracted using a soxhlet extraction unit. The kinetics of HVO removal of a gelled emulsion body is shown

in **Fig. 3.11**. Nearly 55% of the HVO present in the dried emulsion body is removed in the first one hour of soxhlet extraction. Further, the rate of HVO removal decreases with time. More than 99 % of the HVO can be removed in 8 hours. No deformation or crack is observed during the HVO removal. There is no measurable shrinkage observed in the dried emulsion bodies during the HVO removal.

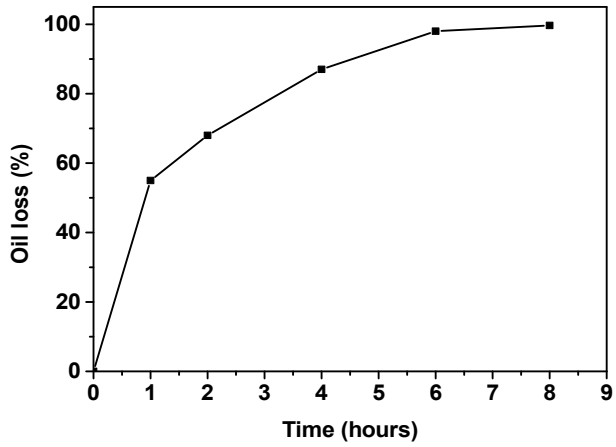

Fig 3.11 Typical HVO extraction kinetics of a gelled emulsion body

Although removal of HVO from the dried gelled emulsion bodies by soxhlet extraction using toluene is possible, the toxicity of toluene remains as a major concern. Moreover, HVO removal requires a soxhlet extraction setup, which adds complexity, especially in the case of large emulsion bodies. Various low toxic solvents such as methanol, ethanol, isopropanol, petroleum ether, etc. have been screened for the solubility of HVO at room temperature. Among them the HVO has a high solubility in petroleum ether at room temperature. The solubility is estimated as nearly 65g HVO in 100ml of petroleum ether at room temperature (~25 ^{o}C). Kinetic study on the removal of HVO from the dried emulsion bodies indicates that more than 98% of HVO can be removed by simply immersing the dried emulsion

bodies in petroleum ether at room temperature for 12 hours (solvent is renewed in every 4 hours). No deformation is observed during HVO removal and subsequent drying in ambient atmosphere at room temperature.

3.3.6 Porosity

The oil removed emulsion bodies undergo uniform shrinkage during sintering. The sintering shrinkage decreases with an increase in alumina slurry concentration. On the other hand, the sintering shrinkage shows an increasing trend with an increase in HVO to AAS volume ratio. **Table 3.2** shows the sintering shrinkage of alumina foams prepared at various HVO to AAS volume ratios and alumina slurry concentrations. **Fig. 3.12** shows the effect of emulsion composition on porosity of the alumina foams. The porosity of alumina foams obtained from the emulsions prepared from aqueous slurry of a specified alumina concentration increases with an increase in HVO to AAS volume ratio. On the other hand, at particular HVO to AAS volume ratio, the porosity increases with a decrease in alumina concentration in the aqueous slurry. In the case of the alumina foams obtained from the emulsions prepared from slurries of 10 and 20 vol.% alumina concentrations, the porosity increase with an increase in HVO to AAS volume ratio is more or less linear and slow. The porosity obtained are in the ranges of 87.14 to 92.5 vol.% and 77.5 to 89.3 vol.% from the emulsions of HVO to AAS volume ratios in the range of 1.34 to 2.69 prepared from aqueous slurries of 10 and 20 vol.% alumina concentrations, respectively. On the other hand, the alumina foams obtained from emulsions prepared from the slurry of 30 vol.% alumina loading show a rapid increase in porosity from 70.7 to 79 vol.% when the HVO to AAS volume ratio increases from 1.34 to 1.88. Thereafter, the porosity increases slowly

to 84 vol.% when the HVO to AAS volume ratio further increases to 2.69. Maximum porosity of the alumina foams obtained at HVO to AAS volume ratio of 2.69 increases from 84 to 92.5 vol.% when the alumina slurry concentration decreases from 30 to 10 vol.%.

Table 3.2 The sintering shrinkage of alumina foams prepared at various HVO to AAS volume ratios and alumina slurry concentrations

HVO to AAS volume ratio	Sintering shrinkage vol.%		
	10 vol.% AAS	20 vol.% AAS	30 vol.% AAS
1.34	48.28	44.43	37.01
1.61	47.41	44.64	37.37
1.88	49.27	44.99	37.5
2.15	50.13	45.19	39.29
2.41	53.46	46.66	39.38
2.69	54.98	47.32	40.87

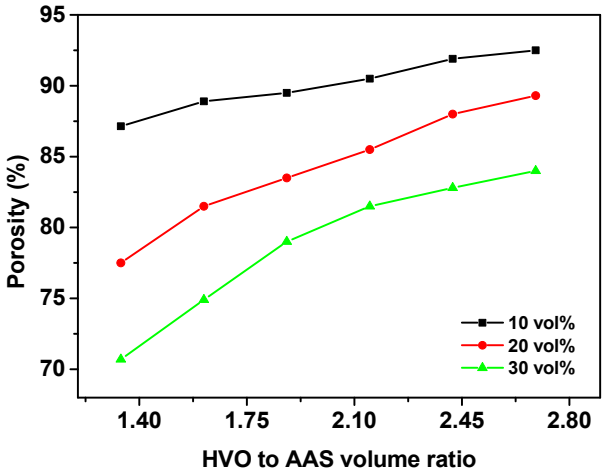

Fig 3.12 Effect of emulsion composition on porosity of the alumina foams.

The increase in porosity with an increase in HVO to AAS volume ratio is due to the increase in volume fraction of the pore template. The increase in porosity with a decrease in alumina slurry concentration can be explained as follows: The gelled emulsion can be considered as solid HVO particles embedded in close packed shells of gelled alumina slurries. The gelled alumina slurry undergoes large shrinkage whereas the HVO particles undergo negligible shrinkage during the drying of the gelled emulsions. The drying shrinkage of the gelled alumina slurries increases with a decrease in alumina concentration. In addition, the struts and cell walls of dried and oil removed gelled emulsion bodies obtained at lower alumina concentration contain loosely packed alumina particles. These loosely packed cell walls and struts undergo large shrinkage during sintering. This large shrinkage of the struts and cell walls at lower alumina slurry concentrations resulted in widening of the cells. This results in an increase in cell size with the decrease of alumina slurry concentrations even if there is no change in the size of oil droplets. The decrease in the thickness of cell walls and struts and an increase in the size of cells results in an increase in porosity.

3.3.7 Microstructure and cell size

Fig. 3.13 shows the SEM photomicrographs of alumina foams obtained from emulsions at HVO to AAS volume ratios of 1.34 and 2.69 prepared from aqueous slurries of alumina concentrations 10, 20 and 30 vol.%. The alumina foams show open cellular structure. The cells are interconnected through circular pores. At a particular HVO to AAS volume ratio, the interconnectivity of the cells decreases with an increase in concentration of alumina in the aqueous slurry. On the other hand, at a specific alumina slurry concentration the interconnectivity of

the cells increases with an increase in HVO to AAS volume ratio. At all the alumina concentrations, the nearly spherical morphology of the cells changes to polygonal morphology when the HVO to AAS volume ratio crosses 1.88. This is because the emulsion changes from medium internal phase to high internal phase when the HVO to AAS volume ratio crosses 1.88. A decrease in thickness of the strut and cell wall is seen in the microstructure with a decrease in alumina slurry concentration and an increase of HVO to AAS volume ratio. The representative SEM image showing the grain structure of struts and cell walls is given in f**ig.14.** The dense fine grained microstructure of cell walls and struts is evidenced in the micrograph. The average grain size calculated from the high magnification SEM image is **1.37 μm.**

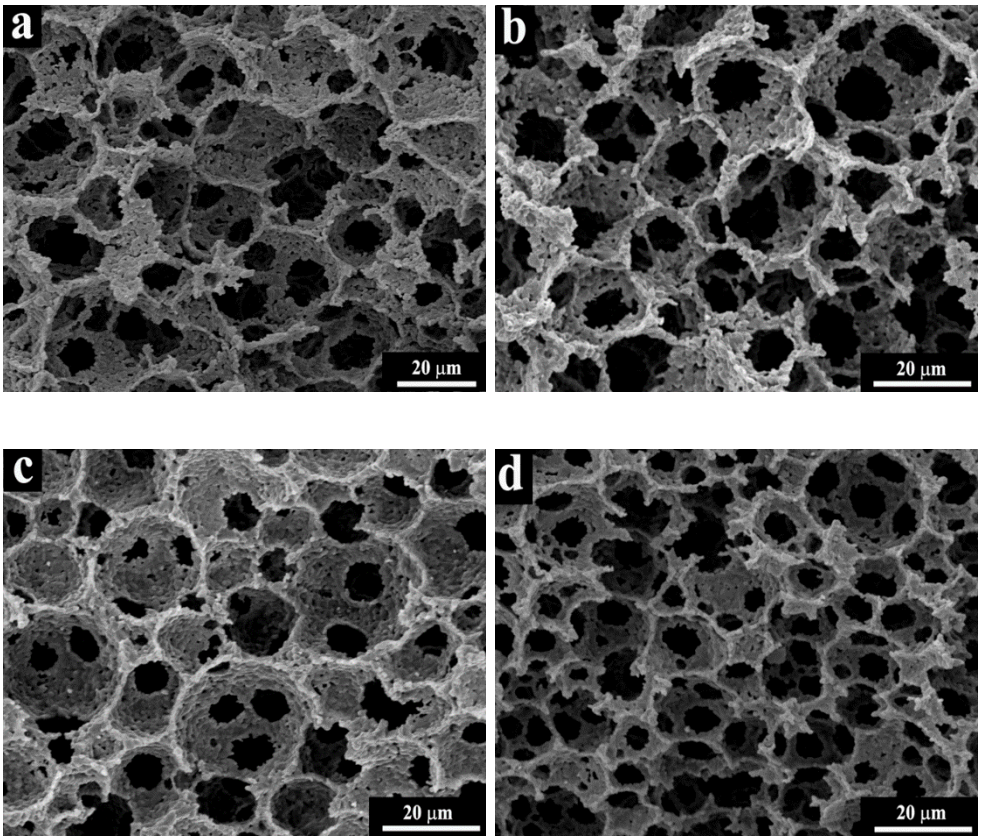

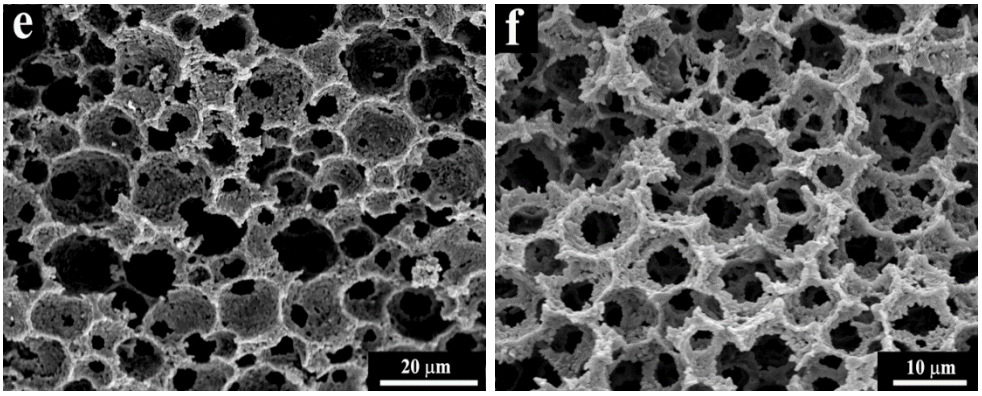

Fig 3.13 The SEM photomicrographs of the alumina foams: (a) 10 vol.%, 1.34; (b) 10 vol.%, 2.69; (c) 20 vol.%, 1.34; (d) 20 vol.%, 2.69; (e) 30 vol.%, 1.34; and (f) 30 vol.%, 2.69.

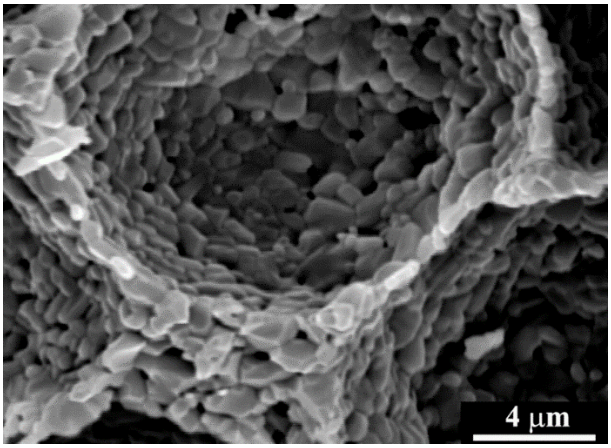

Fig 3.14 SEM image showing grain structure of cell walls and struts

The effect of alumina slurry concentration and HVO to AAS volume ratio on the average cell size of alumina foams is shown in **Fig. 3.15**. At all alumina slurry concentrations, the average cell size of the alumina foams decreases with an increase in HVO to AAS volume ratio up to 1.88 and then increases when the HVO to AAS volume ratio is increases to 2.14. The cell size remains more or less constant or shows a marginal decrease with a further increase in the HVO to AAS volume

ratio. It is interesting to note that the shift in the trend of pore size change is observed when the emulsion composition changes from medium internal phase to high internal phase. On the other hand, at a fixed HVO to AAS volume ratio, the alumina foams obtained from the emulsions prepared at slurries of lower alumina concentration showed higher average cell size. The average cell size range (20 to 8 μm) obtained by this method is much lower than that of alumina foams obtained by most of the polymer foam template methods and foaming of powder suspensions (Dhara & Bhargava, 2003; Sepulveda, 1997; Studart et al., 2006; Zhu et al., 2001). It is well known that the liquid emulsion droplets undergo coalescence during ageing due to Ostwald ripening resulting in their growth. It appears that the freezing of the HVO droplets prevents their growth by Ostwald ripening during the drying of emulsions. This is the reason for the relatively low cell size and narrow cell size distribution obtained in the present method.

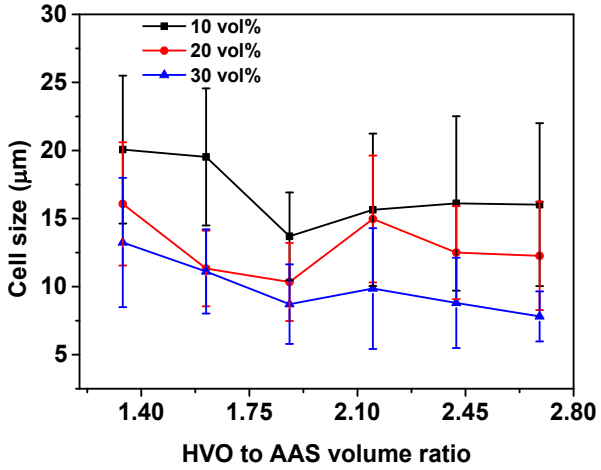

Fig 3.15 Effect of emulsion composition on cell size of the alumina foams

3.3.8 Effect of stirring speed

An increase in stirring speed breaks the oil into smaller droplets, which resulted in the decrease of the cell size. **Fig. 3.16** shows the SEM photomicrographs of the alumina foams obtained from HVO- in- AAS emulsions at HVO to AAS volume ratio of 1.34 prepared at various stirring speeds. It is clear from the micrographs that the cell size decreases and cell interconnectivity increases with an increase in stirring speed. **Fig. 3.17** shows the effect of stirring speed on cell size of alumina ceramics. The average cell size of alumina foams prepared at HVO to AAS volume ratio of 1.34 decreases from 13.24 to 3.6 μm when the stirring speed increases from 350 to 1050 rpm. It is also worthy to note that the increase in stirring speed made the cell size distribution narrow.

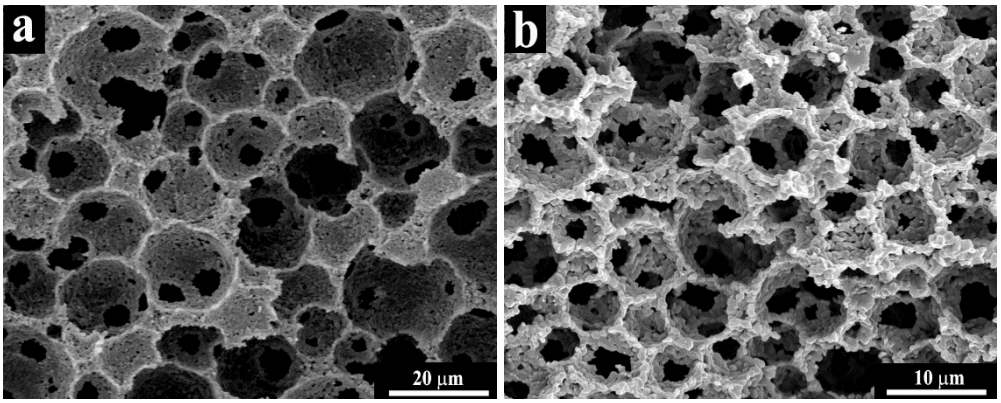

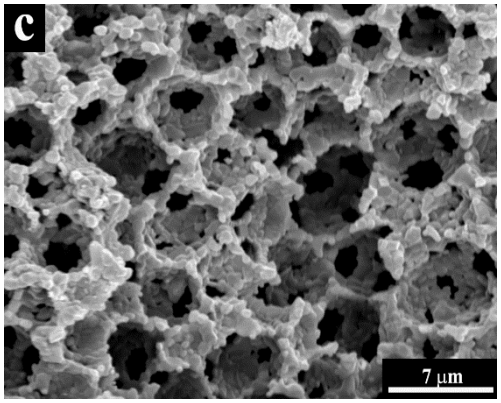

Fig 3.16 SEM photomicrographs of alumina foams prepared at HVO to AAS volume ratio of 1.34 at the various mixing speeds of (a) 350 rpm, (b) 700 rpm and (c) 1050 rpm.

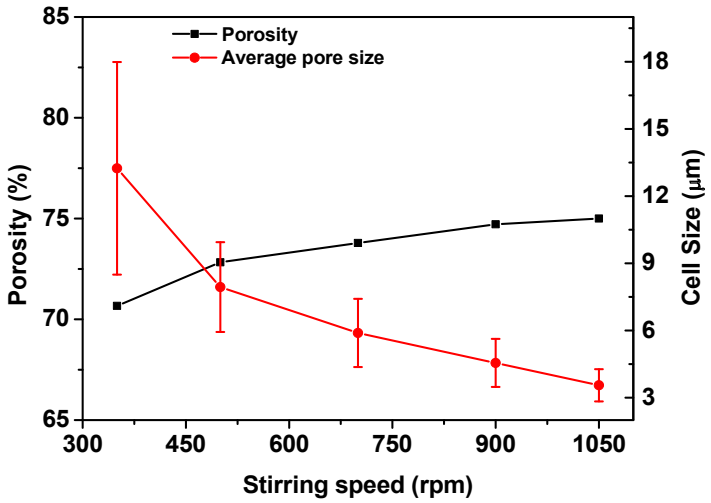

Fig 3.17 Effect of mixing speed on porosity and cell size of the alumina foams prepared at an HVO to AAS volume ratio of 1.34

The decrease in HVO droplet size with an increase in the stirring speed is further evidenced from the viscosity of the emulsions (Chanamai & McClements, 2000). The viscosity of the emulsions at HVO to AAS volume ratio of 1.34 prepared at various stirring speed is shown in **Fig. 3.18**. The viscosity of the emulsions measured at a shear rate of 9.3 s^{-1} increases from 0.95 to 1.2 Pa.s when the stirring

increases from 350 to 900 rpm. A further increase in stirring speed to 1050 rpm increases the viscosity of the emulsion to 1.45 Pa.s. The incorporation of a considerable amount of gas bubbles has been observed at the stirring speed of 1050 rpm. The relatively higher increase in viscosity with an increase in the stirring speed from 900 to 1050 rpm is due to the incorporated air bubbles. The decrease in droplet size with an increase in stirring speed increases the yield stress of the emulsions. The yield stress of the emulsions prepared at an HVO to AAS volume ratio of 1.34 increases from 3.39 to 7.91 Pa when the stirring speed increases from 350 to 1050 rpm.

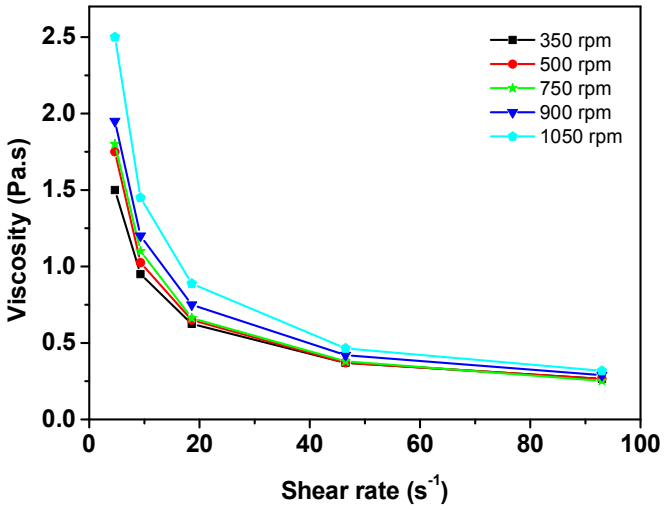

Fig 3.18 Viscosity versus shear rate plot of HVO-in-AAS emulsions at HVO to AAS volume ratio of 1.34 prepared at various mixing speeds.

3.3.9 Compressive strength of the alumina foams

Fig. 3.19 shows the stress–strain graph of the alumina foams prepared at various HVO to AAS volume ratios. The alumina foams prepared at HVO to AAS volume ratio of 2.15 and below (porosity lower than 81.5%) showed stress–strain behavior

similar to a brittle solid. That is, the stress rapidly decreased after reaching a maximum value. On the other hand, the alumina foams prepared at HVO to AAS volume ratio higher than 2.15 showed a plateau region after the highest stress value typical of a brittle elastic foam material. The highest stress value in the stress–strain graph is taken as the compressive strength.

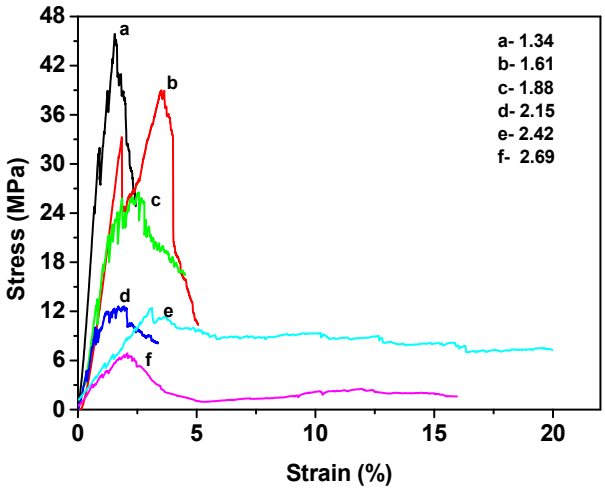

Fig 3.19 Compressive stress-strain graphs of alumina foams prepared at various HVO to AAS volume ratios.

Compressive strength of macroporous brittle solids depends on the porosity, pore size, pore interconnectivity and thickness of the cell wall and strut (Gibson & Ashby, 1997; Oliveira et al., 2006; Verma et al., 2013). In general, compressive strength decreases with an increase of porosity and cell size. In addition, macroporous ceramics with higher thickness of the cell walls and strut and lower cell interconnectivity show higher compressive strength. The effect of porosity on the compressive strength and Young's modulus of alumina foams is shown in **Fig. 3.20**. The compressive strength of the alumina foams linearly and rapidly decreases from 39.6 to 6.5 MPa when the porosity increases from 70.7 to 84 vol.%. A

remarkable shift in the slope of the porosity-compressive strength graph is observed beyond the porosity of 84 vol.%. That is, the compressive strength slowly decreases from 6.5 to 2.74 MPa when the porosity increases from 84 to 92.5%. It is interesting to note that the alumina foams of similar porosities obtained from slurries of different alumina concentrations show more or less same compressive strength. The Young's modulus of the alumina foams also shows the similar trend with porosity. The Young' modulus decreases from 2350 MPa to 350 MPa when the porosity increases from 70.7 to 84%. Further increase of porosity to 92.5 % decreases the Young's modulus to 64.5 MPa.

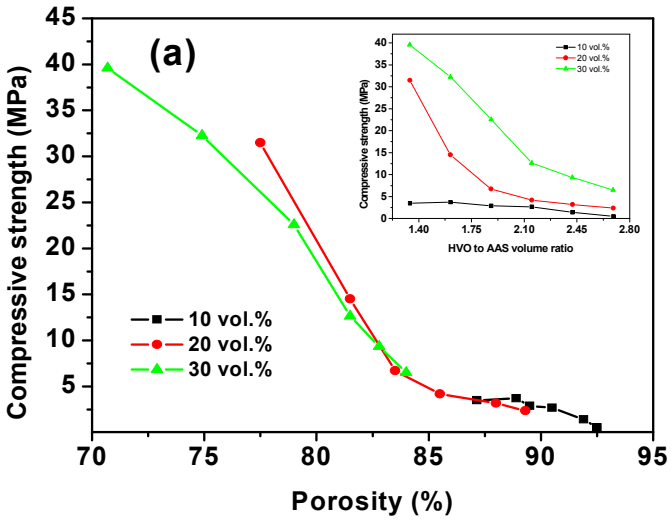

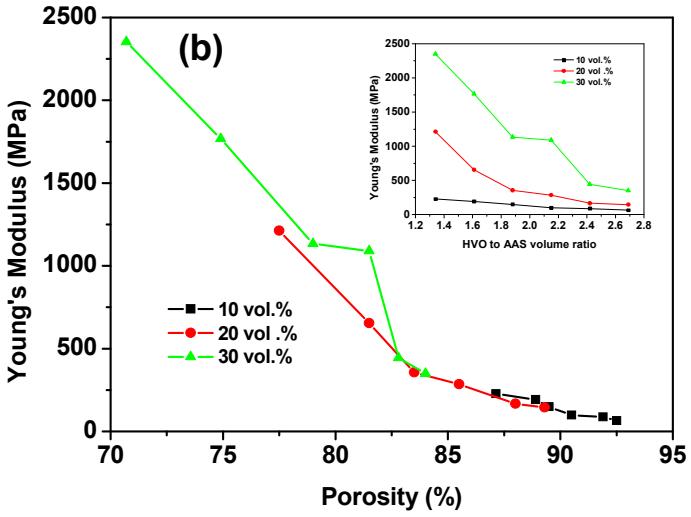

Fig 3.20 Effect of porosity (effect of HVO to AAS volume ratio and AAS concentration is shown as insert) on the (a) compressive strength and (b) Young's modulus of alumina foams.

The compressive strength and Young's modulus of the alumina foams prepared from the HVO-in-AAS emulsions are modeled using equations **(7)** proposed by Gibson and Ashby (Gibson & Ashby, 1997, Verma et al., 2013). The equation is given in chapter 2. The plots of $\ln(\sigma/\sigma_0)$ versus $\ln(\rho/\rho_0)$ and $\ln(E/E_0)$ versus $\ln(\rho/\rho_0)$ are shown in **Fig. 3.21**. The model plots are generated by considering the strength (σ_0) and Young's modulus (E_0) of fully dense alumina ceramic as 3 GPa and 416 GPa, respectively (Munro, 1997). The values of model constants C and n as well as the correlation coefficient R^2 are given in **Table 3.3**. The correlation coefficient close to one indicates a high degree of matching between the experimental results with the model graph. The compressive strength data show higher correlation coefficients of 0.933 and 0.935 at 20 and 30 vol.% alumina slurry concentrations, respectively. On the other hand, the Young's modulus data show

higher correlation coefficients of 0.943 and 0.967 at 10 and 20 vol.% alumina slurry concentrations, respectively. The values of C and n for the relation between E/E_0 and ρ/ρ_0 are expected to be ~ 1 and ~ 2, respectively, for brittle open cellular foams with a cubic array of cells (Gibson & Ashby, 1997; Magdeski, 2010; Verma et al., 2013). However, the 'n' values obtained in the present case are nearly 3. The Gibson and Ashby model is based on a completely interconnected foam with array of cubic cells of uniform size. The foams obtained in the present case have spherical cells, which are partially connected through circular pores. The deviation in the 'n' values is due to the deviation in the microstructure of the foam. The deviation in the values of C and n from that theoretically proposed by Gibson and Ashby is also attributed to the observed cell size distribution and the presence of residual pores in the cell walls and struts.

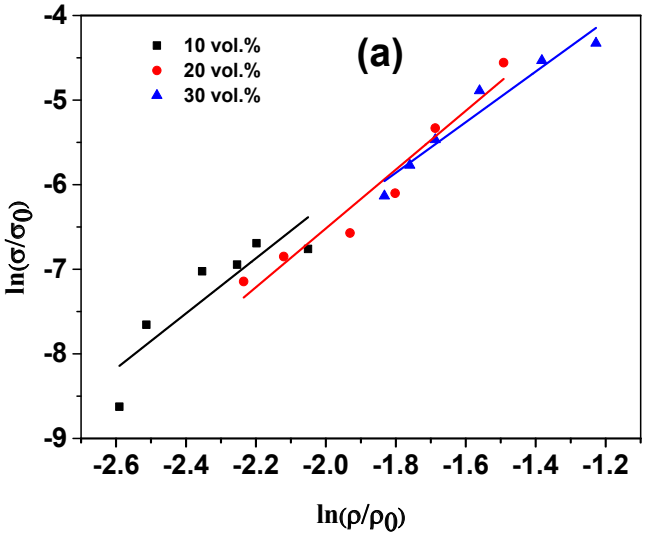

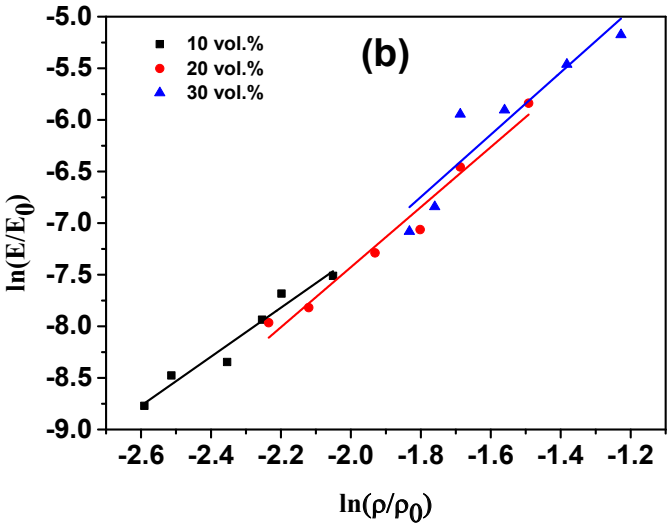

Fig 3.21 Log–log plots of (a) σ/σ_0 against ρ/ρ_0 and (b) E/E_0 against ρ/ρ_0.

Table 3.3 Values of model constants C, n and correlation coefficient R^2

Alumina Slurry concentration	Compressive strength			Young's modulus		
	n	C	R^2	n	C	R^2
10 vol.%	3.25	1.346	0.732	2.37	0.07	0.943
20 vol.%	3.47	1.546	0.935	2.91	0.2	0.967
30 vol.%	2.99	0.624	0.933	3.02	0.269	0.848

3.3.10 Preparation of large alumina foam bodies

The capability of the process for fabrication of large foam bodies is tested by casting the HVO-in-AAS emulsions in a rectangular steel mould of cavity size 10 cm x 10 cm x 2 cm. The gelled emulsion could be easily removed without any deformation. **Fig. 3.22** shows the rectangular mould with the gelled emulsion.

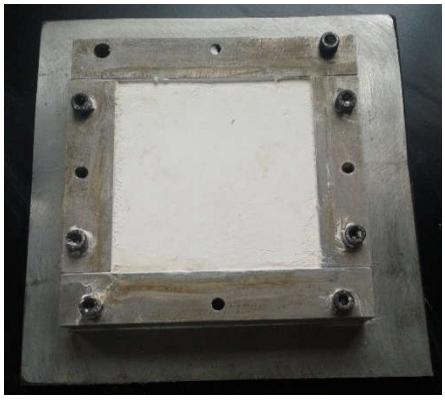

Fig 3.22 Photograph of the rectangular mould with gelled emulsion body

The large rectangular gelled emulsion bodies could be dried in ambient atmosphere without any crack. On the other hand, slight warpage was observed, especially in the case of gelled emulsion bodies prepared from 10 vol.% aqueous alumina slurry, in the first 24 hours of drying. However, warped rectangular bodies could be restored to the original shape by keeping it topside bottom for overnight. That is, at this stage, gelled bodies are sufficiently flexible to adjust itself to the original shape due to gravity. Photographs of a gelled emulsion body showing warpage during the initial 24 hours of drying and restoration of its shape by keeping it topside bottom are shown in **Fig. 3.23.**

Fig 3.23 Photographs showing (a) warpage in the initial period of drying and (b) restoration of the original shape by keeping topside bottom

The oil removal from the large body was performed by keeping the dried body in petroleum ether bath at 60 ^{o}C. The petroleum ether was replaced with fresh one after every five hours. Nearly 6 extractions, with 500 ml petroleum ether at a time, were required for the removal of ~ 98 % HVO present in the large dried emulsion body. After the oil extraction, the body was dried overnight in an air oven at 60 ^{o}C to remove the petroleum ether present in the pores. Large bodies do not show crack or deformation during sintering at 1550 ^{o}C. The photograph of a large sintered alumina foam body of 92.5 % porosity is shown in **Fig. 3.24.**

Fig 3.24 Photograph of a large sintered alumina foam body of 92.5 vol.% porosity.

3.4 Conclusions

The hydrogenated vegetable oil (HVO) dispersed in aqueous alumina slurry (AAS) medium in presence of sodium dodecyl sulphate to form medium and high internal phase HVO-in-AAS emulsions. The HVO-in-AAS emulsions showed an increase in viscosity (0.225 to 2.07 Pa.s) and yield stress (0.3 to 10.3 Pa) with an increase in HVO to AAS volume ratio and alumina concentration in the AAS. The emulsions cast in moulds underwent gelation when cooled to room temperature due

to the solidification of HVO and physical cross-linking of carrageenan. Compressive strength (20 to 150 kPa) and Young's modulus (120 to 1550 kPa) of the gelled emulsions increased with an increase in HVO to AAS volume ratio and an increase in AAS concentrations. The compressive strength and Young's modulus values were adequate for resisting the deformation of gelled emulsion bodies during mould removal and further handling. The gelled emulsion bodies could be successfully dried in open air atmosphere without any humidity control. Room temperature extraction with a relatively less toxic solvent, petroleum ether, is used for HVO removal. The maximum porosity of the alumina foam obtained at a HVO to AAS volume ratio of 2.69 increased from 84 to 92.5 % when the alumina slurry concentration decreased from 30 to 10 vol.%. The cell morphology changed from spherical to polygonal when the emulsion composition changed from medium internal phase to high internal phase. The Young's modulus values fitted with the model equation proposed by Gibson and Ashby showed large deviation in the model parameters, n and C, from the proposed values. Large alumina foam bodies could be fabricated by freeze gelcasting of HVO-in-AAS emulsions.

Chapter 4

Processing of Alumina Foams by Thermo-Foaming of Powder Dispersions in Molten Sucrose

4.1 Introduction

The current processing methods for the preparation of ceramic foams use synthetic organic additives such as binders, surfactants and solvents. Replacement of these processing additives with non-toxic naturally renewable molecules is of great economic and environmental importance. Natural renewable molecules such as proteins and polysaccharides are studied for the foaming and setting of aqueous powder suspensions for the preparation of cellular ceramic foams (Garrn et al., 2004; Ortega et al., 2003; Yin et al., 2013). Bhargava et al (Dhara & Bhargava, 2003; Pradhan & Bhargava, 2004) used sucrose, a naturally renewable molecule of agricultural origin, to control the drying shrinkage of wet-alumina foams prepared from ovalbumin-based aqueous alumina slurries. Prabhakaran et al (Prabhakaran et al, 2005) reported the foaming of alumina powder suspensions in an aqueous resin prepared by heating acidic sucrose solutions using aluminium nitrate as blowing agent. Jana and Ganesan (Jana & Ganesan, 2011) reported the preparation of alumina foam with 98.5 vol.% porosity by foaming and setting of a resin prepared by heating aqueous sucrose solution containing aluminium nitrate followed by organic burnout and sintering. In the present Chapter, the thermo-foaming of alumina powder dispersions in molten sucrose for the preparation of alumina foams with a range of porosities and cell size is studied. A two stage sintering strategy for

preparation of large foam bodies and the use of magnesium nitrate as a blowing and setting agent for accelerating the foaming and setting process is also studied.

4.2 Experimental

4.2.1 Materials

α-Alumina powder (A16SG, ACC Alcoa, Kolkata) of average particle size 0.34 μm and specific surface area 10.4 m^2/g was used. Analytical reagent grade sucrose, magnesium nitrate hexahydrate [$Mg(NO_3)_2$. 6 H_2O] (**MN**) and acetone were procured from Merck India Ltd., Mumbai.

4.2.2 Preparation of alumina foams

The process flowchart for the preparation of alumina foams is shown in **Fig. 4.1**. The sucrose (200 g) and alumina powder in various weight ratios were intimately mixed by planetary ball milling (Fritsch, Germany) in acetone medium for 4 hours using zirconia grinding media of 10 mm diameter in 500 ml zirconia jars. The sucrose to acetone and sucrose to zirconia balls weight ratios were 1:3 and 1:6, respectively. The ball milling speed was 200 RPM. The slurries thus obtained were dried in glass trays at 80 ^oC in an air oven. The sucrose-alumina powder mixtures were heated in 2.5 liter borosilicate glass trays at 185 ^oC in an air oven for the melting of sucrose. The melt was stirred well with a glass rod to get uniform dispersion of the alumina powder in the molten sucrose. The alumina powder dispersions in the molten sucrose were kept in an air oven at temperatures ranging from 120-180 ^oC for foaming and setting to form sucrose polymer-alumina powder composite foams. The foams were cut into rectangular bodies of 6 cm x 6 cm x 4 cm size and heated in an electrically heated furnace up to 1600 ^oC for the removal

of the organics and sintering. The heating rates used were 0.5 ^{o}C /minute up to 600 ^{o}C and 1^{o}C/minute from 600 to 1600 ^{o}C. A holding time of 2 hours was given at 600 ^{o}C and 1600 ^{o}C.

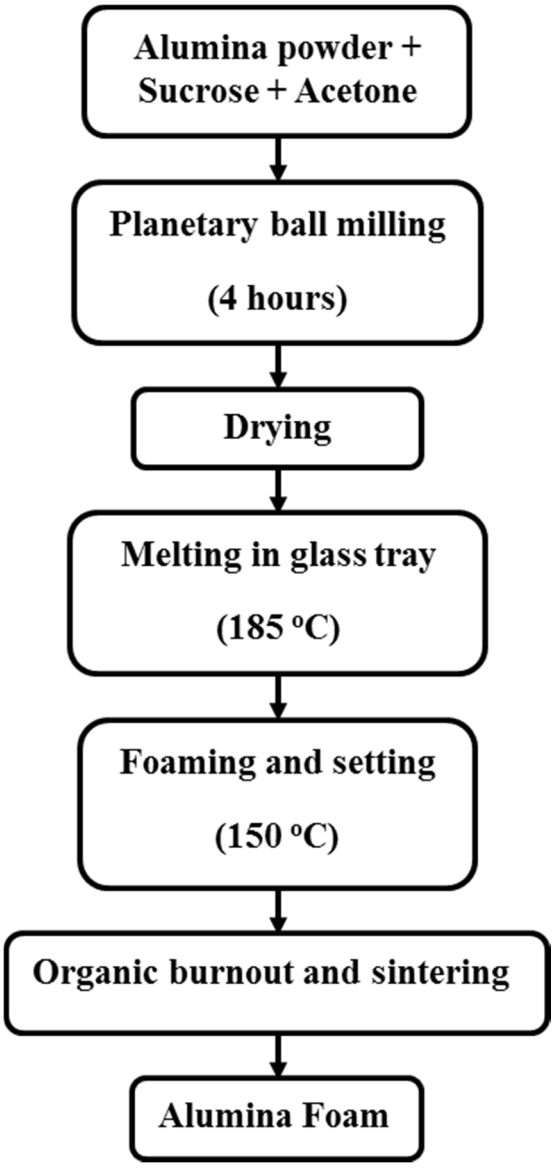

Fig 4.1 Flowchart of the thermo-foaming process for the preparation of alumina foams

For the preparation of large foam bodies, the sucrose polymer-alumina powder composite foam bodies were heated in an inert atmosphere furnace at 900

^{o}C for 2 hours for pyrolysis of the sucrose polymer. The heating rate used was 0.5 ^{o}C/minute. The carbon bonded alumina foams thus obtained were heated in an electrically heated sintering furnace up to 1600 ^{o}C in air atmosphere for removal of the carbon and subsequent sintering. The heating rates used were 2^{o}C/minute from room temperature to 400 ^{o}C, 0.5 ^{o}C/minute from 400 to 600 ^{o}C and 2 ^{o}C/ minute from 600 ^{o}C to 1600 ^{o}C. The holding time at 1600 ^{o}C was 2 hours.

In order to accelerate the foaming and setting of the alumina powder dispersions in molten sucrose, various concentrations of **MN** was also added to the sucrose-alumina powder mixture before ball milling.

4.2.3 Characterization

4.2.3.1 Viscosity studies

The viscosity measurement of the alumina powder dispersions in molten sucrose was carried out at various shear rates at temperatures ranging from 120-160 ^{o}C using a rheometer (MCR 102 Modular Compact Rheometer, Anton Paar, USA) with a cone and plate measurement system (CP-25, 25 mm diameter and angle 2^{o}).

4.2.3.2 Torque-time measurements

The torque-time measurements were carried out using a torque rheometer [Brabender Plasti-Corder, GmbH, Germany]. About 50 cm^3 of the sucrose-alumina powder mixture containing various concentrations of magnesium nitrate prepared by the planetary ball milling was loaded in to the internal mixing unit of the rheometer at a temperature of 185^{o}C and at a rotor speed of 10 RPM. The mixing at 185 ^{o}C was continued for 10 minutes at which the sucrose melts and properly

mixes with the alumina powder and then the temperature was lowered to 130 ^{o}C. The torque data was collected with time until the torque reaches 100 N m.

4.2.3.3 Foaming and setting time measurements

Mixtures containing 100 gm sucrose and different concentrations of alumina (60-180 gm) were melted in 2.5 l borosilicate glass trays to form homogenous melts. The melts were heated in an air oven at various temperatures in the range of 120–180 ^{o}C .The heights of the foams were noted after every half an hour. The time after which there is no further increase in the foam height was measured as the foaming time. After the completion of foaming, the foams were physically inspected at an interval of 1 h. The time required for the soft foam to get transform into a hard one is determined as the foam setting time

4.2.3.4 Determination of Foam Rise

Mixtures containing 100 gm sucrose and different concentrations of alumina (60-180 gm) were melted in 2.5 l borosilicate glass trays to form homogenous melts. The melts were heated in an air oven at various temperatures in the range of 120–180 ^{o}C for foaming and setting .The ratio of the final height of the foam to the initial height of the resin was taken as the foam rise (equation 8).

$$\boldsymbol{Foam\ rise = \frac{Final\ height\ of\ the\ foam}{Initial\ height\ of\ the\ resin}} \quad \text{---------- (8)}$$

4.2.3.5 Contact angle measurements

The static contact angle of molten sucrose on an alumina surface was measured by the sessile drop method using a Goniometer (OCA 20, Dataphysics,

Germany). The sample for contact angle measurement was prepared by melting a small grain of sucrose on a polished alumina surface in an air oven at 180 ^{o}C.

4.2.3.6 Thermogravimetric analysis (TGA)

The thermogravimetric analysis of the sucrose polymer-alumina powder composite foam and carbon bonded alumina foam samples was carried out in an air atmosphere at 5^{o}C/minute using a thermogravimetric analyzer (Q-50, TA Instruments, USA).

4.2.3.7 Gravimetric analysis

The carbon content of carbon bonded alumina foam bodies was estimated by gravimetric method. Carbon bonded alumina foam bodies of 5 cm x 5 cm x 2.5 cm size were heated at 600 ^{o}C in a muffle furnace for 2 hours for burnout of the carbon. The weight loss of the body was estimated as carbon content.

4.2.3.8 Differential scanning calorimetry (DSC)

The differential scanning calorimetric (DSC, TA instruments) measurements of sucrose, **MN** and sucrose-**MN** mixtures were carried out at a heating rate of 5 ^{o}C/minute in nitrogen atmosphere. The sucrose-**MN** mixture containing various concentrations of **MN** for DSC measurements were prepared by the planetary ball milling.

4.2.3.9 Shrinkage measurements

The volume shrinkage during pyrolysis and sintering was calculated from the initial and final dimensions of respective foam bodies.

4.2.3.10 Porosity measurements

The density was obtained from the weight and volume of the rectangular foam bodies. Porosity was calculated from the foam density and theoretical density of alumina (3.98 g/cm^3).

4.2.3.11 Microstructural analysis

The microstructure of the foams was observed using a scanning electron microscope (SEM, FEI Quanta FEG200). The samples for SEM analysis were prepared by cutting the sintered alumina foam samples using a knife. The samples were sputter coated with gold before the analysis.

4.2.3.12 Cell size measurements

The cell size was measured on the magnified image of the alumina foams observed using a vision inspection system with a CCD color camera (Vision 300 GL, TESA Technologies, Switzerland). The values reported were average of 50 measurements.

4.2.3.13 Compressive strength

The compressive strength of the alumina foams was measured using a universal testing machine (Instron 5500, Instron, USA) at a loading rate of 0.5 mm/minute using the sintered alumina foam samples of 25 mm x 25 mm x 12 mm size (ASTM standard C365/C365-05).

4.3 Results and Discussion

4.3.1 Effect of alumina powder to sucrose weight ratio and foaming temperature

4.3.1.1 Dispersion of alumina powder in molten sucrose

Thorough mixing of sucrose and alumina powder is achieved by the planetary ball milling. When the sucrose-alumina powder mixture is heated at 185 ^{o}C, the sucrose undergoes melting. The molten sucrose containing large number of hydroxyl groups wets the hydrophilic alumina particle surface that promotes the powder dispersion**.** **Fig. 4.2** shows the viscosity versus shear rate plot of alumina powder dispersions of various alumina powder to sucrose weight ratios **($W_{A/S}$)** measured at 150 ^{o}C. The molten sucrose without the alumina powder shows viscosity in the range of 3.34–3.14 Pa s at shear rates in the range of 2–210 s^{-1}. The alumina powder dispersions in molten sucrose shows shear thinning flow behaviour. The viscosity and shear thinning behaviour of the alumina powder dispersions increase with the increase in $W_{A/S}$. The viscosity and flow behaviour of the alumina powder dispersions in molten sucrose depend mainly on two attractive interactions. One is the intermolecular hydrogen bonding in sucrose and the other is van der Waals interaction between the alumina particles. The relatively high viscosity of the molten sucrose is due to the intermolecular hydrogen bonding. It is well known that the interparticle interactions in powder dispersions increase with the increase in powder loading (Parfitt, 1973). The increase in the viscosity and shear thinning behaviour with the increase in alumina powder loading is due to the increase in the interparticle interactions.

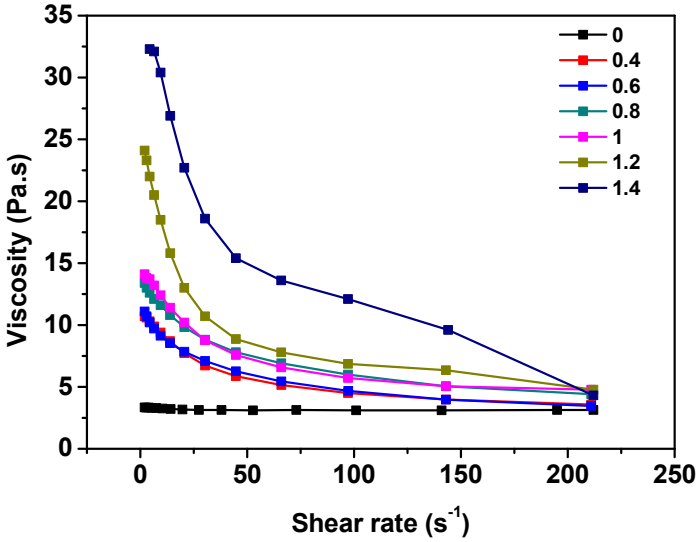

Fig 4.2 Viscosity versus shear rate plot of alumina powder dispersions of various $W_{A/S}$ measured at 150 °C

Fig. 4.3 shows the effect of temperature and $W_{A/S}$ on the viscosity of alumina powder dispersions in molten sucrose measured at a shear rate of 10 s^{-1}. The decrease in viscosity with an increase in temperature is due to the weakening of the intermolecular hydrogen bonding as well as an increase in molecular mobility. At a particular temperature, the viscosity of the dispersions increases with an increase in $W_{A/S}$ due to the increased interparticle Van der Waals interactions (Parfitt, 1973). This effect is more dominant at lower temperatures. The viscosity increase is slow up to a $W_{A/S}$ of 1.4 and thereafter rapid. For example, the viscosity at 120 °C increases slowly from 25.5 to 44.4 Pa.s when the $W_{A/S}$ increases from 0.8 to 1.4. Further increase in the $W_{A/S}$ to 1.6 results in a rapid increase in the viscosity of the dispersion to 117 Pa.s. At $W_{A/S}$ beyond 1.6, dispersion shows enormously high viscosities. For example, the dispersion at a $W_{A/S}$ of 1.8 shows a viscosity of 1140 Pa.s at 120 °C.

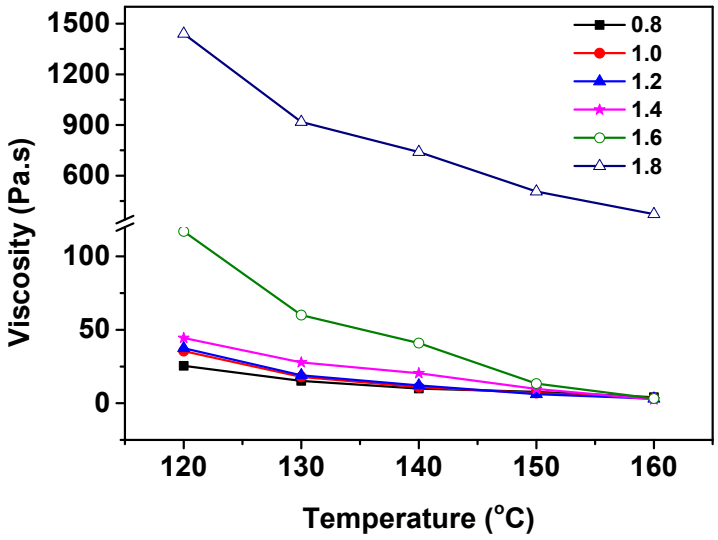

Fig 4.3 Effect of temperature on the viscosity of the powder dispersion in molten sucrose at various $\mathbf{W_{A/S}}$ (shear rate 10 s^{-1}).

4.3.1.2 Foaming and setting mechanism

The thermo-foaming of molten sucrose in presence of blowing agents such as aluminium nitrate and boric acid has been reported earlier (Narasimman & Prabhakaran, 2012, 2013). The foaming of molten sucrose involves formation of glucose and fructose anhydride followed by their condensation through the –OH groups to form caramelan and caramelen with the molecular formula $C_{24}H_{36}O_{18}$ and $C_{36}H_{50}O_{25}$, respectively (Darder & Ruiz-Hitzky, 2005; DeMan, 1999).The condensation reactions further continue to form humin or caramelin, solid products with average molecular formula $C_{125}H_{188}O_{80}$. The water vapour produced by the –OH condensation nucleate bubbles in the alumina powder dispersions. These bubbles grow by continued generation of water vapour. The bubbles generated in the molten sucrose due to the water vapour produced by the condensation reactions are stabilized by the rapid increase in viscosity. The setting of the foamed

dispersions is due to viscosity increase by the continued condensation polymerization.

The viscosity variations with time of the alumina powder dispersion and the neat molten sucrose, measured at a shear rate of 10 s^{-1} at 150 ^{o}C is shown in **Fig. 4.4**. The initial decrease in viscosity of the alumina powder dispersion observed up to 1.5 hours is due to the breakdown of the particle agglomerates. After 1.5 hours, the viscosity of the alumina powder dispersion and the neat molten sucrose increased with time. The rate of viscosity increase is higher for the alumina powder dispersion. This indicates that the alumina powder facilitates the –OH to –OH condensation reaction. That is, the alumina particles in the dispersion promote foaming and foam setting by facilitating the –OH condensation**.** In addition to the catalytic activity towards –OH condensation the higher thermal conductivity of alumina facilitates faster attainment of thermal equilibrium in the system. The viscosity of the alumina powder dispersion reaches 9.15 Pa.s at the end of 3.5 hours when its foaming is complete. Though the neat molten sucrose reaches this viscosity value at the end of 4.3 hours, the foaming initiated only after 15 hours. This indicates that the viscosity increase due to enhanced –OH to –OH condensation is not the only factor which stabilizes the bubbles in the alumina powder dispersions. It has been reported that the particles with suitable wetting characteristics can stabilize bubbles by adsorbing on the gas-liquid interface (Studart et al., 2006). The bubble stabilization by the particle is reported for the foaming of liquids, polymers and powder suspensions (Alargova et al., 2004; Binks & Horozov, 2005; Gonzenbach et al., 2006, 2007; Thareja et al., 2008). It has been reported that the solid-liquid contact angle in the range of 60 to 80^{o} is ideal for stabilizing the bubbles

by adsorbing on the air-liquid interface. The contact angle of molten sucrose measured on a polished alumina surface is 63° as seen in **Fig. 4.5**. In the present case, it appears that the alumina particles stabilize the bubbles in the dispersion having low viscosity by forming coverage on the gas–liquid interface that enable the foaming of the dispersions.

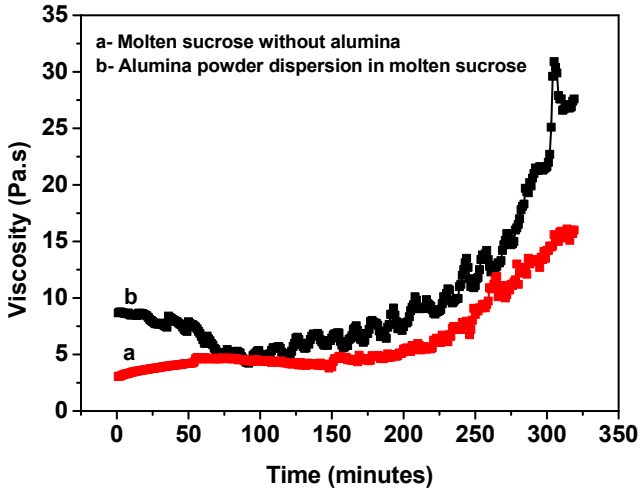

Fig 4.4 Viscosity variation with time of molten sucrose and alumina powder dispersion in molten sucrose at 150 °C.

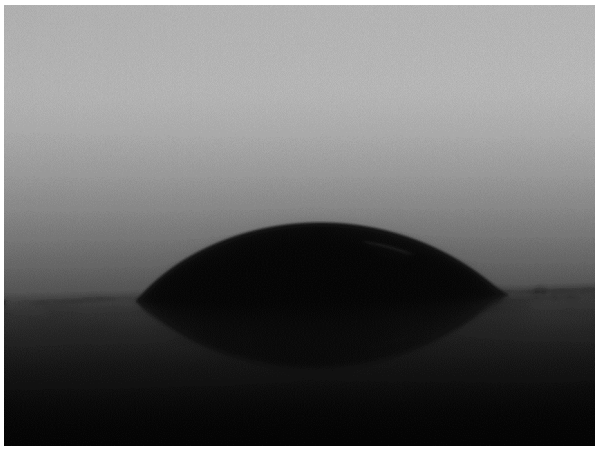

Fig 4.5 Photograph showing the contact angle of molten sucrose on an alumina surface

Fig. 4.6 shows the photograph of alumina powder dispersion in a 2.5 liter glass tray before foaming and after foaming & foam setting. The thermo-foamed bodies show uniform structure throughout. In contrast, in the case of the alumina powder dispersions in aqueous sucrose resin reported earlier, the foams produced had a hard surface layer that has to be discarded (Prabhakaran et al., 2005). Further, in direct casting of foamed aqueous powder suspensions, cracks were formed on the foams cast in the moulds unless dried with extreme care (Pradhan & Bhargava, 2008). In the present case, no cracks are observed during the setting of the foamed suspensions.

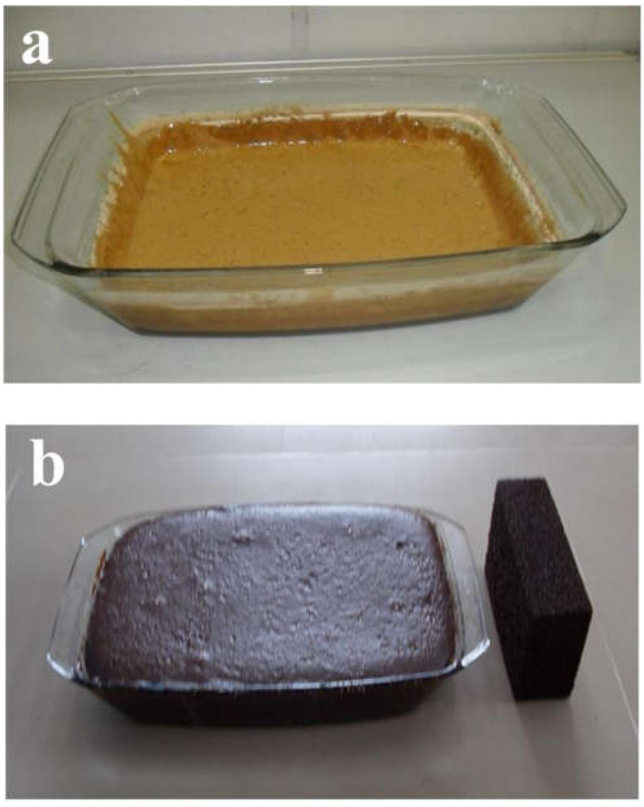

Fig 4.6 Photographs of (a) alumina powder dispersion in a 2.5 l glass tray and (b) the foam obtained by foaming at 150 ^{o}C.

4.3.1.3 Foaming & setting time and foam rise

Fig. 4.7 shows the effect of temperature on foaming and setting of alumina powder dispersions of various $W_{A/S}$. At all the studied $W_{A/S}$, the foaming time and foam setting time decrease significantly with an increase in foaming temperature. For example, the foaming time at a $W_{A/S}$ of 0.8 decreases from 17.5 to 0.5 hours when the foaming temperature increases from 120 to 170 °C. The corresponding decrease in foam setting time is from 98 to 7.5 hours. On the other hand, at a particular foaming temperature, the foaming time and foam setting time increases with a decrease of $W_{A/S}$. The difference observed in foaming time and foam setting time between powder dispersions of consecutive $W_{A/S}$ is higher at lower foaming temperature. That is, at 120 °C, the foaming time decreases from 17.5 to 6.5 hours when the $W_{A/S}$ increases from 0.8 to 1.6. However, at 150 °C, the decrease in foaming time is from 3 to 1.5 hours. The corresponding decrease in foam setting time is from 98 to 32.75 hours at 120 °C and 21 to 9 hours at 150 °C.

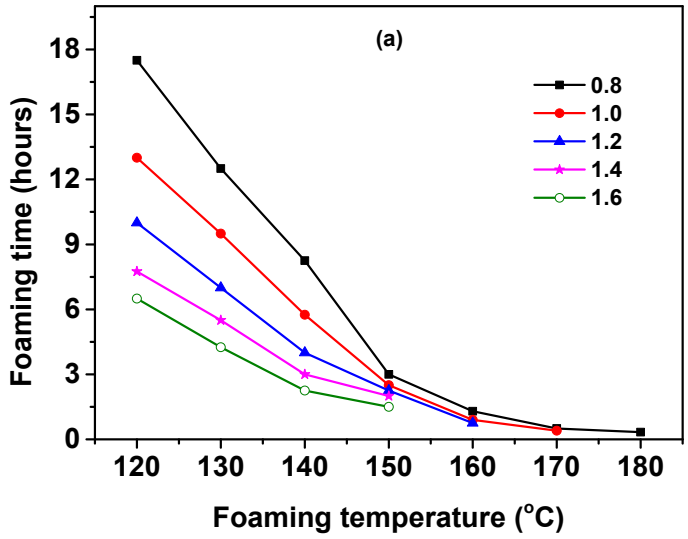

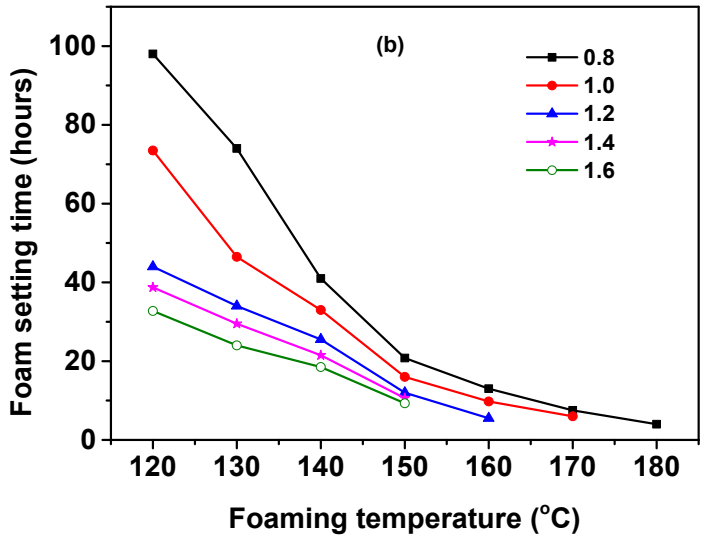

Fig 4.7 Effect of foaming temperature on (a) foaming time and (b) foam setting time of dispersions at various $W_{A/S}$

The foam rise, a measure of foam volume, is the ratio of the final foam height to the initial dispersion height. **Fig. 4.8** shows the effect of temperature and $W_{A/S}$ on the foam rise of alumina powder dispersions in molten sucrose. At all studied $W_{A/S}$, the foam rise increases with an increase in foaming temperature, reaches a maximum at a certain temperature and then decreases. The temperature at which the foam volume reaches maximum is termed as critical foaming temperature. The decrease of foam rise beyond the critical foaming temperature is due to the foam collapse. The critical foaming temperature decreases with an increase in the $W_{A/S}$**.** That is the critical foaming temperature decreases from 170 to 140 ^{o}C when the $W_{A/S}$ increases from 0.8 to 1.6. On the other hand, below the critical foaming temperature, the foam rise of dispersion shows only a minor variation with the $W_{A/S}$**.**

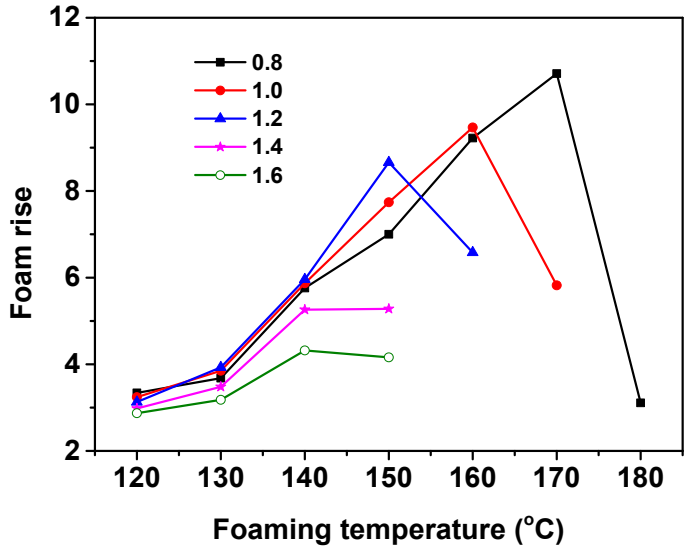

Fig 4.8 Effect of foaming temperature and $W_{A/S}$ on the foam rise of alumina powder dispersions in molten sucrose.

4.3.1.3 Foam sintering

Fig. 4.9 shows the TG and DTG plots of the foam samples prepared at various alumina powders to sucrose weight ratios. The foam samples obtained from the neat sucrose resin and the alumina powder dispersions show two peaks in the DTG. The low temperature peak is mainly due to the dehydration of the sucrose polymer and the high temperature peak corresponds to the burnout of the dehydrated sucrose polymer. The peak corresponding to the dehydration slightly shifts to lower temperatures with the increase in alumina concentration. On the other hand, the peak corresponding to the burnout shifts considerably to lower temperatures with the increase in the alumina concentration. Moreover, the temperature for the complete burnout of the organics from the foam samples decreased with the increase in alumina concentration. This shows that the alumina powder catalyzes the dehydration and oxidation of the sucrose polymer.

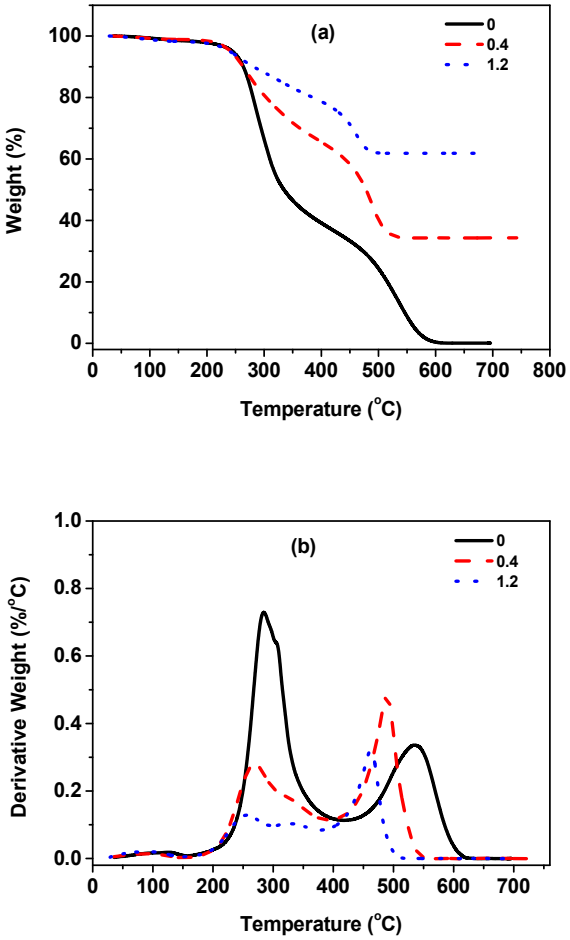

Fig 4.9 The (a) TG and (b) DTG plots of the foam samples prepared at various $W_{A/S}$.

The sucrose polymer-alumina powder composite foam bodies undergo relatively large shrinkage during sintering. **Fig. 4.10** shows the effect of $W_{A/S}$ and foaming temperature on the total volume shrinkage during sintering of sucrose polymer-alumina powder composite foam bodies. The volume shrinkage during sintering increases with a decrease in the $W_{A/S}$. On the other hand, the foam bodies prepared at a particular $W_{A/S}$ show only a marginal decrease in volume shrinkage with an increase in foaming temperature. The composite foam bodies prepared at various foaming temperatures at a particular $W_{A/S}$ have more or less same

composition but different foam volume due to a difference in the cell size. The sintering shrinkage depends largely on the alumina powder loading in the composite foam and not on the foam volume (cell size). The foam samples of 6 cm x 6 cm x 4 cm size at the $W_{A/S}$ below 0.6 undergo crack during the burnout of the sucrose polymer. Only foams prepared at $W_{A/S}$ above 0.8 survive without cracking.

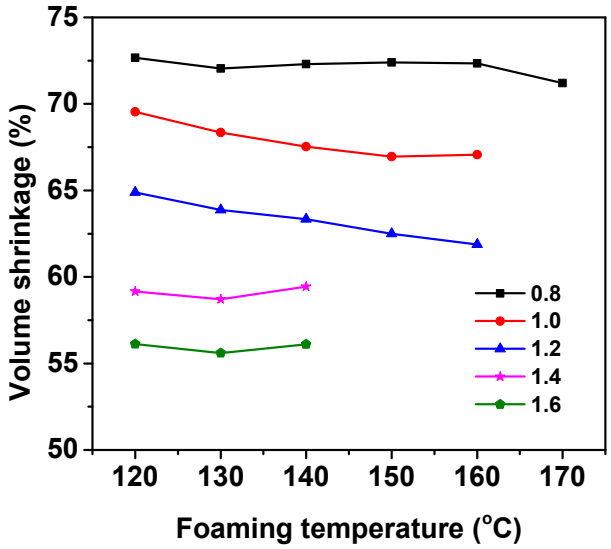

Fig 4.10 Effect of $W_{A/S}$ and foaming temperature on sintering shrinkage of foam bodies.

4.3.1.4 Microstructure and cell size of the alumina foams

It has been reported that the microstructure of the alumina foams prepared by the foaming of alumina powder suspensions in aqueous sucrose resin using aluminium nitrate blowing agent depends on the alumina powder to sucrose weight ratio (Prabhakaran et al., 2005). The foams obtained showed reticulated and cellular microstructures at the alumina powder to sucrose weight ratios in the ranges of 0.97 to 1.12 and 1.25 to 1.45, respectively. In contrast, the alumina foams prepared by thermo-foaming of powder dispersions in molten sucrose show interconnected cellular structure irrespective of the $W_{A/S}$ and foaming temperature. At all studied

$W_{A/S}$, thermo-foaming produces near-spherical cells up to the critical foaming temperature. On the other hand, the partially collapsed foam obtained beyond the critical foaming temperature contains oval shaped cells. The SEM photomicrograph of the alumina foams prepared at various foaming temperatures at a $W_{A/S}$ of 1 is shown in **Fig. 4.11**. The spherical cells up to the critical foaming temperature (160^{o}C at $W_{A/S}$ of 1) and a change in shape of the cells from spherical to oval beyond the critical foaming temperature are clearly evidenced from the SEM photomicrograph. The increase in cell size due to bubble growth with an increase of foaming temperature is also evidenced from the microstructure. Similar cell structure and a similar change in cell structure beyond the critical foaming temperature are observed in all studied $W_{A/S}$. The dense strut is also evidenced from the high magnification SEM image (**Fig.4.11d).**

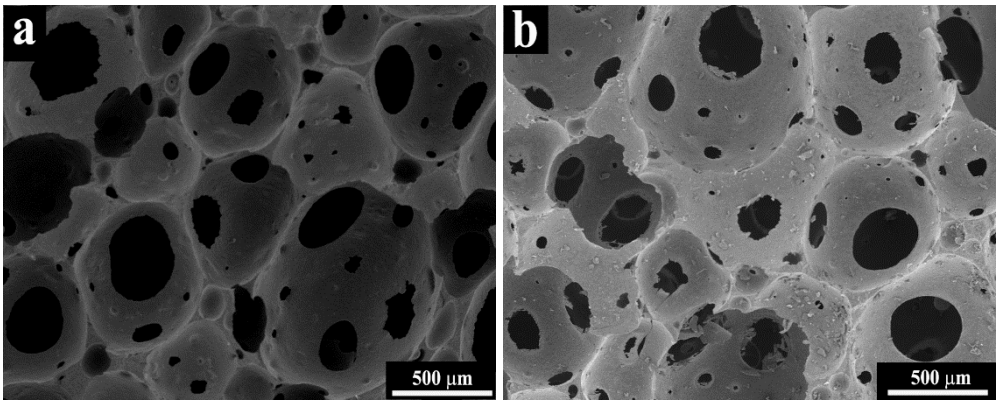

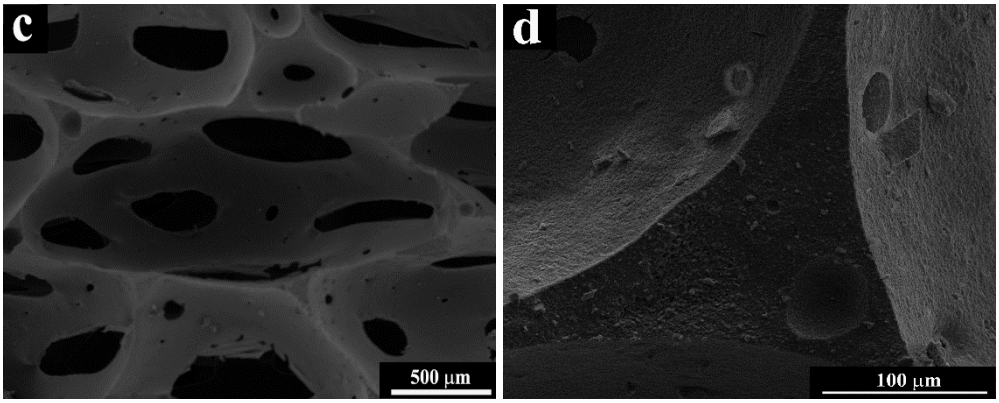

Fig 4.11 The SEM photomicrograph of alumina foams prepared at the foaming temperatures of (a) 120 ºC, (b) 160 ºC, (c) 170 ºC and (d) strut region at a $\mathbf{W_{A/S}}$ of 1.

Fig. 4.12 shows the effect of foaming temperature on the average cell size of the alumina foams prepared at various $\mathbf{W_{A/S}}$. At a particular foaming temperature, the cell size of alumina foams shows only a marginal increase with an increase in $\mathbf{W_{A/S}}$. For example, the average cell size of alumina foam prepared at a foaming temperature of 120ºC increases from 0.55 to 0.7 mm when the $\mathbf{W_{A/S}}$ increases from 0.8 to 1.6. On the other hand, the cell size of alumina foams prepared at various $\mathbf{W_{A/S}}$ shows a considerable increase with an increase in foaming temperature. The increase in cell size is gradual up to a foaming temperature of 150 ºC and thereafter rapid. The study suggests that the average cell size of alumina foams can be controlled in a wide range of 0.55 to 1.6 mm by controlling the $\mathbf{W_{A/S}}$ and foaming temperature.

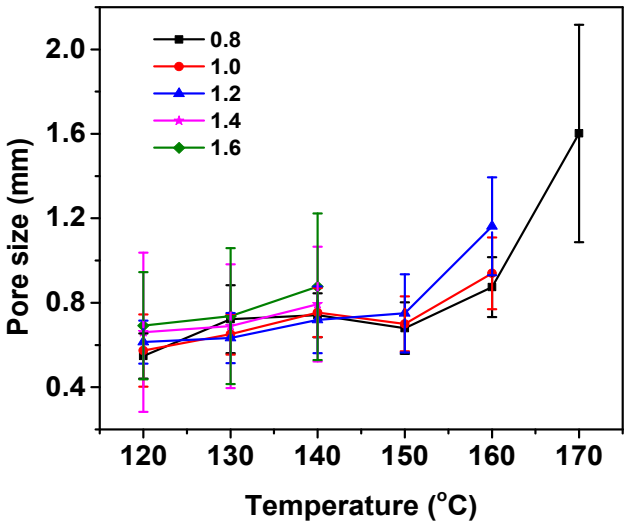

Fig 4.12 Effect of foaming temperature and $W_{A/S}$ on the average cell size of alumina foams.

4.3.1.5 Porosity

The porosity of the alumina foam prepared at a particular $W_{A/S}$ increases with an increase in foaming temperature up to the critical foaming temperature. The increase in porosity is due to the increase in cell size with an increase in foaming temperature. Beyond the critical foaming temperature, decrease in porosity is observed due to the densification by partial foam collapse. On the other hand, at foaming temperatures in the range of 120 to 140 °C, the porosity shows a marginal decrease with an increase in $W_{A/S}$ even though the cell size shows a marginal increase. The observed decrease in porosity with an increase in $W_{A/S}$ is attributed to an increase in the strut thickness. However, a reverse trend in porosity with an increase in $W_{A/S}$ is observed at foaming temperatures above 140 °C. The average thickness of struts increases from 0.148 to 0.186 mm when the alumina to sucrose weight ratio increases from 0.8 to 1.4.The alumina foams with porosity in the wide range of 83.4 to 94.6 vol.% are prepared from alumina powder dispersions in molten

sucrose by thermo-foaming at temperatures in the range of 120 to 170 °C. **Fig. 4.13** shows the effect of foaming temperature and $W_{A/S}$ on the porosity of alumina foams.

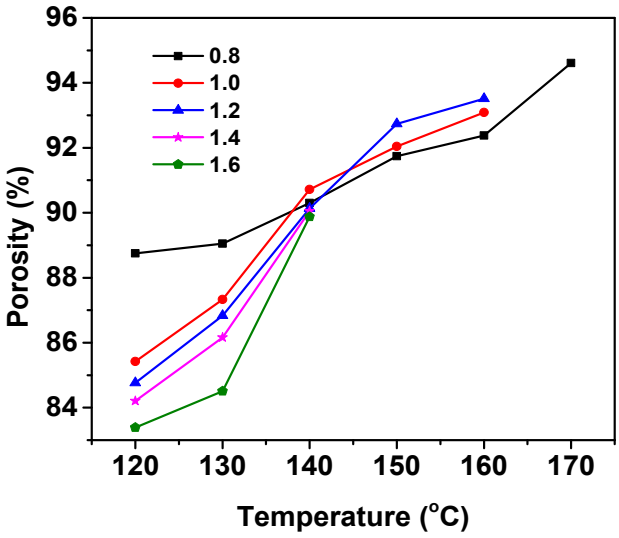

Fig 4.13 Effect of foaming temperature and $W_{A/S}$ on porosity of alumina foams

4.3.1.6 Compressive strength

Fig. 4.14 shows the typical compressive stress–strain graph of the ceramic foams prepared by thermo-foaming of alumina powder dispersions in molten sucrose. An elastic region followed by a yield point, a plateau region and a region of strain hardening, typical for a rigid cellular material are observed in the stress–strain curves. The Young's modulus is calculated from the initial linear region and the stress corresponding to the maximum in the stress–strain graph is taken as the compressive strength.

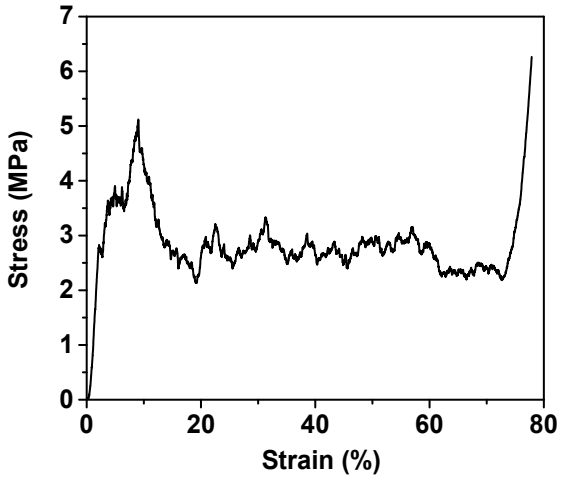

Fig 4.14 Compressive stress–strain graph of the alumina foams at various $\mathbf{W_{A/S}}$

The compressive strength of macroporous brittle solids depends on the porosity, pore size, pore interconnectivity and thickness of the cell wall and strut (Gibson & Ashby, 1997; Studart et al., 2006). The compressive strength decreases with an increase in porosity, increase in cell size and increase in cell interconnectivity and decrease in strut thickness. The effect of foaming temperature on the compressive strength and Young's modulus of the alumina foams prepared at various $\mathbf{W_{A/S}}$ is shown in **Fig. 4.15**. At all studied $\mathbf{W_{A/S}}$ the compressive strength decreases with an increase in foaming temperature as the porosity and cell size of the foams increases. For example, the compressive strength of alumina foam prepared at a $\mathbf{W_{A/S}}$ of 1 decrease from 8.53 to 1.13 MPa when the foaming temperature increases from 120 to 160 ^{o}C due to an increase in porosity from 85.4 to 93 vol.% and an increase in cell size from 0.57 to 0.94 mm. Similarly, at a given foaming temperature, the compressive strength of alumina foams prepared at the $\mathbf{W_{A/S}}$ in the range of 0.8 to 1.2 shows a marginal increase with an increase in the $\mathbf{W_{A/S}}$. This is attributed to the marginal decrease in porosity and increase in strut

thickness with an increase in $W_{A/S}$. The Young's modulus of the alumina foams shows the similar trend with the foaming temperature and $W_{A/S}$. For example, the Young's modulus at a $W_{A/S}$ of 1 decreases from 809 to 72 MPa when the foaming temperature increases from 120 to 160 °C. On the other hand, the alumina foams prepared at the $W_{A/S}$ of 1.4 and 1.6 show lower compressive strength and Young's modulus than that of the foam prepared at a $W_{A/S}$ of 0.8.

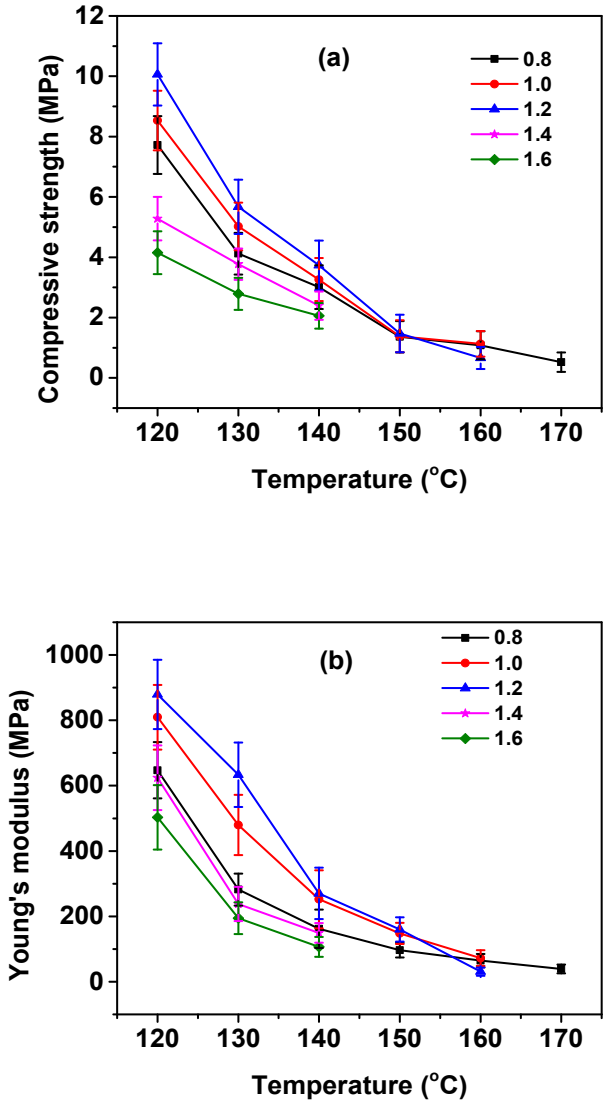

Fig 4.15 Effect of foaming temperature and $W_{A/S}$ on (a) compressive strength and (b) Young's modulus of the alumina foams.

The lower compressive strength and Young's modulus of alumina foams at the $\mathbf{W_{A/S}}$ of 1.4 and 1.6 in spite of their lower porosity are evidenced from their microstructures. The microstructure of the alumina foams prepared at the $\mathbf{W_{A/S}}$ of 1.4 and 1.6 contains a large number of pinholes on the cell walls. In addition, large numbers of micro-bubbles are observed in the struts. Also, the high magnification SEM images show micro pores in inter and intra granular regions. **Fig. 4.16** shows typical SEM microstructures showing pinholes on the cell walls, micro bubbles in the struts and micro pores in the inter and intra granular region in the foam prepared at a $\mathbf{W_{A/S}}$ of 1.4. It appears that alumina powder disperses well in molten sucrose up to a $\mathbf{W_{A/S}}$ of 1.2. The agglomeration of alumina particles in the molten sucrose medium starts at a $\mathbf{W_{A/S}}$ beyond 1.2. This is clearly evidenced in the increase in viscosity with $\mathbf{W_{A/S}}$ of the dispersions (**Fig. 4.3**). The sintering of these particle agglomerates creates pinholes on the cell walls and struts and micro pores in inter and intra granular region. It appears that the bubbles nucleated in the thick struts during the later stages of the foaming of alumina powder dispersions or initial stages of foam setting are stabilized due to the high viscosity at higher $\mathbf{W_{A/S}}$. It is well known that the pores present in the struts limit the strength of brittle foam materials (Jun etal., 2006). The lower strength and Young's modulus of foams prepared at the $\mathbf{W_{A/S}}$ of 1 .4 and 1.6 are due to the pinholes present on the cell walls, higher population of the micro bubbles in the struts and micro pores present in the inter and intra granular regions.

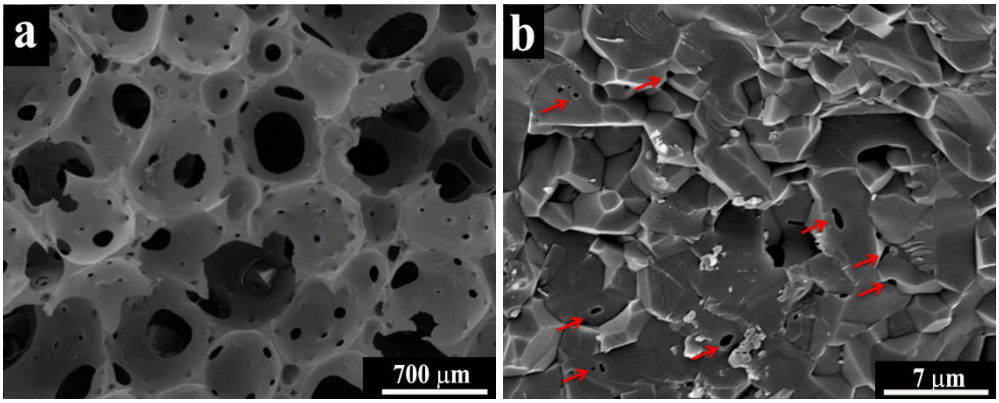

Fig 4.16 SEM photomicrograph of alumina foam at a $\mathbf{W_{A/S}}$ of 1.4 showing (a) pinholes on the cell walls and struts and (b) inter- and intra-granular porosity.

The plots of $\ln(\sigma/\sigma_0)$ versus $\ln(\rho/\rho_0)$ and $\ln(E/E_0)$ versus $\ln(\rho/\rho_0)$ (Gibson & Ashby, 1997; Verma et al., 2013) of alumina foams prepared at various foaming temperatures and $\mathbf{W_{A/S}}$ are shown in **Fig. 4.17**. The values of model constants C and n as well as the correlation coefficient R^2 are given in **Table 4.1**. The correlation coefficient close to one indicates a high degree of matching between the experimental results with the model graph. The compressive strength and Young's modulus data show moderate value of correlation coefficients at the $\mathbf{W_{A/S}}$ in the range of 0.8 to 1.4. On the other hand, very low values of correlation coefficients are obtained at a $\mathbf{W_{A/S}}$ of 1.6. The values of C and n for the relation between E/E_0 and ρ/ρ_0 are expected to be ~ 1 and ~ 2, respectively, for brittle open cellular foams with a cubic array of cells (Gibson & Ashby, 1997; Magdeski, 2010; Oliveira et al., 2006). The values for 'C' and 'n' largely deviate from the values predicted by Gibson and Ashby, especially at higher $\mathbf{W_{A/S}}$ of 1.4 and 1.6. The Gibson and Ashby model is based on completely interconnected foam with an array of cubic cells of uniform size. The large deviation in the values of C and 'n' and low value of correlation coefficient at the $\mathbf{W_{A/S}}$ of 1.4 and 1.6 is attributed to the pinholes on the

cell walls and micro bubbles present in the struts as well as deviation in the cell shape.

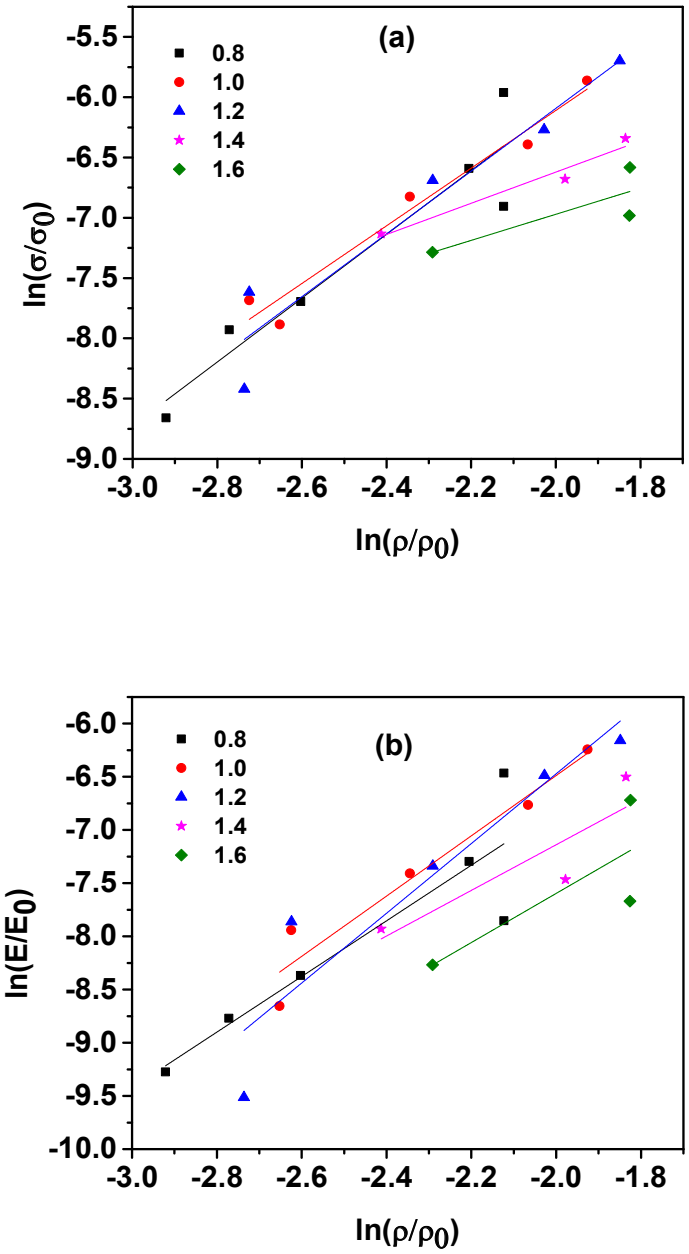

Fig 4.17 Log-log plots of (a) σ/σ_0 against ρ/ρ_0 and (b) E/E_0 against ρ/ρ_0

Table 4.1. Values of model constants C, n and correlation coefficient R^2

$W_{A/S}$	Compressive strength			Young's modulus		
	n	C	R^2	n	C	R^2
0.8	2.6439	0.45282	0.80715	2.61536	0.2066	0.76755
1.0	2.39182	0.26553	0.95627	2.54939	0.23939	0.92145
1.2	2.60297	0.41217	0.90459	3.27825	0.30570	0.83479
1.4	1.29276	0.13061	0.922	2.14521	0.0579	0.56829
1.6	1.08198	0.06039	0.3668	2.30915	0.50986	0.26453

4.3.2 Fabrication of large alumina foams

The studies on large foam body fabrication are restricted to $W_{A/S}$ in the range of 0.6 to 1.2 as particle agglomeration is likely at higher $W_{A/S}$. The direct binder burnout in air below 600 ^oC followed by sintering at 1600 ^oC of sucrose polymer-alumina powder composite foam bodies of size larger than 5 cm x 5 cm x 2 cm results in formation of severe cracks. The formation of crack is due to the large volume shrinkage (75 to 60 vol.% at $W_{A/S}$ in the range of 0.6 to 1.2). The corresponding linear shrinkage is in the range of 39.1 to 29.1%. The shrinkage of the foam bodies mainly occurs in two stages. The first stage of shrinkage is during the sucrose polymer burnout at temperature below 600^oC and the second stage of shrinkage is during sintering at temperatures in the range of 1200 to 1600 ^oC. **Fig. 4.18** shows the total shrinkage and shrinkage during the sucrose polymer burnout as a function of $W_{A/S}$. The shrinkage during sucrose polymer burnout decreases from 49.2 to 31.7 vol. % when the $W_{A/S}$ increases from 0.6 to 1.2. The corresponding linear shrinkage observed is in the range of 20.5 to 11.3 %. This shows that a major portion (65.6 to

52.83%) of the total volume shrinkage takes place during the sucrose polymer burnout.

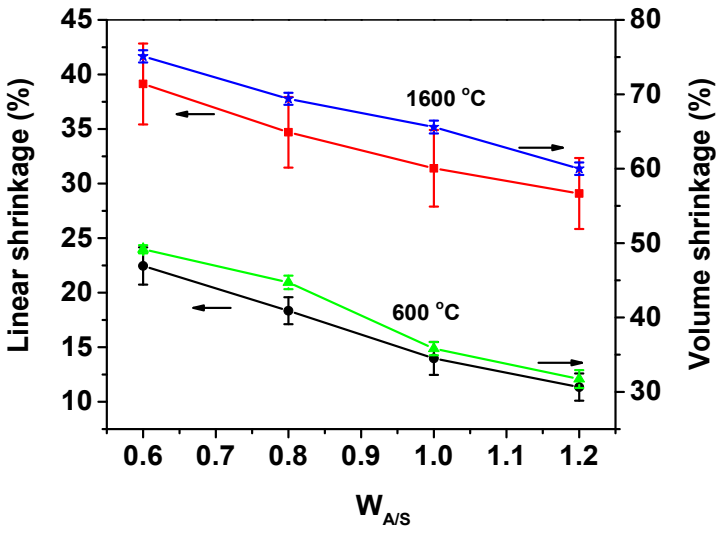

Fig 4.18 The shrinkage during polymer burnout and sintering of sucrose polymer-alumina powder composite foam bodies prepared at various $W_{A/S}$

It is well known that burnout of polymeric binder from ceramic green bodies containing a large amount of organic creates high strain which results in the development of internal stresses in the bodies. The stress-strain development during binder removal from ceramic green bodies is well studied by both experimental methods and mathematical modeling (Feng et al., 2002; Lam et al., 2000; Maximenko & Van Der Biest, 1998; Tsai, 1991; Tseng & Hsu, 1999).The magnitude of strain and stress developed during binder burnout depends on the nature and amount of binder. In the present case, the alumina powder-sucrose polymer composite foam bodies prepared at $W_{A/S}$ in the range of 0.6 to 1.2 contain 56 to 38 wt% of sucrose polymer. In addition to the shrinkage, a large volume of gases evolves due to thermal decomposition of the high amount of the sucrose

polymer present which creates internal pressure. Moreover, during the thermal decomposition of the sucrose polymer binder, the strength of the cell walls and struts of the foams decreases. It appears that, at a certain stage, the internal stresses developed become higher than the strength of the struts and cell walls. At this stage, cracks originate in the foam bodies. The cracks that originate during the sucrose polymer burnout are aggravated during sintering at higher temperatures as seen in **fig. 4.19**.

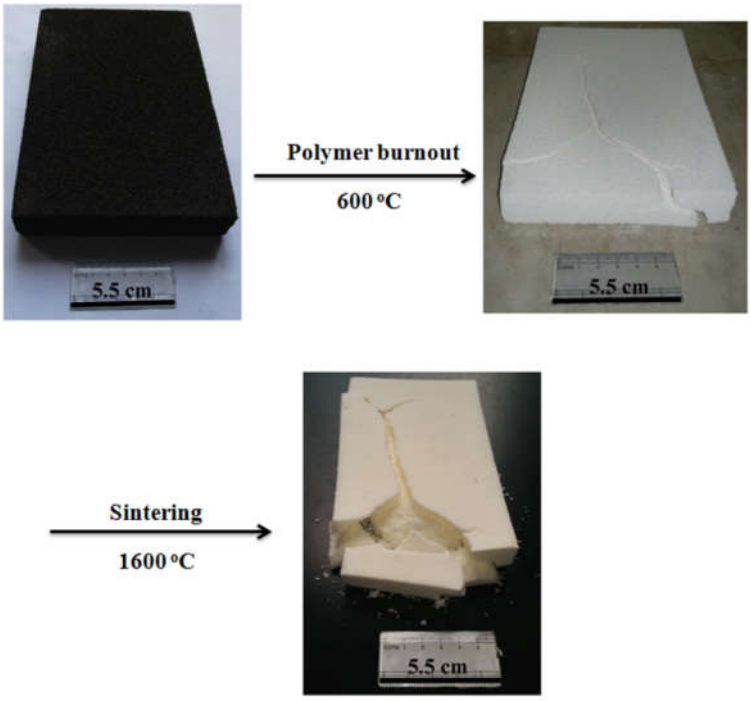

Fig 4.19 Photograph of large alumina foam body obtained by direct binder burnout and sintering showing severe cracks. ($W_{A/S}$ is 1).

The way to alleviate the problem is to retain a binder phase during the first stage of shrinkage. **Fig. 4.20** shows the TGA graph in air and nitrogen atmosphere of sucrose polymer-alumina powder composite foam at a $W_{A/S}$ of 0.6. The TGA in air atmosphere shows a weight loss of 56% at 525 °C corresponding to the complete

burnout of the sucrose polymer. However, the TGA in nitrogen atmosphere shows a weight loss of only 39.8 % up to 900 ^{o}C. The difference in weight loss in air and nitrogen atmosphere is because of the carbon retained due to the pyrolysis of the sucrose polymer. Calculations from the TGA results show that the sucrose polymer in the sucrose polymer-alumina powder composite foam retains 28.9 wt% of carbon during pyrolysis. This carbon produced from the sucrose polymer binds the alumina particles. That is, the heat treatment of sucrose polymer-alumina powder composite foams in inert atmosphere produces carbon bonded alumina foams.

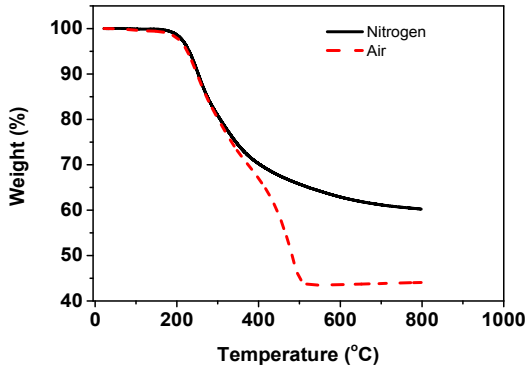

Fig 4.20 TGA graph of sucrose polymer–alumina powder composite foam sample heated in air and nitrogen atmosphere ($\mathbf{W}_{A/S}$ is 0.6)

The volume shrinkage during pyrolysis of sucrose polymer alumina composites foams is in the range of 49 to 32 %. The corresponding linear shrinkage observed is 20 to 13 %. Interestingly, the shrinkage during pyrolysis of sucrose polymer-alumina powder composite foam bodies are more or less the same as that observed during the sucrose polymer burnout. This indicates that the carbon produced by pyrolysis of sucrose polymer just fills the voids present in the alumina particle assembly. Gravimetric estimation shows the presence of 32 to 20 wt% carbon in

carbon bonded alumina foam bodies obtained by pyrolysis of sucrose polymer-alumina powder composite foams prepared at the $W_{A/S}$ in the range of 0.6 to 1.2. The corresponding volume percentage (calculated by considering the density of carbon and alumina as 2.26 and 3.98 g/cm^3, respectively) of carbon in the carbon bonded alumina foams are in the range of 46.13 to 30.6. The pyrolysis shrinkage and amount of carbon retained in the carbon bonded alumina foams are shown in **Fig. 4.21**. The large sucrose polymer-alumina powder composite foam bodies do not show any visible crack during the pyrolysis. This indicates that the carbon produced binds the alumina particles which provide adequate strength to cell walls and struts to resist the formation of crack due to the internal stresses produced during the pyrolysis.

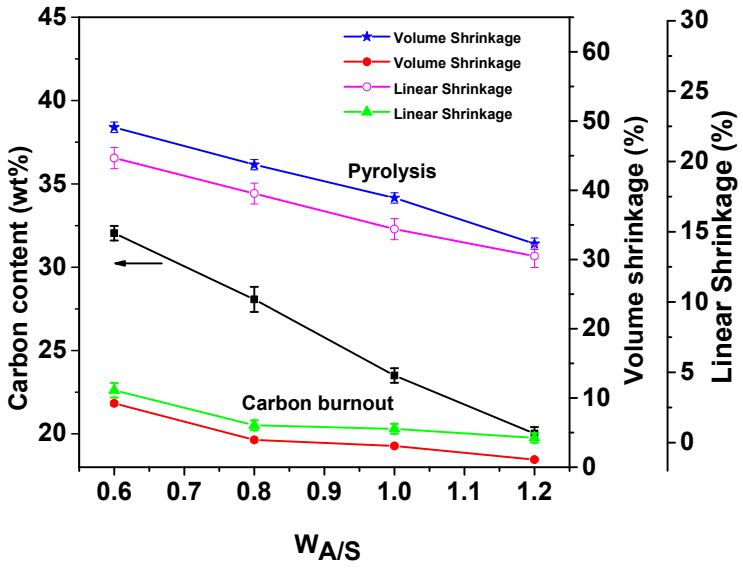

Fig 4.21 Pyrolysis shrinkage, shrinkage during carbon burnout and carbon content in the carbon bonded alumina foam as a function of $W_{A/S}$

Fig. 4.22 shows the TGA in air of a carbon bonded alumina foam sample at a $\mathbf{W_{A/S}}$ of 0.6. The sample shows a weight loss of only 2.5 % up to 400 ^{o}C. The burnout of the whole carbon present in the sample takes place at temperatures in the range of 400 to 600 ^{o}C. Therefore, a slow heating rate of 0.5 ^{o}C/minute was used from 400 to 600 ^{o}C for carbon burnout from large bodies. The carbon bonded alumina foam bodies prepared at a $\mathbf{W_{A/S}}$ of 0.6 show a relatively high shrinkage of 9.2 vol.% during the carbon burnout stage as seen in **fig. 4.21**. However, at higher $\mathbf{W_{A/S}}$, the shrinkage observed during carbon burnout is in the range of 3.9 to 1.1 vol.% (linear shrinkage in the range of 1.24 to 0.34 %). The carbon bonded alumina large foam bodies prepared at $\mathbf{W_{A/S}}$ in the range of 0.8 to 1.2 do not show any visible cracks during the carbon burnout stage as the internal stresses generated are relatively low due to the low linear strain of 1.24 to 0.34 %. However, cracks are sometimes observed during carbon burnout from carbon bonded alumina large foam bodies prepared at a $\mathbf{W_{A/S}}$ of 0.6 due to the development of internal stresses as a result of large shrinkage during the carbon burnout. Unlike the green alumina foams obtained after sucrose polymer burnout, the green alumina foams obtained after carbon burnout have very good stability against collapse while handling.

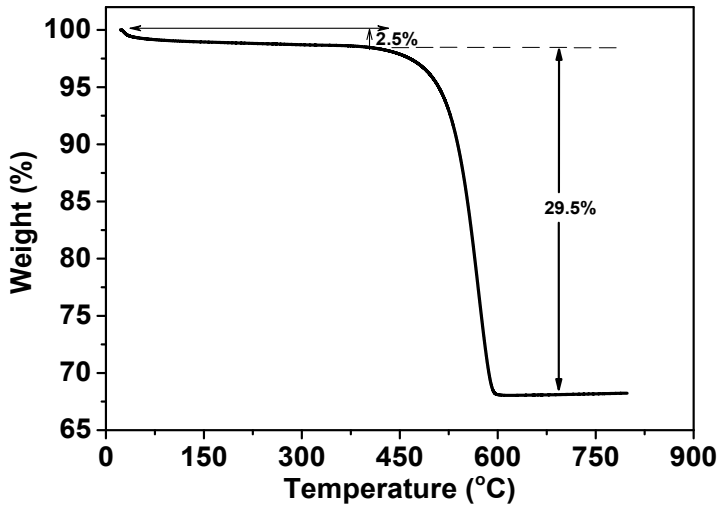

Fig 4.22 TGA of a carbon bonded alumina foam sample heated in air at 5 °C/min ($W_{A/S}$ is 0.6)

Microstructure changes during pyrolysis were studied by SEM. **Fig. 4.23 a & b** show SEM photomicrographs of a fractured strut region of sucrose polymer-alumina powder composite foam and carbon bonded alumina foam at a $W_{A/S}$ of 1. In the sucrose polymer-alumina powder composite foam, the alumina particles are embedded in a relatively thick sheath of the polymer matrix. On the other hand, in carbon bonded alumina foam, the alumina particles are bonded by a thin layer of carbon produced from the sucrose polymer. The shrinkage during the pyrolysis drags the alumina particles close to each other. It is also likely that the alumina particles undergo rearrangement to the more compact structure during polymer pyrolysis. This results in improved alumina particle packing. The improved alumina particle packing as a result of particle drag and rearrangement during polymer pyrolysis is clearly evidenced in the SEM photomicrograph of the alumina green foam obtained after carbon burnout from carbon bonded alumina foam. The SEM

photomicrographs of the fractured strut region of alumina green foams obtained after polymer burnout from sucrose polymer-alumina powder composite foam and carbon burnout from carbon bonded alumina foam are shown in **Fig. 4.23 c & d**. It is interesting to note that the alumina green foam obtained after sucrose polymer burnout from sucrose polymer-alumina powder composite foam shows loosely packed alumina particles (**fig.4.23c**). It appears that the alumina particles establish some weak bond with each other (may be the initiation of necking) during the pyrolysis at 900 ^{o}C. This is further evidenced by the fact that the large alumina green foam bodies obtained after carbon burnout from carbon bonded alumina foams have very good handling strength. In contrast, the alumina green foams obtained by sucrose polymer burnout from sucrose polymer-alumina powder composite foams are highly fragile to handle. It is interesting to note that the introduction of an additional pyrolysis step does not produce much variation in the final porosity of the sintered alumina foams. That is, the porosity remains in the same range of 94 to 93.3%. Large green alumina foams of 18 cm x 10 cm x 2.5 cm size after carbon burnout do not produce any visible crack during subsequent sintering. The photograph of large sucrose polymer-alumina powder composite foam, carbon bonded alumna foam obtained by pyrolysis, alumina green foam obtained by carbon burnout and sintered alumina foam are shown in **Fig. 4.24**.

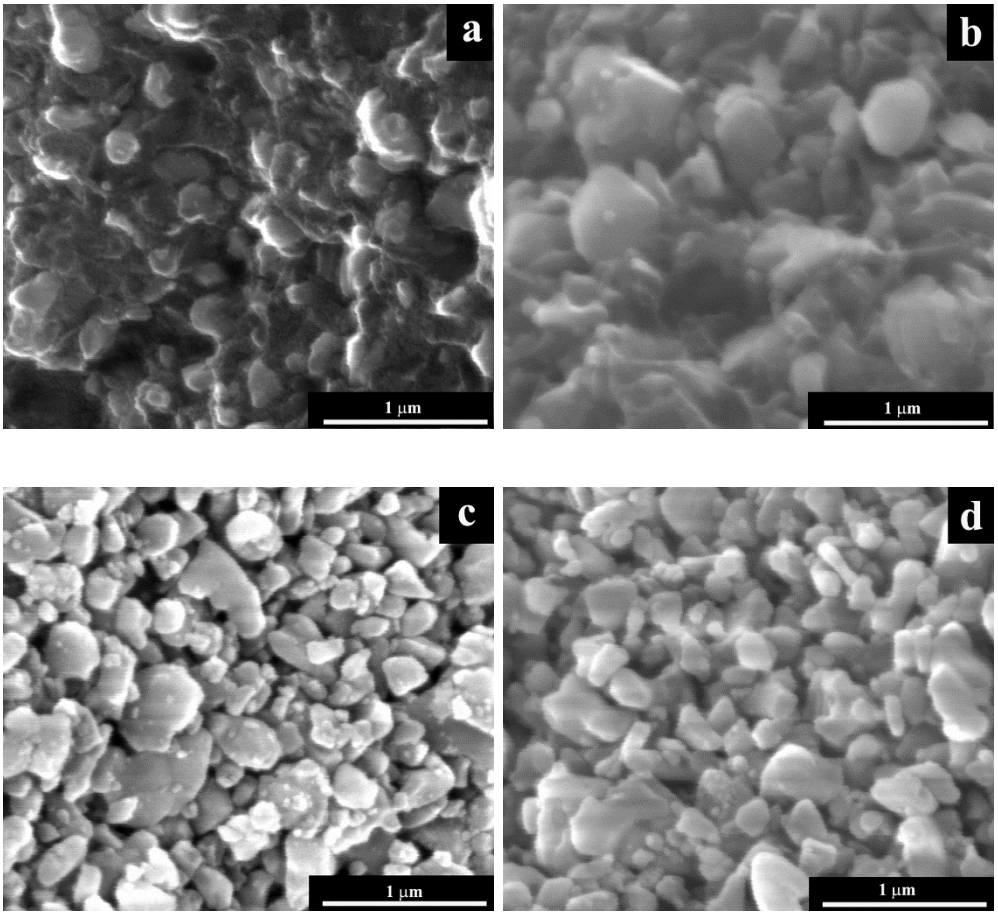

Fig 4.23 High magnification SEM photomicrograph of fractured strut region of (a) sucrose polymer–alumina powder composite foam, (b) carbon bonded-alumina foam, (c) green alumina foam after sucrose polymer burnout and (d) green alumina foam after carbon burnout prepared at $\mathbf{W_{A/S}}$ of 1.

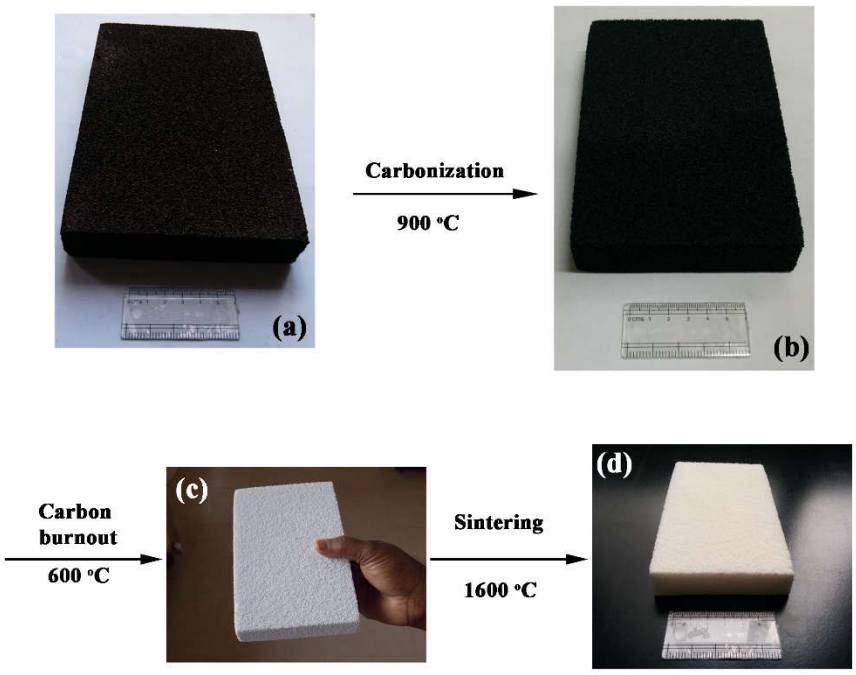

Fig 4.24 Photograph showing crack free large alumina foam body prepared by the two stage sintering ($W_{A/S}$ is 1).

4.3.3 Green machining

Green machining is an important aspect in ceramic processing as the machining of sintered bodies to produce ceramic components with required size and contour is very difficult (Butler et al., 1989; Filser et al., 2003; Nunn & Kirby, 1996; Su et al., 2008). Though the machining of dense green bodies obtained by gelcasting and powder pressing are widely studied, the green machining of ceramic foams is rarely reported (Dhara & Bhargava, 2003; Dhara & Su, 2005; K. Prabhakaran et al., 2001; Wu & McAnany, 1995). The requirements for green machining are (1) the green foam should have sufficient strength to hold in the conventional lathe, milling machine and drilling machine, (2) the machined surfaces should have very good finish and (3) the green machining should not induce any crack during the

subsequent sintering. **Fig. 4.25** shows the compressive strength and Young's modulus of sucrose polymer-alumina powder composite foams and carbon bonded alumina foams as a function of $\mathbf{W_{A/S}}$. The compressive strength and Young's modulus of sucrose polymer-alumina powder composite foams show marginal increase from 0.6 to 0.9 MPa and 16 to 40 MPa, respectively, when the $\mathbf{W_{A/S}}$ increases from 0.6 to 1.2. The particle packing in struts and cell walls of alumina powder–sucrose polymer composite foam bodies depends on the $\mathbf{W_{A/S}}$. At lower $\mathbf{W_{A/S}}$, the sucrose polymer forms a thick layer around the alumina particles which prevent the close packing of alumina particles. The thickness of the sucrose polymer layer decreases with an increase in $\mathbf{W_{A/S}}$ that leads to improved particle packing. The increase in compressive strength and Young's modulus with an increase in $\mathbf{W_{A/S}}$ despite a decrease in sucrose polymer content (from 56 to 38 wt%) is due to the increase in particle packing in the strut and cell walls of the foam. There is a considerable improvement in the compressive strength up on pyrolysis. Contrary to the sucrose polymer-alumina powder composite foams, the compressive strength of carbon bonded alumina foams decreases from 2.06 to 1.3 MPa when the $\mathbf{W_{A/S}}$ increases from 0.6 to 1.2. The corresponding decrease in Young's modulus is from 75.2 to 38.2 MPa. In general, the compressive strength and Young's modulus of a brittle foam decreases when the porosity and cell size increases and strut thickness decreases. In the present case, the compressive strength and Young's modulus depends also on the amount of carbon which binds the alumina particles. The bulk density of carbon bonded alumina foams decreases from 0.274 to 0.259 g/cm^3 when the $\mathbf{W_{A/S}}$ increases from 0.6 to 1.2. The porosity of the carbon bonded alumina foams calculated by considering the theoretical density of alumina (3.98 g/cm^3) and

graphite (2.26 g/cm^3) shows a marginal increase from 91.25 to 92.48 vol.%. However, an increase in cell size and strut thickness with an increase in $\mathbf{W_{A/S}}$ from 0.6 to 1.2 is observed. The decrease in compressive strength and Young's modulus with an increase in $\mathbf{W_{A/S}}$ can be attributed to the decrease in carbon content which bind the alumina particles, increase in porosity and increase in cell size.

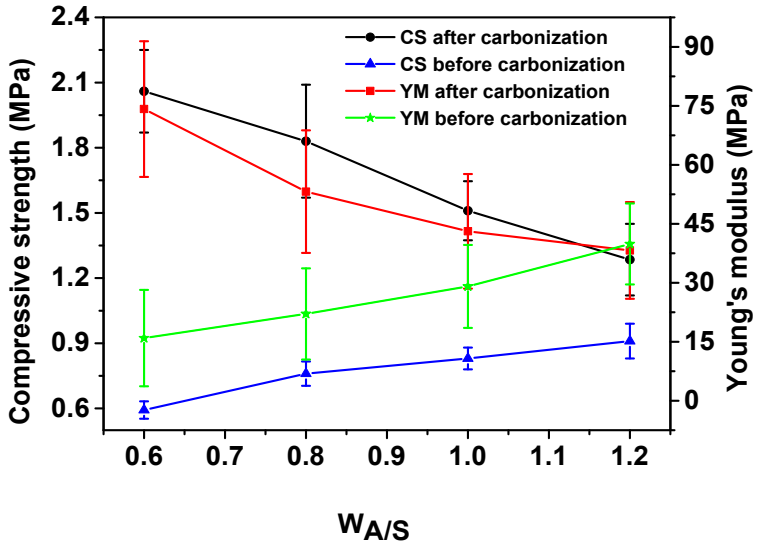

Fig 4.25 Compressive strength (CS) and Young's modulus (YM) of sucrose polymer-alumina powder composite foams and carbon bonded alumina foams as a function of $\mathbf{W_{A/S}}$.

The compressive strength of sucrose polymer alumina powder composite foams is sufficient for their easy handling and light machining with an emery paper. The possibility of light machining in green foam is reported in the literature (Dhara & Bhargava, 2003). However, the attempts to machine by holding them in a milling machine and a drilling machine result in severe damage to the foam bodies. On the other hand, the strength of the carbon bonded alumina foams is sufficiently high to hold them in a milling machine or drilling machine without any damage. A

photograph of a rectangular carbon bonded alumina foam body revealing slots made by milling using a conventional high speed steel tool is shown in **Fig. 4.26**. The green machined surface shows very good finish. Moreover, sharp edges and corners can be produced by the green machining of carbon bonded alumina foams. The green machined carbon bonded alumina foam bodies prepared at $\mathbf{W_{A/S}}$ in the range of 0.8 to 1.2 do not show any visible crack during the subsequent carbon burnout and sintering. **Fig. 4.27** shows the photograph of sintered alumina ceramic foams prepared by carbon burnout and sintering of the green machined carbon bonded alumina foams showing the slots made by milling and holes made by drilling.

Fig 4.26 Photograph showing slots made by milling on rectangular carbon bonded alumina foam body in a conventional milling machine using a high speed steel tool

Fig 4.27 Photograph of alumina foam bodies prepared by carbon burnout and sintering of green machined carbon bonded alumina foam bodies. The slots are made by milling and holes are made by drilling.

4.3.4 Effect of blowing agent

The alumina powder dispersions in molten sucrose takes undesirably long time for thermo-foaming and setting. Any additive which catalyzes the –OH condensation can act as blowing and setting agent for alumina powder dispersions in molten sucrose. We have used magnesium nitrate as a blowing and setting agent and studied the foaming characteristics of alumina powder dispersions at a $\mathbf{W_{A/S}}$ of 1 at two foaming temperatures of 130 and 140 ^{o}C. The effect of **MN** concentration on the foaming and setting time of the alumina powder dispersion in molten sucrose is shown in **fig. 4.28**. At both the studied foaming temperatures, the foaming time and setting time show a drastic decrease when the **MN** concentration increases from 0 to 4 wt%. The foaming time and setting time show a gradual decrease with a further increase in **MN** concentration to 16 wt%. For example, at 130 ^{o}C, the foaming time and setting time decreases from 9.5 and 44 hours to 2.5 and 11.3 hours, respectively,

when the **MN** concentration increases from 0 to 4 wt%. Further increase in **MN** concentration to 16 wt% decreases the foaming and setting time to 1.25 and 3.5 hours, respectively. The decrease in foaming and setting time observed at 140 ^{o}C is from 5.75 to 0.5 and 38.75 to 1.75 hours, respectively, when the **MN** concentration increases from 0 to 16 wt%.

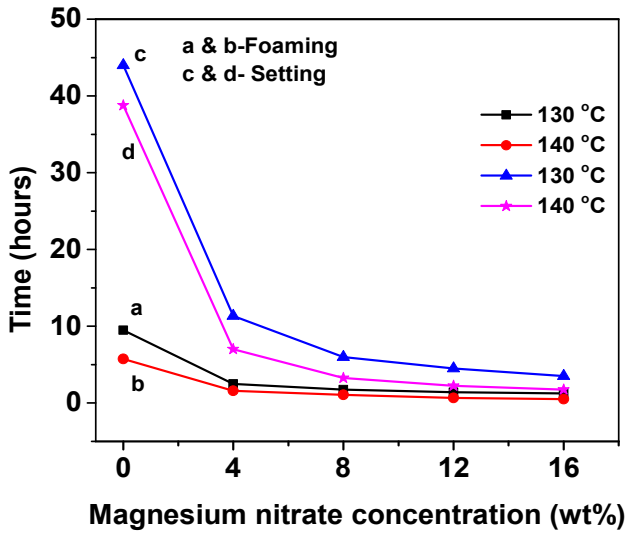

Fig 4.28 Effect of **MN** concentration and foaming temperature on the foaming and setting time of the alumina powder dispersion in molten sucrose

It is well known that H^{+} ions are very good catalyst for the –OH condensation (Finar, 2007). The **MN** undergoes hydrolysis to form magnesium hydroxide and nitric acid, as given in equation (8). The H^{+} produced by the ionization of the nitric acid catalyzes the –OH condensation. The water required to initiate the hydrolysis of **MN** is obtained either from the water of hydration of **MN** or from the initial slow –OH condensation which takes place in the absence of a catalyst. As the concentration of **MN** increases the amount of H^{+} produced in the system increases, which enhances the rate of –OH condensation. This in turn

increases the rate of formation of water vapour leading to a decrease in foaming time and an increase in the foam volume. The decrease in foam setting time with an increase in **MN** concentration shows that the **MN** acts as a foam setting agent. The faster setting of the thermo-foamed alumina powder dispersion is due to the faster polymerization and cross-linking through –OH condensation catalyzed by the H^+ generated by the hydrolysis of **MN**.

$$\mathbf{Mg(NO_3)_2 + 2H_2O \longrightarrow Mg(OH)_2 + 2H^+ + 2NO_3^-} \qquad \mathbf{(8)}$$

At both the studied foaming temperatures, the foam rise, a measure of foam volume increases with an increase in magnesium nitrate concentration up to 12 wt%. Further increase in **MN** concentration to 16 wt% does not produce any significant change in the foam rise. At 130 ^oC, the foam rise increases from 3.8 to 9 when the **MN** concentration increases from 0 to 16 wt%. The corresponding increase in foam rise at 140 ^oC is from 5.8 to 13. Attempts made to foam the alumina powder dispersions containing **MN** at 150 ^oC leads to much faster foaming and setting, however, results in foam collapse. The foam collapse is due to the rupture of bubbles before setting when the pressure inside the bubbles is greater than the strength of cell walls. At 150 ^oC, the rate of formation of water vapour inside the bubbles is so rapid that the pressure inside the bubbles exceeds the cell wall strength, leading to the bubble rupture and foam collapse. The effect of **MN** concentration on the foam rise is shown in **fig. 4.29**.

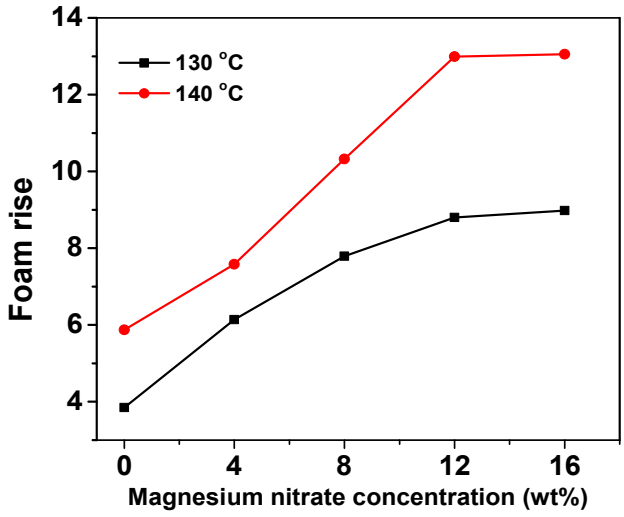

Fig 4.29 Effect of **MN** concentration on the foam rise

The addition of **MN** not only decreases the foaming and setting time but also makes the preparation of alumina powder dispersions in molten sucrose easier as the **MN** decreases the melting point of sucrose. It is well known that the addition of a solute (**MN**) decreases the melting point of a solvent (sucrose) (Atkins & De Paula, 2006; Berry et al., 2001). The decrease in melting point of sucrose by the addition of **MN** is evidenced from the DSC graph shown in **fig. 4.30**. The sucrose and **MN** show endothermic peaks corresponding to their melting at 180 and 89 ^{o}C, respectively. Up on the addition of **MN** the endothermic peak corresponding to the melting of sucrose shifted to a lower temperature of nearly 160 ^{o}C. That is, when heated at 185 ^{o}C, the sucrose in sucrose-alumina powder- **MN** mixtures melts and achieves a uniform dispersion much faster than the sucrose-alumina powder mixture.

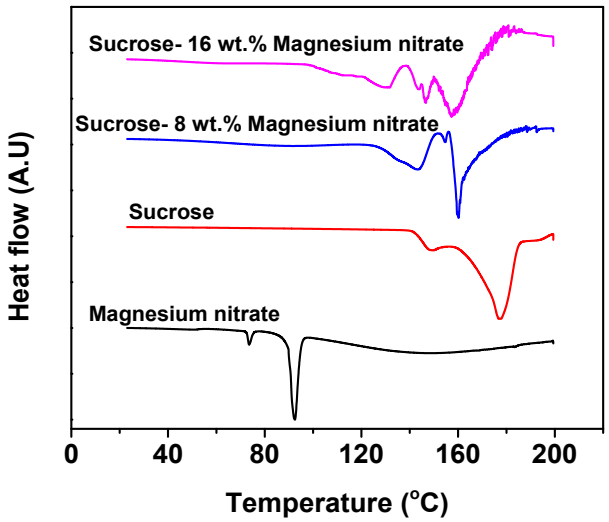

Fig 4.30 DSC plot showing a decrease in melting point of sucrose with the addition of **MN**

The increase in the rate of polymerization through –OH condensation, responsible for faster foaming and setting, with an increase in **MN** concentration is further evidenced from the torque-time measurements. **Fig. 4.31** shows the torque-time plots of alumina powder dispersions in molten sucrose containing various concentrations of the **MN** measured at 130 °C. The mixtures show slightly higher torque value during melting and mixing. After achieving uniform dispersion, the alumina dispersion in molten sucrose without **MN** show a low and steady torque of nearly 0.2 Nm up to 500 minutes. The low torque value even at 500 minutes is due to the sluggish polymerization in the absence of a catalyst and the same was also evidenced in the long foam setting time of 44 hours. On the other hand, the alumina powder dispersion containing **MN** does not show any considerable torque increase up to a certain time, followed by a slow increase and then a rapid increase. The time at which the rapid increase in torque observed, decreases with an increase in **MN**

concentration. The time at which the torque value reaches 100 Nm decreases from 300 to 190 minutes when the **MN** concentration increases from 4 to 16 wt%. The early increase in torque at higher **MN** concentration is due to the faster increase in molecular weight of sucrose polymer by accelerated –OH condensation because of H^+ generated by the hydrolysis of the **MN**.

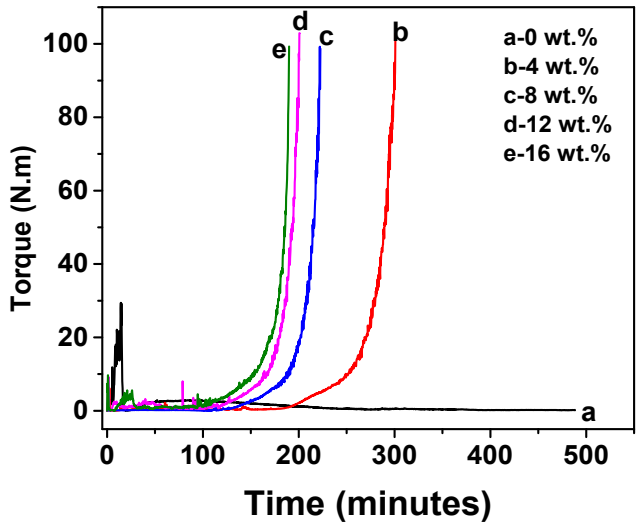

Fig 4.31 Torque-time plots of alumina powder dispersions in molten sucrose containing various concentrations of the **MN** measured at 130 ^oC.

The thermo-foamed bodies prepared at various **MN** concentrations do not show any crack or deformation during pyrolysis of the sucrose polymer and subsequent carbon burn out and sintering. The photograph of a large rectangular alumina foam body of size 18 cm x 15 cm x 3.5 cm prepared by thermo-foaming at a **MN** concentration of 8 wt.% is shown in **fig. 4.32**. The shrinkage of foam bodies observed during pyrolysis of sucrose polymer and total shrinkage (sum of shrinkage during pyrolysis and sintering) decreases with an increase in **MN** concentration. The foam bodies prepared at a foaming temperature of 130 ^oC and at the **MN**

concentrations in the range of 0 to 16 wt% shows shrinkage in the range of 39.2 to 32.4 vol.% during pyrolysis of the sucrose polymer. The corresponding shrinkage observed in the foam bodies prepared at a foaming temperature of 140 ^{o}C is in the range of 38.8 to 27.7 vol.%. The total shrinkage observed in the foam bodies prepared at foaming temperatures of 130 and 140 ^{o}C are in the ranges of 68.3 to 65.1 vol.% and 67.5 to 60.1 vol.%, respectively. The thermo-foaming of alumina powder dispersions without **MN** shows nearly same shrinkage for the foam bodies prepared at various foaming temperatures from powder dispersion of a particular $\mathbf{W_{A/S}}$ despite the fact that the foam volume increases with an increase in foaming temperature. That is, the shrinkage depends on the alumina powder packing in the thermo-foamed body and is independent of the cell size. In the present case, it appears that the magnesium ions interact with the sucrose polymer due to co-ordination with the -OH groups. These interactions are expected to bring the polymer molecules closer and thereby increase the density of the sucrose polymer. The interaction between the magnesium ions and –OH groups in sucrose polymer is evidenced from a slight shift in the absorption peak corresponding to –OH stretching vibrations. The sucrose polymer prepared without and with **MN** shows peaks corresponding to –OH stretching vibrations at 3407 and 3382 cm^{-1}, respectively as seen in **fig 4.33**. The decrease in sintering shrinkage with an increase in **MN** concentration is attributed to an increase in packing of alumina particles in the thermo-foamed body due to a decrease in volume (increase in density) of the polymer layer present in between the particles.

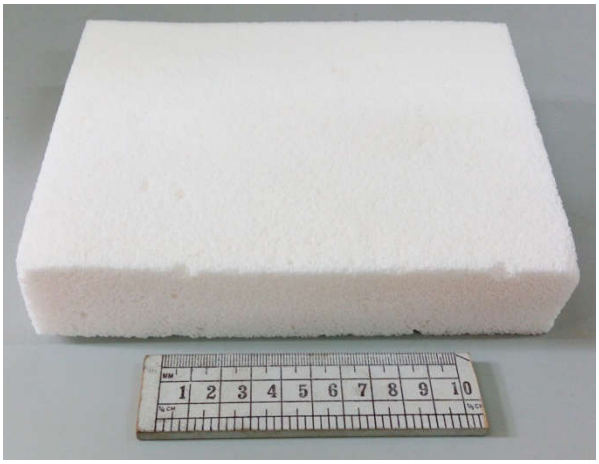

Fig 4.32 Photograph of a large alumina foam body fabricated by thermo-foaming of alumina powder dispersions in molten sucrose using **MN** blowing agent

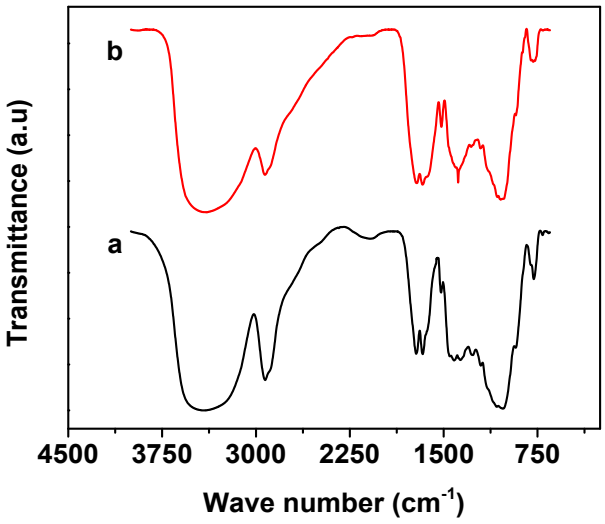

Fig 4.33 Infrared spectrum of sucrose polymer prepared (a) without and (b) with **MN** blowing agent

The effect of **MN** concentration and foaming temperature on porosity of alumina foam is shown in **fig. 4.34**. At the both studied foaming temperatures, the addition of **MN** blowing agent shows an initial rapid increase in porosity of the alumina foam. At a foaming temperature of 130 ^{o}C, the porosity increase from 87.3

to 92.7 vol.% when the **MN** concentration increases from 0 to 4 wt%. Further increase in **MN** concentration up to 16 wt% slowly increases the porosity to 93.8 vol.%. Similarly, at a foaming temperature of 140 ºC, the porosity increases from 90.7 to 95.6 vol.% when the **MN** concentration increases from 0 to 16 wt%. The increase in porosity with an increase in **MN** concentration and foaming temperature is in accordance with the observed foam rise and sintering shrinkage.

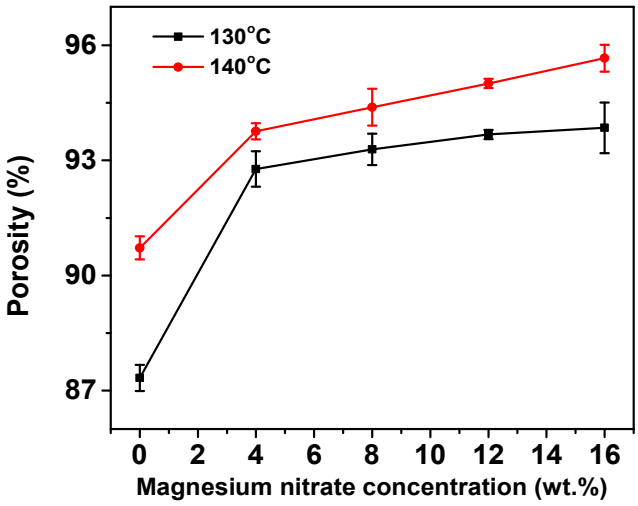

Fig 4.34 Effect of **MN** concentration and foaming temperature on porosity of alumina foams

The alumina foams prepared without **MN** blowing agent show cellular microstructure with nearly spherical cells, which are partially interconnected through circular openings. The foams prepared at a **MN** concentration of 4 wt% also show similar microstructure. However, a clear transition in the microstructure of the foam is observed, irrespective of the foaming temperature, when the **MN** concentration increases from 4 to 8 wt%. That is, the microstructure changes from partially interconnected cellular to completely open reticulate-like when the **MN**

concentration increases from 4 to 8 wt%. The foam microstructure remains similar at **MN** concentration in the range of 8 to 16 wt%. **Fig. 4.35** shows the SEM photomicrographs of alumina foams prepared at various **MN** concentrations. The **MN** used as a blowing agent produces 0.63 to 2.51 wt% of MgO in the alumina during burnout and sintering. The MgO is a well-known sintering additive used to suppress the grain growth of alumina ceramics (Bennison & Harmer, 1983). A decrease in average grain size of alumina foams from 2.14 to 1.16 μm is observed when the **MN** concentration increases from 0 to 16 wt%. The high magnification images of alumina foams prepared without **MN** and with 16 wt% **MN** blowing agent are shown in **Fig. 4.36**.

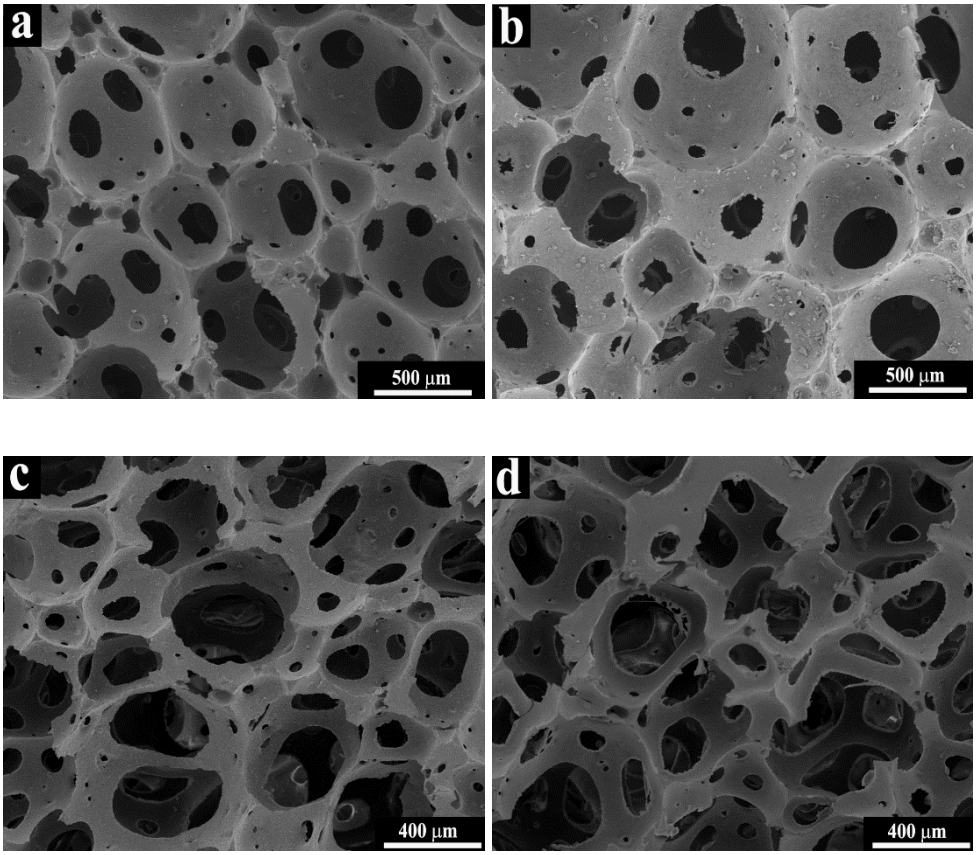

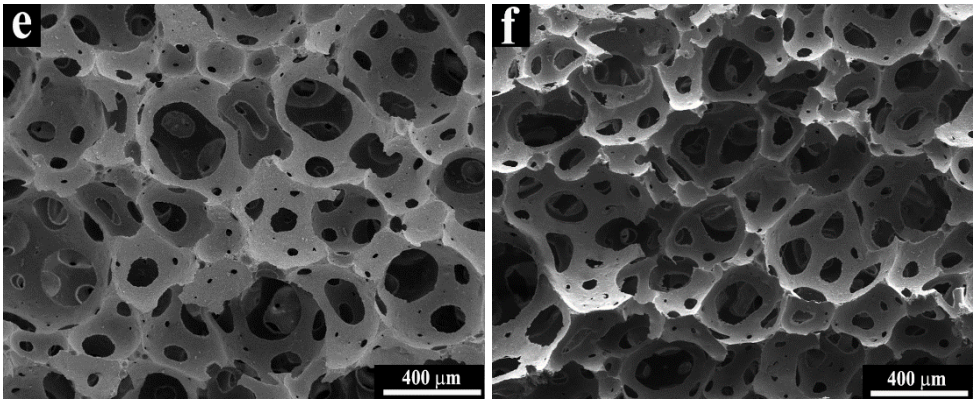

Fig 4.35 SEM photographs of alumina foams prepared at 0 wt% (a & b), 8 wt% (c & d) and 16 wt% (e & f) **MN** concentrations and at foaming temperatures 130 ^{o}C (a, c & e) and 140 ^{o}C (b, d, & f)

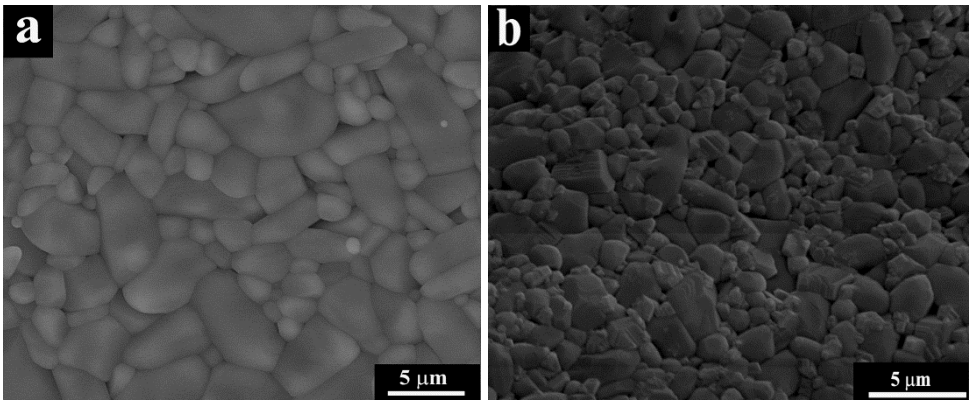

Fig 4.36 High magnification SEM photomicrographs showing grain structure of alumina foam prepared (a) without **MN** and (b) with 16 wt% **MN** concentration

Fig. 4.37 shows the effect of **MN** concentration on the average cell size of the alumina foams. The average cell size of the alumina foams decreases with an increase in **MN** concentration. At a foaming temperature of 130 ^{o}C, the average cell size decreases from 0.65 to 0.45 mm when the **MN** concentration increases from 0 to 16 wt.%. The corresponding decrease in average cell size observed at the foaming temperature of 140 ^{o}C is from 0.75 to 0.4 mm. In general, the cell size increases

with an increase in foaming temperature. However, in presence of the **MN**, the foams prepared at a foaming temperature of 140 ^{o}C shows lower cell sizes compared to that prepared at 130 ^{o}C. The cell size of foam depends on the nucleation and growth of bubbles in the powder dispersion. It appears that, the faster –OH condensation in the presence of **MN** and at higher foaming temperature results in a high concentration of water vapour in the dispersion which is responsible for the nucleation of a large number of bubbles. That is, the number of nucleated bubbles increases with an increase in **MN** concentration. These bubbles grow with the incorporation of water vapour produced due to the continued –OH condensation. As the number of bubbles nucleated in a given volume of the dispersion increases their growth decreases as the total volume of water vapour generated from a given amount of sucrose remains nearly constant. It is also well known that the viscous forces restrict the growth of bubbles in a medium. That is, faster increase in viscosity due to the increase in rate of –OH condensation with an increase in **MN** concentration and foaming temperature also restricts the bubble growth. The lower cell size observed at a higher foaming temperature (140 ^{o}C) in the presence of **MN** is due to the higher rate of bubble nucleation and restricted bubble growth due to higher concentration of water vapour and faster increase in viscosity, respectively, due to the higher rate of –OH condensation. The high standard deviation observed indicates relatively broad distribution of cell sizes in the foams. This shows that it is hard to control the cell sizes to a narrow range by the thermo-foaming process.

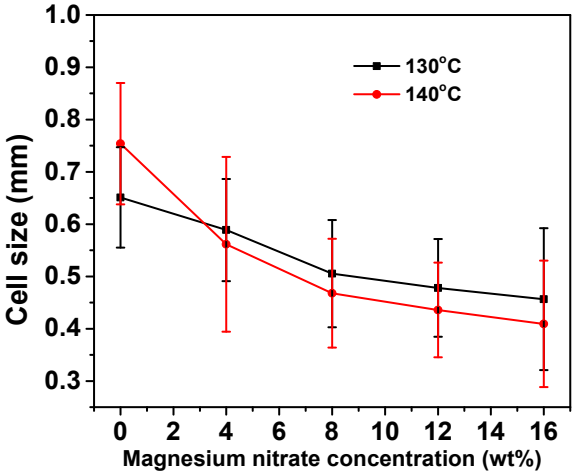

Fig 4.37 Effect of **MN** concentration and foaming temperature on the cell size of the alumina foams.

Fig. 4.38 shows the effect of **MN** concentration and foaming temperature on the compressive strength and Young's modulus of the alumina foams. The compressive strength of the alumina foams prepared at a foaming temperature of 130 ºC drastically decrease from 5.02 to 1.55 MPa when the **MN** concentration increases from 0 to 4 wt%. This is due to a drastic increase in porosity from 87.3 to 92.7 vol. %. Further increase in **MN** concentration to 16 wt% slowly increases the porosity to 93.8 vol.% and hence registers a slow decrease in compressive strength to 1.06 MPa. The alumina foam prepared at the foaming temperature of 140 ºC show a similar trend in compressive strength with an increase in **MN** concentration, but the values (3.26 to 0.38 MPa) are lower than that of alumina foams prepared at a foaming temperature of 130 ºC. The lower compressive strength is due to the higher porosity (90.7 to 95.6 vol.%) achieved by foaming at a higher temperature of 140 ºC. The Young' modulus shows the similar trend as compressive strength with an increase in **MN** concentration. The Young's modulus of alumina foams

prepared at the foaming temperatures of 130 and 140 °C decreases from 480 to 70 MPa and 252 to 2.25 MPa, respectively, when the **MN** concentration increases from 0 to 16 wt.%. The observed decrease in compressive strength and Young's modulus with an increase in **MN** concentration and foaming temperature, in spite of a decrease in cell size, are due to the increase in porosity and cell interconnectivity.

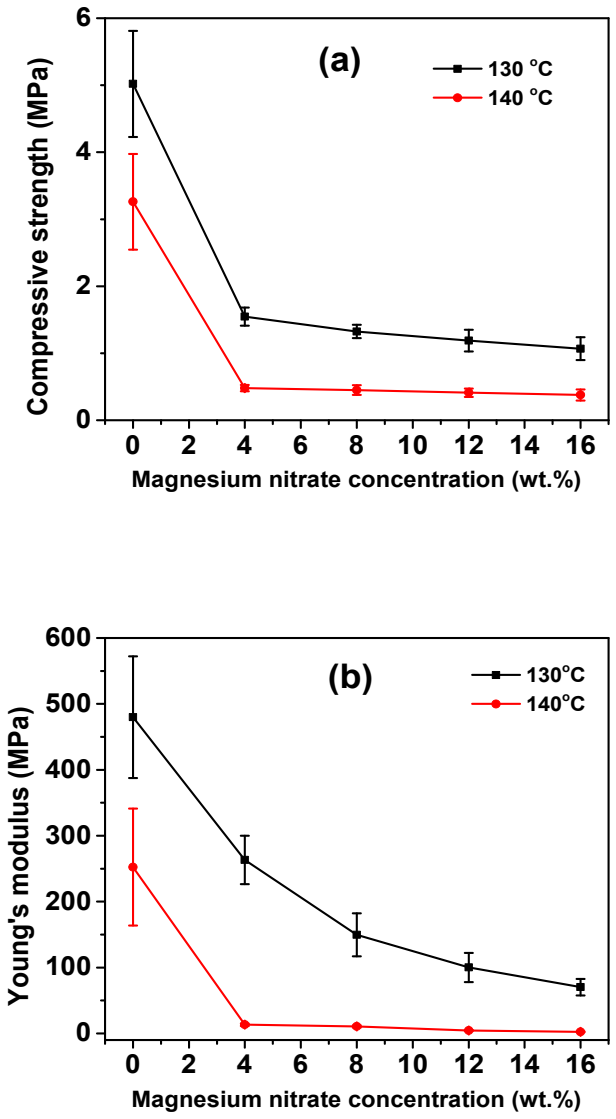

Fig 4.38 Effect of **MN** concentration and foaming temperature on the compressive strength and Young's modulus of alumina foams.

4.4 Conclusions

Open cellular alumina foams with porosity in the range of 83.4 to 94.6 vol.% have been prepared by the thermo-foaming of alumina powder dispersions in molten sucrose. The hydrophilic interactions between the alumina surface and sucrose hydroxyl groups promote the alumina powder dispersion in the molten sucrose. The bubbles produced in the alumina powder dispersions due to the water vapour generated by the –OH to –OH condensation are stabilized by the alumina particles adsorbed on the gas-liquid interface and the increase in viscosity. The foaming and foam setting time of alumina powder dispersions decrease with an increase in foaming temperature and an increase in $\mathbf{W_{A/S}}$. The foam volume increases considerably with an increases in foaming temperature, reaches a maximum at a critical foaming temperature and then decreases due to foam collapse. The critical foaming temperature decreases with an increase in the $\mathbf{W_{A/S}}$. A decrease in foaming and foam setting time and an increase in foam volume with an increase in foaming temperature are due to an increase in the rate of –OH condensation as well as a decrease in viscosity of the dispersion. The sintering shrinkage decreases largely with an increase in $\mathbf{W_{A/S}}$ and marginally with an increase in foaming temperature. Direct binder burnout followed by sintering of large precursor foam bodies produced by thermo-foaming of alumina powder dispersions in molten sucrose resulted in severe cracks. Pyrolysis of the sucrose polymer binder before sintering in air atmosphere prevents sintering crack in large foam bodies. The carbon produced from the sucrose polymer binds the alumina particles during the initial stage of shrinkage and increases the strength of cell walls and struts that resist cracking due to the internal stresses. The drag and

rearrangement of alumina particles during pyrolysis lead to solid contact between alumina particles as evidenced from microstructure analysis. The carbon bonded alumina foam bodies have relatively high compressive strength and are amenable to machining in the green state using conventional tools and equipments. The magnesium nitrate (**MN)** is used as a blowing and setting agent for the thermo-foaming of alumina powder dispersions in molten sucrose. The **MN** decreases the melting point of sucrose from 180 to 160 ^{o}C which makes the preparation of the powder dispersion easy. A remarkable decrease in foaming time (5.75 to 0.5 hours) and setting time (38.75 to 1.75 hours) and an increase in the foam rise (5.8 to 13) are observed with an increase in **MN** concentration from 0 to 16 wt.%. The porosity increases from 90.7 to 95.6 vol.% and cell size decreases from 0.75 to 0.4 mm with an increase in **MN** concentration from 0 to 16 wt%. A clear transition from partially interconnected cellular to completely interconnected reticulate-like foam structure occurs when the **MN** concentration increases from 4 to 8 wt%. The compressive strength and Young's modulus observed are comparable with that reported for alumina foams of similar porosities. The compressive strength and the Young's modulus of the alumina foams modeled according to the equations proposed by Gibson and Ashby show moderate to low correlation coefficient and large deviation in model constants such as C and n, especially at higher $\mathbf{W_{A/S}}$.

Chapter 5

Processing of mullite foams by thermo-foaming of alumina-silica co-dispersions in molten sucrose

5.1 Introduction

Mullite ($3Al_2O_3.2SiO_2$) foams are extensively used in the field of high temperature thermal insulation due to their low thermal conductivity, moderate thermal expansion coefficient, good chemical durability and excellent high temperature mechanical properties (Hildmann & Schneider, 2004; Schneider et al., 2008; Schneider & Eberhard, 1990; She & Ohji, 2003). These materials also find applications as catalyst support and filter for molten metal (Akpinar et al., 2012; Barea et al., 2005; Roncari et al., 2000; Tulliani et al., 1999). The mullite foams are prepared from a colloidal suspension of either mullite powder or its precursors such as alumina and kaolin (Bai, 2010; Chen et al., 2008; Liu et al., 2001). Processes based on polymer foam template (Akpinar et al., 2012; Roncari et al., 2000) and foaming and setting of powder suspensions are reported (Konegger et al., 2015; Kong et al., 2007; Liu et al., 2001) for the preparation of mullite foams. The mullite foams produced by most of the reported processes have relatively low porosity. In the present chapter, we study the preparation of low density mullite foams by thermo-foaming of alumina-silica powder dispersions in molten sucrose followed by reaction sintering. The effect of ceramic (alumina + silica) powder to sucrose weight ratio, foaming temperature and magnesium nitrate blowing agent on the foaming & setting characteristics of ceramic powder dispersions in molten sucrose and properties of resultant mullite foams is studied.

5.2 Experimental

5.2.1 Materials

The α-alumina (A16SG, ACC Alcoa, and Kolkata, India) and silica (Alfa-Aesar, USA) powders were of average particles size 0.34 and 2 μm, respectively. The surface area of the alumina and silica powders was 10.4 and 2 m^2/g, respectively. The SEM photomicrograph of the silica powder is shown in **Fig. 5.1.** The silica powder contains particles of near spherical shape. Analytical reagent grade sucrose, magnesium nitrate [$Mg(NO_3)_2.6\ H_2O$] and acetone were procured from Merck India Ltd. Mumbai.

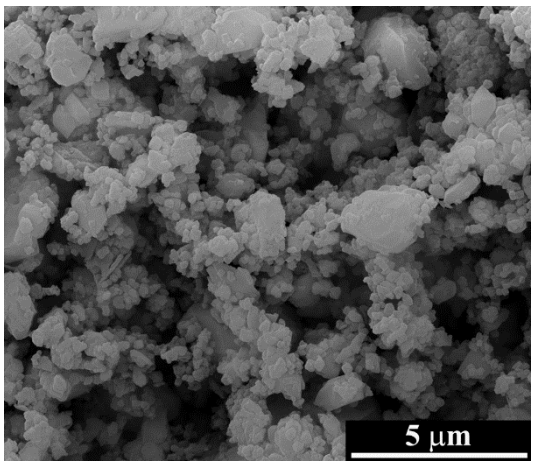

Fig 5.1 SEM photomicrograph of the silica powder

5.2.2 Preparation of mullite foams

The sucrose (200 g), alumina powder and silica powder were mixed by planetary ball milling in acetone medium for 2 hours at a speed of 200 RPM. The zirconia grinding jar of 500 cm^3 capacity and zirconia grinding media of 10 mm diameter were used. The sucrose to acetone and sucrose to zirconia ball weight ratios were 1:3 and 1:6, respectively. The ceramic (alumina + silica) powder to sucrose weight ratio was varied in the range of 0.8 to 1.8. The mole ratio of alumina and silica was

always maintained at 3:2 as in mullite. The slurry obtained after planetary ball milling was dried in a borosilicate glass tray at 70 ^{o}C. The sucrose-alumina-silica mixture thus obtained was heated in an air oven at 185 ^{o}C to melt the sucrose. The melt was stirred well with a glass rod to achieve uniform dispersion of alumina and silica particles in molten sucrose. The alumina-silica powder dispersion in molten sucrose was heated in an air oven at temperatures in the range of 120 to 170 ^{o}C for foaming and setting. The solid foam thus obtained was cut into rectangular bodies of 6 cm x 6 cm x 4 cm size and heated in an electrically heated furnace in air up to 1600 ^{o}C for removal of the organics and reaction sintering. The heating rate was 0.5^{o}C/ minute up to 600 ^{o}C and 2 ^{o}C/minute from 600 to 1600 ^{o} C. A holding time of 2 hours was given at 1500 ^{o}C and 1600 ^{o}C.

In order to study the effect of blowing agent, magnesium nitrate was added to the sucrose-alumina-silica mixture before the planetary ball milling. The amount of magnesium nitrate was in the range of 4 to 16 wt% of sucrose in the mixture.

5.2.3 Characterization

5.2.3.1 Determination of foaming characteristics

During foaming, the foam height was visually observed every 15 min. The time after which there is no further increase in the foam height was measured as the foaming time. After the completion of foaming, the foams were physically inspected at an interval of 1 h. The time required for the soft foam to get transformed into a hard one is determined as the foam setting time. The ratio of the initial height of the powder dispersion to the final height of the solid foam was taken as the foam rise.

5.2.3.2 Viscosity measurements

Viscosity measurements of the powder dispersion in molten sucrose were carried out at temperatures in the range of 120–150°C using a Rheometer (Anton Paar MCR 102, Austria). The plate and plate method was used for the viscosity measurements. The zero gap was 0.8 mm. The shear rate was in the range of 2–1000 s^{-1}.

5.2.3.3 XRD analysis

The XRD analysis of the mullite foams was carried out using an X-ray diffraction analyzer (X'pert Pro, Philips). The samples for XRD analysis were prepared by crushing the foams using a mortar and pestle.

5.2.3.4 Shrinkage and porosity

The sintering shrinkage was calculated from the initial and final dimensions of the foam bodies. The porosity of the foam bodies was calculated from the bulk density determined from their weights and dimensions.

5.2.3.5 Cell size

The average cell size of the mullite foams was measured on the magnified image of the foam bodies observed using a vision inspection system with a CCD color camera (Vision 300 GL; TESA Technologies, Switzerland). The reported values are average of 50 measurements.

5.2.3.6 Microstructure

The microstructure of the mullite foam bodies were observed on the fractured surfaces using a scanning electron microscope (SEM; FEI Quanta FEG200, Hillsboro, OR). The samples were sputter coated with gold before the SEM analysis.

5.2.3.7 Compressive strength

The compressive strength measurement of the mullite foams was carried out using a Universal Testing Machine (Instron 5984; Instron, Norwood, MA) at a crosshead speed of 0.5 mm/min using samples of 24 mm x 24 mm x 12 mm size (ASTM standard C365/C365M-05)

5.3. Results and Discussion

5.3.1 Dispersion of the ceramic powders in molten sucrose

A homogeneous dispersion of alumina and silica powders in molten sucrose is formed when the sucrose-alumina-silica mixtures heated in a borosilicate glass tray at 185 ^{o}C due to the hydrophilic interaction between sucrose hydroxyls with the alumina and silica particle surfaces. The dispersions, in general, show high viscosity with shear thinning flow behavior. The high viscosity is due to the strong intermolecular hydrogen bonding interaction between the sucrose hydroxyls. The viscosity and shear thinning behavior of the dispersions increases slowly with an increase in ceramic powder (alumina+ silica) to sucrose weight ratio up to 1.6. Further increase in ceramic powder to sucrose weight ratio to 1.8 rapidly increases the viscosity and shear thinning character. Hereafter ceramic powder to sucrose weight ratio is denoted as $\mathbf{W_{P/S}}$. **Fig. 5.2** shows viscosity versus shear rate plot of alumina-silica powder dispersions in molten sucrose measured at 140 ^{o}C. The increase in viscosity and shear thinning character with an increase in $\mathbf{W_{P/S}}$ is due to an increase in the particle to particle interaction. The remarkably high viscosity observed at $\mathbf{W_{P/S}}$ of 1.8 indicates the attainment of maximum powder loading limit.

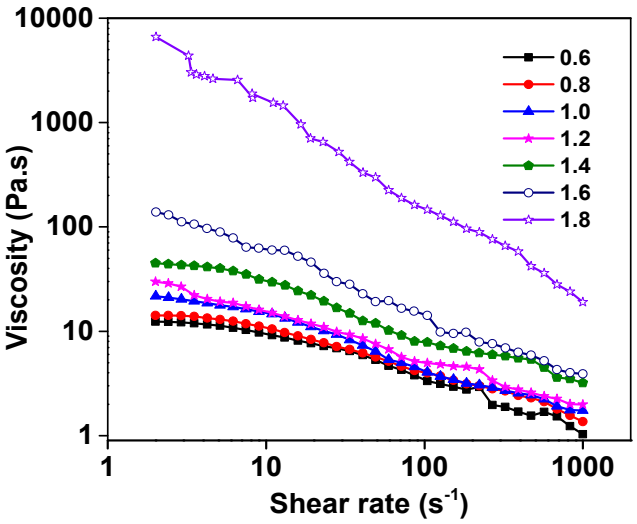

Fig.5.2 Effect of $W_{P/S}$ on the viscosity of ceramic powder dispersions in molten sucrose at 140 ^{o}C.

5.3.2 Foaming of the powder dispersions

The dispersions undergo slow foaming when heated in an air oven at 140 ^{o}C by the nucleation and growth of bubbles due to the water vapour generated as a result of –OH to –OH condensation. The foamed dispersions set into hard foam bodies due to the continued polymerization through –OH condensations. The foaming time, foam setting time and foam rise depend on the $W_{P/S}$. The foaming time decreases from 10.25 to 0.75 hours and total time for foaming and setting decreases from 59 to 16 hours when the $W_{P/S}$ increases from 0.6 to 1.8. On the other hand, the foam rise increases from 4.75 to 5.5 when the $W_{P/S}$ increases from 0.6 to 1.4 and thereafter shows a decreasing trend. The decrease in foaming time and foam setting time and an increase in foam rise with an increase in $W_{P/S}$ indicate that the ceramic particles catalyzes the –OH condensation. The ceramic particles also expected to stabilize the bubbles by adsorbing on the air-molten sucrose interface

(Binks & Horozov, 2005; Gonzenbach et al., 2007; Gonzenbach et al., 2007)**. Fig. 5.3** shows the effect of $W_{P/S}$ on the foaming time, foam setting time and foam rise of ceramic powder dispersions in molten sucrose at 140 ^{o}C. The decrease in foam rise after a $W_{P/S}$ of 1.4 is due to the partial foam collapse. The foam collapse at $W_{P/S}$ above 1.4 is attributed to the cell wall rupture due to lower strength because of the presence of particle agglomerates.

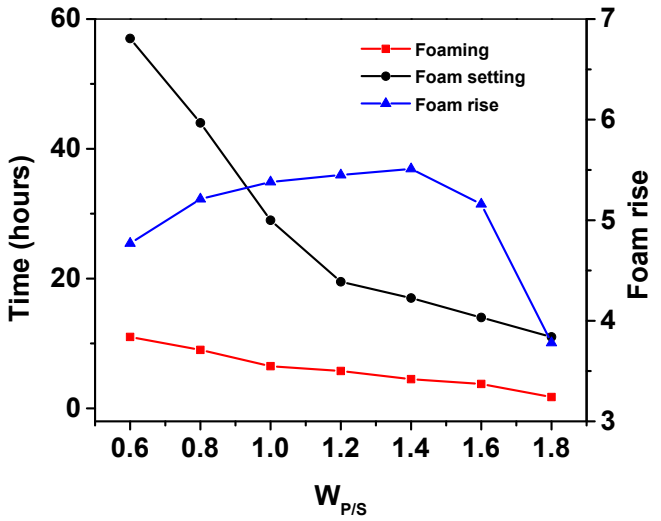

Fig. 5.3 Effect of $W_{P/S}$ on the foaming time, foam setting time and foam rise of ceramic powder dispersions in molten sucrose at a foaming temperature of 140 ^{o}C

5.3.3 Mullite formation by reaction sintering

The XRD spectra of the foams sintered at various temperatures is shown in **Fig.5.4**. The reaction of alumina and silica to form mullite is initiated at a temperature of 1500 ^{o}C. This is evidenced by the appearance of peaks corresponding to the (210), (220), (121) and (420) planes of mullite along with the characteristic peaks of alumina and silica in the XRD spectrum. On the other hand, the foams sintered at 1600 ^{o}C shows no reflection corresponding to alumina and

silica, but all peaks corresponding to mullite phase. This suggests the formation of pure mullite phase from the alumina and silica at 1600 ^{o}C.

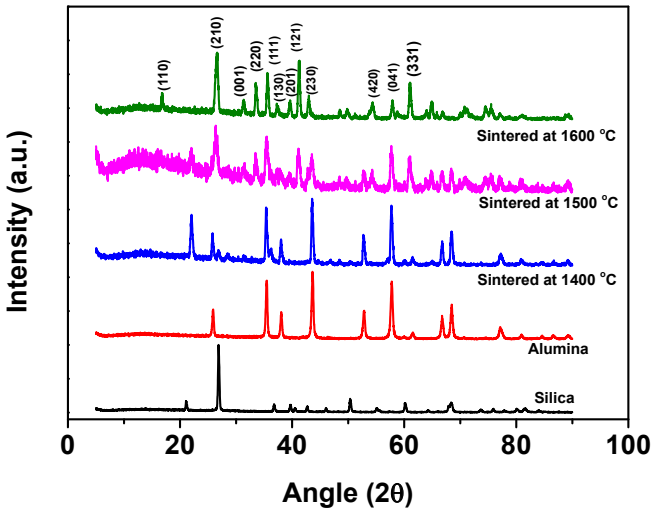

Fig. 5.4 XRD spectra showing the effect of sintering temperature on mullite phase formation

5.3.4 Shrinkage, porosity and compressive strength

The volume shrinkage during sintering, porosity, cell size, compressive strength and Young's modulus of the mullite foams prepared at various $\mathbf{W_{P/S}}$ is given in **Table 5.1**. The sucrose polymer-ceramic powder composite foam bodies undergo relatively large shrinkage during sintering. The volume shrinkage during sintering decreases with an increase in the $\mathbf{W_{P/S}}$. The volume shrinkage shows a gradual decrease from 51 to 33 % on an increase of $\mathbf{W_{P/S}}$ from 0.6 to 1.4. On further increase of $\mathbf{W_{P/S}}$ to 1.6 and 1.8, the shrinkage values decrease rapidly to 22.8 and 19 vol.%, respectively. The average cell size of mullite foam increases from 0.73 to 2.31 mm when the $\mathbf{W_{P/S}}$ increases from 0.6 to 1.8. The increase in cell size with an increase in $\mathbf{W_{P/S}}$ is because of an enhanced bubble growth due to an increase in

the rate of –OH condensation as well as the increase in bubble stability. The increase in bubble stability is due to the adsorption of ceramic particles on the molten sucrose-air interface and an increase in viscosity with an increase in $\mathbf{W_{P/S}}$. The mullite foams prepared at $\mathbf{W_{P/S}}$ in the range of 0.6 to 1.4 show porosity in a close range of 93.75 to 93.45 vol.%. Within this narrow range, a regular trend in porosity with $W_{P/S}$ is not observed. The mullite foams prepared at $\mathbf{W_{P/S}}$ of 1.6 and 1.8 show slightly lower porosity of 93.07 and 92.69 vol.%, respectively, due to partial foam collapse. The narrow range of observed porosity in spite of an increase in foam rise and a decrease in sintering shrinkage with an increase in $\mathbf{W_{P/S}}$ indicates an increase in thickness of cell walls and struts with $\mathbf{W_{P/S}}$. The strut thickness measured from SEM images using ImageJ software increases from 81 to 222 μm when the $\mathbf{W_{P/S}}$ increases from 0.6 to 1.8.

The compressive strength of macroporous brittle solids depends on the porosity, pore size, pore interconnectivity and thickness of the cell wall and strut (Ashby & Medalist, 1983; Gibson & Ashby, 1997; Oliveira et al., 2006). The compressive strength decreases with an increase in cell size and porosity. The compressive strength increases from 0.91 to 1.15 MPa on increasing $\mathbf{W_{P/S}}$ from 0.6 to 0.8. On further increase of $\mathbf{W_{P/S}}$ from 1.0 to 1.8, the compressive strength values decrease from 0.86 to 0.49 MPa. Although all the prepared mullite foams show porous struts and similar porosity, there is a drastic decrease in compressive strength at $\mathbf{W_{P/S}}$ above 0.8. One of the reasons for the decrease in compressive strength with an increase of $\mathbf{W_{P/S}}$ is the increase in cell size. Another reason may be the agglomeration of alumina and silica particles in molten sucrose medium at $\mathbf{W_{P/S}}$ higher than 0.8. The Young's modulus values show a trend similar to that of

compressive strength. The Young's modulus increases from 272 to 492 MPa when the $W_{P/S}$ increases from 0.6 to 0.8. On further increase of $W_{P/S}$ to 1.8, decrease the Young's modulus to 85 MPa.

Table 5.1 Effect of $W_{P/S}$ on the volume shrinkage, porosity, cell size, compressive strength and Young's modulus of the mullite foams

$W_{P/S}$	Volume shrinkage (vol. %)	Porosity (vol. %)	Cell size (mm)	Compressive strength (MPa)	Young's modulus (MPa)
0.6	50.9	93.73	0.73 ± 0.18	0.91 ± 0.1	272 ± 25
0.8	44.5	93.46	0.78 ± 0.28	1.15 ± 0.2	492 ± 36
1.0	39.2	93.74	0.84 ± 0.3	0.86 ± 0.1	196 ± 21
1.2	35.4	93.45	0.93 ± 0.32	0.82 ± 0.09	175 ± 19
1.4	32.8	93.75	1.29 ± 0.35	0.59 ± 0.1	108 ± 15
1.6	23	93.07	1.58 ± 0.4	0.49 ± 0.08	85 ± 12
1.8	19	92.69	2.31 ± 0.5	-	-

5.3.5 Microstructure of the mullite foams

The SEM photomicrograph of the sintered mullite foams prepared at various $W_{P/S}$ is shown in **Fig. 5.5**. The mullite foams show interconnected cellular structure irrespective of the $W_{P/S}$. The foams show near spherical cells up to a $W_{P/S}$ of 1.4. Further increase in $W_{P/S}$ results in a change of cell morphology from near-spherical to oval due to the partial foam collapse. The high magnification SEM images of the strut region and cell walls of the mullite foams are shown in **Fig. 5.6**. The needle-shaped grains on the cell walls and struts confirm the formation of mullite (Liu et

al., 2001; Wang et al., 2016). However, the mullite foams prepared at all the studied $W_{P/S}$ show porous struts and cell walls showing improper densification.

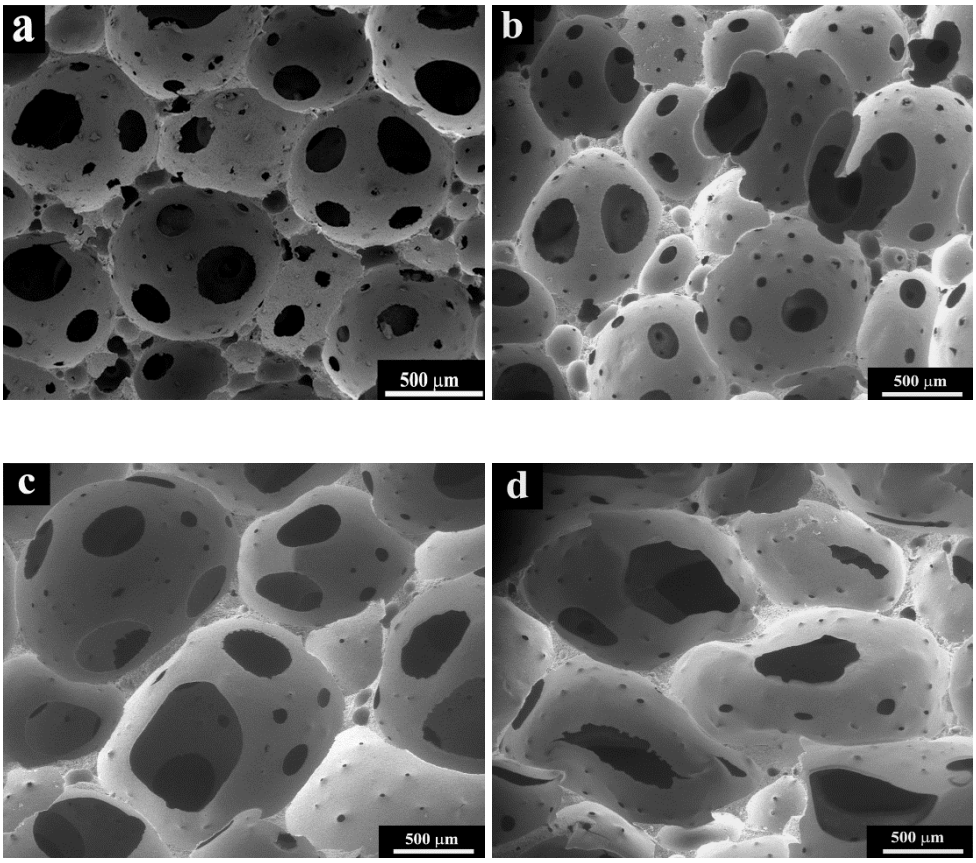

Fig.5.5 SEM photomicrograph of mullite foams prepared at $W_{P/S}$ of (a) 0.8, (b) 1.2, (c) 1.6 and (d) 1.8

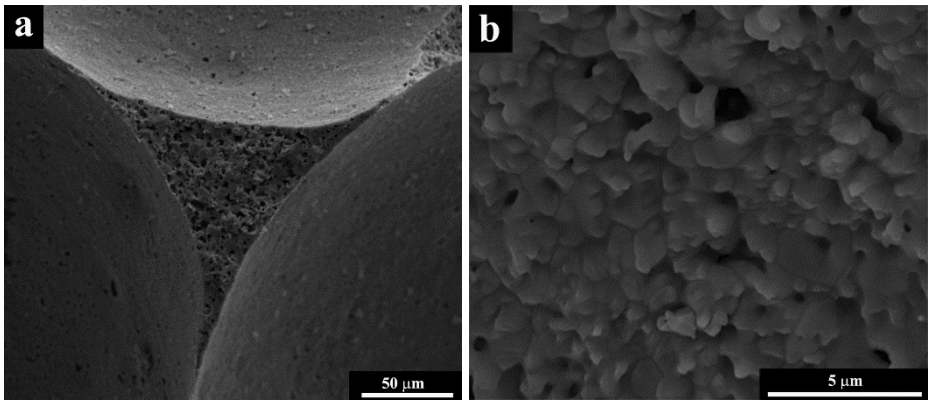

Fig. 5.6 SEM photomicrograph of (a) strut and (b) cell wall of the mullite foams

5.3.6 Effect of foaming temperature

The foaming characteristics of ceramic powder dispersion in molten sucrose depend not only on the $W_{P/S}$ but also on the foaming temperature. As particle agglomeration leading to decrease in strength and Young's modulus is observed at $W_{P/S}$ beyond 0.8, the powder dispersion prepared at $W_{P/S}$ of 0.8 is used to study the effect of foaming temperature. The thermo-foaming is studied at temperatures in the range of 120 to 170 ^{o}C. The effect of foaming temperature on the foaming time, setting time and foam rise of alumina-silica powder dispersions in molten sucrose prepared at a $W_{P/S}$ of 0.8 is shown in **Fig. 5.7.** The foaming time decreases from 21 to 0.75 h and foam setting time decrease 112 to 9 h when the foaming temperature increases from 120 to 170 ^{o}C. The foam rise increases from 3.41 to 8.85 when the foaming temperature increases from 120 to 160 ^{o}C. The further increase in the foaming temperature to 170 ^{o}C results in a decrease of foam rise to 6.42 due to partial foam collapse. The decrease in foaming and foam setting time and an increase in foam rise with an increase in foaming temperature are due to an increase in the rate of –OH condensation with an increase in foaming temperature. The partial foam collapse observed at foaming temperatures above 160 ^{o}C is due to rupture of the formed bubbles when the pressure inside the bubbles exceeds the strength of cell walls.

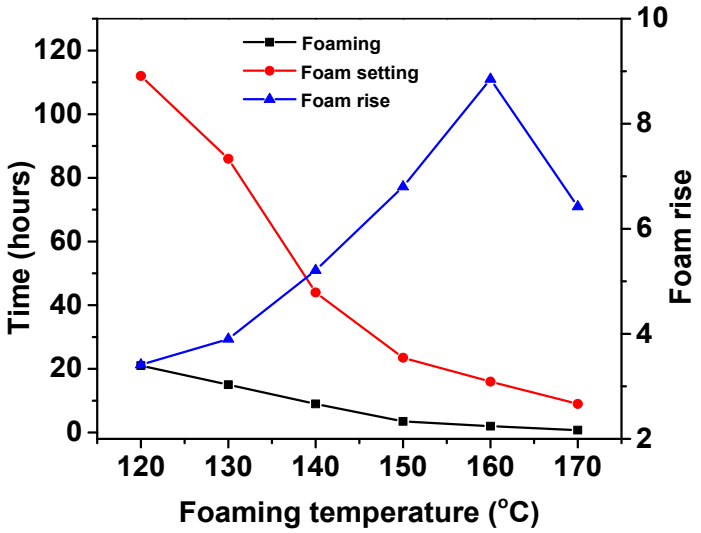

Fig.5.7 Effect of foaming temperature on the foaming time, foam setting time and foam rise of powder dispersions prepared at $W_{P/S}$ 0.8

The effect of foaming temperature on the sintering shrinkage, porosity, cell size, compressive strength and Young's modulus of the mullite foams prepared at $W_{P/S}$ of 0.8 is shown in **Table 5.2**. The foams prepared at foaming temperatures in the range of 120 to 170 °C shows approximately the same sintering shrinkage (44.76 to 44.43 vol.%) even though the foam rise increases remarkably with foaming temperature. This shows that sintering shrinkage is independent of the initial foam volume and depends only on the $W_{P/S}$. The mullite foams prepared at all the studied foaming temperatures shows an interconnected cellular structure with near spherical cells. The cell size increases from 0.63 to 1.02 mm when the foaming temperature increases from 120 to 160 °C. The increase in cell size with an increase in the foaming temperature is because of an enhanced bubble growth due to an increase in the rate of –OH condensation. The standard deviation observed in cell size data increases with an increase in foaming temperature. That is, the foams

prepared at lower foaming temperatures have more uniform cells compared to that prepared at higher foaming temperatures. The porosity of the mullite foams increases from 92.7 to 94.92 vol.% when the foaming temperature increases from 120 to 160 ^{o}C. The increase in porosity is due to the increase in cell size with an increase in foaming temperature. The compressive strength and Young's modulus of mullite foams decrease from 1.46 to 0.58 MPa and 722 to 120 MPa, respectively, when the foaming temperature increases from 120 to 160 ^{o}C. The decrease in compressive strength and Young's modulus with an increase in foaming temperature is due to an increase in the porosity and cell size of the mullite foams. It is worthy to note that, the compressive strength of 1.34 MPa achieved at a foaming temperature of 130 ^{o}C is more than four times higher than that of mullite foam of similar porosity prepared by direct foaming of alumina/aluminium filled phenylmethylpoly(silsesquioxane) (Konegger et al., 2015).

Table 5.2 Effect of foaming temperature on the total shrinkage, porosity, cell size, compressive strength and Young's modulus of mullite foams prepared at $\mathbf{W_{P/S}}$ 0.8

Foaming temperature ^{o}C	Total shrinkage (vol. %)	Porosity (vol. %)	Cell size (mm)	Compressive strength (MPa)	Young's modulus (MPa)
120	44.64	92.71	0.63 ± 0.12	1.46 ± 0.3	722 ± 58
130	44.76	93.60	0.70 ± 0.08	1.34 ± 0.26	615 ± 47
140	44.57	93.74	0.78 ± 0.28	1.15 ± 0.2	492 ± 48
150	44.43	94.92	0.93 ± 0.26	0.62 ± 0.18	284 ± 36
160	44.53	94.78	1.02 ± 0.32	0.58 ± 0.17	120 ± 26

5.3.7 Effect of MN blowing agent

Porous struts due to improper densification and large cell size are the factors limiting the compressive strength of the prepared mullite foams. Though lower foaming temperature gave foams with smaller and uniform cells, the foaming and setting of the powder dispersion took a long time (84 hours at 130 ^{o}C). Generally, blowing agents decrease the foaming time and setting agents speed up the foam setting by accelerating the polymerization. The blowing agents not only reduce the foaming time but also alter the cell size by altering the bubble nucleation and growth rates (Aram & Mehdipour-Ataei, 2016; Klempner & Frisch, 1991). **MN** is used as a blowing and setting agent for the preparation of alumina foams from powder dispersion in molten sucrose. In this, the H^{+} ions generated from the nitric acid produced by the hydrolysis of magnesium nitrate (Equation 8) catalyzes the –OH to –OH condensation and thereby accelerate the foaming and setting of the powder dispersions in molten sucrose. The magnesium oxide produced from the **MN** is expected to act as a sintering aid for mullite that results in foams with dense struts (Dong et al., 2011; Laura Montanaro et al., 2000).

$$\mathbf{Mg(NO_3)_2 + 2H_2O \longrightarrow Mg(OH)_2 + 2H^{+} + 2NO_3^{-}} \qquad \mathbf{(8)}$$

The effect of **MN** concentration on the foaming time, setting time and foam rise of ceramic powder dispersion at a $\mathbf{W_{P/S}}$ of 0.8 is shown in **Fig. 5.8**. The incorporation of **MN** drastically decreases the foaming time and foam setting time of the ceramic powder dispersion in molten sucrose. The foaming time and foam setting time decrease from 15 to 3.25 h and 86 to 12 h, respectively, when the **MN** concentration increases from 0 to 4 wt%. Further increase in **MN** concentration

results in a gradual decrease in foaming and foam setting time. On increasing the **MN** concentration to 16 wt% the foaming and setting time decrease to 1.75 and 4.75 hours, respectively. The incorporation of **MN** not only decreases the foaming and foam setting time but also increases the foam rise. The foam rise increases from 3.9 to 10.38 when the **MN** concentration increases from 0 to 16 wt%. The decrease in foaming time and foam setting time and an increase in foam volume with an increase in **MN** concentration are due to the enhancement in the rate of –OH condensation.

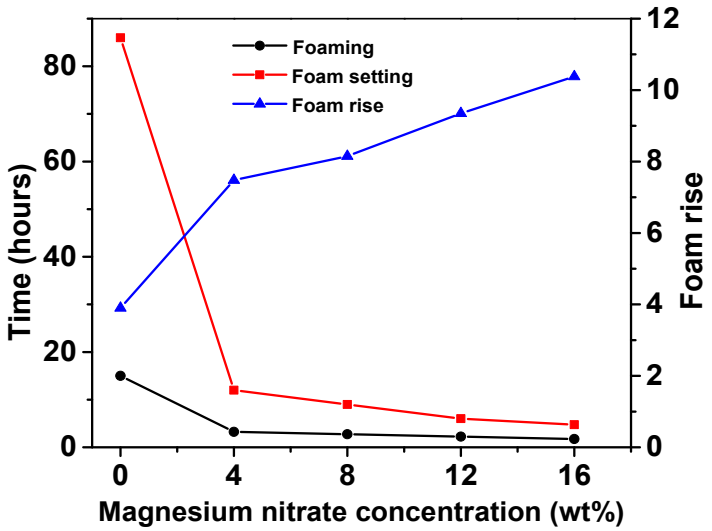

Fig 5.8 Effect of **MN** concentration on the foaming time, foam setting time and foam rise

Fig. 5.9 shows SEM photomicrographs of mullite foams prepared at various **MN** concentrations. The **MN** concentration has a remarkable effect on the foam microstructure. The mullite foam obtained at a **MN** concentration of 4 wt% shows microstructure similar to the one prepared without blowing agent **(Fig. 5.5a).** A further increase in the **MN** concentration results in an increase in cell

interconnectivity. The interconnectivity of the cells reached to the level of reticulated foams when the **MN** concentration reaches to 12 wt%. The thinning of the cell walls and struts with an increase in **MN** concentration is clearly visible in the microstructure. The strut thickness measured from SEM images using ImageJ software decreases from 96 to 23 μm when the **MN** concentration increases from 0 to 16 wt%. The mullite foams prepared at 4 and 8 wt% **MN** concentrations show porous struts as those prepared without **MN**. However, the mullite foams prepared at 12 and 16 wt% **MN** concentrations show dense struts. The MgO is a commonly used sintering additive for mullite (Dong et al., 2011; Montanaro et al., 1997; Montanaro et al., 2000). The effect on densification is more pronounced at MgO concentrations in the range of 2 to 4 wt% of mullite. The enhanced densification in presence of MgO is due to the formation of a liquid phase (Al_2O_3-SiO_2-MgO) which facilitates faster diffusion (Dong et al., 2011). At 4 and 8 wt% **MN** concentrations, the amount of MgO produced is 0.9 and 1.8 wt% of mullite, respectively. On the other hand, at 12 and 16 wt% **MN** concentrations, the amount of MgO produced is 2.7 and 3.6 wt% of mullite, respectively. That is, the MgO produced at 12 and 16 wt% **MN** concentrations is sufficient for mullite densification. The enhanced densification is evidenced from high magnification SEM images of struts and cell walls showing their nonporous nature. **Fig. 5.10** shows the SEM images of the struts of mullite foams prepared at 8 and 12 wt% **MN** concentration. The transformation from porous to dense struts with an increase in **MN** concentration from 8 to 12 wt% is clearly evidenced from the microstructures.

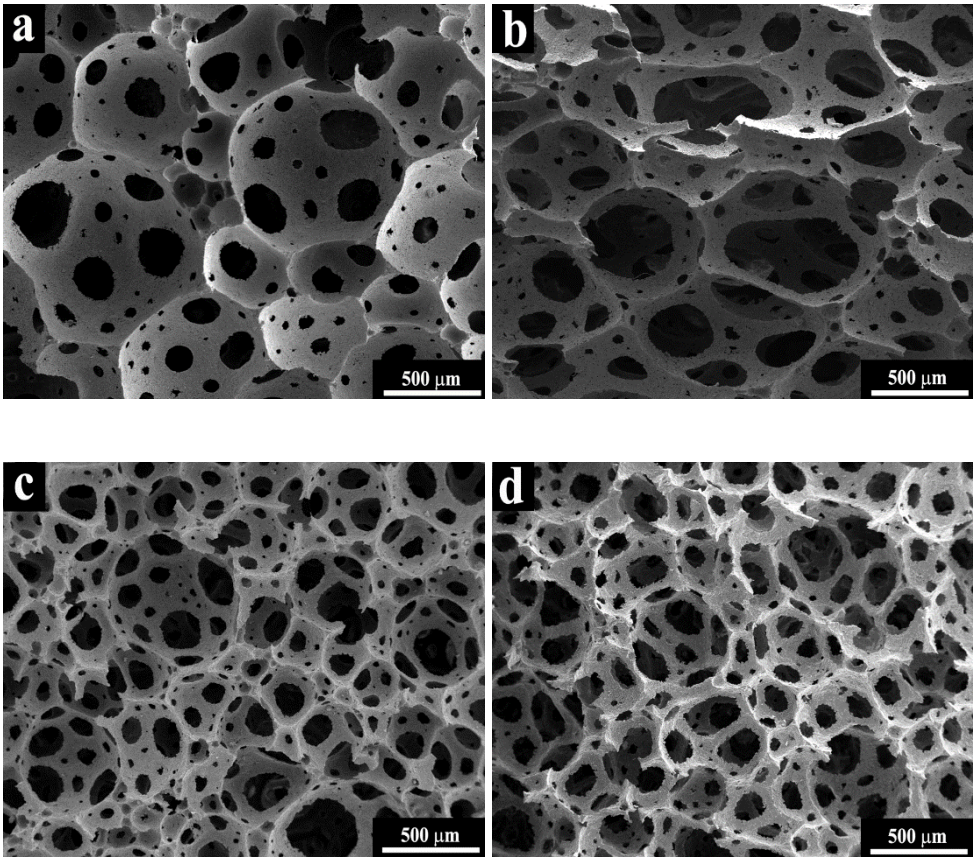

Fig. 5.9 SEM photomicrographs of mullite foams prepared at (a) 4 wt%, (b) 8 wt%, (c) 12 wt% and (d) 16 wt% **MN** concentration

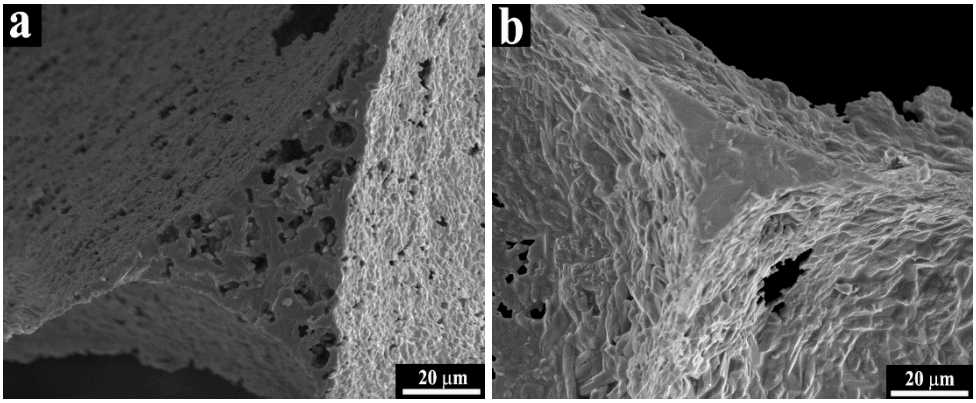

Fig.5.10 Strut images of foams prepared at (a) 8 wt% and (b) 12 wt% **MN** concentration

The effect of **MN** concentration on the sintering shrinkage, cell size, porosity, compressive strength and Young's modulus of the mullite foams prepared at a $\mathbf{W_{P/S}}$ of 0.8 and a foaming temperature of 130 ^{o}C is shown in **Table 5.3**. The sintering shrinkage increases with an increase in **MN** concentration. The sintering shrinkage increases from 44.76 to 59.94 vol.% when the **MN** concentration increases from 0 to 16 wt%. The foams prepared at a particular $\mathbf{W_{P/S}}$ are expected to show similar shrinkage irrespective of the initial foam volume (foam rise). The increase in sintering shrinkage with an increase in **MN** concentration is due to the enhanced densification of struts and cell walls in presence of MgO produced from the **MN**. The mullite foams prepared at **MN** concentrations in the range of 0 to 8 wt% show more or less the same average cell size of ~ 0.7 mm. At higher **MN** concentrations, the average cell size decreases to nearly 0.5 mm.

The porosity of the mullite foams increases from 93.46 to 96.28 vol.% when the **MN** concentration increases from 0 to 8 wt%. Further increase in the **MN** concentration decreases the porosity. The porosity of the foams prepared at **MN** concentrations of 12 and 16 wt% are 95.24 and 95.77 vol.%, respectively. The decrease in porosity beyond 8 wt% **MN** concentration, in spite of an increase in foam rise, is due to densification of porous struts and cell walls by the MgO assisted liquid phase sintering. The compressive strength of the mullite foams decreases from 1.34 to 0.21 MPa when the **MN** concentration increases from 0 to 8 wt%. This is due to increase in porosity with the addition of **MN**. Further increase in **MN** concentration to 12 wt% increases the compressive strength to 0.48 MPa due to a decrease in porosity and cell size as well as the proper densification of cell walls and struts. Even though foams at 16 wt% magnesium nitrate concentration show

dense struts, the compressive strength is lower than that prepared at 12 wt% **MN** concentration. This is attributed to the observed slight increase in porosity and cell size. The Young's modulus also shows a similar trend. The Young's modulus decreases from 615 to 12 MPa when the **MN** concentration increases from 0 to 8 wt%. The Young's modulus values at 12 and 16 wt% **MN** concentrations are 38 and 9.36 MPa, respectively.

Table 5.3 Effect of **MN** concentration on the total shrinkage, porosity, cell size, compressive strength and Young's modulus of the mullite foams

MN concentration (wt%)	Sintering shrinkage (vol. %)	Porosity (vol. %)	Cell size (mm)	Compressive strength (MPa)	Young's modulus (MPa)
0 (0)*	44.76	93.46	0.70 ± 0.08	1.34 ± 0.26	615 ± 47
4 (.0.9)	50.55	96.16	0.56 ± 0.14	0.31 ± 0.08	22 ± 3
8(1.8)	55.27	96.28	0.70 ± 0.20	0.21 ± 0.09	12 ± 1.6
12(2.7)	58.02	95.24	0.49 ± 0.09	0.48 ± 0.1	38 ± 2.4
16 (3.6)	59.94	95.77	0.58 ± 0.14	0.22 ± 0.05	9.6 ± 1.9

*Value given in parenthesis is the concentration of MgO produced in wt% of mullite

5.4. Conclusions

Ultra low-density mullite foams have been prepared by thermo-foaming of alumina-silica powder dispersions in molten sucrose, followed by pyrolysis and reaction sintering. The foaming time and foam setting time decrease and foam rise increases with an increase in ceramic powder to sucrose weight ratio, foaming temperature and **MN** concentration. The phase pure mullite foam is formed by the

reaction sintering of thermo-foamed bodies at 1600 ^{o}C. The reaction sintering of the thermo-foamed bodies without **MN** show porous cell walls and struts due to improper densification. The MgO produced from **MN** aids the densification of mullite by forming a liquid phase as evidenced from the non-porous struts and cell walls at higher **MN** concentrations. The interconnectivity of the cells increases with an increase in **MN** concentration and reached the level of reticulated foams at **MN** concentration of 12 wt% and above. The maximum porosity obtained is higher than that reported for mullite foams prepared by other processing routes. The maximum compressive strength achieved was more than four times that of mullite foams of similar porosity prepared by other processing routes.

Chapter 6

Processing of Silicon Carbide Foams by Thermo-Foaming of Silicon Powder Dispersions in Molten Sucrose

6.1 Introduction

Silicon carbide (SiC) foams attract special attention due to their high-temperature strength, high hardness and stiffness, corrosion and wear resistance, low thermal expansion coefficient and high thermal shock resistance (Eom et al., 2013). The SiC foams are prepared either using pre-ceramic polymers as precursors or from the colloidal suspension of SiC powders. Various processes based on freeze casting (Fukushima et al., 2010), gelcasting (Mouazer et al., 2004), and polymer foam templating (Mouazer, et al., 2005) have been studied for the preparation of SiC green foams from the powder suspensions. On the other hand, in pre-ceramic polymer based processes, pre-ceramic polymer foams with suitable pore architecture is prepared by polymer bead templating(Kim et al., 2008), emulsion templating (Vakifahmetoglu et al., 2011), polyurethane foam templating (Nangrejo & Edirisinghe, 2002), direct foaming (Fukushima & Colombo, 2012) and freeze casting of pre-ceramic polymer solutions(Yoon et al., 2007). The siliconization of carbon foams, obtained by the pyrolysis of wood or pitch based foams, by impregnation of molten silicon or silicon vapour is also used for the preparation of SiC foams (Greil et al., 1998a, 1998b; Vogli et al., 2002; Zhang et al., 2009). The present chapter reports preparation of SiC foams from sucrose and silicon powder. In this, sucrose is used as a low cost naturally renewable carbon source. The carbon-silicon composite foams are prepared by incorporating a suitable amount of silicon

powder in molten sucrose followed by thermo-foaming, setting and pyrolysis. The carbon and silicon in the carbon-silicon composite foam react at high-temperature heat treatment to form SiC ceramic foam. The advantage of this process is that it uses naturally renewable carbon precursor, avoids the high-temperature infiltration of molten silicon and achieves very high porosity. The effect of **MN** on foaming and setting time and properties of the resulting SiC foam is also studied.

6.2 Experimental

6.2.1 Materials

The analytical reagent grade sucrose, magnesium nitrate hexahydrate **(MN)** and acetone were procured from Merck India Ltd. Mumbai. The silicon powder of specific surface area 4.5 m^2/g (measured using a surface area analyzer) containing particles in the size range of 1 to 5 μm was procured from Alfa-Aesar, USA. The silicon powder particles have irregular morphology as shown in **Fig 6.1.** The alumina powder of average particle size 0.34 μm and specific surface area 10.4 m^2/g used as a sintering additive was procured from ACC Alcoa, Kolkata. The yttria powder of average particle size 0.56 μm and specific surface area 2.86 m^2/g was procured from Indian Rare Earth Ltd. Mumbai.

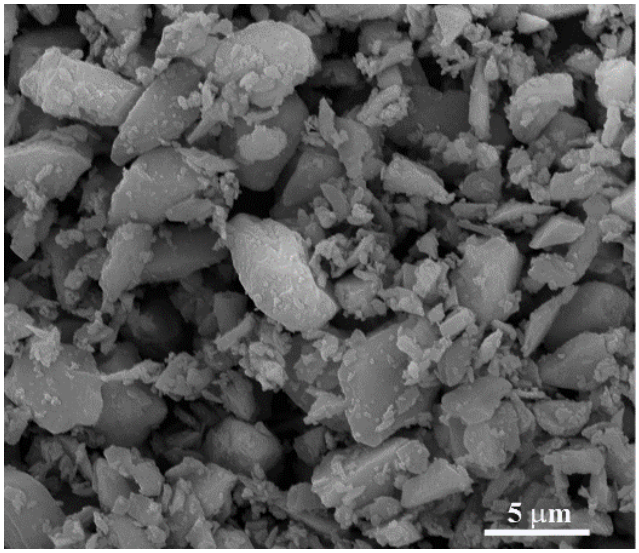

Fig 6.1 The SEM photomicrograph of silicon powder

6.2.2 Preparation of SiC foams

The flowchart for the preparation of silicon carbide foam is shown in **Fig. 6.2**. The mixtures of composition given in **Table 6.1** consisting of sucrose, silicon powder, alumina powder and yttria powder were prepared by planetary ball milling in acetone medium followed by drying in an air oven at 70 ^{o}C. The amount of silicon powder was taken by anticipating various carbon yield from sucrose in the range of 20 to 25 wt%. The amount of alumina and yttria sintering additives used was 6 and 4 wt%, respectively, of SiC, expected from the silicon powder taken in each composition. The zirconia grinding jar of 500 ml capacity and zirconia grinding balls of 10 mm diameter were used for planetary ball milling. The total powder to ball and powder to acetone weight ratios were 1:4 and 1:2, respectively. The ball milling was carried out for 2 hours at a speed of 200 RPM. The sucrose-silicon powder mixtures taken in a 2.5 liter borosilicate glass tray were heated in an air oven at 185 ^{o}C to melt the sucrose. The melt was thoroughly stirred with a glass rod to achieve a uniform dispersion of silicon powder in the molten sucrose. The silicon

powder dispersions in molten sucrose were heated at various temperatures in the range of 130 to 150 ºC for foaming and setting to form sucrose polymer-silicon powder composite foams. The sucrose polymer-silicon powder composite foams obtained were cut into bodies of 8 cm x 6 cm x 4 cm size and heated up to 1500 ºC in an inert atmosphere furnace. The heating rate was 0.5ºC /minute up to 900 ºC and 2 ºC from 900 ºC to the final temperature.

In order to study the effect of blowing agent, **MN** was added to the sucrose-silicon powder-sintering additives mixture before the planetary ball milling. The amount of **MN** used was in the range of 2 to 6 wt% of sucrose in the mixture.

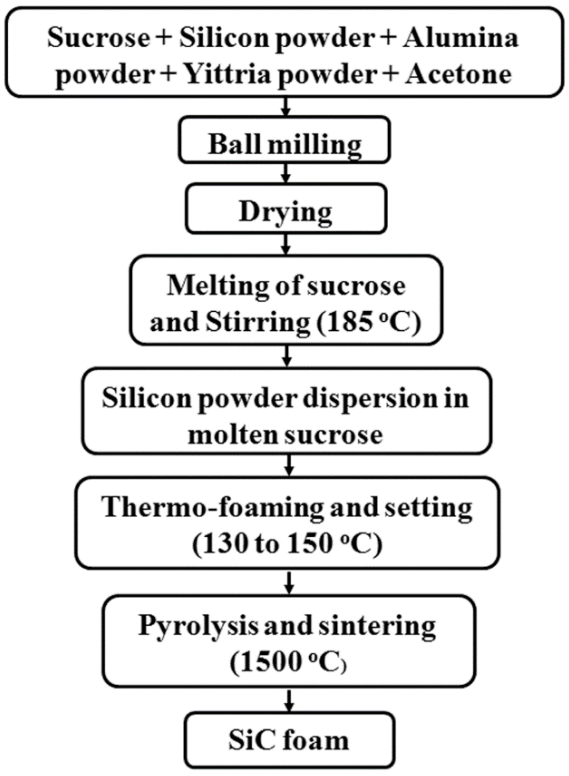

Fig 6.2 Flowchart for the preparation of SiC foam from sucrose and silicon powder

Table 6.1 Compositions used for thermo-foaming

Sample	Sucrose (g)	Anticipated Carbon yield (g)	Silicon powder (g)	Alumina (g)	Yttria (g)
A	100	20	46.81	4.01	2.67
B	100	22	51.49	4.41	2.94
C	100	24	56.13	4.81	3.20
D	100	25	58.50	5.01	3.34

6.2.3 Characterization

6.2.3.1 Foaming & setting time and foam rise

During foaming, the foam height was visually observed every 15 minutes. The time after which there is no further increase in the foam height was measured as the foaming time. After the completion of foaming, the foams were physically inspected at an interval of 1 h. The time required for the soft foam to get transformed into a hard one is determined as the foam setting time. The ratio of final height of the foam to the initial height of the silicon powder dispersion in molten sucrose is taken as the foam rise.

6.2.3.2 Viscosity measurements

Viscosity measurements of the silicon powder dispersion in molten sucrose were carried out at temperatures in the range of 120 to 150 ^{o}C using a Rheometer (Anton Paar MCR 102, Austria). The plate and plate method was used for the viscosity measurements. The zero gap was 0.8 mm. The shear rate used was in the range of 2 –1000 s^{-1}.

6.2.3.3 XRD analysis

. The XRD analysis was carried out using an X-ray diffraction analyzer (X'pert Pro, Philips, USA). The samples for XRD analysis were prepared by crushing the sintered foam bodies using a mortar and pestle.

6.2.3.4 TGA analysis

Thermogravimetric analysis (TGA) of the SiC foam samples was carried out using a thermogravimetric analyzer (Q-50, TA Instruments, USA) in an air atmosphere at a heating rate of 5°C/min. The samples for the TGA were prepared by crushing the sintered SiC foam bodies using a mortar and pestle.

6.2.3.5 Shrinkage and porosity

Volume shrinkage during heat treatment was calculated from the initial and final dimensions of the foam bodies. The porosity of the foam bodies was obtained from the bulk density calculated from their weights and dimensions.

6.2.3.6 Microstructure and cell size

The microstructure of the foam bodies was observed on the fractured surfaces using a scanning electron microscope (SEM, FEI Quanta FEG200, Hillsboro, OR). The average cell size was measured on the magnified image of the silicon carbide foams observed using a vision inspection system with a CCD color camera (Vision 300 GL, TESA Technologies, Switzerland).

6.2.3.7 Compressive strength

The compressive strength measurement was carried out using a Universal Testing Machine (Instron 5984; Instron, Norwood, USA) at a crosshead speed of 0.5mm/min using sintered SiC foam samples of 24 mm x 24 mm x 12 mm size (ASTM standard C365/C365M-05).

6.3 Results and Discussion

6.3.1 Thermo-foaming of silicon powder dispersions in molten sucrose

A homogenous dispersion of the silicon powder in molten sucrose is obtained by melting the sucrose in the sucrose-silicon powder mixture at 185 ^{o}C and stirring with a glass rod. The silicon powder dispersions undergo foaming and subsequent setting into sucrose polymer-silicon powder composite foam when heated in an air oven at temperatures in the range of 130 to 150 ^{o}C. The foaming of silicon powder dispersions in molten sucrose is due to the nucleation and growth of bubbles by water vapour generated as a result of –OH to –OH condensation of glucose and fructose anhydride molecules produced from the sucrose (DeMan, 1999; Narasimman & Prabhakaran, 2012, 2013). These bubbles are stabilized by the viscosity increase due to the polymerization through the –OH condensation as well as the adsorption of silicon particles on the liquid-gas interface. The setting of the foamed silicon powder dispersion is due to the continued polymerization through the –OH condensation. The stabilization of bubbles by the adsorption of silicon particles on the liquid-gas interface is further evidenced from the contact angle measurements. The contact angle of molten sucrose measured on a silicon wafer surface is 72.5^{o}. The photograph showing the contact angle of molten sucrose on a silicon wafer surface is shown in **fig. 6.3.** It has been reported that particles with contact angle in the range of 80 to 60^{o} adsorb on the air-liquid interface and thereby stabilize the bubbles generated in the liquid medium. The observed contact angle of molten sucrose on the silicon surface is within the range required for particle stabilization of bubbles.

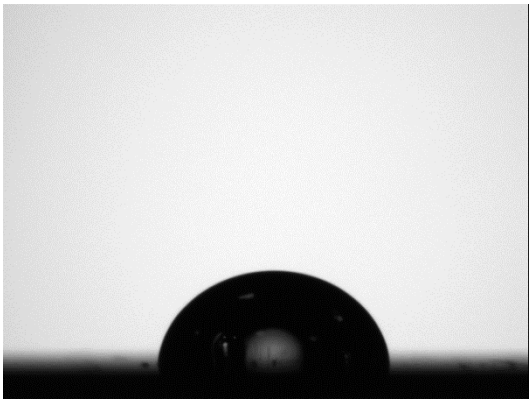

Fig 6.3 Photograph showing the contact angle of molten sucrose on a silicon wafer surface

The foaming characteristics of the silicon powder dispersions in molten sucrose depend on the rate of formation of water vapour due to –OH condensation as well as the viscosity of the dispersion. The higher rate of –OH condensation accelerate the nucleation and growth of bubbles. On the other hand, bubble growth is favored by lower viscosity and bubble stability is more at higher viscosity. **Fig. 6.4** shows viscosity versus shear rate plot of silicon powder dispersion in molten sucrose obtained from sucrose-silicon powder mixture of composition C (**Table 6.1**) measured at various temperatures. The dispersion shows the shear thinning flow behavior at temperatures in the range of 120 to 150 ^{o}C. The viscosity of the dispersion measured at a shear rate of 2 s^{-1} decreases from 101 Pa.s to 21.4 Pa.s when the temperature increases from 120 to 150 ^{o}C. The decrease in viscosity with an increase in temperature is due to the breakdown of the hydrogen bonding interaction between the sucrose hydroxyls.

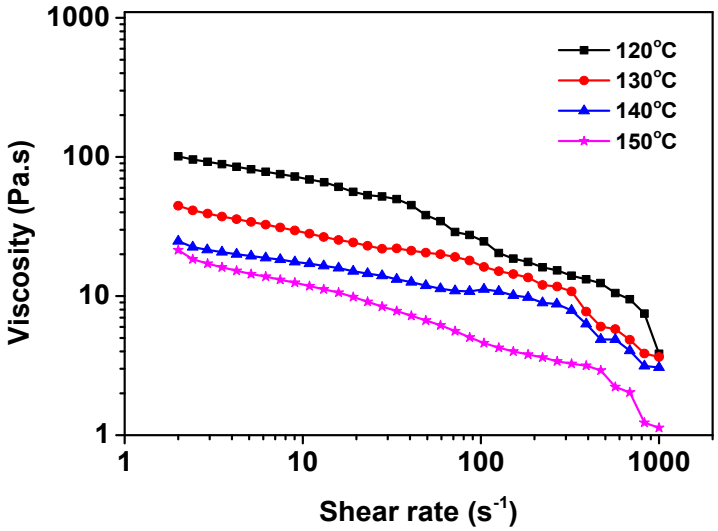

Fig 6.4 Effect of temperature on the viscosity versus shear rate plot of silicon powder dispersion in molten sucrose

Silicon powder dispersions prepared are thermo-foamed at various temperatures in the range of 120 to 150 ºC. The foaming characteristics of the silicon powder dispersion as a function of foaming temperature is given in **fig 6.5**. There is hardly any foaming observed at 120 ºC. The very poor foaming observed at 120 ºC is attributed to the high viscosity as well as the sluggish –OH condensation. On the other hand, the dispersion slowly foamed to 5.60 and 7.15 times its original volume at temperatures of 130 and 140 ºC, respectively. At 150 ºC, though the silicon powder dispersion undergoes rapid foaming to large foam volume, partially collapses before setting. The low foam rise of 4.18 at 150 ºC is due to the partial foam collapse. The foaming time decreases from 5.5 to 1.5 hours and the total time for foaming and setting decreases from 42 to 18 hours when the foaming temperature increases from 130 to 150 ºC. The decrease in foaming time and the increase in foam volume with an increase in foaming temperature are due

to an increase in the rate of –OH condensation as well as a decrease in viscosity of the silicon powder dispersion. At 150 °C, the rapid generation of water vapour in the low viscous silicon powder dispersions results in excessive bubble growth. The pressure developed in the bubbles due to the rapid generation of water vapour exceeds the strength of cell walls that results in bubble rupture before foam setting, leading to the partial foam collapse.

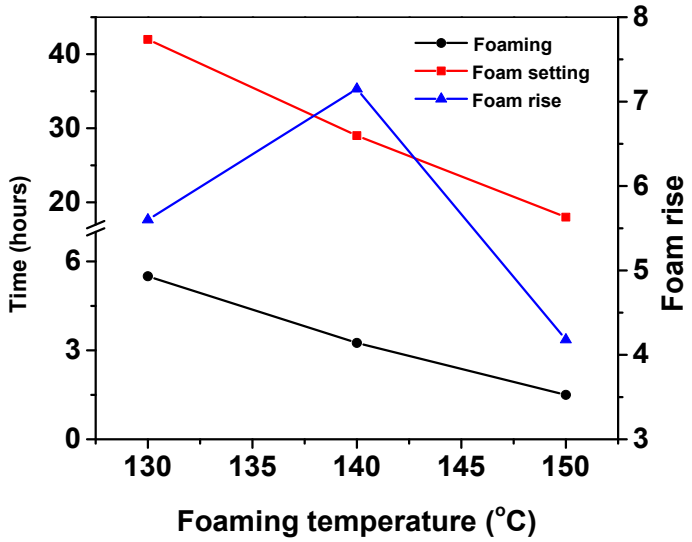

Fig 6.5 Effect of temperature on foaming characteristics of silicon powder dispersion in molten sucrose

6.3.2 Pyrolysis and sintering

The sucrose polymer in the sucrose polymer-silicon powder composite foams undergoes pyrolysis during heating in an argon atmosphere to form carbon-silicon composite foams. **Fig. 6.6** is the SEM photomicrograph of the carbon-silicon composite foam obtained by pyrolysis of sucrose polymer-silicon powder composite foam at 600 °C. The interconnected cellular structure, preferential adsorption of fine silicon particle on the cell wall surface and uniform distribution of silicon particles in the carbon matrix are evidenced in the SEM microstructures.

This preferential adsorption of silicon particles on the cell wall surface is one of the reasons for the bubble stability responsible for the foaming. This is further supported by the fact that the silicon powder dispersion took a short time (5.5 hours at 130 ^{o}C) for foaming when compared to the molten sucrose without silicon powder (72 hours at 130 ^{o}C).

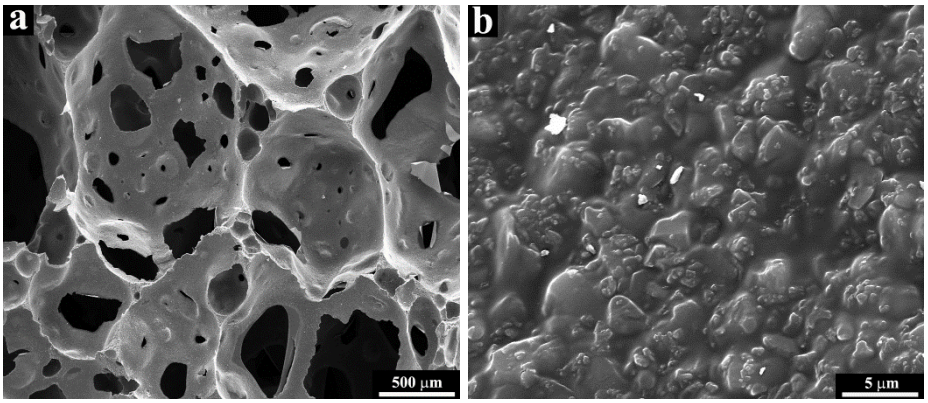

Fig 6.6 SEM photomicrograph of carbon-silicon composite foam showing (a) cell structure and (b) cell wall at high magnification

Fig 6.7 shows XRD spectrum of the sucrose polymer-silicon powder composite foam heat treated in an inert atmosphere at various temperatures. The XRD spectrum of the foam pyrolyzed at 900 ^{o}C shows all peaks corresponding to the elemental silicon and no peak corresponding to carbon. This indicates that the carbon produced by the pyrolysis of sucrose polymer is amorphous in nature. The XRD spectrum of the foam heat treated at 1500 ^{o}C for 2 hours shows all peaks corresponding to β-silicon carbide and no peaks corresponding to carbon and silicon indicating the completion of the carbon-silicon reaction.

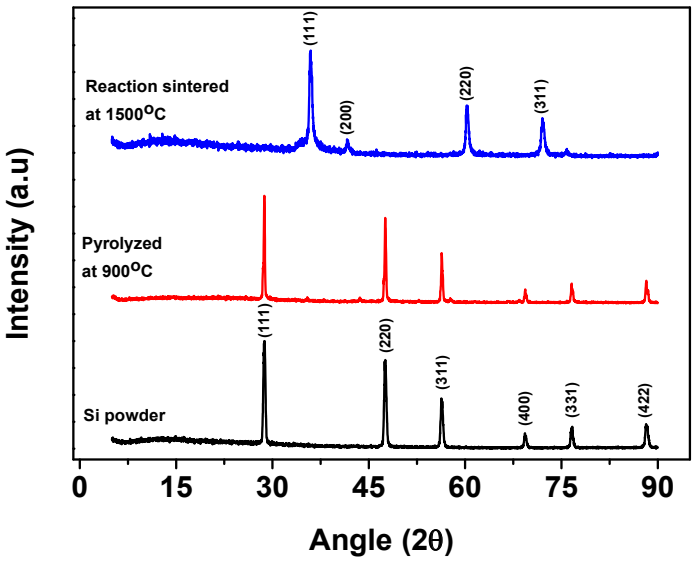

Fig 6.7 XRD spectrum of sucrose polymer-silicon powder composite foam heat treated at various temperatures in an inert atmosphere

The sucrose in the sucrose-silicon mixture is expected to leave 20 to 25 wt% carbon during pyrolysis. To arrive at an optimum composition for the formation of SiC foam free of excess carbon and silicon, sucrose-silicon powder mixtures of compositions shown in **Table 6.1** are studied. Though the foams obtained from all the studied sucrose-silicon powder compositions sintered at 1500 °C show no peak corresponding to free carbon and silicon in the XRD spectrum, the TGA analysis shows the presence of unreacted carbon in SiC foams prepared from sucrose-silicon mixtures of composition A and B. **Fig. 6.8** shows the TGA of sintered SiC foam samples prepared from sucrose-silicon powder mixtures of various compositions. The SiC foam samples prepared at all the studied compositions show negligible weight loss up to 550 °C. On the other hand, the SiC foam samples obtained from compositions A and B show weight losses of ~ 0.84 % and 0.46 %, respectively, from 550 to 750 °C, corresponding to the burnout of free carbon. However, the SiC

foam obtained from the sucrose-silicon powder mixture of composition C shows apparently no weight loss up to 750 °C indicating complete conversion of carbon to SiC. The SiC foams obtained from all the sucrose-silicon powder compositions show a weight gain of < 1% from 750 to 800 °C. This is due to the oxidation of both silicon carbide and a trace amount of unreacted silicon. To understand the effect of sintering additives on the conversion of carbon and silicon to silicon carbide, an experiment was conducted with sucrose-silicon powder mixture of composition C without the sintering additives. It is interesting to note that the sintered SiC foam prepared from composition C without the sintering additives shows a weight loss of nearly 4% from 550 to 750 °C indicating the presence of 4 wt.% unreacted carbon. This shows that the sintering additives promote the reaction between carbon and silicon to form silicon carbide.

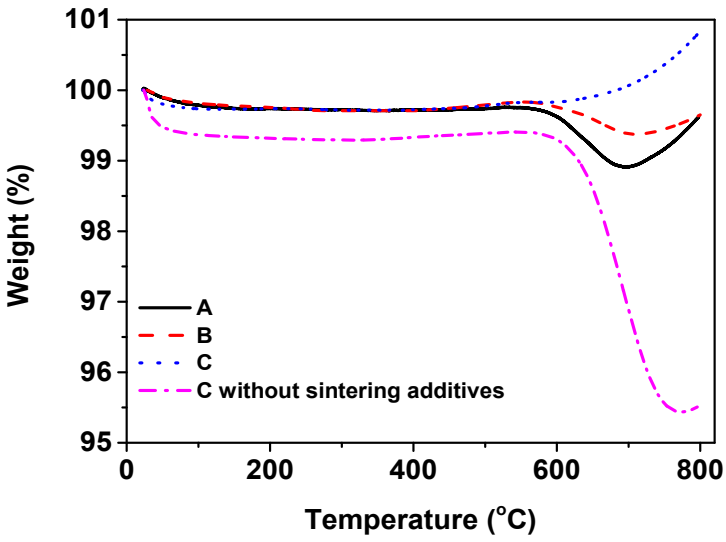

Fig 6.8 The TGA of sintered SiC foams prepared at various sucrose-silicon powder compositions

A possible mechanism by which the sintering additives promote the reaction between silicon and carbon can be as follows: During the heat treatment at 1500 °C,

reaction of liquid silicon with carbon and densification of the formed SiC takes place simultaneously. The SiC formed by the reaction between liquid silicon and carbon form a solid layer on the remaining carbon surface. Thus formed SiC layer on the carbon surface slows down the reaction of the remaining carbon with the molten silicon. However, the liquid phase formed from additives such as alumina and yittria in presence of silica (present on the surface of silicon particles) enhances the densification of the formed SiC by dissolution and recrystallization mechanism. The dissolution of the SiC layer in the liquid phase formed from the sintering additives exposes the unreacted carbon for reaction with the molten silicon leading to the completion of the silicon-carbon reaction.

6.3.3 Porosity and Microstructure

The bulk densities of the green foams obtained at foaming temperatures of 130, 140 and 150 ^{o}C are 0.177, 0.142 and 0.244 g/cm^3, respectively. The higher green density at a foaming temperature of 150 ^{o}C is because of low foam rise due to the partial foam collapse. The green foams show a weight loss of nearly 36.9% up to 900 ^{o}C due to the carbonization of the sucrose polymer. The total volume shrinkage observed during carbonization and subsequent sintering is in the range of 29.9 to 31.2% as seen in **Table 6.2**. The bulk density of the sintered SiC foam decreases from 0.168 to 0.128 g/cm^3 when the foaming temperature increases from 130 to 140 ^{o}C. The further increase in foaming temperature to 150 ^{o}C results in an increase in bulk density to 0.227 g/cm^3 due to densification by the partial foam collapse. The porosity, calculated from the foam density and theoretical density of SiC with sintering additives, increases from 94.9 to 96.1% when the foaming temperature increases from 130 to 140 ^{o}C and then decreases to 93.1% when the

foaming temperature increases to 150 ºC. The porosity obtained is in tune with the observed green density, weight loss during carbonization and the total shrinkage.

Table 6.2 Properties of SiC foam as a function of foaming temperature

Foaming temperature (ºC)	Density (g/cm^3)	Porosity (%)	Cell size (mm)	Compressive strength (MPa)	Young's modulus (MPa)
130	0.168	94.9	1.12 ± 0.32	0.16 ± 0.03	14.90 ± 1.20
140	0.128	96.1	1.32 ± 0.39	0.06 ± 0.005	5.76 ± 0.90
150	0.227	93.1	1.61 ± 0.36	0.41 ± 0.08	24.17 ± 1.80

Fig. 6.9 shows the SEM photomicrograph of sintered silicon carbide foams prepared at various foaming temperatures. The carbon-silicon composite foam retains the interconnected cellular structure after reaction sintering at 1500 ºC. Near-spherical cells are observed in foams prepared at foaming temperatures of 130 and 140 ºC. On the other hand, the foam prepared at a foaming temperature of 150 ºC shows oval shaped cells due to the partial collapse of bubbles before foam setting. The cell size increases from 1.11 to 1.61 mm when the foaming temperature increases from 130 to 150 C (**Table 6.2**). The SEM image of the strut region of the sintered SiC foam is shown in **Fig. 6.9d**. The struts are well formed and free of large cracks and voids.

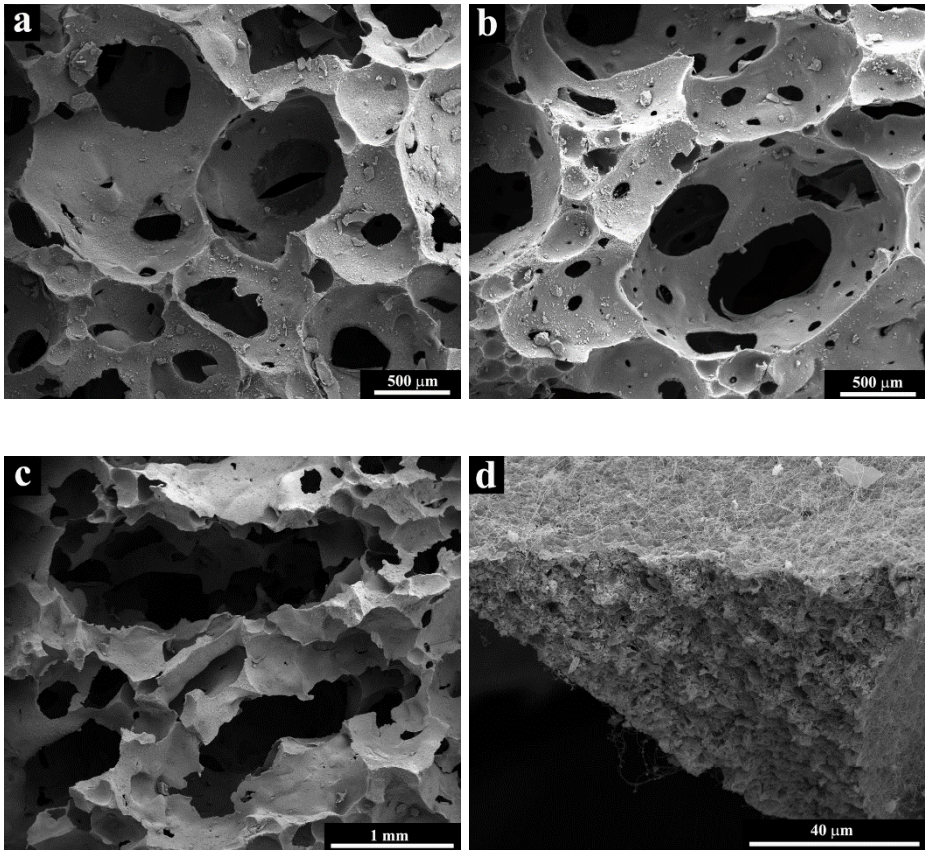

Fig 6.9 SEM photomicrographs of sintered SiC foams prepared at various foaming temperatures (a) 130 ºC, (b) 140 ºC, (c) 150 ºC and (d) strut region of the SiC foam

The SEM image at high magnification shows that the cell wall surface is covered with well-defined nanowires. The majority of nanowires show diameters in the range of 35 to 55 nm. However, few of them have diameter nearly 200 nm. **Fig. 6.10** shows the high magnification SEM images of the cell wall surface of SiC foam. The EDAX analysis of the nanowires show that they are composed of 43 wt% silicon, 41 wt% carbon, 10.6 wt% oxygen and 3.4 wt% aluminium. The stoichiometric SiC nanowire is expected to contain 70 wt% silicon and 30 wt% carbon. This indicates that the nanowires formed are not phase pure SiC. They are SiC nanowires enriched with carbon impurities. The EDAX spectrum of the

nanowires is shown in fig 6.10c. The fractured strut region shows the presence of SiC nano grains of near spherical morphology. The average grain size observed is 165 nm. Presence of the nanowires is also observed in the fractured strut region. However, the population of SiC nanowires on the cell wall surfaces is much higher than that observed in the fractured strut region. The larger population of SiC nanowires on the free cell wall surfaces compared to the fractured strut region indicates that the closely packed SiC grains sterically hinder the nanowires growth in the inter-granular region. **Fig. 6.11** shows the high magnification images of fractured strut region of the SiC foam.

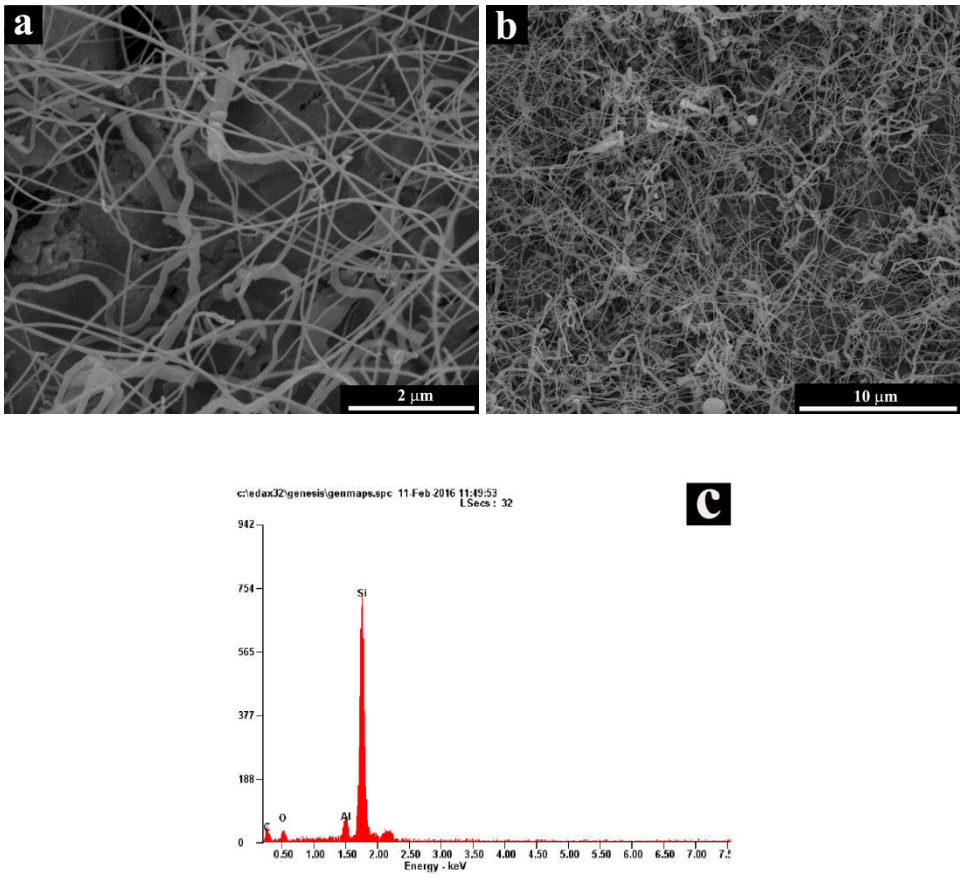

Fig 6.10 SEM photomicrographs of a cell wall surface at (a) 5000 and (b) 20000 magnifications and (c) EDAX of the nanowires

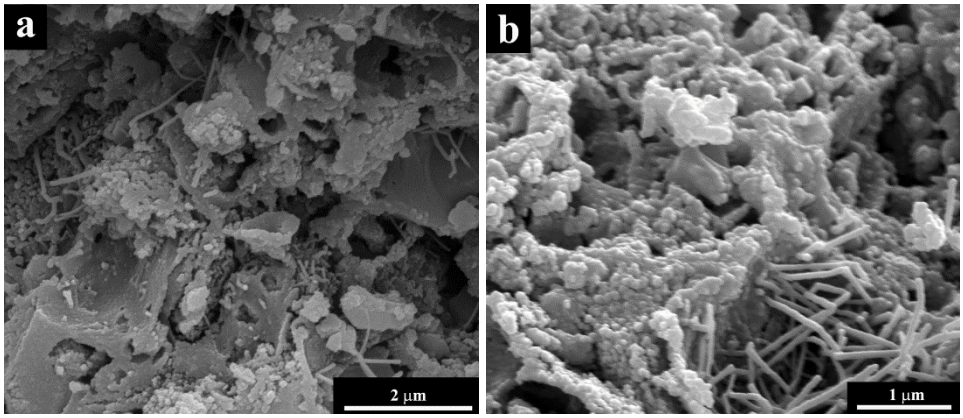

Fig 6.11 SEM photomicrographs of fractured strut region at (a) 20000 and (b) 30000 magnifications

6.3.3.4 Mechanism of growth of nanowires

Decoration of cell wall surface of ceramic foams with various one-dimensional nanostructures such as carbon nanotubes, nanofibers of carbon and SiC and nanowires of SiC and Si_3N_4 has been reported in the literature (Cordier et al., 2005; Fukushima et al., 2012; Gundiah et al., 2002; Yoon et al., 2007; Zhu et al., 2005). These nanostructures are produced on the cell wall surfaces either by chemical vapour deposition or from suitable pre-ceramic polymers in presence of catalyst such as iron and nickel. In most of the cases, the nanostructures produced on the cell wall surfaces had a length in the range of 2 to 3 μm (Fukushima et al., 2012). The growth of the nanostructures was by a vapour-liquid-solid (VLS) mechanism in which gaseous precursor molecules first dissolve in a liquid droplet formed by the catalysts at high temperature. The crystallization of nanostructures takes place upon the supersaturation of the catalyst droplet with the precursor molecules. The growth mechanism was evidenced from the presence of a spherical nodule of catalyst at the tip of the nanostructure. On the other hand, growth of SiC

nanowires in absence of a metallic catalyst is also reported in the literature (Fu et al., 2006; Prabhakaran et al., 2008; Wei et al., 2006). In this, the growth of nanowires is by the vapour–solid (VS) mechanism. In the VS mechanism SiO vapour produced by the reaction of SiO_2 present on the silicon surface with carbon or silicon reacts with carbon to form SiC nanowires. In the present case, any catalyst is added intentionally. However, the silicon powder used contains 0.03 wt% of iron as impurity. Therefore, the mechanism of formation of SiC nanowires during the sintering of carbon-silicon composite foam is both by the VLS mechanism due to the catalytic effect of iron impurity present in silicon powder and by the VS mechanism. The absence of nodule at the end of the nanowires may be due to the low concentration of iron catalyst. In contrast to the nanowires grown by VLS mechanism with added iron catalyst, the majority of SiC nanowires produced on the cell wall surfaces of SiC foams in the present method have length >10 μm. This suggests that the VS may be the prominent mechanism for the growth of SiC nanowires in the present case.

6.3.3.5 Compressive strength

Fig. 6.12 shows the compressive stress-strain graph of the sintered SiC foams prepared at various foaming temperatures. The observed stress-strain behavior is typical of brittle cellular foam materials (Gibson & Ashby, 1997). That is, an initial linear region followed by a plateau and a densification region are observed in the stress-strain graph. The stress corresponding to the plateau region is taken as the compressive strength and slope of the initial linear part is taken as the Young's modulus. The SiC foams prepared at foaming temperatures of 130 and 140 ^{o}C show compressive strength of 0.16 and 0.06 MPa, respectively. The

corresponding Young's moduli are 14.9 and 5.76 MPa, respectively (**Table 6.2**). The decrease in compressive strength and Young's modulus observed when the foaming temperature increases from 130 to 140 ºC is due to an increase in porosity and cell size. However, the foam prepared at a foaming temperature of 150 ºC shows a higher compressive strength and Young's modulus of 0.41 MPa and 24.7 MPa, respectively. The higher compressive strength and Young's modulus are attributed to the higher foam density due to partial foam collapse. Though the observed compressive strength and Young's modulus are very low, the values are comparable with that of the SiC foams of similar porosity and cell size reported in the literature (Studart et al., 2006).

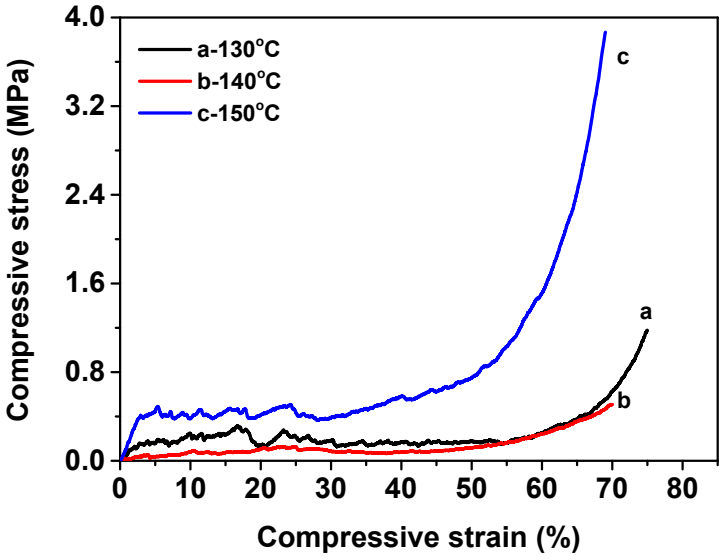

Fig 6.12 Compressive stress-strain graph of sintered SiC foams prepared at various foaming temperatures

The relatively small shrinkage (29.9 to 31.2 vol.%) during carbonization of sucrose polymer in the silicon powder-sucrose polymer composite foam and subsequent sintering enables the preparation of large SiC foam bodies without any

crack and deformation. The photograph of sintered SiC foam bodies prepared with and without sintering additives is shown in **Fig .6.13**. The black color of the foam body prepared without sintering additives is due to the presence of unreacted carbon.

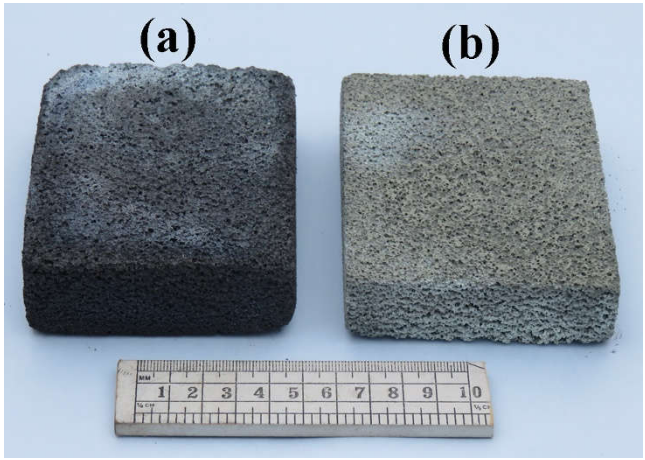

Fig 6.13 Photograph of large SiC foam bodies prepared (a) without and (b) with sintering additives

6.3.3.6 Effect of Magnesium nitrate

The effect of magnesium nitrate **(MN)** on foaming characteristics of the silicon powder dispersions in molten sucrose was studied at 130 ^{o}C. The sucrose in sucrose-silicon powder-**MN** mixtures melts easily compared to the sucrose-silicon powder mixture when heated in a glass tray at 185 ^{o}C as the **MN** lowers the melting point of sucrose. **Fig. 6.14** shows the foaming time, setting time and foam rise of silicon powder dispersions in molten sucrose at 130 ^{o}C as a function of **MN** concentration. The foaming time deceases from 5.5 to 2.25 hours, setting time decreases from 42 to 10.75 hours and foam rise, a measure of the foam volume, increases from 5.6 to 8, when the **MN** concentration increases from 0 to 6 wt% of the sucrose. The accelerated foaming and setting and increase in foam volume with

an increase in **MN** concentration are due to the catalytic effect of **MN**. That is, H^+ generated by the ionization of nitric acid produced by the hydrolysis of **MN** acts as a catalyst for the –OH condensation.

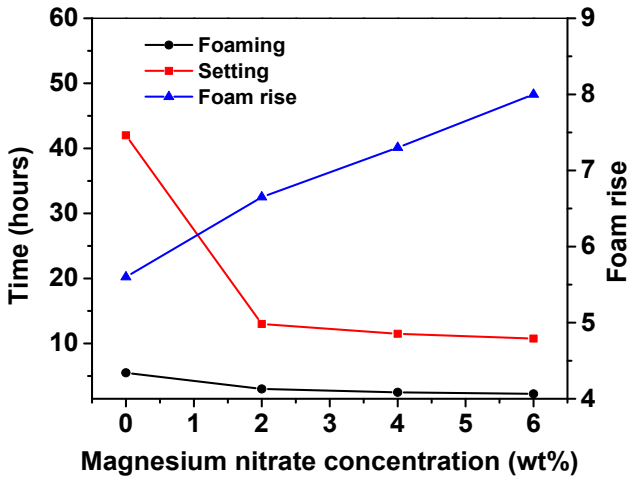

Fig 6.14 Effect of **MN** concentration on foaming & setting time and foam rise of silicon powder dispersions in molten sucrose

The thermo-foamed sucrose-silicon powder mixture containing 100 g sucrose, 56.13 g silicon powder and the sintering additives on pyrolysis at 900 ^oC produce stoichiometric carbon-silicon composite foams (**Table 6.1**). However, the carbon-silicon composite foams obtained from the above sucrose-silicon powder formulation thermo-foamed with various concentrations of **MN** blowing agent contain carbon content lower than the stoichiometric composition. The TGA graphs of silicon-carbon composite foams obtained by pyrolysis at 900 ^oC of thermo-foamed bodies prepared at various **MN** concentrations is shown in **Fig. 6.15.** The carbon-silicon composite foams obtained at 2, 4 and 6 wt% **MN** contain 24.1, 23.5 and 21.06 wt% carbon against 27.2 wt% carbon in the stoichiometric carbon-silicon composite foam. That is, the incorporation of **MN** decreases the carbon yield from sucrose. In addition, the oxidative stability of the carbon slightly increases with an

increase in **MN** concentration. This is evidenced by the slight increase in the oxidation onset temperature in TGA with an increase in MN concentration. One of the reasons for the lower carbon yield may be the oxidation of sucrose polymer by nitric acid generated from the **MN**. Another reason may be the lower molecular weight of the sucrose polymer formed in presence of **MN**. The sucrose-silicon powder compositions are optimized to achieve stoichiometric carbon-silicon composite foams by performing thermo-foaming followed by carbonization at various sucrose-silicon powder compositions in presence of 2, 4 and 6 wt% **MN.** The optimized compositions and carbon content in the resulting carbonized body estimated by TGA are given in **Table 6.3**. The carbon content in the carbon-silicon composite foam bodies obtained from the optimized silicon powder-sucrose compositions at 2, 4 and 6 wt% **MN** are 27.3, 27.02 and 27.26 wt%, respectively. The carbon content achieved is close to the stoichiometric amount required for reaction with the silicon present in it.

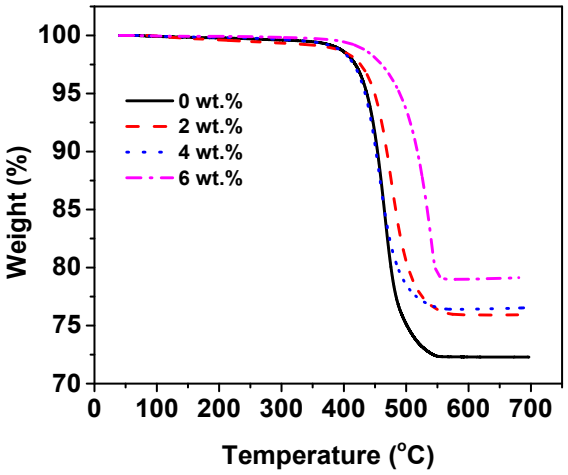

Fig. 6.15 TGA of carbon-silicon composite foam samples obtained by carbonization of sucrose polymer-silicon powder composites prepared at various **MN** concentrations

Table 6.3 Optimized sucrose-silicon powder composition and carbon content of the obtained silicon-carbon composite foams

Sucrose (gm)	Silicon powder (gm)	Alumina (g)	Yttria (g)	**MN** (g)	Carbon content of silicon-carbon composite body (wt %)	MgO produced from **MN** (g)
100	56.13	4.8075	3.205	0	27.20	0
122	56.13	4.8075	3.205	2.44 (2)*	27.30	0.383
126	56.13	4.8075	3.205	5.04 (4)	27.02	0.792
132	56.13	4.8075	3.205	7.92 (6)	27.26	1.245

*value in the parenthesis is the percentage of **MN** by weight of sucrose

The reaction sintering of the carbon-silicon composite foams containing the sintering additives at 1500 ^{o}C results in silicon carbide foams as evidenced from the XRD analysis. The XRD spectrum of SiC foams prepared at various magnesium nitrates concentrations is shown in **Fig. 6.16**. The XRD spectrum shows all peaks corresponding to β-SiC. However, no peaks corresponding to the unreacted carbon and silicon are observed. In addition, no peaks corresponding to the sintering additives and their expected reaction products such as magnesium aluminate spinel and YAG are also observed even at the highest studied **MN** concentration. On the other hand, the obtained SiC foams prepared with **MN** blowing agent show a weight loss in the range of 0.5 to 0.67 % at temperatures in the range of 200 to 650 ^{o}C corresponding to the burnout of unreacted carbon. The TGA of SiC foams prepared at various **MN** concentrations is shown in **Fig. 6.17.** The small weight gain observed

at higher temperatures is due to the oxidation of either the SiC or the unreacted silicon.

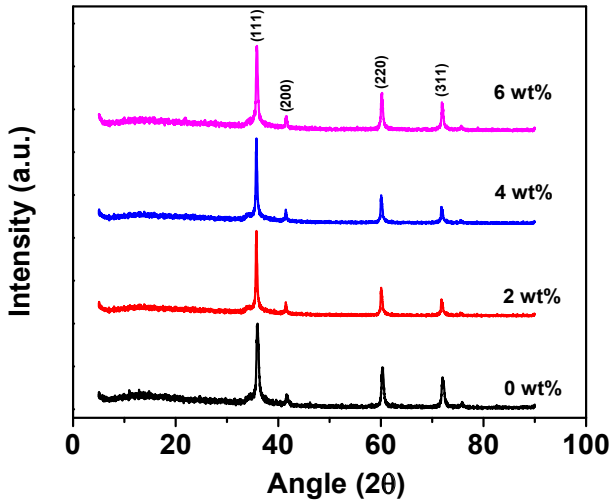

Fig. 6.16 XRD spectrum of SiC foams prepared at various **MN** concentrations

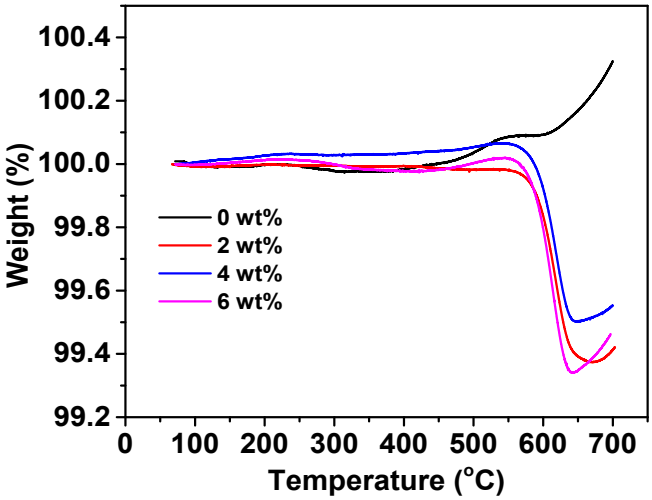

Fig 6.17 TGA of SiC foams prepared at various **MN** concentrations

The total shrinkage observed during pyrolysis of sucrose polymer-silicon powder composites followed by the reaction sintering increases from 31.2 to 39.4 vol.% when the **MN** concentration increases from 0 to 6 wt.%. A photograph containing sucrose polymer-silicon powder composite foam and the corresponding

SiC foam obtained by pyrolysis and reaction sintering showing their relative size is shown in **Fig. 6.18**. The cell sizes of the SiC foams show a drastic decrease from 1.12 to 0.58 mm when the **MN** concentration increases from 0 to 2 wt %. Further increase in **MN** concentration to 4 and 6 wt % decreases the cell size to 0.55 and 0.56 mm, respectively. It appears that a large amount of water vapour is produced in a short time by the –OH condensation of sucrose in presence of the nitric acid catalyst generated by the hydrolysis of **MN**. This leads to the nucleation of a large number of bubbles in the silicon powder dispersions in molten sucrose. The nucleation of a large number of bubbles restricts their growth leading to lower cell size as the total amount of water vapour produced from a fixed weight of sucrose remains constant. The bulk density of the SiC foams decreases from 0.168 to 0.080 g/cm^3 when the **MN** concentration increases from 0 to 6 wt%. This corresponds to an increase of porosity from 94.9 to 97.5 vol.%. The increase in porosity with an increase in **MN** concentration is due to the observed increase in foam volume (foam rise). The effect of **MN** blowing agent concentration on the sintering shrinkage, foam density and cell size of the SiC foams is shown in **Fig. 6.19**.

Fig 6.18 Photograph of (a) sucrose polymer-silicon powder composite foam and (b) SiC foam

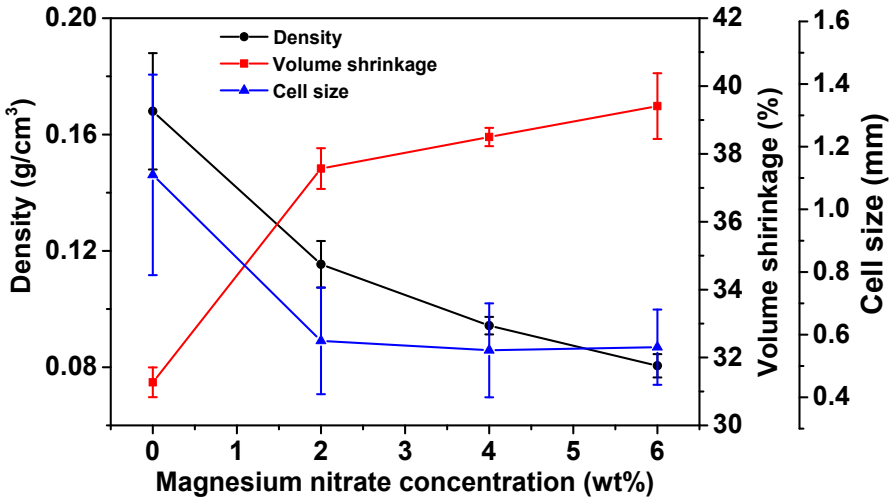

Fig. 6.19 Effect of **MN** concentration on the sintering shrinkage of sucrose polymer-silicon powder composite foam and density & cell size of SiC foams

Fig. 6.20 shows the SEM photomicrograph of the SiC foams prepared at various **MN** concentrations. The SiC foams produced with and without **MN** blowing agent show an interconnected cellular structure. The drastic reduction in the size of cells and cell windows with the introduction of **MN** blowing agent is clearly visible in the SEM photomicrographs. In addition, SiC foams prepared with **MN** blowing agent contain near spherical cells and cells have a more uniform size.

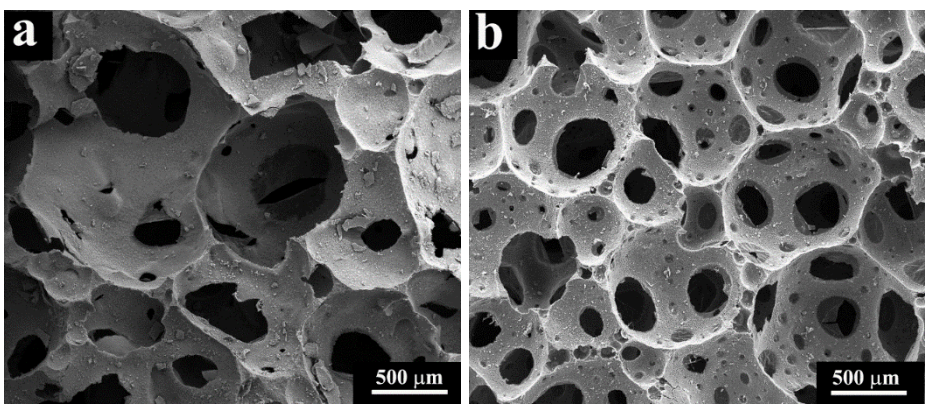

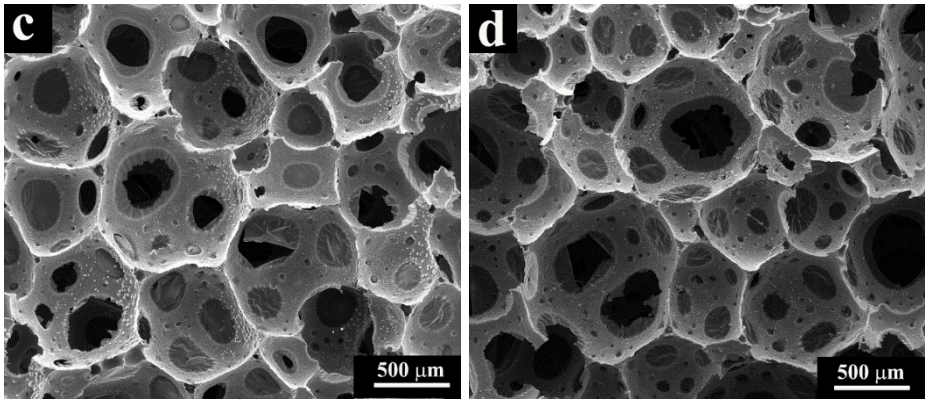

Fig. 6.20 The SEM photomicrographs of SiC foams prepared at (a) 0 wt%, (b) 2 wt% (c) 4 wt% and (d) 6 wt% of **MN**

The SiC foams prepared with the **MN** blowing agent also show the presence of nanowires of similar size (30 to 55 nm) on the cell walls. However, the population of the nanowires on the cell walls varies with the **MN** concentration. The SiC foam prepared at 4 wt% **MN** shows the maximum population of the nanowires. **Fig. 6.21** shows the high magnification SEM images of the cell wall surfaces. The SiC foam prepared without **MN** blowing agent and with 2 wt% **MN** contains uniform distribution of SiC nanowires throughout the cell wall surface. However, the cell wall surfaces of the SiC foam prepared at 4 wt % **MN** contain hemispherical bunches of SiC nanowires. On the other hand, the SiC nanowires are rarely observed on the cell walls of SiC foam prepared at 6 wt% **MN**. It can be inferred that the MgO produced from the **MN** has a role in the growth of SiC nanowires. The amount of MgO produced from 2, 4 and 6 wt % magnesium nitrate is 0.478, 0.981 and 1.553 wt%, respectively, of the SiC formed from the silicon and carbon. The reason for the maximum nanowires growth observed at 0.981 wt% MgO is not clear.

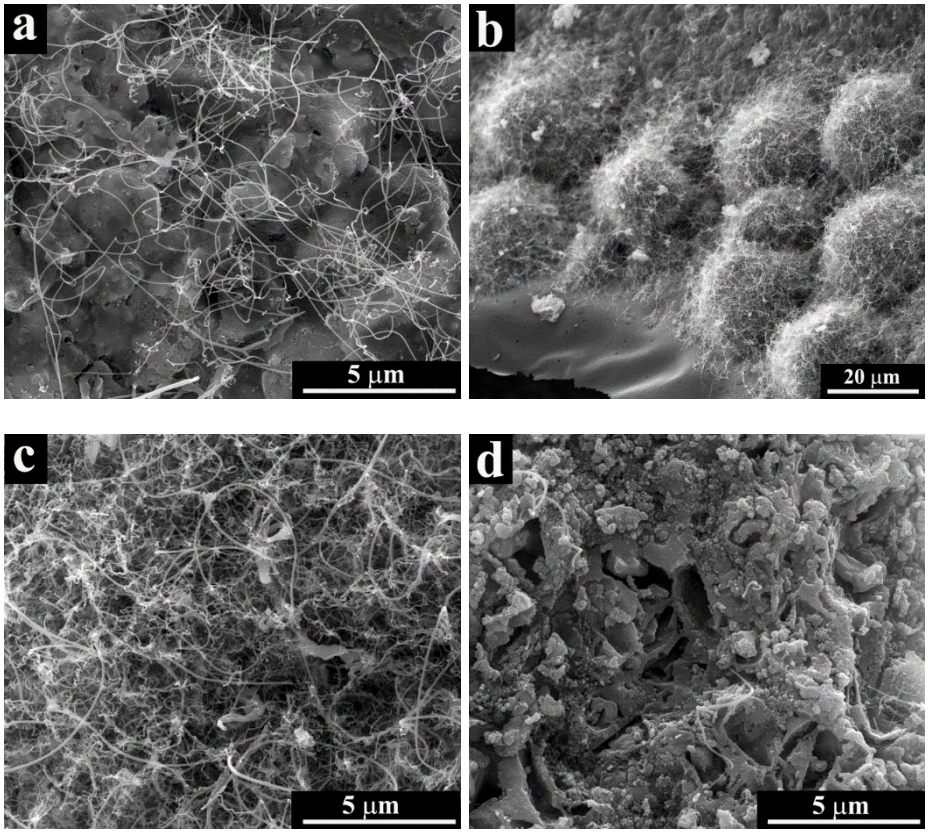

Fig. 6.21 High magnification SEM image of the cell walls of SiC foams prepared at various **MN** concentrations showing the presence of SiC nanowire (a) 2 wt% (b) 4 wt% low magnification, (c) 4 wt% high magnifiicaton (d) 6 wt%

The stress-strain graph of the SiC foams prepared at **MN** concentrations in the range of 0 to 6 wt% is shown in **Fig. 6.22**. The stress-stain graph shows an initial linear region followed by a plateau and a region of densification. The slope of the initial linear region is taken as the Young's modulus and stress corresponding to the platau region is taken as the compressive strength. The average compressive strength of the SiC foams increases from 0.160 to 0.324 MPa when the **MN** concentration increases from 0 to 4 wt%. Further increase in **MN** concentration to 6 wt% decreases the compressive strength to 0.183 MPa. The specific compressive strength of the SiC foam increases from 0.95 to 3.43 MPa $g^{-1}cm^3$ when the **MN** concentration increases from 0 to 4 wt% and then decreases to 2.27 MPa $g^{-1}cm^3$

with a further increase in MN concentration to 6 wt%. The Young's modulus also shows a similar trend. That is, Young's modulus increases from 14.90 to 77.25 MPa when the **MN** concentration increases from 0 to 4 wt% and then decreases to 24.17 MPa when MN concentration increases to 6 wt%. The effect of **MN** concentration on the compressive strength, specific compressive strength and Young's modulus of SiC foams is shown in **Fig. 6.23**. The increase in compressive strength observed with an increase in **MN** concentration despite a decrease in the density is due to the observed large decrease in cell size.

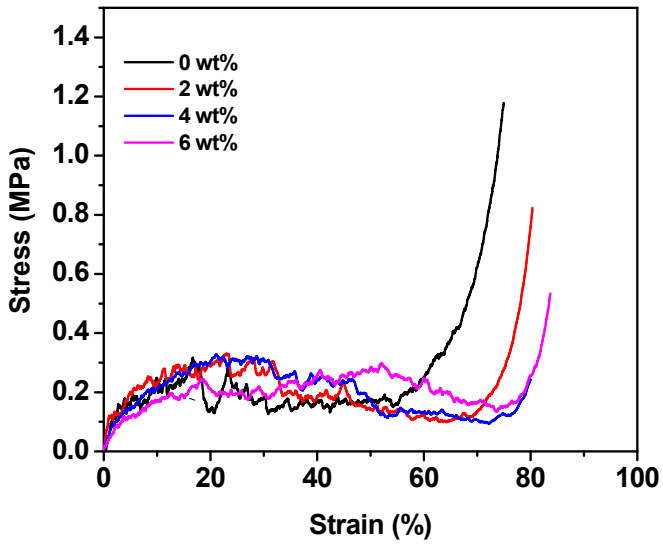

Fig 6.22 Compressive stress-strain graph of SiC foams prepared at various **MN** concentrations

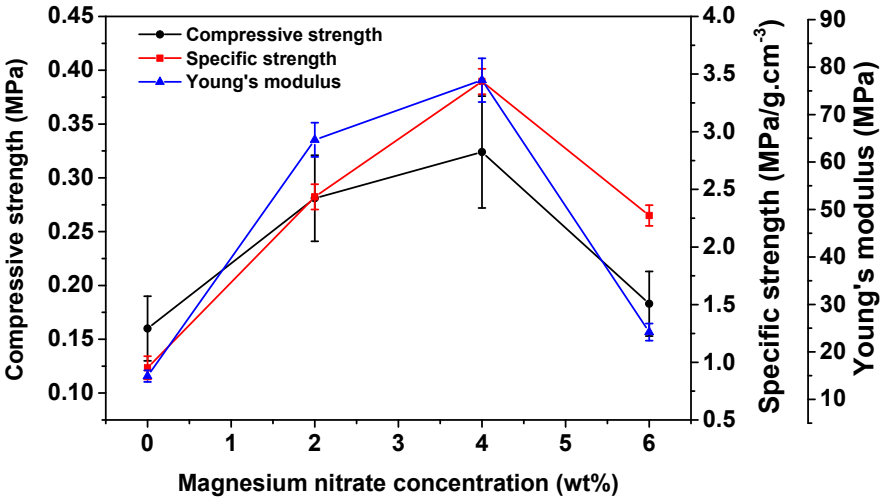

Fig. 6.23 The effect of **MN** concentration on compressive strength, specific compressive strength and Young's modulus of SiC foams

6.4 Conclusions

Open cellular SiC foams of density in the range of 0.128 to 0.227 g/cm^3 are prepared by thermo-foaming of silicon powder dispersion in molten sucrose followed by pyrolysis and reaction sintering at 1500 ^{o}C. Stable foams are obtained at foaming temperatures of 130 and 140 ^{o}C whereas partial foam collapse is observed at 150 ^{o}C. The sucrose in the sucrose-silicon powder mixture leaves 24 wt% carbon during pyrolysis. The sintering additives such as alumina and yttria promotes the carbon-silicon reaction. The carbon enriched SiC nanowires of diameter in the range of 35 to 55 nm are observed on the cell wall surfaces as well as in the fractured strut region. The nanowire growth is by both VLS and VS mechanisms. The total volume shrinkage during pyrolysis and reaction sintering is relatively small that enables the fabrication of large SiC foam bodies without crack.

The MN acts as blowing and setting agent for the thermo-foaming of silicon powder dispersions in molten sucrose. The compositions of sucrose–silicon powder mixture in the presence of 2 to 6 wt% **MN** are optimized to achieve stoichiometric carbon-silicon composite foams as the **MN** decreases the carbon yield of sucrose. The SiC foam density (0.168 to 0.080 $g.cm^{-3}$) and cell size (1.12 to 0.55 mm) decrease with an increase in **MN** concentration. The SiC foam prepared at 4 wt% **MN** shows the highest compressive strength (0.324 MPa) and specific compressive strength (3.43 MPa $g^{-1}cm^3$).

Chapter 7

Conclusions and Future work

7.1 Conclusions

Ceramic foams are macroporous ceramics with porosity greater than 60 vol.%. They have high specific strength, low density, low thermal conductivity, controlled permeability, high surface area, corrosion resistance, high temperature stability, good bio-compatibility, chemical inertness and low dielectric constant. Porous ceramics find excellent applications as high temperature thermal insulation, filter media for molten metal, lightweight structural parts, catalyst support, bio-implants, scaffold for tissue engineering and pre-form for polymer-ceramic and metal-ceramic composites. Ceramic foams are prepared via powder pressing and colloidal processing techniques. In the former technique, pores are created by adding fugitive pore templates to the ceramic powder followed by compaction, template burnout and sintering. On the other hand, in the latter technique ceramic foams are prepared from ceramic powder dispersions prepared in a solvent medium. Various techniques such as freeze casting, emulsion templating, direct foaming, replication and sacrificial template routes are used for the fabrication ceramic foams from powder dispersions. The colloidal processing techniques are advantageous over the powder pressing as it produces highly porous ceramics with controlled pore size and porosity. This thesis investigates on novel methods for the processing of ceramic foams. Emulsion templating method based on two oil phases such as naphthalene and hydrogenated vegetable oil which are solid at room temperature is studied for the preparation of alumina foams. A thermo-foaming method based on

powder dispersions in molten sucrose is also studied for the preparation of low density alumina, mullite and silicon carbide foams. A brief review of the preparation methods and applications of ceramic foams is given in **Chapter 1**.

The processing of porous ceramics by an emulsion templating method using naphthalene as the oil phase is introduced in **Chapter 2**. The naphthalene-in-aqueous alumina slurry emulsions (AAS) with naphthalene to alumina slurry volume ratios in the range of 1 to 1.86 prepared from slurries of 10, 20 and 30 vol.% alumina concentration are studied to prepare ceramic foams. The emulsions show a viscosity in the range of 0.175 to 1.025 Pa.s at a constant shear rate of 9.3 s^{-1} and yield stress in the range of 0.7 to 5.3 Pa. The emulsions cast in the glass moulds form stable gels on cooling to room temperature (~30 ^{o}C) due to the solidification of naphthalene and physical cross-linking of the carrageenan present in the alumina slurry. The compressive strength and Young's modulus of the gelled emulsion bodies increase with an increase in naphthalene to alumina slurry volume ratio and a decrease in the alumina slurry concentration. Alumina ceramics foams obtained from emulsions of naphthalene to alumina slurry volume ratios in the range of 1 to 1.86 prepared from alumina slurries of concentration in the range of 30 to 10 vol.% show porosity in the range of 65 to 90 vol.%. The average compressive strength and Young's modulus values obtained are in the ranges of 0.60 to 28.75 MPa and 36 to 1230 MPa, respectively, for the alumina ceramics foams with porosity in the range of 65 to 90 vol.%.

Although, naphthalene is successfully used as an oil phase for preparing porous alumina ceramics, the use of it in large scale processes is limited by its toxicity. The processing of alumina ceramic foams by using hydrogenated

vegetable oil (HVO) as an oil phase is described in **Chapter 3**. The freeze gelcasting of HVO-in-AAS emulsions of HVO to AAS volume ratios in the range of 1.34 to 2.69 prepared from slurries of various alumina concentrations is studied to prepare ceramic foams. Medium and high internal phase emulsions are prepared by dispersing HVO containing sodium dodecyl sulphate emulsifying agent in 10, 20 and 30 vol.% AAS containing carrageenan at 85 ^{o}C. The HVO-in-AAS emulsions show an increase in viscosity (0.225 to 2.07 Pa.s) and yield stress (0.3 to 10.3 Pa) with an increase in HVO to AAS volume ratio and alumina concentration in the AAS. The emulsions have low viscosity and yield stress, suitable for casting. The emulsions cast in moulds undergo gelation on cooling to room temperature due to the solidification of HVO and physical cross-linking of carrageenan. Compressive strength (20 to 150 kPa) and Young's modulus (120 to 1550 kPa) of the gelled emulsions increase with an increase in HVO to AAS volume ratio and an increase in AAS concentrations. The gelled emulsion bodies are successfully dried in an open air atmosphere without any humidity control. The HVO from the dried emulsion bodies are removed by soxhlet extraction using toluene or by immersing in petroleum ether at room temperature. The maximum porosity of the alumina ceramic foams obtained at a HVO to AAS volume ratio of 2.69 increases from 84 to 92.5 vol.% when the alumina slurry concentration decreases from 30 to 10 vol.%. The cell size and cell interconnectivity of the ceramics depend on the alumina slurry concentration and HVO to AAS volume ratio. The compressive strength of the alumina ceramic foams linearly and rapidly decreases from 39.6 to 2.74 MPa when the porosity increases from 70.7 to 92.5 vol.%. The Young's modulus decreases from 2350 MPa to 64.5 MPa when the porosity increases from 70.7 to 92.5 vol.%.

The Young's modulus values fitted with the model equation proposed by Gibson and Ashby show large deviation in the model parameters, n and C, from the theoretically proposed values.

In **Chapter 4**, the thermo-foaming of alumina powder dispersions in molten sucrose for the preparation of alumina foams is described. The hydrophilic interactions between the alumina surface and sucrose hydroxyl groups promote the alumina powder dispersion in the molten sucrose. The bubbles produced in the alumina powder dispersions due to the water vapour generated by the –OH to –OH condensation are stabilized by the alumina particles adsorbed on the gas-liquid interface and the increase in viscosity. The foaming and setting time of alumina powder dispersions decreases with an increase in foaming temperature and an increase in alumina powder to sucrose weight ratio ($\mathbf{W_{A/S}}$). The foam volume increases considerably with an increase in foaming temperature, reaches a maximum at a critical foaming temperature and then decreases due to foam collapse. The critical foaming temperature decreases with an increase in the $\mathbf{W_{A/S}}$. The sintering shrinkage decreases largely with an increases in $\mathbf{W_{A/S}}$ and marginally with an increase in foaming temperature. The porosity (83.4 to 94.6 vol.%) and cell size (0.55 to 1.6 mm) of the alumina foams increase with an increase in foaming temperature (120 to 170 ^{o}C) and a decrease in $\mathbf{W_{A/S}}$ (0.8 to 1.6). The compressive strength and Young's modulus of the alumina foams decrease with an increase in foaming temperature at all $\mathbf{W_{A/S}}$. The drastic decrease in compressive strength and modulus beyond a $\mathbf{W_{A/S}}$ of 1.2 is due to the pores generated on the cell walls and struts as a result of particle agglomeration.

Chapter 4 also investigates the effect of a pyrolysis step before sintering for the preparation of large alumina foam bodies. The direct binder burnout followed by sintering of large bodies produced by thermo-foaming of alumina powder dispersions in molten sucrose results in severe cracks due to large shrinkage observed in the range of 32 to 49 vol.%. An intermediate pyrolysis of the sucrose polymer binder prevents the cracking of large foam bodies as the carbon produced by pyrolysis binds the alumina particles during the initial stages of shrinkage. The particle drag and rearrangement leading to the formation of firm contacts between the alumina particles during the pyrolysis is evidenced from the SEM analysis. The compressive strength (2 to 1.3 MPa) of the carbon bonded alumina foam bodies are high enough so as to make them amenable for machining operations such as milling and drilling. The machined large carbon bonded-alumina foams do not show any cracks during subsequent carbon burnout and sintering.

The accelerated foaming and setting of alumina powder dispersions in molten sucrose in presence of magnesium nitrate (**MN)** is also described in **Chapter 4**. The **MN** decreases the melting point of sucrose from 180 to 160 ^{o}C which makes the preparation of the powder dispersions easy. The H^{+} ions produced by the hydrolysis of **MN** catalyzes the –OH to –OH condensation reaction leading to faster foaming and setting of alumina powder dispersions in molten sucrose. A remarkable decrease in foaming time (5.75 to 0.5 h) and setting time (38.75 to 1.75 h) and an increase in the foam rise (5.8 to 13) is observed with an increase in **MN** concentration from 0 to 16 wt.%. The porosity increases from 90.7 to 95.6 vol.% and cell size decreases from 0.75 to 0.4 mm with an increase in **MN** concentration from 0 to 16 wt%. A clear transition from partially interconnected cellular to

completely interconnected reticulate-like foam structure occurs when the **MN** concentration increases from 4 to 8 wt%.

In **Chapter 5**, preparation of low-density mullite foams by thermo-foaming of alumina-silica powder dispersions in molten sucrose, followed by pyrolysis and reaction sintering is described. The foaming & setting time decreases and foam rise increases with an increase in ceramic powder to sucrose weight ratio, foaming temperature and **MN** concentration. The phase pure mullite foam is formed by the reaction sintering of thermo-foamed bodies at 1600 ^{o}C. The reaction sintering of the thermo-foamed bodies without **MN** showed porous cell walls and struts due to improper densification. The MgO produced from **MN** aids the densification of mullite by forming a liquid phase as evidenced from the non-porous struts and cell walls at higher **MN** concentrations. The interconnectivity of the cells increases with an increase in **MN** concentration and reached the level of reticulated foams at **MN** concentration of 12 wt% and above. The maximum porosity of 94.92 and 96.28 vol.% achieved without and with magnesium nitrate, respectively, is the highest reported for mullite foams. The maximum compressive strength of 1.34 MPa achieved at 93.6 vol.% porosity is more than four times that of mullite foams of similar porosity prepared by other processing routes.

The preparation of open cellular SiC foams of low density by thermo-foaming of silicon powder dispersion in molten sucrose followed by pyrolysis and reaction sintering at 1500 ^{o}C is described in **Chapter 6**. In this, the carbon produced by the pyrolysis of sucrose polymer is utilized for the formation of SiC by reaction sintering. Stable foams are obtained at foaming temperatures of 130 and 140 ^{o}C whereas partial foam collapse is observed at 150 ^{o}C. The bubbles generated in the

dispersion by water vapour produced by the –OH condensation is stabilized by the adsorption of silicon particles on the air-molten sucrose interface as well as the viscosity increase due to the polymerization. The composition of a sucrose-silicon powder mixture for producing SiC foam without considerable unreacted carbon is optimized. The sucrose in the sucrose-silicon powder mixture leave 24 wt% carbon during pyrolysis. The sintering additives such as alumina and yttria promoted the carbon-silicon reaction. The carbon enriched SiC nanowires of diameter in the range of 35 to 55 nm are observed on the cell wall surfaces as well as in the fractured strut region. The nanowire growth is by both vapour-liquid-solid and vapour-solid mechanisms. The total volume shrinkage during pyrolysis and reaction sintering is relatively small that enables the fabrication of large SiC foam bodies without crack. Accelerated foaming & setting and increase in foam volume of silicon powder dispersions in molten sucrose is achieved in presence of **MN** blowing and setting agent. The compositions of sucrose–silicon powder mixture in the presence of 2 to 6 wt% **MN** are optimized to achieve stoichiometric carbon-silicon composite foams for reaction sintering as the **MN** decreases the carbon yield of sucrose. The SiC foam density (0.168 to 0.080 g/cm^3) and cell size (1.12 to 0.55 mm) decrease with an increase in **MN** concentration. The SiC foam prepared at 4 wt% **MN** shows the highest compressive strength (0.324 MPa) and specific compressive strength (3.43 MPa g^{-1}cm^3).

7.2 Future plan of work

The ceramic foams prepared via emulsion templating process have high porosity and near spherical cell structure. The foams prepared at higher oil concentration are expected to have low thermal conductivity and high acoustic absorption property. Therefore, it is proposed to study the thermal conductivity and acoustic absorption properties of the low density alumina foams prepared using emulsion templating method for possible thermal and sound insulation applications.

The alumina, mullite and SiC foams prepared using **MN** blowing agent show ultra-low density and sufficient strength. The study of the thermal conductivity of these foams is proposed for their possible applications in thermal protection systems. The SiC foams with carbon enriched SiC nanowires on the cell wall surfaces are expected to show relatively good EMI shielding property. Therefore, a study of electrical conductivity and EMI shielding effectiveness of the ultralight SiC foams is also proposed.

Currently, the thermo-foaming process is studied for the preparation of alumina, mullite and SiC ceramics. The future extension of this method to other oxide ceramic systems of interest such as zirconia, PZT and silica is proposed. In addition, preparation of other refractory carbide (ZrC, TiC etc.) foams from respective oxides by thermo-foaming followed by carbothermal reduction is also proposed.

References

1. Ahmad, R., Ha, J.-H., & Song, I.-H. (2013). Particle-stabilized ultra-low density zirconia toughened alumina foams. *Journal of the European Ceramic Society, 33*(13), 2559-2564.
2. Akpinar, S., Kusoglu, I. M., Ertugrul, O., & Onel, K. (2012). In situ mullite foam fabrication using microwave energy. *Journal of the European Ceramic Society, 32*(4), 843–848.
3 Alargova, R. G., Warhadpande, D. S., Paunov, V. N., & Velev, O. D. (2004). foam superstabilization by polymer microrods. *Langmuir, 20*(24), 10371-10374.
4. Alves-Rosa, M. A., Martins, L., Pulcinelli, S. H., & Santilli, C.V. (2013) Design of microstructure of zirconia foams from the emulsion template properties. *Soft Matter*, *9*(2), 550–558.
5. Amirbayat, J., & Hearle, J. W. S. (1969). Properties of unit composites as determined by the properties of the interface. Part I: Mechanism of matrix-fibre load transfer. *Fibre Science and Technology*, *2*(2), 123–141.
6. Andersson, L., & Bergström, L. (2008). Gas-filled microspheres as an expandable sacrificial template for direct casting of complex-shaped macroporous ceramics. *Journal of the European Ceramic Society*, *28*(15), 2815–2821.
7. Araki, K., & Halloran, J. W. (2004a). New freeze-casting technique for ceramics with sublimable vehicles. *Journal of the American Ceramic Society, 87*(10), 1859–1863.
8. Araki, K., & Halloran, J. W. (2004b). Room-Temperature Freeze Casting for ceramics with nonaqueous sublimable vehicles in the naphthalene-

camphor eutectic system. *Journal of the American Ceramic Society*, *87*(11), 2014-2019

9. Araki, K., & Halloran, J. W. (2005). Porous ceramic bodies with interconnected pore channels by a novel freeze casting technique. *Journal of the American Ceramic Society*, *88*(5), 1108–1114.
10. Aram, E., & Mehdipour-Ataei, S. (2016). A review on the micro- and nanoporous polymeric foams: Preparation and properties. *International Journal of Polymeric Materials and Polymeric Biomaterials*, *65*(7), 358-375.
11. Ashby, M. F., & Medalist, R. F. M. (1983). The mechanical properties of cellular solids. *Metallurgical Transactions A*, *14*(9), 1755–1769.
12. Askeland, D. R., & Phulé, P. P. (2003). Principles of Solidification. *The Science and Engineering of Materials, Cengage Learning, New Delhi,* 301-344.
13. Atkins, P., & De Paula, J. (2006). Physical chemistry, 8th edition, *Oxford University Press, New York*, 150–155.
14. Aveyard, R., Binks, B. P., & Clint, J. H. (2003). Emulsions stabilised solely by colloidal particles. *Advances in Colloid and Interface Science*, *100,* 503-546
15. Bai, J. (2010). Fabrication and properties of porous mullite ceramics from calcined carbonaceous kaolin and α-Al2O3. *Ceramics International*, *36*(2), 673-678.
16. Bakumov, V., Schwarz, M., & Kroke, E. (2009). Emulsion processing of polymer-derived porous Si/C/(O) ceramic bodies. *Journal of the European Ceramic Society, 29(*13), 2857-2865.
17. Barea, R., Osendi, M. I., Miranzo, P., & Ferreira, J. M. F. (2005).

Fabrication of highly porous mullite materials. *Journal of the American Ceramic Society, 88*(3), 777-779

18. Barg, S., de Moraes, E. G., Koch, D., & Grathwohl, G. (2009). New cellular ceramics from high alkane phase emulsified suspensions (HAPES). *Journal of the European Ceramic Society, 29*(12), 2439–2446.
19. Barg, S., Soltmann, C., Andrade, M., Koch, D., & Grathwohl, G. (2008). Cellular ceramics by direct foaming of emulsified ceramic powder suspensions. *Journal of the American Ceramic Society*, *91*(9), 2823–2829.
20. Barnes, H. A. (1994). Rheology of emulsions — a review. *Colloids and Surfaces A: Physicochemical and Engineering Aspects*, *91*, 89–95.
21. Bellmann, C. (2004). Stability of Dispersions. *Chemical Engineering & Technology*, *27*(9), 937–942.
22. Bennison, S. J., & Harmer, M. P. (1983). Effect of MgO solute on the kinetics of grain growth in $A1_2O_3$. *Journal of the American Ceramic Society*, *66*(5), C-90-C-92.
23. Bergström, L. (2001). Colloidal processing of ceramics. *Handbook of Applied Surface and Colloid Chemistry*, *1*, 201–217.
24. Berry, R. S., Rice, S. A., & Ross, J. (2001). Physical Chemistry, 2nd edition. *Oxford University Press, New York.*
25. Biasetto, L., Francis, A., Palade, P., Principi, G., & Colombo, P. (2008). Polymer-derived microcellular SiOC foams with magnetic functionality. *Journal of Materials Science*, *43*(12), 4119–4126.
26. Binks, B. P. (2002). Particles as surfactants—similarities and differences. *Current Opinion in Colloid & Interface Science*, *7*(1), 21–41.
27. Binks, B. P., & Horozov, T. S. (2005). Aqueous foams stabilized solely by silica nanoparticles. *Angewandte Chemie*, *117*(24), 3788–3791.

28. Blome, J. C. (1981, May 5). Molten metal filter. US Patent 4,265,659.

29. Bowen, L. J. (1994, August 23). Method for making piezoelectric ceramic/polymer composite transducers. US Patent 5,340,510.

30. Butler, N. D., Dawson, D. J., & Wordsworth, R. (1989). Shaping complex ceramic components by green machining. *Fabrication Technology Swansea,* 53–58.

31. Cao, J., Rambo, C. R., & Sieber, H. (2004). Manufacturing of microcellular, biomorphous oxide ceramics from native pine wood. *Ceramics International*, *30*(7), 1967–1970.

32. Cesarno, J., & Aksay, I. A. (1988). Processing of highly concentrated aqueous alpha-alumina suspensions stabilized with polyelectrolytes. *Journal of the American Ceramic Society*, *71*(12), 1062–1067.

33. Chanamai, R., & McClements, D. J. (2000). Dependence of creaming and rheology of monodisperse oil-in-water emulsions on droplet size and concentration. *Colloids and Surfaces A: Physicochemical and Engineering Aspects*, *172*(1), 79–86.

34. Chang, J. C., Lange, F. F., & Pearson, D. S. (1994). Viscosity and yield stress of alumina slurries containing large concentrations of electrolyte. *Journal of the American Ceramic Society*, *77*(1), 19–26.

35. Chen, F., Shen, Q., Yan, F., & Zhang, L. (2007). Pressureless sintering of α-Si_3N_4 porous ceramics using a H_3PO_4 pore forming agent. *Journal of the American Ceramic Society*, 90(8), 2379–2383.

36. Chen, G., Qi, H., Xing, W., & Xu, N. (2008). Direct preparation of macroporous mullite supports for membranes by in situ reaction sintering. *Journal of Membrane Science*, *318*(1–2), 38–44.

37. Chen, Q., Baino, F., Spriano, S., Pugno, N. M., & Vitale-Brovarone, C.

(2014). Modelling of the strength–porosity relationship in glass-ceramic foam scaffolds for bone repair. *Journal of the European Ceramic Society, 34*(11), 2663–2673.

38. Chen, R., Wang, C.-A., Huang, Y., Ma, L., & Lin, W. (2007). Ceramics with special porous structures fabricated by freeze-gelcasting: using tert-butyl alcohol as a template. *Journal of the American Ceramic Society*, *90*(11), 3478–3484.
39. Chin, C. H., Muchtar, A., Azhari, C. H., Razali, M., & Aboras, M. (2015). Optimization of pH and dispersant amount of Y-TZP suspension for colloidal stability. *Ceramics International*, *41*(8), 9939–9946.
40. Choi, H. J., Yang, T. Y., Yoon, S. Y., Kim, B. K., & Park, H. C. (2012). Porous alumina/zirconia layered composites with unidirectional pore channels processed using a tertiary-butyl alcohol-based freeze casting. *Materials Chemistry and Physics*, *133*(1), 16–20.
41. Chuanuwatanakul, C., Tallon, C., Dunstan, D. E., & Franks, G. V. (2011). Controlling the microstructure of ceramic particle stabilized foams: influence of contact angle and particle aggregation. *Soft Matter*, *7*(24), 11464–11474
42. Clarke, D. R. (1992). Interpenetrating phase composites. *Journal of the American Ceramic Society*, *75*(4), 739–758.
43. Colombo, P., & Bernardo, E. (2003). Macro- and micro-cellular porous ceramics from preceramic polymers. *Composites Science and Technology*, *63*(16), 2353–2359.
44. Colombo, P., Griffoni, M., & Modesti, M. (1998). Ceramic foams from a preceramic polymer and polyurethanes: preparation and morphological investigations. *Journal of Sol-Gel Science and Technology*, *13*(1), 195-199.

45. Colombo, P., Mera, G., Riedel, R., & Sorarù, G. D. (2010). Polymer-derived ceramics: 40 years of research and innovation in advanced ceramics. *Journal of the American Ceramic Society*, *93*(7), 1805–1837.

46. Colombo, P., & Modesti, M. (1999). Silicon oxycarbide foams from a silicone preceramic polymer and polyurethane. *Journal of Sol-Gel Science and Technology*, *14*(1), 103–111.

47. Colombo, P., & Modesti, M. (2004). Silicon oxycarbide ceramic foams from a preceramic polymer. *Journal of the American Ceramic Society*, *82*(3) 573–578.

48. Cordier, A., Flahaut, E., Viazzi, C., Laurent, C., & Peigney, A. (2005). In situ CCVD synthesis of carbon nanotubes within a commercial ceramic foam. *Journal of Materials Chemistry*, *15*(37), 4041–4050.

49. Darder, M., & Ruiz-Hitzky, E. (2005). Caramel-clay nanocomposites. *Journal of Materials Chemistry*, *15*(35–36), 3913–3918.

50. DeMan, J. M. (1999). Principles of food chemistry. (3rd ed.). *Chapman & Hall.*

51. Derjaguin, B. V, & Landau, L. D. (1941). Theory of stability of highly charged lyophobic sols and adhesion of highly charged particles in solutions of electrolytes. *Acta Physicochim. URSS*, *14*, 663–652.

52. Descamps, M., Duhoo, T., Monchau, F., Lu, J., Hardouin, P., Hornez, J. C., & Leriche, A. (2008). Manufacture of macroporous β-tricalcium phosphate bioceramics. *Journal of the European Ceramic Society*, *28*(1), 149–157.

53. Descamps, M., Richart, O., Hardouin, P., Hornez, J. C., & Leriche, A. (2008). Synthesis of macroporous β-tricalcium phosphate with controlled porous architectural. *Ceramics International*, *34*(5), 1131–1137.

54. Deville, S. (2008). Freeze-casting of porous ceramics: a review of current

achievements and issues. *Advanced Engineering Materials*, *10*(3), 155-169.

55. Deville, S., Saiz, E., & Tomsia, A. P. (2006). Freeze casting of hydroxyapatite scaffolds for bone tissue engineering. *Biomaterials*, *27*(32) 5480–5489

56. Deville, S., Saiz, E., & Tomsia, A. P. (2007). Ice-templated porous alumina structures. *Acta Materialia*, *55*(6), 1965–1974.

57. Dhara, S., & Bhargava, P. (2003). A Simple Direct Casting Route to Ceramic Foams. *Journal of the American Ceramic Society*, *86*(10), 1645-1650.

58. Dhara, S., & Su, B. (2005). Green Machining to Net Shape Alumina Ceramics Prepared Using Different Processing Routes. *International Journal of Applied Ceramic Technology*, *2*(3), 262–270.

59. Ding, S., Zhu, S., Zeng, Y.-P., & Jiang, D. (2007). Fabrication of mullite-bonded porous silicon carbide ceramics by in situ reaction bonding. *Journal of the European Ceramic Society*, *27*(4), 2095–2102.

60. Dong, Y., Hampshire, S., Zhou, J., Ji, Z., Wang, J., & Meng, G. (2011). Sintering and characterization of fly ash-based mullite with MgO addition *Journal of the European Ceramic Society*, *31*(5), 687–695.

61. Du, Z., Bilbao-Montoya, M. P., Binks, B. P., Dickinson, E., Ettelaie, R., & Murray, B. S. (2003). Outstanding stability of particle-stabilized bubbles. *Langmuir*, *19*(8), 3106–3108.

62. Eom, J.-H., Kim, Y.-W., & Raju, S. (2013). Processing and properties of macroporous silicon carbide ceramics: A review. *Journal of Asian Ceramic Societies*, *1*(3), 220–242.

63. Ewais, E. M. M., Barg, S., Grathwohl, G., Garamoon, A. A., & Morgan, N.

N. (2011). Processing of Open Porous Zirconia via Alkane-Phase Emulsified Suspensions for Plasma Applications. *International Journal of Applied Ceramic Technology*, *8*(1), 85–93.

64. Feng, Z. C., He, B., & Lombardo, S. J. (2002). Stress distribution in porous ceramic bodies during binder burnout. *Journal of Applied Mechanics*, *69*(4), 497–501.

65. Filser, F., Kocher, P., & Gauckler, L. J. (2003). Net-shaping of ceramic components by direct ceramic machining. *Assembly Automation*, *23*(4), 382–390.

66. Finar, I. L. (2007). Organic Chemistry. Vol. II: Stereochemistry and the Chemistry of Natural Products. *Delhi: Pearson Education.*

67. Freni, S., Calogero, G., & Cavallaro, S. (2000). Hydrogen production from methane through catalytic partial oxidation reactions. *Journal of Power Sources*, *87*(1–2), 28–38.

68. Fu, Q.-G., Li, H.-J., Shi, X.-H., Li, K.-Z., Wei, J., & Hu, Z.-B. (2006). Synthesis of silicon carbide nanowires by CVD without using a metallic catalyst. *Materials Chemistry and Physics*, *100*(1), 108–111.

69. Fu, Q., Rahaman, M. N., Dogan, F., & Bal, B. S. (2008a). Freeze casting of porous hydroxyapatite scaffolds. I. Processing and general microstructure. *Journal of Biomedical Materials Research. Part B, Applied Biomaterials*, *86*(1), 125–135

70. Fu, Q., Rahaman, M. N., Dogan, F., & Bal, B. S. (2008b). Freeze casting of porous hydroxyapatite scaffolds. II. Sintering, microstructure, and mechanical behavior. *Journal of Biomedical Materials Research. Part B, Applied Biomaterials*, *86*(2), 514–522

71. Fuji, M., Kato, T., Zhang, F.-Z., & Takahashi, M. (2006). Effects of

surfactants on the microstructure and some intrinsic properties of porous building ceramics fabricated by gelcasting. *Ceramics International*, *32*(7), 797–802.

72. Fukushima, M., & Colombo, P. (2012). Silicon carbide-based foams from direct blowing of polycarbosilane. *Journal of the European Ceramic Society*, *32*(2), 503–510.

73. Fukushima, M., Nakata, M., Zhou, Y., Ohji, T., & Yoshizawa, Y. (2010). Fabrication and properties of ultra highly porous silicon carbide by the gelation–freezing method. *Journal of the European Ceramic Society*, *30*(14), 2889–2896.

74. Fukushima, M., Yoshizawa, Y., & Colombo, P. (2012). Decoration of Ceramic Foams by Ceramic Nanowires via Catalyst-Assisted Pyrolysis of Preceramic Polymers. *Journal of the American Ceramic Society*, *95*(10), 3071–3077.

75. Garrn, I., Reetz, C., Brandes, N., Kroh, L. W., & Schubert, H. (2004). Clot-forming: the use of proteins as binders for producing ceramic foams. *Journal of the European Ceramic Society*, *24*(3), 579–587.

76. Gibson, L. J., & Ashby, M. F. (1997). Cellular solids. Structure and properties. *Cambridge University Press, Cambridge.*

77. Giroux, T., Hwang, S., Liu, Y., Ruettinger, W., & Shore, L. (2005). Monolithic structures as alternatives to particulate catalysts for the reforming of hydrocarbons for hydrogen generation. *Applied Catalysis B: Environmental*, *56*(1–2), 95–110.

78. Gonzenbach, U. T., Studart, A. R., Steinlin, D., Tervoort, E., & Gauckler, L. J. (2007). Processing of particle-stabilized wet foams into porous ceramics. *Journal of the American Ceramic Society*, *90*(11), 3407–3414.

79. Gonzenbach, U. T., Studart, A. R., Tervoort, E., & Gauckler, L. J. (2006). Ultrastable particle-stabilized foams. *Angewandte Chemie (International Ed. in English)*, *45*(21), 3526–30.

80. Gonzenbach, U. T., Studart, A. R., Tervoort, E., & Gauckler, L. J. (2007a). Macroporous ceramics from particle-stabilized wet foams. *Journal of the American Ceramic Society*, *90*(1), 16–22

81. Gonzenbach, U. T., Studart, A. R., Tervoort, E., & Gauckler, L. J. (2007b). Tailoring the microstructure of particle-stabilized wet foams. *Langmuir*, *23*(3), 1025–1032.

82. Greil, P., Lifka, T., & Kaindl, A. (1998a). Biomorphic cellular silicon carbide ceramics from wood: I. Processing and Microstructure. *Journal of the European Ceramic Society*, *18*(14), 1961–1973.

83. Greil, P., Lifka, T., & Kaindl, A. (1998b). Biomorphic cellular silicon carbide ceramics from wood: II. Mechanical Properties. *Journal of the European Ceramic Society*, *18*(14), 1975–1983.

84. Gundiah, G., Madhav, G. V, Govindaraj, A., Seikh, M. M., & Rao, C.N.R. (2002). Synthesis and characterization of silicon carbide, silicon oxynitride and silicon nitride nanowires. *Journal of Materials Chemistry*, *12*(5), 1606-1611.

85. Guo, L.-C., Zhang, Y., Uchida, N., & Uematsu, K. (1997). Influence of temperature on stability of aqueous alumina slurry containing polyelectrolyte dispersant. *Journal of the European Ceramic Society, 17*(2) 345–350.

86. Guo, X., Zhou, Z., Ma, G., Wang, S., Zhao, S., & Zhang, Q. (2012). Effect of forming process on the integrity of pore-gradient Al2O3 ceramic foams by gelcasting. *Ceramics International*, *38*(1), 713–719.

87. Guo, X., Zhou, Z., Wang, S., Zhao, S., Zhang, Q., & Ma, G. (2012). A Novel method for preparation of interconnected pore-gradient ceramic foams by gelcasting. *Journal of Porous Materials*, *19*(5), 853–858.

88. Guzman, I. Y. (2003). Certain principles of formation of porous ceramic structures. Properties and applications (a review). *Glass and Ceramics*, *60*(9), 280–283.

89. Hammel, E. C., Ighodaro, O. L.-R., & Okoli, O. I. (2014). Processing and properties of advanced porous ceramics: An application based review. *Ceramics International*, *40*(10), 15351–15370.

90. Han, J., Hong, C., Zhang, X., Du, J., & Zhang, W. (2010). Highly porous ZrO2 ceramics fabricated by a camphene-based freeze-casting route: Microstructure and properties. *Journal of the European Ceramic Society 30*(1), 53–60

91. He, L.-H., & Swain, M. (2011). A novel polymer infiltrated ceramic dental material. *Dental Materials*, *27*(6), 527–534.

92. He, X., Zhou, X., & Su, B. (2009). 3D interconnective porous alumina ceramics via direct protein foaming. *Materials Letters 63*(11) 830-832.

93. Hildmann, B., & Schneider, H. (2004). Heat capacity of mullite – new data and evidence for a high-temperature phase transformation. *Journal of the American Ceramic Society*, *87*(2), 227–234.

94. Hong, C., Zhang, X., Han, J., Du, J., & Han, W. (2009). Ultra-high-porosity zirconia ceramics fabricated by novel room-temperature freeze-casting. *Scripta Materialia*, *60*(7), 563–566.

95. Hong, C., Zhang, X., Han, J., Du, J., & Zhang, W. (2010). Camphene-based freeze-cast ZrO2 foam with high compressive strength. *Materials Chemistry and Physics 119*(3) 359-362.

96. Hotze, E. M., Phenrat, T., & Lowry, G. V. (2010). Nanoparticle aggregation: challenges to understanding transport and reactivity in the environment. *Journal of Environmental Quality*, *39*, 1909–1924.

97. Hou, Z., Ye, F., Liu, L., & Liu, Q. (2012). Fabrication of gradient porous β-SiAlON ceramics via a camphene-based freeze casting process. *Materials Science and Engineering: A*, *558*, 742–746.

98. Hu, J., Russell, J. J., Ben-Nissan, B., & Vago, R. (2001). Production and analysis of hydroxyapatite from Australian corals via hydrothermal process. *Journal of Materials Science Letters*, *20*(1), 85–87.

99. Hu, L., Wang, C.-A., Huang, Y., Sun, C., Lu, S., & Hu, Z. (2010). Control of pore channel size during freeze casting of porous YSZ ceramics with unidirectionally aligned channels using different freezing temperatures. *Journal of the European Ceramic Society*, *30*(16), 3389–3396.

100. Hull, D., & Clyne, T. W. (1996). An introduction to composite materials (2nd ed.). *Cambridge University press, Cambridge*.

101. Hutmacher, D. W. (2000). Scaffolds in tissue engineering bone and cartilage. *Biomaterials*, *21*(24), 2529–2543.

102. Imhof, A., & Pine, D. J. (1997). Ordered macroporous materials by emulsion templating. *Nature*, *389*(6654), 948–951.

103. Imhof, A., & Pine, D. J. (1998). Uniform macroporous ceramics and plastics by emulsion templating. *Advanced Materials*, *10*(9), 697–700.

104. Isobe, T., Kameshima, Y., Nakajima, A., Okada, K., & Hotta, Y. (2007). Gas permeability and mechanical properties of porous alumina ceramics with unidirectionally aligned pores. *Journal of the European Ceramic Society*, *27*(1), 53–59.

105. Isobe, T., Tomita, T., Kameshima, Y., Nakajima, A., & Okada, K. (2006).

Preparation and properties of porous alumina ceramics with oriented cylindrical pores produced by an extrusion method. *Journal of the European Ceramic Society*, *26*(6), 957–960.

106. Jana, P., & Ganesan, V. (2011). Processing of low-density alumina foam. *Journal of the European Ceramic Society*, *31*(1), 75–78

107. Jang, D.-H., Kim, Y.-W., Song, I.-H., Kim, H.-D., & Park, C. B. (2006). Processing of highly porous, open-cell, microcellular silicon carbide ceramics by expansion method using expandable microspheres. *Journal of the Ceramic Society of Japan*, *114*(1330), 549–553.

108. Janney, M. A., Omatete, O. O., Walls, C. A., Nunn, S. D., Ogle, R. J., & Westmoreland, G. (2005). Development of low-toxicity gelcasting systems. *Journal of the American Ceramic Society*, *81*(3), 581–591.

109. Ji, H. Bin, Kim, W. Y., Yang, T. Y., Yoon, S. Y., Kim, B. K., & Park, H. C. (2010). Freeze casting of aqueous coal fly ash/alumina slurries for preparation of porous ceramics. *Journal of Physics and Chemistry of Solids*, *71*(4), 503–506.

110. Jin, Y.-J., & Kim, Y.-W. (2010). Low temperature processing of highly porous silicon carbide ceramics with improved flexural strength. *Journal of Materials Science*, *45*(1), 282–285

111. Jones, R. W. (1999). Near net shape ceramics by freeze casting. *Advances in Science and Technology*, C49–C61.

112. Jun, I.-K., Koh, Y.-H., & Kim, H.-E. (2006). Fabrication of a highly porous bioactive glass-ceramic scaffold with a high surface area and strength. *Journal of the American Ceramic Society*, *89*(1), 391–394

113. Jun, I.-K., Koh, Y.-H., Song, J.-H., Lee, S.-H., & Kim, H.-E. (2006). Improved compressive strength of reticulated porous zirconia using carbon

coated polymeric sponge as novel template. *Materials Letters 60*(20) 2507-2510

114. Jun, I.-K., Song, J.-H., Choi, W.-Y., Koh, Y.-H., Kim, H.-E., & Kim, H.-W. (2007). Porous Hydroxyapatite Scaffolds Coated With Bioactive Apatite-wollastonite-glass-ceramics. *Journal of the American Ceramic Society*, *90*(9), 2703–2708

115. Kalita, S. J., Bose, S., Hosick, H. L., & Bandyopadhyay, A. (2003). Development of controlled porosity polymer-ceramic composite scaffolds via fused deposition modeling. *Materials Science and Engineering: C, 23*(5), 611–620.

116. Kim, Y.-W., Eom, J.-H., Guo, Y., Zhai, W., Park, C. B., & Song, I.-H. (2011). Processing of open-cell silicon carbide foams by steam chest molding and carbothermal reduction. *Journal of the American Ceramic Society*, *94*(2), 344–347.

117. Kim, Y.-W., Eom, J.-H., Wang, C., & Park, C. B. (2008). Processing of porous silicon carbide ceramics from carbon-filled polysiloxane by extrusion and carbothermal reduction. *Journal of the American Ceramic Society*, *91*(4), 1361–1364.

118. Kim, Y.-W., Kim, S.-H., Song, I.-H., Kim, H.-D., & Park, C. B. (2005). Fabrication of open-cell, microcellular silicon carbide ceramics by carbothermal reduction. *Journal of the American Ceramic Society, 88*(10), 2949–2951.

119. Kim, Y.-W., Kim, S.-H., Wang, C., & Park, C. B. (2003). Fabrication of microcellular ceramics using gaseous carbon dioxide. *Journal of the American Ceramic Society*, *86*(12), 2231–2233

120. Kim, Y.-W., Kim, S.-H., Xu, X., Choi, C.-H., Park, C. B., & Kim, H.-D.

(2002). Fabrication of porous preceramic polymers using carbon dioxide. *Journal of Materials Science Letters*, *21*(21), 1667–1669

121. Kim, Y.-W., Lee, K.-H., Lee, S.-H., & Park, C. B. (2003). Fabrication of porous silicon oxycarbide ceramics by foaming polymer liquid and compression molding. *Journal of the Ceramic Society of Japan*, *111*(1299), 863–864.

122. Kim, Y.-W., & Park, C. B. (2003). Processing of microcellular preceramics using carbon dioxide. *Composites Science and Technology*, *63*(16), 2371-2377.

123. Klempner, D., & Frisch, K. C. (1991). Handbook of polymeric foams and foam technology. *Oxford University Press. New York.*

124. Komlev, V. S., Barinov, S. M., Girardin, E., Oscarsson, S., Rosengren, Å., Rustichelli, F., & Orlovskii, V. P. (2003). Porous spherical hydroxyapatite and fluorhydroxyapatite granules: processing and characterization. *Science and Technology of Advanced Materials, 4*(6), 503–508.

125. Konegger, T., Felzmann, R., Achleitner, B., & Brouczek, D. (2015). Mullite-based cellular ceramics obtained by a combination of direct foaming and reaction bonding. *Ceramics International*, *41*(7), 8630–8636.

126. Kong, D., Yang, H., Wei, S., Li, D., & Wang, J. (2007). Gel-casting without de-airing process using silica sol as a binder. *Ceramics International, 33*(2), 133–139.

127. Konopka, K., Olszówka-Myalska, A., & Szafran, M. (2003). Ceramic–metal composites with an interpenetrating network. *Materials Chemistry and Physics*, *81*(2–3), 329–332.

128. Krajewski, A., Ravaglioli, A., Roncari, E., Pinasco, P., & Montanari, L.

(2000). Porous ceramic bodies for drug delivery. *Journal of Materials Science: Materials in Medicine*, *11*(12), 763–771.

129. Krauss Juillerat, F., Gonzenbach, U. T., Elser, P., Studart, A. R., & Gauckler, L. J. (2011). Microstructural Control of Self-Setting Particle-Stabilized Ceramic Foams. *Journal of the American Ceramic Society, 94*(1), 77–83.

130. Krauss Juillerat, F., Gonzenbach, U. T., & Gauckler, L. J. (2012). Tailoring the hierarchical pore structures in self-setting particle-stabilized foams made from calcium aluminate cement. *Materials Letters70* 152-154.

131. Krauss Juillerat, F., Gonzenbach, U. T., Studart, A. R., & Gauckler, L.J. (2010). Self-setting particle-stabilized foams with hierarchical pore structures. *Materials Letters 64*(13) 1468-1470.

132. Lam, Y. C., Yu, S. C. M., Tam, K. C., & Shengjie, Y. (2000). Simulation of polymer removal from a powder injection molding compact by thermal debinding. *Metallurgical and Materials Transactions A*, *31*(10), 2597–2606.

133. Landau, M. V, Shter, G. E., Titelman, L., Gelman, V., Rotter, H., Grader, G. S., & Herskowitz, M. (2006). Alumina foam coated with nanostructured chromia aerogel: efficient catalytic material for complete combustion of chlorinated VOC. *Industrial & Engineering Chemistry Research*, *45*(22), 7462–7469.

134. Lee, S.-H., Jun, S.-H., Kim, H.-E., & Koh, Y.-H. (2007). Fabrication of porous PZT-PZN piezoelectric ceramics with high hydrostatic figure of merits using camphene-based freeze casting. *Journal of the American Ceramic Society*, *90*(9), 2807–2813.

135. Lemos, A. F., & Ferreira, J. M. F. (2004). The valences of egg white for

designing smart porous bioceramics: as foaming and consolidation agent. *Key Engineering Materials*, *254–256*, 1045–1050.

136. Lewis, J. A. (2004). Colloidal processing of ceramics. *Journal of the American Ceramic Society*, *83*(10), 2341–2359.

137. Li, Y., Chen, F., Li, L., Zhang, W., Yu, H., Shan, Y., Shen, Q., & Jiang, H. (2010). Gas pressure sintering of arbitrary porous silicon nitride ceramics with high mechanical strength. *Journal of the American Ceramic Society*, *93*(6), 1565-1568.

138. Lissant, K. J. (1970). Geometry of emulsions. *Journal of the Society of Cosmetic Chemists*, *21*(3), 141–154.

139. Liu, D.-M. (1997). Influence of porosity and pore size on the compressive strength of porous hydroxyapatite ceramic. *Ceramics International*, *23*(2), 135–139.

140. Liu, P., & Chen, G.-F. (2014). Porous materials: processing and applications (First edit). *Oxford, UK: Elsevier.*

141. Liu, W., Du, L., Wang, Y., Yang, J., & Xu, H. (2013). Effects of foam composition on the microstructure and piezoelectric properties of macroporous PZT ceramics from ultrastable particle-stabilized foams. *Ceramics International*, *39*(8), 8781–8787.

142. Liu, W., Xu, J., Wang, Y., Xu, H., Xi, X., & Yang, J. (2013).Processing and properties of porous PZT ceramics from particle-stabilized foams via gelcasting. *Journal of the American Ceramic Society*, *96*(6), 1827-1831.

143. Liu, Y.-F., Liu, X.-Q., Li, G., & Meng, G.-Y. (2001). Low cost porous mullite-corundum ceramics by gelcasting. *Journal of Materials Science*, *36*(15), 3687–3692.

144. Liu, Y.-F., Liu, X.-Q., Wei, H., & Meng, G.-Y. (2001). Porous mullite ceramics from national clay produced by gelcasting. *Ceramics International*, *27*(1), 1–7.

145. Luyten, J., Thijs, I., Vandermeulen, W., Mullens, S., Wallaeys, B., & Mortelmans, R. (2005). Strong ceramic foams from polyurethane templates. *Advances in Applied Ceramics*, *104*(1), 4–8.

146. Lyckfeldt, O., & Ferreira, J. M. F. (1998). Processing of porous ceramics by "starch consolidation." *Journal of the European Ceramic Society*, *18*(2), 131–140.

147. Magdeski, J. S. (2010). The porosity dependence of mechanical properties of sintered alumina. *Journal of the University of Chemical Technology and Metallurgy*, *45*(2), 143–148.

148. Manoharan, V. N., Imhof, A., Thorne, J. D., & Pine, D. J. (2001). Photonic crystals from emulsion templates. *Advanced Materials*, *13*(6), 447–450.

149. Mao, X., Wang, S., & Shimai, S. (2008). Porous ceramics with tri-modal pores prepared by foaming and starch consolidation. *Ceramics International*, *34*(1), 107–112.

150. Mathieu, L., Bourban, P., & Manson, J. (2006). Processing of homogeneous ceramic/polymer blends for bioresorbable composites. *Composites Science and Technology*, *66*(11–12), 1606–1614.

151. Mattern, A., Huchler, B., Staudenecker, D., Oberacker, R., Nagel, A., & Hoffmann, M. J. (2004). Preparation of interpenetrating ceramic–metal composites. *Journal of the European Ceramic Society*, *24*(12), 3399–3408.

152. Maximenko, A., & Van Der Biest, O. (1998). Finite element modelling of binder removal from ceramic mouldings. *Journal of the European Ceramic Society*, *18*(8), 1001–1009.

153. Menner, A., Haibach, K., Powell, R., & Bismarck, A. (2006). Tough reinforced open porous polymer foams via concentrated emulsion templating. *Polymer*, *47*(22), 7628–7635.

154. Mizutani, M., Takase, H., Adachi, N., Ota, T., Daimon, K., & Hikichi, Y (2005). Porous ceramics prepared by mimicking silicified wood. *Science and Technology of Advanced Materials*, *6*(1), 76–83.

155. Montanaro, L., Perrot, C., Esnouf, C., Thollet, G., Fantozzi, G., & Negro, A. (2000). Sintering of industrial mullites in the presence of magnesia as a sintering aid. *Journal of the American Ceramic Society*, *83*(1), 189–196.

156. Montanaro, L., Tulliani, J. M., Perrot, C., & Negro, A. (1997). Sintering of industrial mullites. *Journal of the European Ceramic Society*, *17*(14), 1715–1723.

157. Moon, Y.-W., Shin, K.-H., Koh, Y.-H., Choi, W.-Y., & Kim, H.-E. (2011). Production of highly aligned porous alumina ceramics by extruding frozen alumina/camphene body. *Journal of the European Ceramic Society, 31*(11) 1945-1950.

158. Moon, Y.-W., Shin, K.-H., Koh, Y.-H., Choi, W.-Y., & Kim, H.-E. (2012). Porous alumina ceramics with highly aligned pores by heat-treating extruded alumina/camphene body at temperature near its solidification point. *Journal of the European Ceramic Society*, *32*(5), 1029–1034.

159. Mouazer, R., Mullens, S., Thijs, I., Luyten, J., & Buekenhoudt, A. (2005). Silicon carbide foams by polyurethane replica technique. *Advanced Engineering Materials*, *7*(12), 1124–1128.

160. Mouazer, R., Thijs, I., Mullens, S., & Luyten, J. (2004). SiC Foams Produced by gelcasting: synthesis and characterization. *Advanced*

Engineering Materials, *6*(5), 340–343.

161. Munro, R. G. (1997). Evaluated material properties for a sintered alpha-alumina. *Journal of the American Ceramic Society*, *80*(8), 1919-1928.

162. Nangrejo, M. R., & Edirisinghe, M. J. (2002). Porosity and strength of silicon carbide foams prepared using preceramic polymers. *Journal of Porous Materials*, *9*(2), 131–140.

163. Narasimman, R., & Prabhakaran, K. (2012). Preparation of low density carbon foams by foaming molten sucrose using an aluminium nitrate blowing agent. *Carbon*, *50*(5), 1999–2009.

164. Narasimman, R., & Prabhakaran, K. (2013). Preparation of carbon foams with enhanced oxidation resistance by foaming molten sucrose using a boric acid blowing agent. *Carbon*, *55*, 305–312.

165. Nunn, S. D., & Kirby, G. H. (1996). Green machining of gelcast ceramic materials. *Ceramic Engineering and Science. Proceedings, 17*(3) 209.

166. Ohji, T., & Fukushima, M. (2012). Macro-porous ceramics: processing and properties. *International Materials Reviews*, *57*(2), 115–131.

167. Okada, K., Shimizu, M., Isobe, T., Kameshima, Y., Sakai, M., Nakajima, A., & Kurata, T. (2010). Characteristics of microbubbles generated by porous mullite ceramics prepared by an extrusion method using organic fibers as the pore former. *Journal of the European Ceramic Society*, *30*(6) 1245–1251.

168. Okada, K., Uchiyama, S., Isobe, T., Kameshima, Y., Nakajima, A., & Kurata, T. (2009). Capillary rise properties of porous mullite ceramics prepared by an extrusion method using organic fibers as the pore former. *Journal of the European Ceramic Society*, *29*(12), 2491–2497.

169. Oliveira, F. A. C., Dias, S., Vaz, M. F., & Fernandes, J. C. (2006). Behaviour of open-cell cordierite foams under compression. *Journal of the European Ceramic Society*, *26*(1), 179–186.

170. Omatete, O. O., Janney, M. A., & Nunn, S. D. (1997). Gelcasting: from laboratory development toward industrial production. *Journal of the European Ceramic Society*, *17*(2), 407–413.

171. Omatete, O. O., Janney, M. A., & Strehlow, R. A. (1991). Gelcasting: a new ceramic forming process. *American Ceramic Society Bulletin*, *70*(10), 1641–1649.

172. Ortega, F. S., Valenzuela, F. A. O., Scuracchio, C. H., & Pandolfelli, V.C. (2003). Alternative gelling agents for the gelcasting of ceramic foams. *Journal of the European Ceramic Society*, *23*(1), 75–80.

173. Ota, T., Imaeda, M., Takase, H., Kobayashi, M., Kinoshita, N., Hirashita, T., … Hikichi, Y. (2000). Porous Titania Ceramic Prepared by Mimicking Silicified Wood. *Journal of the American Ceramic Society*, *83*(6), 1521-1523

174. Pal, R. (1996). Effect of droplet size on the rheology of emulsions. *AIChE Journal*, *42*(11), 3181–3190.

175. Palazzo, B., Sidoti, M. C., Roveri, N., Tampieri, A., Sandri, M., Bertolazzi, L., … Contro, R. (2005). Controlled drug delivery from porous hydroxyapatite grafts: An experimental and theoretical approach. *Materials Science and Engineering: C*, *25*(2), 207–213.

176. Parfitt, G. D. (1973). Fundamental aspects of dispersion. Dispersion of Powder in Liquids, second edition. *Wiley & Sons, New York*, 1–47.

177. Pickering, S. U. (1907). CXCVI.—emulsions. *Journal of the Chemical Society Transactions*, *91*, 2001–2021.

178. Potoczek, M. (2008a). Gelcasting of alumina foams using agarose solutions. *Ceramics International*, *34*(3), 661–667.

179. Potoczek, M. (2008b). Hydroxyapatite foams produced by gelcasting using agarose. *Materials Letters 62*(6) 1055-1057.

180. Potoczek, M., Zima, A., Paszkiewicz, Z., & Ślósarczyk, A. (2009). Manufacturing of highly porous calcium phosphate bioceramics via gel-casting using agarose. *Ceramics International*, *35*(6), 2249–2254.

181. Prabhakaran, K., Gokhale, N. M., Sharma, S. C., & Lal, R. (2005). A novel process for low-density alumina foams. *Journal of the American Ceramic Society*, *88*(9), 2600–2603.

182. Prabhakaran, K., Melkeri, A., Gokhale, N. M., & Sharma, S. C. (2007) Preparation of macroporous alumina ceramics using wheat particles as gelling and pore forming agent. *Ceramics International*, *33*(1), 77–81.

183. Prabhakaran, K., Pavithran, C., Brahmakumar, M., & Ananthakumar, S. (2001). Gelcasting of alumina using urea–formaldehyde III. Machinable green bodies by copolymerisation with acrylic acid. *Ceramics International*, *27*(2), 185–189.

184. Prabhakaran, K., Sooraj, R., Melkeri, A., Gokhale, N. M., & Sharma, S.C. (2009). A new direct coagulation casting process for alumina slurries prepared using poly(acrylate) dispersant. *Ceramics International, 35*(3) 979–985.

185. Prabhakaran, P. V, Sreejith, K. J., Swaminathan, B., Packirisamy, S., & Ninan, K. N. (2008). Silicon carbide wires of nano to sub-micron size from phenol-furfuraldehyde resin. *Journal of Materials Science*, *44*(2), 528.

186. Pradhan, M., & Bhargava, P. (2004). Effect of Sucrose on Fabrication of Ceramic Foams from Aqueous Slurries. *Journal of the American Ceramic*

Society, *88*(1), 216–218.

187. Pradhan, M., & Bhargava, P. (2008). Defect and microstructural evolution during drying of soapnut-based alumina foams. *Journal of the European Ceramic Society*, *28*(16), 3049–3057.

188. Pryor, M. J., & Gray, T. J. (1976, March 30). Ceramic foam filter. US Patent 3,947,363

189. Rahaman, M., & Rahaman, M. N. (2006*). Ceramic processing*. *CRC press*.

190. Ribeiro, F., Silva, J. M., Silva, E., Vaz, M. F., & Oliveira, F. A. C. (2011). Catalytic combustion of toluene on Pt zeolite coated cordierite foams. *Catalysis Today*, *176*(1), 93–96.

191. Rice, P. M., Kingery, W. D., Bowen, H. K., Uhlmann, D. R., Onoda, G. Y., Hench, L. L. … Matthewson, M. J. (1997). Physical ceramics: principles for ceramic science and engineering. *Wiley.*

192. Rice, R. W. (1993). Comparison of stress concentration versus minimum solid area based mechanical property-porosity relations. *Journal of Materials Science*, *28*(8), 2187–2190.

193. Richardson, J. ., Peng, Y., & Remue, D. (2000). Properties of ceramic foam catalyst supports: pressure drop. *Applied Catalysis A: General*, *204*(1), 19–32.

194. Richerson, D. W. (2005). Modern ceramic engineering: properties, processing, and use in design. *CRC press.*

195. Rocha, R. M., Moura, E. A. B., Bressiani, A. H. A., & Bressiani, J. C. (2008). SiOC ceramic foams synthesized from electron beam irradiated methylsilicone resin. *Journal of Materials Science*, *43*(13), 4466.

196. Rodríguez-Lorenzo, L. M., Vallet-Regí, M., & Ferreira, J. M. F. (2002). Fabrication of porous hydroxyapatite bodies by a new direct

consolidation method: starch consolidation. *Journal of Biomedical Materials Research*, *60*(2), 232–40.

197. Roncari, E., Galassi, C., & Bassarello, C. (2000). Mullite suspensions for reticulate ceramic preparation. *Journal of the American Ceramic Society*, *83*(12), 2993–2998.

198. Roohani-Esfahani, S.-I., Chen, Y., Shi, J., & Zreiqat, H. (2013). Fabrication and characterization of a new, strong and bioactive ceramic scaffold for bone regeneration. *Materials Letters*, *107*, 378–381

199. Rosen, M. J., & Kunjappu, J. T. (2012). Surfactants and interfacial phenomena. *John Wiley & Sons.*

200. Roy, D. M., & Linnehan, S. K. (1974). Hydroxyapatite formed from coral skeletal carbonate by hydrothermal exchange. *Nature*, *247*(5438), 220–222.

201. Rul, S., Laurent, C., Peigney, A., & Rousset, A. (2003). Carbon nanotubes prepared in situ in a cellular ceramic by the gelcasting-foam method. *Journal of the European Ceramic Society*, *23*(8), 1233–1241.

202 Scheffler, M., & Colombo, P. (2005). Cellular ceramics: structure, manufacturing, properties and applications. *Wiley-VCH Verlag GmbH & Co. KGaA, Weinheim, FRG*

203. Scherer, G. W. (1990). Theory of drying. *Journal of the American Ceramic Society*, *73*(1), 3–14.

204. Schneider, H., & Eberhard, E. (1990). Thermal expansion of mullite. *Journal of the American Ceramic Society*, *73*(7), 2073–2076.

205. Schneider, H., Schreuer, J., & Hildmann, B. (2008). Structure and properties of mullite—A review. *Journal of the European Ceramic Society*, *28*(2), 329–344.

206. Seol, Y.-J., Park, D. Y., Park, J. Y., Kim, S. W., Park, S. J., & Cho, D.-W.

(2013). A new method of fabricating robust freeform 3D ceramic scaffolds for bone tissue regeneration. *Biotechnology and Bioengineering*, *110*(5), 1444–1455.

207. Sepulveda, P. (1997). Gelcasting foams for porous ceramics. *American Ceramic Society Bulletin*, *76*(10), 61–65.

208. Sepulveda, P., & Binner, J. G. (1999). Processing of cellular ceramics by foaming and in situ polymerisation of organic monomers. *Journal of the European Ceramic Society*, *19*(12), 2059–2066.

209. Sepulveda, P., Ortega, F. S., Innocentini, M. D. M., & Pandolfelli, V.C. (2000). Properties of highly porous hydroxyapatite obtained by the gelcasting of foams. *Journal of the American Ceramic Society*, *83*(12), 3021–3024.

210. She, J., & Ohji, T. (2003). Fabrication and characterization of highly porous mullite ceramics. *Materials Chemistry and Physics*, *80*(3), 610–614.

211. Shibuya, M., Takahashi, T., & Koyama, K. (2007). Microcellular ceramics by using silicone preceramic polymer and PMMA polymer sacrificial microbeads. *Composites Science and Technology*, *67*(1), 119–124.

212. Sieber, H., Hoffmann, C., Kaindl, A., & Greil, P. (2000). Biomorphic cellular ceramics. *Advanced Engineering Materials*, *2*(3), 105–109.

213. Sofie, S. W., & Dogan, F. (2004). Freeze casting of aqueous alumina slurries with glycerol. *Journal of the American Ceramic Society*, *84*(7), 1459-1464.

214. Song, I.-H., Kwon, I.-M., Kim, H.-D., & Kim, Y.-W. (2010). Processing of microcellular silicon carbide ceramics with a duplex pore structure. *Journal of the European Ceramic Society*, *30*(12), 2671–2676.

215. Sopyan, I., Sulaiman, N. S., Gustiono, D., & Herdianto, N. (2005). Porous hydroxyapatite-gelatin composites with functions of bone substitutes and drug releasing agents: a preliminary study. In *Microelectronics, MEMS, and Nanotechnology* (p. 60360C–60360C). International Society for Optics and Photonics.

216. Studart, A. R., Gonzenbach, U. T., Akartuna, I., Tervoort, E., & Gauckler, L. J. (2007). Materials from foams and emulsions stabilized by colloidal particles. *Journal of Materials Chemistry*, *17*(31), 3283–3289.

217. Studart, A. R., Gonzenbach, U. T., Tervoort, E., & Gauckler, L. J. (2006) Processing routes to macroporous ceramics: a review. *Journal of the American Ceramic Society*, *89*(6), 1771–1789.

218. Su, B., Dhara, S., & Wang, L. (2008). Green ceramic machining: A top-down approach for the rapid fabrication of complex-shaped ceramics. *Journal of the European Ceramic Society*, *28*(11), 2109–2115.

219. Sun, B., Fan, T., & Zhang, D. (2002). Porous TiC ceramics derived from wood template. *Journal of Porous Materials*, *9*(4), 275–277.

220. Sun, B., Fan, T., Zhang, D., & Okabe, T. (2004). The synthesis and microstructure of morph-genetic TiC/C ceramics. *Carbon*, *42*(1), 177–182.

221. Tadros, T. F. (2006). Applied surfactants: principles and applications. *John Wiley & Sons.*

222. Takahashi, T., & Colombo, P. (2003). SiOC Ceramic Foams through Melt Foaming of a Methylsilicone Preceramic Polymer. *Journal of Porous Materials*, *10*(2), 113–121.

223. Takahashi, T., Münstedt, H., Colombo, P., & Modesti, M. (2001). Thermal evolution of a silicone resin/polyurethane blend from preceramic to ceramic foam. *Journal of Materials Science*, *36*(7), 1627–1639.

224. Takahashi, T., Münstedt, H., Modesti, M., & Colombo, P. (2001). Oxidation resistant ceramic foam from a silicone preceramic polymer/polyurethane blend. *Journal of the European Ceramic Society*, *21*(16), 2821–2828.

225. Tang, Y., Qiu, S., Wu, C., Miao, Q., & Zhao, K. (2016). Freeze cast fabrication of porous ceramics using tert-butyl alcohol–water crystals as template. *Journal of the European Ceramic Society 36*(6) 1513-1518.

226. Thareja, P., Ising, B. P., Kingston, S. J., & Velankar, S. S. (2008). Polymer Foams Stabilized by Particles Adsorbed at the Air/Polymer Interface. *Macromolecular Rapid Communications*, *29*(15), 1329–1334.

227. Travitzky, N. (2012). Processing of ceramic–metal composites. *Advances in Applied Ceramics*, *111*(5–6), 286–300.

228. Tsai, D.-S. (1991). Pressure buildup and internal stresses during binder burnout: Numerical analysis. *AIChE Journal*, *37*(4), 547–554.

229. Tseng, W. J., & Hsu, C.-K. (1999). Cracking defect and porosity evolution during thermal debinding in ceramic injection moldings. *Ceramics International*, *25*(5), 461–466.

230. Tulliani, J.-M., Lombardi, M., Palmero, P., Fornabaio, M., & Gibson, L.J. (2013). Development and mechanical characterization of novel ceramic foams fabricated by gel-casting. *Journal of the European Ceramic Society*, *33*(9), 1567–1576.

231. Tulliani, J.-M., Montanaro, L., Bell, T. J., & Swain, M. V. (1999). Semiclosed-cell mullite foams: preparation and macro- and micromechanical characterization. *Journal of the American Ceramic Society*, *82*(4), 961–968.

232. Ungureanu, S., Sigaud, G., Vignoles, G. L., Lorrette, C., Birot, M., Derre,

A. … Backov, R. (2011). Tough silicon carbide macro/mesocellular crack-free monolithic foams. *Journal of Materials Chemistry*, *21*(38), 14732–14740.

233. Vakifahmetoglu, C., Balliana, M., & Colombo, P. (2011). Ceramic foams and micro-beads from emulsions of a preceramic polymer. *Journal of the European Ceramic Society*, *31*(8), 1481–1490.

234. van Oss, C. J., & Giese, R. F. (2003). Surface modification of clays and related materials. *Journal of Dispersion Science and Technology*, *24*(3–4), 363–376.

235. Verma, J., Mitra, R., & Vijayakumar, M. (2013). Processing of silica foam using steam heating and its characterization. *Journal of the European Ceramic Society*, *33*(5), 943–951.

236. Verwey, E. J. W., & Overbeek, J. T. G. (1948). Theory of stability of lyophobic colloids'. *Elsevier, Amsterdam, The Netherlands*.

237. Vitorino, N., Abrantes, J. C. C., & Frade, J. R. (2013). Cellular ceramics processed by paraffin emulsified suspensions with collagen consolidation. *Materials Letters, 98,* 120-123.

238. Vogli, E., Sieber, H., & Greil, P. (2002). Biomorphic SiC-ceramic prepared by Si-vapor phaseinfiltration of wood. *Journal of the European Ceramic Society*, *22*(14), 2663–2668.

239. Vogt, U. F., Gorbar, M., Dimopoulos-Eggenschwiler, P., Broenstrup, A., Wagner, G., & Colombo, P. (2010). Improving the properties of ceramic foams by a vacuum infiltration process. *Journal of the European Ceramic Society*, *30*(15), 3005–3011.

240. Wang, M., Du, H., Guo, A., Hao, R., & Hou, Z. (2012). Microstructure control in ceramic foams via mixed cationic/anionic surfactant. *Materials*

Letters, 88, 97-100.

241. Wang, X., Li, J., Guan, W., Fu, M., & Liu, L. (2016). Emulsion- templated high porosity mullite ceramics with sericite induced textured structures. *Materials & Design*, *89*, 1041–1047.

242. Wang, Y., Chen, Z., Yu, S., Saeed, M.-U., Xu, T., Wang, W., & Pan, Y. A novel ultra-light reticulated SiC foam with hollow skeleton. *Journal of the European Ceramic Society*, *37*(1), 53–59.

243. Waschkies, T., Oberacker, R., & Hoffmann, M. J. (2009). Control of lamellae spacing during freeze casting of ceramics using double-side cooling as a novel processing route. *Journal of the American Ceramic Society*, *92*, S79–S84.

244. Wei, J., Li, K.-Z., Li, H.-J., Fu, Q.-G., & Zhang, L. (2006). Growth and morphology of one-dimensional SiC nanostructures without catalyst assistant. *Materials Chemistry and Physics*, *95*(1), 140–144.

245. White, R. A., Weber, J. N., & White, E. W. (1972). Replamineform: a new process for preparing porous ceramic, metal, and polymer prosthetic materials. *Science*, *176*(4037), 922–924.

246. Wilson, A. J. (1989). Foams: physics, chemistry and structure. *Springer Science & Business Media.*

247 Wu, X. L. K., & McAnany, W. J. (1995). Acrylic binder for green machining. *American Ceramic Society Bulletin*, *74*(5), 61–64.

248. Xia, Y., Zeng, Y.-P., & Jiang, D. (2012). Microstructure and mechanical properties of porous Si_3N_4 ceramics prepared by freeze-casting. *Materials & Design, 33,* 98-103.

249. Yang, J.-F., Zhang, G.-J., Kondo, N., Ohji, T., & Kanzaki, S. (2005). Synthesis of Porous Si_3N_4 Ceramics with Rod-Shaped Pore Structure.

Journal of the American Ceramic Society, *88*(4), 1030–1032.

250. Yang, T. Y., Ji, H. B., Yoon, S. Y., Kim, B. K., & Park, H. C. (2010). Porous mullite composite with controlled pore structure processed using a freeze casting of TBA-based coal fly ash slurries. *Resources, Conservation and Recycling*, *54*(11), 816–820.

251. Yang, T. Y., Lee, J. M., Yoon, S. Y., & Park, H. C. (2010). Hydroxyapatite scaffolds processed using a TBA-based freeze-gel casting/polymer sponge technique. *Journal of Materials Science: Materials in Medicine*, *21*(5), 1495–1502.

252. Yin, L., Zhou, X., Yu, J., Wang, H., Zhao, S., Luo, Z., & Yang, B. (2013a) New consolidation process inspired from making steamed bread to prepare Si_3N_4 foams by protein foaming method. *Journal of the European Ceramic Society*, *33*(7), 1387–1392.

253. Yin, L., Zhou, X., Yu, J., Wang, H., Zhao, S., Luo, Z., & Yang, B. (2013b). Preparation of Si3N4 ceramic foams by simultaneously using egg white protein and fish collagen. *Ceramics International*, *39*(1), 445–448.

254. Yoon, B.-H., Choi, W.-Y., Kim, H.-E., Kim, J.-H., & Koh, Y.-H. (2008). Aligned porous alumina ceramics with high compressive strengths for bone tissue engineering. *Scripta Materialia*, *58*(7), 537–540.

255. Yoon, B.-H., Koh, Y.-H., Park, C.-S., & Kim, H.-E. (2007). Generation of large pore channels for bone tissue engineering using camphene-based freeze casting. *Journal of the American Ceramic Society*, *90*(6), 1744–1752.

256. Yoon, B.-H., Lee, E.-J., Kim, H.-E., & Koh, Y.-H. (2007). Highly aligned porous silicon carbide ceramics by freezing polycarbosilane/camphene solution. *Journal of the American Ceramic Society*, *90*(6), 1753–1759.

257. Yoon, B.-H., Park, C.-S., Kim, H.-E., & Koh, Y.-H. (2007). In situ synthesis of porous silicon carbide (SiC) ceramics decorated with SiC nanowires. *Journal of the American Ceramic Society*, *90*(12), 3759–3766.

258. Yoon, B.-H., Park, C.-S., Kim, H.-E., & Koh, Y.-H. (2008). In-situ fabrication of porous hydroxyapatite (HA) scaffolds with dense shells by freezing HA/camphene slurry. *Materials Letters 62*(10) 1700-1703.

259. Yu, J., Yang, J., Li, S., Li, H., & Huang, Y. (2012). Preparation of Si_3N_4 foam ceramics with nest-like cell structure by particle-stabilized foams. *Journal of the American Ceramic Society*, *95*(4), 1229–1233.

260. Zeschky, J., Goetz-Neunhoeffer, F., Neubauer, J., Jason Lo, S. H., Kummer, B., Scheffler, M., & Greil, P. (2003). Preceramic polymer derived cellular ceramics. *Composites Science and Technology*, *63*(16), 2361–2370.

261. Zeschky, J., Höfner, T., Arnold, C., Weißmann, R., Bahloul-Hourlier, D., Scheffler, M., & Greil, P. (2005). Polysilsesquioxane derived ceramic foams with gradient porosity. *Acta Materialia*, *53*(4), 927–937.

262. Zhang, F.-Z., Kato, T., Fuji, M., & Takahashi, M. (2006a). Gelcasting fabrication of porous ceramics using a continuous process. *Journal of the European Ceramic Society*, *26*(4–5), 667–671.

263. Zhang, F.-Z., Kato, T., Fuji, M., & Takahashi, M. (2006b). Gelcasting fabrication of porous ceramics using a continuous process. *Journal of the European Ceramic Society*, *26*(4), 667–671.

264. Zhang, G.-J., Yang, J.-F., & Ohji, T. (2004). Fabrication of porous ceramics with unidirectionally aligned continuous pores. *Journal of the American Ceramic Society*, *84*(6), 1395–1397.

265. Zhang, R., Fang, D., Pei, Y., & Zhou, L. (2012). Microstructure,

mechanical and dielectric properties of highly porous silicon nitride ceramics produced by a new water-based freeze casting. *Ceramics International 38*(5) 4373-4377.

266. Zhang, Y., Hu, L., Han, J., & Jiang, Z. (2010). Freeze casting of aqueous alumina slurries with glycerol for porous ceramics. *Ceramics International, 36*(2), 617–621.

267. Zhang, Y., Zuo, K., & Zeng, Y.-P. (2009). Effects of gelatin addition on the microstructure of freeze-cast porous hydroxyapatite ceramics. *Ceramics International*, *35*(6), 2151–2154.

268. Zhang, Z., Wang, F., Yu, X., Wang, Y., Yan, Y., Li, K., & Luan, Z. (2009). Porous silicon carbide ceramics produced by a carbon foam derived from mixtures of mesophase pitch and Si particles. *Journal of the American Ceramic Society*, *92*(1), 260–263.

269. Zhu, S., Xi, H.-A., Li, Q., & Wang, R. (2005). In situ growth of β- SiC nanowires in porous SiC ceramics. *Journal of the American Ceramic Society*, *88*(9), 2619–2621.

270. Zhu, X.-W., Jiang, D.-L., & Tan, S.-H. (2001). Impregnating process of reticulated porous ceramics using polymeric sponges as the templates. *Journal of Inorganic Materials-Beijing*, *16*(6), 1144–1150.

271. Zollfrank, C., Kladny, R., Sieber, H., & Greil, P. (2004). Biomorphous SiOC/C-ceramic composites from chemically modified wood templates. *Journal of the European Ceramic Society*, *24*(2), 479–487.

272. Zuo, K. H., Zeng, Y.-P., & Jiang, D. (2010a). Effect of polyvinyl alcohol additive on the pore structure and morphology of the freeze-cast hydroxyapatite ceramics. *Materials Science and Engineering: C*, *30*(2), 283–287.

273. Zuo, K. H., Zeng, Y., & Jiang, D. (2010b). Effect of cooling rate and polyvinyl alcohol on the morphology of porous hydroxyapatite ceramics. *Materials & Design 31*(6) 3090-3094.

274. Zuo, K. H., Zhang, Y., Zeng, Y.-P., & Jiang, D. (2011). Pore-forming agent induced microstructure evolution of freeze casted hydroxyapatite. *Ceramics International 37*(1) 407-410.

List of Publications Based on the Thesis

1. Vijayan, S., Narasimman, R., & Prabhakaran, K. (2015). Freeze gelcasting of naphthalene-in-aqueous alumina slurry emulsions for the preparation of macroporous alumina ceramics. *Ceramics International*, *41*(1), 1487–1494.
2. Vijayan, S., Narasimman, R., & Prabhakaran, K. (2015). Effect of emulsion composition on the porosity characteristics of macroporous ceramics prepared by freeze gelcasting of naphthalene-in-aqueous alumina slurry emulsions. *Journal of Ceramic Processing Research*, *16*(6), 712–721.
3. Vijayan, S., Narasimman, R., & Prabhakaran, K. (2014). Freeze gelcasting of hydrogenated vegetable oil-in-aqueous alumina slurry emulsions for the preparation of macroporous ceramics. *Journal of the European Ceramic Society*, *34*(16), 4347–4354.
4. Vijayan, S., Narasimman, R., & Prabhakaran, K. (2015). Effect of emulsion composition on gel strength and porosity in the preparation of macroporous alumina ceramics by freeze gelcasting. *Journal of Asian Ceramic Societies*, *3*(3), 279–286.
5. Vijayan, S., Narasimman, R., Prudvi, C., & Prabhakaran, K. (2014). Preparation of alumina foams by the thermo-foaming of powder dispersions in molten sucrose. *Journal of the European Ceramic Society*, *34*(2), 425–433.
6. Vijayan, S., Wilson, P., & Prabhakaran, K. (2016). Porosity and cell size control in alumina foam preparation by thermo-foaming of powder dispersions in molten sucrose. *Journal of Asian Ceramic Societies*, *4*(3), 344–350.
7. Vijayan, S., Narasimman, R., & Prabhakaran, K. (2016). Fabrication of large alumina foams by pyrolysis of thermo-foamed alumina–sucrose. *Journal of*

Materials Research, *31*(2), 302–309.

8. Vijayan, S., Wilson, P., & Prabhakaran, K. (2016). Low density ceramic foams from alumina-sucrose using magnesium nitrate as a blowing and setting agent. *Journal of Materials Research*, *31*(19), 3027–3035.
9. Vijayan, S., Wilson, P., & Prabhakaran, K. (2017). Ultra low-density mullite foams by reaction sintering of thermo-foamed alumina-silica powder dispersions in molten sucrose. *Journal of the European Ceramic Society*, *37*(4), 1657–1664.
10. Vijayan, S., Wilson, P., Sreeja, R., & Prabhakaran, K. (2016). Low-Density Open Cellular Silicon Carbide Foams from Sucrose and Silicon Powder. *Journal of the American Ceramic Society*, *99*(12), 3866–3873.
11. Vijayan, S., Wilson, P., Sreeja, R., & Prabhakaran, K. (2017). Ultralight SiC foams with improved strength from sucrose and silicon powder using magnesium nitrate blowing agent. *Materials Letters, 194,* 126-129.

Patent

- K. Prabhakaran K, Sujith Vijayan, A method for the preparation of macroporous ceramics with the wide range of porosities, Indian Patent File No. 1544/CHE/2014.